



UNIVERSITÀ DEGLI STUDI DI TRENTO

Facoltà di Scienze Matematiche Fisiche e Naturali

Development of Solar Sensitive Thin Film for Water Splitting and Water Heating using Solar Concentrator

DOCTOR OF PHILOSOPHY IN PHYSICS

By

Rupali S. Dholam

A dissertation submitted to the Doctorate School of
University of Trento, Italy.
In partial fulfillment of requirements
For the degree of Doctor of Philosophy

Supervisor:

Prof. Antonio Miotello

Co-Supervisor:

Dr. Nainesh Patel

December 2010

Contents

Chapter 1: Towards A Sustainable Energy	5
1.1 Reasons to change Current energy system	6
1.2 Renewable energy : A wave of the future	12
1.3 Renewable sources	13
1.4 Solar Energy	15
1.5 Solar powered hydrogen conversion: Towards renewable energy future	17
1.6 Different ways to harvest and use solar energy	22
1.7 Solar Power concentrator: Efficient way to utilize more solar energy	23
1.8 Outline of Thesis	27
1.9 References	29
Chapter 2: Solar sensitive TiO₂ thin film for hydrogen production by photocatalytic water splitting	31
2.1 Introduction	32
2.1.1 Mechanism of hydrogen production in photo-electrochemical cell	33
2.1.2 The Semiconductor Photoanode	37
2.1.3 Brief Overview of Titanium Dioxide	45
2.1.4 Applications of TiO ₂ photocatalyst.	47
2.1.5 References	48
2.2 TiO ₂ thin film photocatalyst using physical and chemical methods for hydrogen production	54
2.2.1 Experimental methods	54
2.2.2 Results and Discussion	57
2.2.3 Conclusion	69
2.2.4 References	70
2.3 Visible light active Cr-Fe doped TiO ₂ thin film for water splitting.	73
2.3.1 Experimental methods	73

2.3.2 Results and Discussion	76
2.3.3 Conclusion	94
2.3.4 References	95
2.4 Efficient solar sensitized multilayer Cr-doped TiO ₂ thin film for water Splitting	97
2.4.1 Experimental methods	98
2.4.2 Results and Discussion	100
2.4.3 Conclusion	116
2.4.4 References	118
2.5 Efficient Hydrogen production using vanadium doped TiO ₂ thin film	120
2.5.1 Experimental methods	120
2.5.2 Results and Discussion	122
2.5.3 Conclusion	138
2.5.4 References	139
2.6 Low energy ion-beam modification of TiO ₂ photocatalyst thin film for Visible light absorption	140
2.6.1 Experimental methods	140
2.6.2 Results and Discussion	141
2.6.3 Conclusion	149
2.6.4 References	150
Chapter 3: Development of solar water heating system.	152
3.1 Introduction	153
3.2 Design of solar water heating system	154
3.3 Synthesis of Solar Absorber material: copper oxide	155
3.3.1 Experimental	157
3.3.2 Results and Discussion	158
3.4 Synthesis of multilayer antireflection coatings	166
3.4.1 Experimental	166
3.4.2 Results and Discussion	168
3.5 Efficiency of water heating system	176

3.6 Comparison with flat plate and vacuum tube collectors	179
3.7 Conclusion	180
3.8 References	181
Chapter 4: Development of spectral selective solar absorber for high temperature application.	182
4.1 Introduction	183
4.2 Experimental methods	186
4.3 Results and discussion	191
4.4 Conclusion	196
4.5 References	197
Summary:	198
Acknowledgement:	202
List of Publications:	204
Appendix:	205

Chapter 1

Towards A Sustainable Future

This chapter addresses the question on why it is necessary to focus towards alternative or renewable energy and challenges related to environmental conservation. The first section is dedicated to consider the large volumes of carbon dioxide in the atmosphere created by the increased human activity. Later section specifies the significance of alternative or renewable energy in near future and lists its possible resources. The following sections illustrate advantages and different ways to harvest solar energy. The importance of solar powered hydrogen generation for power generation by means of fuel cell is also revealed. A section is also devoted to efficient solar concentrator to utilize most part of solar spectrum. The chapter is ended with the outline of the thesis with short introduction on each chapter.

1.1 Reasons to change Current energy system

Humanity can prevent catastrophic climate change if we act now and adopt policies that reduce energy usage. The frequent utilization of fossil fuels is affecting globe such as climate change, world energy conflicts and energy source shortages which have threatened world stability. What is needed now is a transformation of the entire global energy system. No one benefits from the release of greenhouse gas emissions, but developed and developing nations alike will benefit in numerous ways from the transition to an energy-efficient and renewable world. The following negative effects make us to think about transformation of current global energy system.

1.1.1 *Decrease in fossil fuel reserves.*

Fossil fuels play a crucial role in the world energy market. The discovery of fossils for energy purpose has turned the wheel of revolution in the history of mankind. Man's fuel needs, since the olden times, have been met through the use of fossil fuels. Fossil fuels, as the name suggests, were formed from the organic remains of prehistoric plants and animals. They are responsible for much of the world's electric power and total energy demands. Since 1900, the world's consumption of fossil fuels has nearly doubled every 20 years (Fig. 1a). It is obvious that current use of fossil fuels in various sectors for heat and power generation (including hydrogen production from them) continues threatening global stability and sustainability. These are locally, regionally, and globally more evident than before. This concern is even further compounded by increasing world population, rapid technological development, increasing energy requirements, etc (Fig. 1b). Although in the past fossil fuels were prime in meeting the energy needs. However, the current global picture does not allow utilizing fossil fuels indefinitely as the principal energy sources due to the rapid increase of world energy demand and energy consumption. So, there is an urgent need to switch to sustainable energy, such as such as solar, wind, and energy carriers such as hydrogen, etc

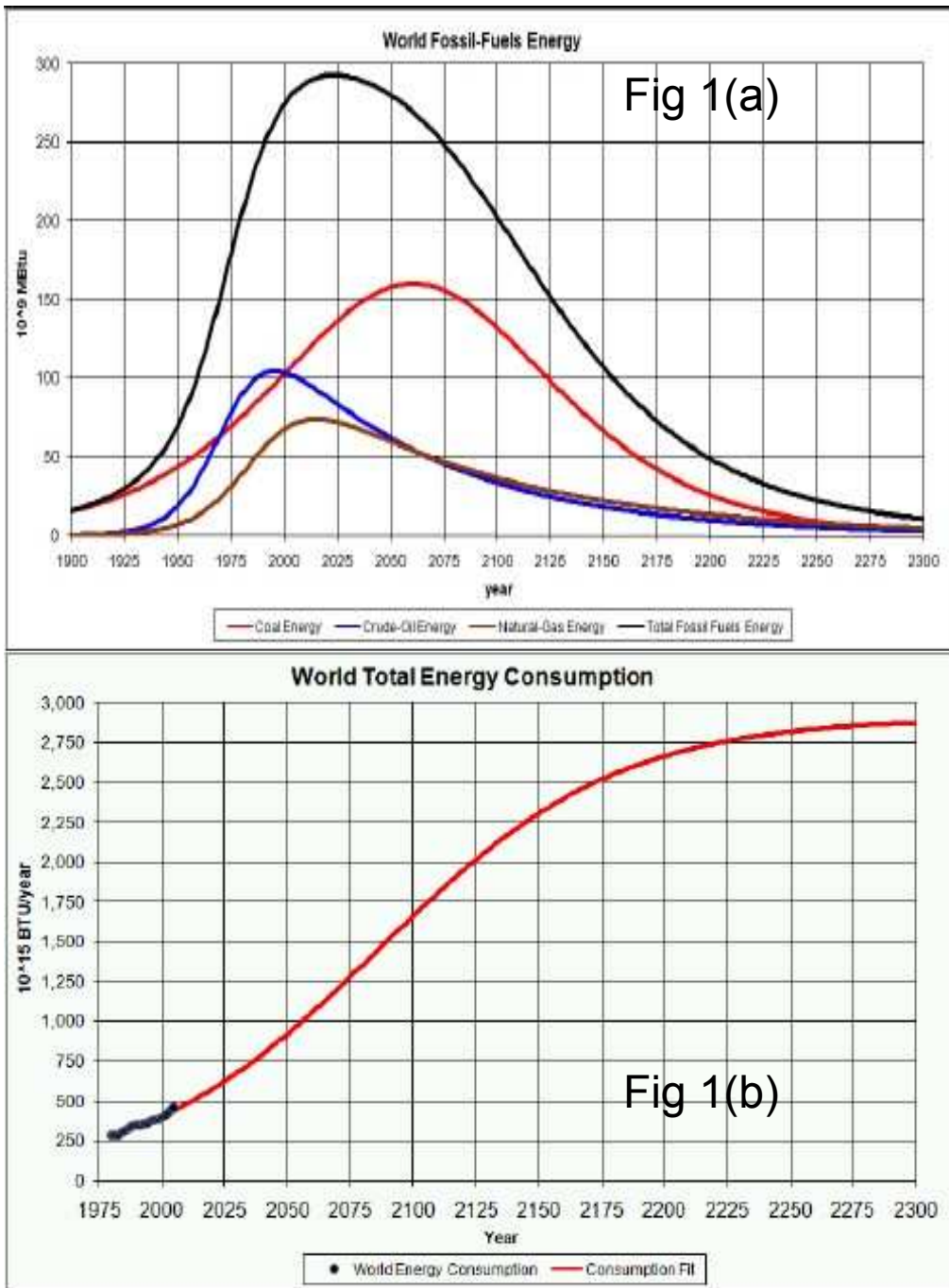


Figure 1 (a) Energy obtainable from fossil fuels as a function of time. (b) Total amount of energy consumption data. The figures are adopted from [1]

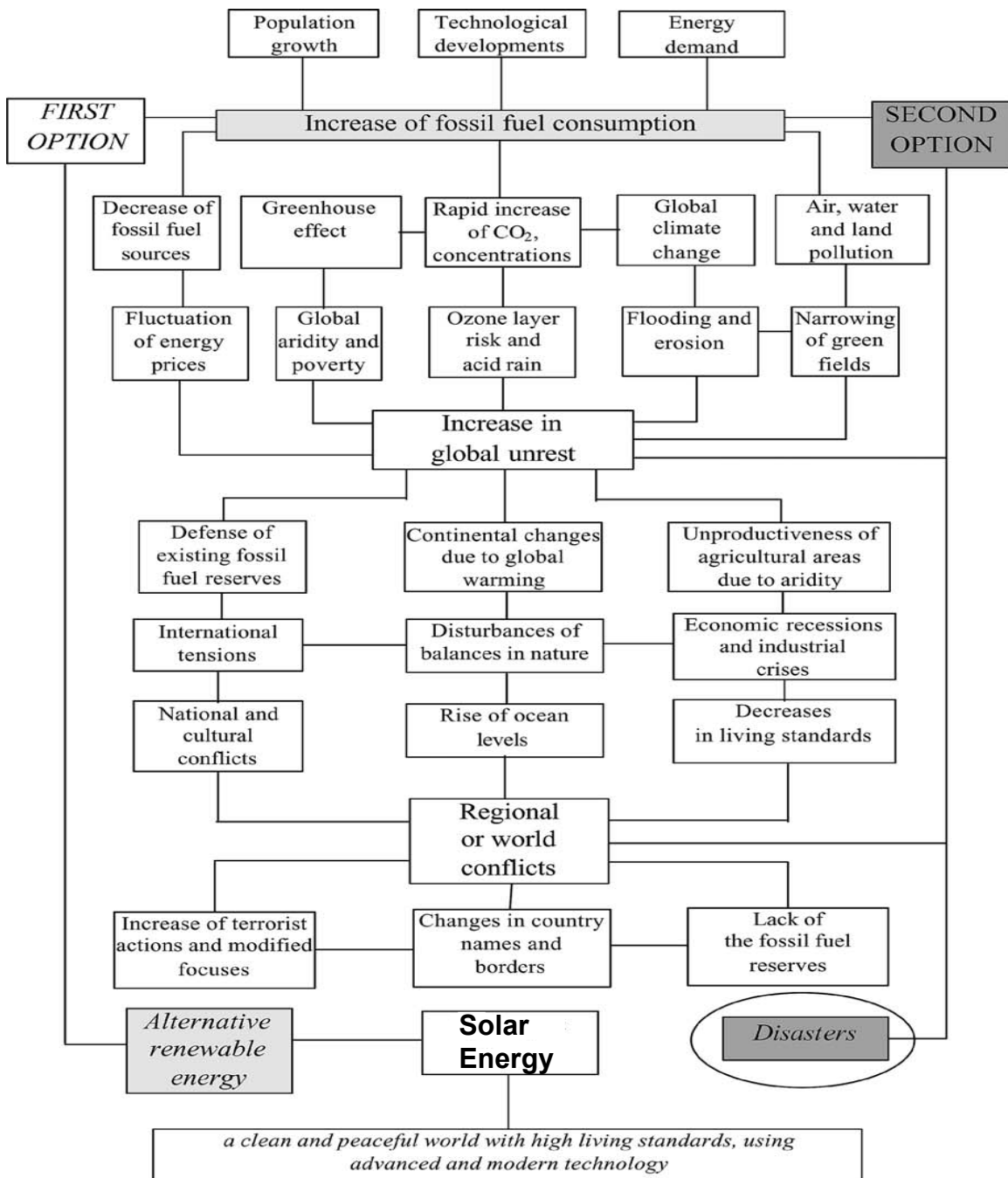


Figure 2: Illustration of possible global problems from increasing use of fossil fuels and the consequent need for hydrogen energy systems. The key drivers are shown at the top. The first option (shown on the left) follows a path of increasing use of renewable and sustainable energy, while the second option (right) allows for increasing use of fossil fuels and the problems related to that path. The figure is adopted from [2]

1.1.2. Global climate change: global warming

The earth has gone through many natural climatic cycles during its long history. The scary part is that we are causing changes at an unbelievable rate, much faster than normal. The burning of fossil fuels such as gasoline, coal, oil, natural gas in combustion reactions releases greenhouse gases like CO_x, SO_x, NO_x, etc at a life-threatening rate and they cause air pollution to the atmosphere (Fig 3). Gas, particulate matter and dust clouds in the atmosphere absorb a significant portion of the solar radiation directed at the Earth and cause a decrease in the oxygen available for the living things and originating global warming (Fig 3). Global Warming, Greenhouse Effect, Climate Change etc. are occurring right now! Most scientists believe that the warming of the climate will lead to more extreme weather patterns [3] such as:

a) More hurricanes and drought

- Longer spells of dry heat or intense rain;
- Scientists have pointed out that Northern Europe could be severely affected with *colder* weather if climate change continues, as the arctic begins to melt and fresher water move to south. It would effectively cut off the Gulf Stream that brings warmth from the Gulf of Mexico.
- In South Asia, the Himalayan glaciers could retreat causing water scarcity in the long run.

b) Super-storms

The world's oceans are approaching 27⁰C or warmer during the summer. This increases the odds of major storms. When water reaches such temperatures, more of it evaporates priming hurricane or cyclone formation. Once born, a hurricane needs only warm water to build and maintain its strength and intensity. Furthermore, "as emissions of greenhouse gases continue to trap more and more of the sun's energy, that energy has to be dissipated, resulting in stronger storms, more intense precipitation and higher winds."

c) Rising Sea Levels

Water expands when heated, and sea levels are expected to rise due to climate change. Rising sea levels will also result as the polar caps begin to melt. Rising sea levels is already affecting many small islands. Rising sea levels will impact many coastlines, and a large mass of humanity lives near the coasts or by major rivers.

d) Increasing ocean acidification

Scientists are finding that oceans have been able to absorb some of the excess CO₂ released by human activity. This helped the planet to cool more than it otherwise could have been if these gases remained in the atmosphere. However, the additional CO₂ being absorbed is also resulting in the acidification of the oceans (when CO₂ reacts with water it produces a weak acid called carbonic acid, changing the sea water chemistry). This change is also occurring rapidly and some marine life may not have the chance to adapt. Some marine creatures are growing thinner shells or skeletons, for example. Some of these creatures play a crucial role in the food chain, and in ecosystem biodiversity.

e) Failing Agricultural Output; Increase in World Hunger

Drought and desertification are starting to spread and intensify in some parts of the world. Failing agriculture in the future was predicted. Since longtime scientists, who looked at projections of global warming's impact on the average temperatures during the growing season, fear that rising temperatures will have a significant impact upon crop yields, most noticeably in the tropics and sub tropics. While warm weather can often be good for some crops, hotter than average temperatures for the entire season is often not good for plants. This would affect at least half the world's population that either live in the region or rely on food coming from that region.

The evidence that humans are causing global warming is strong, but the question of what to do about remains controversial. Economics, sociology, and politics are all important factors in planning for the future. Even if we stop emitting greenhouse gases (GHGs) today, the Earth would still warm by another degree Fahrenheit or so. But what we do from today forward makes a big difference.

Annual Greenhouse Gas Emissions by Sector

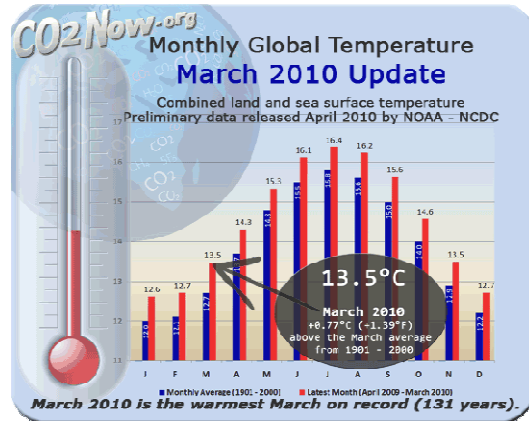
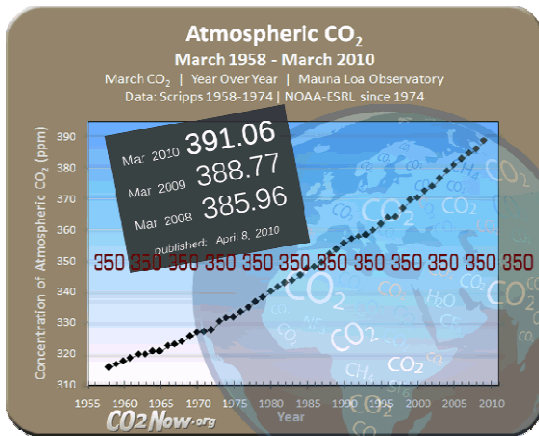
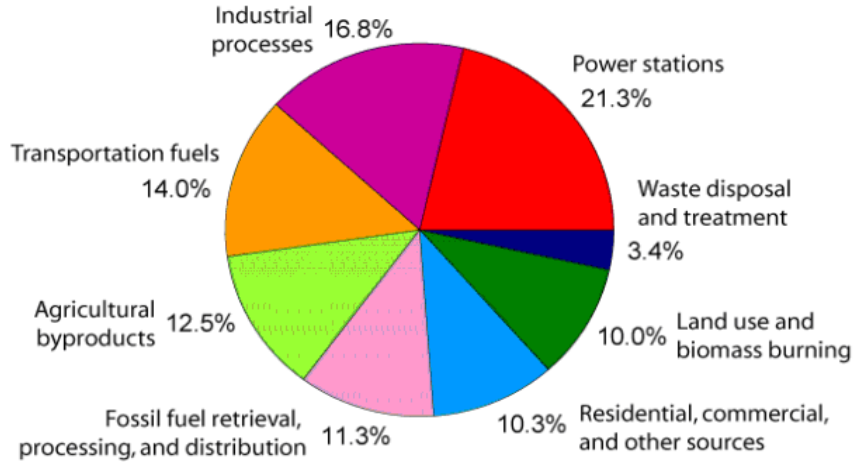


Figure 3: Above graph shows the monthly average concentration of CO₂ in the atmosphere. The concentration of CO₂ in the atmosphere is increasing at an accelerating rate from decade to decade. The graph is collected from ref [4]

1.1.3 Conflicts and wars due to fluctuations of energy prices, economic recessions, decrease of living standards and increase of unrest among countries.

There is clearly a problem of worldwide energy dependence. Oil, which nowadays constitutes around 33% of primary world energy is produced in a small number of countries organized around OPEC (Organization of the Petroleum Exporting Countries), characterized by political instability in their international relationships, at least from the western point of view. For this reason, the price of petroleum is subject to important fluctuations due to economic and political reasons. In the last few years, which have been dominated by the consequences of the Iraq war and the instability in Iran–USA relationships, the price of petroleum has increased to \$75/Brent bbl (1-May-2006), an unprecedented and excessive price for the developed countries that also restricts the progress of developing countries which depend on oil for their energy supply.

The decrease of available fossil fuel reserves and increased fuel costs since the mid- to late-1900s has led to variations in lifestyles and standards of life. These effects have in some regions decreased living standards of entire societies. Problems are often attributed to decreases of fossil fuel energy reserves, and therefore the transition to a sustainable energy should be encouraged.

1.2 Renewable energy: The future.

Most of the energy we use today comes from fossil fuels-coal, oil, and natural gas. These fuels are being consumed more rapidly than they are replaced [5]. This means that someday we could run out of these fuels. In recent years the production and use of renewable fuels has grown more quickly to attain cleaner and less polluting environment. A number of State and Federal Government incentives, and also most of the developed countries have started investing in renewable energy. Sun, wind, and water are perfect energy sources depending on where we are. They are non-polluting, renewable and efficient. The use of renewable energy sources not only helps to reduce global carbon dioxide emissions but also add some much-needed flexibility to the energy resource by decreasing our dependence on limited reserves of fossil fuels. Essentially, these renewable

energy sources create their own energy. The object is to capture and harness their mechanical power and convert it to electricity in the most efficient and productive manner possible. There are more than enough renewable energy sources to supply all of the world's energy needs forever; however, the challenge is to develop the capability to efficiently and economically capture, store and use the energy when needed.

The use of renewable fuels is expected to continue to grow over the next 30 years, although we will still rely on non-renewable fuels to meet most of our energy needs. However, one day much of the energy we use may come from renewable sources as scientists find better ways to develop renewable energy [6].

1.3 Renewable sources

A natural resource is a renewable resource that can be replenished at a rate equal to or greater than its rate of depletion; for example, solar, wind, geothermal and biomass resources. Renewable resources are now a focal point of the environmental movement, both politically and economically. Energy obtained from renewable resources puts much less strain on the limited supply of fossil fuels (non-renewable resources). The problem with using renewable resources on a large scale is a cost problem and in most cases, more research is needed to make their use cost efficient.

There are many forms of renewable energy. Most of these renewable energies depend in one or another way on sunlight. Wind and hydroelectric power are the direct result of differential heating of the Earth's surface which leads to air moving (wind). Solar energy is the direct conversion of sunlight using panels or collectors. Biomass energy is stored sunlight contained in plants. Other renewable energies that do not depend on sunlight are geothermal energy, which is a result of radioactive decay in the crust combined with the original heat of accreting the Earth, and tidal energy, which is a conversion of gravitational energy [7].

Solar : This form of energy relies on the nuclear fusion power from the core of the Sun. This energy can be collected and converted in a few different ways. The range is from solar water heating with solar collectors or attic cooling with solar attic fans for domestic use to

the complex technologies of direct conversion of sunlight to electrical energy using mirrors and boilers or photovoltaic cells. Unfortunately these are currently insufficient to fully power our modern society.

Wind Power : The movement of the atmosphere is driven by differences of temperature at the Earth's surface due to varying sunlight on the Earth's surface. Wind energy can be used to pump water or generate electricity, but requires extensive areal coverage to produce significant amounts of energy.

Hydroelectric energy: This form uses the gravitational potential of elevated water that was lifted from the oceans. It is not strictly speaking renewable since all reservoirs eventually fill up and require very expensive excavation to become useful again. At this time, most of the available locations for hydroelectric dams are already used in the developed world.

Biomass: This is the term for energy from plants. Energy in this form is very commonly used throughout the world. Unfortunately the most popular is the burning of trees for cooking and warmth. This process releases copious amounts of carbon dioxide gases into the atmosphere and is a major contributor to unhealthy air in many areas. Some of the more modern forms of biomass energy are methane generation and production of alcohol for automobile fuel and fueling electric power plants.

Geothermal power: Energy left over from the original accretion of the planet and augmented by heat from radioactive decay seeps out slowly everywhere, everyday. In certain areas the geothermal gradient (increase in temperature with depth) is high enough to generate electricity. This possibility is limited to a few locations on Earth and many technical problems exist that limit its utility. Another form of geothermal energy is Earth energy, a result of the heat storage in the Earth's surface. Soil everywhere tends to stay at a relatively constant temperature, the yearly average, and can be used with heat pumps to heat a building in winter and cool a building in summer. This form of energy can lessen the need for other power to maintain comfortable temperatures in buildings, but cannot be used to produce electricity.

Other forms of energy: Energy from tides, the oceans, and hot hydrogen fusion are other forms that can be used to generate electricity. Each of these suffers from one or another significant drawback and cannot be relied upon at this time to solve the upcoming energy crunch.

1.4 Solar Energy:

Solar energy, without which there would be no life on Earth, is emitted by the sun in the form of radiation. Although solar energy is stronger on the equator than it is at the North or South Pole, it is available everywhere during the day [8]. The Earth receives an incredible supply of solar energy. The sun, an average star, is a fusion reactor that has been burning over 4 billion years. It provides enough energy to the earth in one hour to supply the world's energy need for one year. In one day, it provides more energy than our current population would consume in 27 years. In fact, "The amount of solar radiation striking the earth over a three-day period is equivalent to the energy stored in all fossil energy sources." This energy can be converted into other forms of energy, such as heat and electricity [6].

Present and Future Advantages of Solar Energy

Solar energy enjoys many environmental and economic advantages over other forms of energy currently used [9]. These include:

- Environmentally Friendly
 - Non-polluting: Solar electricity generation produces no emissions while the current alternative, fossil fuel combustion, releases more than a pound of carbon dioxide emissions for every kilowatt hour.
 - Non-consumptive: The sun's radiation is a limitless resource that can be collected without the environmentally destructive processes of mining or pipelines.
- Economically Beneficial
 - By 2027, PV will be the most cost-effective solution (even without any government subsidies or advantages from its environmental cleanliness) in whole world.

- Immediate and permanent savings: Properly financed systems will provide consumers with cheaper electricity from the day of installation.
- Technological advancements: Improvements in solar technologies offer reduced costs and greater efficiency.
- Easily Accessible
 - Security: The price of solar electricity does not fluctuate with politics or supply speculation; there will never be a shortage that will cause solar electricity to become unaffordable.
 - Already distributed: There are no expensive transportation costs for solar electricity because the sun is available everywhere.
 - Leapfrogging: Solar electricity will allow sun-rich developing nations to leapfrog as they are doing with wireless telecommunications to new energy architecture without having to install expensive land-based grids.

Using the sun's energy is no longer wishful thinking from idealists of environmental sustainability; it is the solution to the world's approaching energy crisis and an economic inevitability. We are rapidly moving toward a dramatic and dominant role for solar energy - a trend that should be encouraged by both policy makers and capital markets because, in the end, it benefits everyone.

Disadvantages of solar energy that research activity may solve:

- The initial cost is the main disadvantage of installing a solar energy system, largely because of the high cost of the semi-conducting materials used in manufacturing.
- The cost of solar energy is also high compared to non-renewable utility-supplied electricity. As energy shortages are becoming more common, solar energy is becoming more price-competitive.
- Solar panels require quite a large area for installation to achieve a good level of efficiency.
- The efficiency of the system also relies on the location of the sun, although this problem can be overcome with the installation of certain components.
- The production of solar energy is influenced by the presence of clouds or pollution in the air.

- Similarly, no solar energy will be produced during night time although a battery backup system and/or net metering will solve this problem.
- As far as solar powered cars go - their slower speed might not appeal to everyone caught up in today's rat race.

1.5 Solar powered Hydrogen Generation: Towards renewable energy future

Hydrogen is acclaimed to be an energy carrier of the future. It can be used indeed as a media to store energy. Currently, it is mainly produced by fossil fuels, which release greenhouse gases and other climate-changing emissions. Thermo chemical cycles, such as hybrid-sulphur cycle, metal oxide based cycle and electrolysis of water are the most promising processes for environmentally benign hydrogen production for the future. It can be produced using solar energy in different ways namely; using solar electricity and solar thermal energy. The solar electricity can be used in electrolyzers to dissociate the distilled water into hydrogen and oxygen. The thermal energy can be utilized in (1) low temperature and (2) high temperature applications. The idea of using solar energy is to protect environment from the unwanted greenhouse gas emissions.

Classification of solar hydrogen production

Hydrogen production using solar energy can be mainly classified into four types. (1) photovoltaic (2) solar thermal energy (3) photo electrolysis, and (4) biophotolysis.

The thermal energy from solar energy can be utilized in two ways; low temperature and high temperature applications. Photovoltaic, photo electrolysis and bio photolysis are considered as low temperature application whereas solar thermolysis, solar thermo chemical cycles, solar gasification, solar reforming and solar cracking are high temperature applications of concentrated solar thermal energy. Concentrating solar energy can also be utilized to produce steam and then using the power of steam electricity can be produced. The produced electricity can be utilized to produce hydrogen via electrolysis. Four major ways in which solar energy can be utilized to produce hydrogen are given in Fig. 4

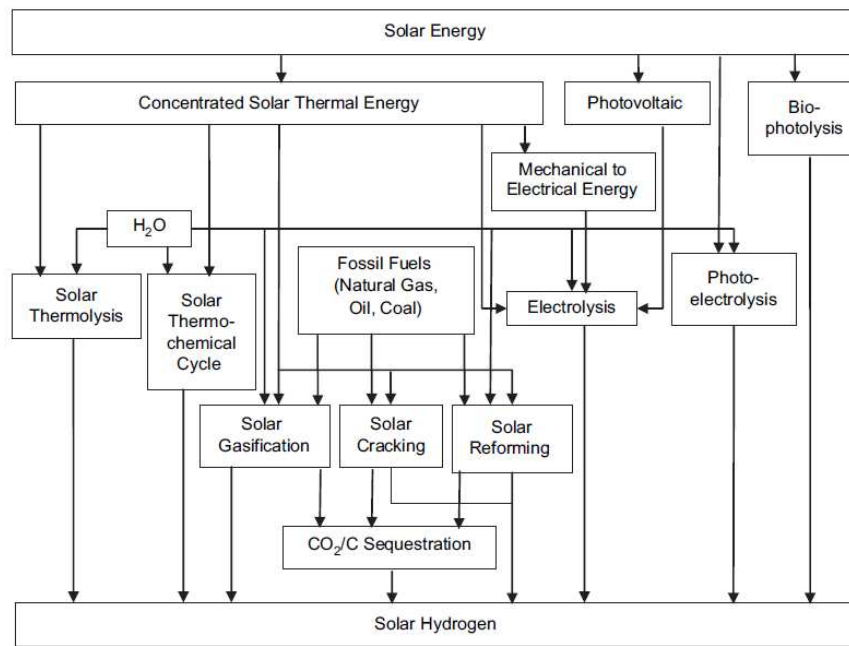


Figure 4: Solar hydrogen production

Solar photovoltaic based electrolysis

In the beginning of 70s the PV panels were utilized to produce hydrogen by electrolysis of water using the electricity produced by the photovoltaic cells [10-13]. The electrolysis of water can be carried out by a current generated from the photovoltaic cells. An extensive research in this area is necessary as the hydrogen produced by this technology is not cost effective. The electrolysis of distilled water using electricity produced by the PV panel takes place in electrolyzer unit and produces hydrogen and oxygen as the end product (Fig 5). One advantage with PV technology is that it does not emit greenhouse gases during the operation. The efficiency of modern photo converters (i.e. photovoltaic's) and electrolyzers' is about 20% and 80% respectively. [14]

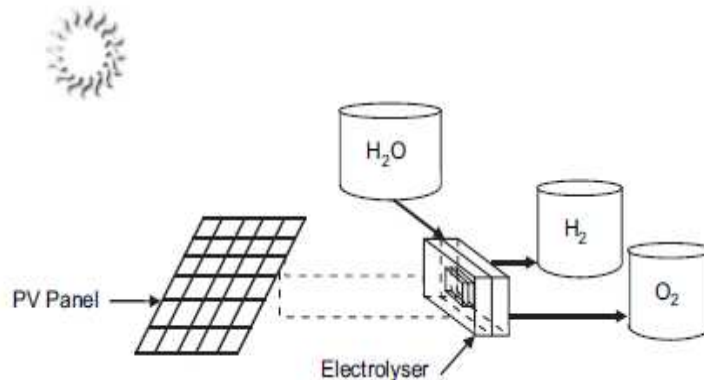


Figure 5: Schematic diagram of photovoltaic hydrogen production system

Solar photo-electrolysis

Another method to convert sunlight into hydrogen is by photo-electrolysis of water that uses photo-electrochemical light collecting systems (PEC-photo-electrochemical cell) to power the electrolysis of water. Fig. 6 shows a schematic of a single PEC proposed by Fujishima and Honda [15]. When exposed to sunlight, a semiconductor photo-electrode (anode or cathode), submerged in an aqueous electrolyte may generate sufficient voltage to split water molecules [16]. The device does not require a separate power generator and electrolyzer. The maximum theoretical efficiency is about 35%. However, the solar-to-hydrogen conversion efficiency of the materials has not yet met requirements for practical use due to the limitation of usable solar spectrum.

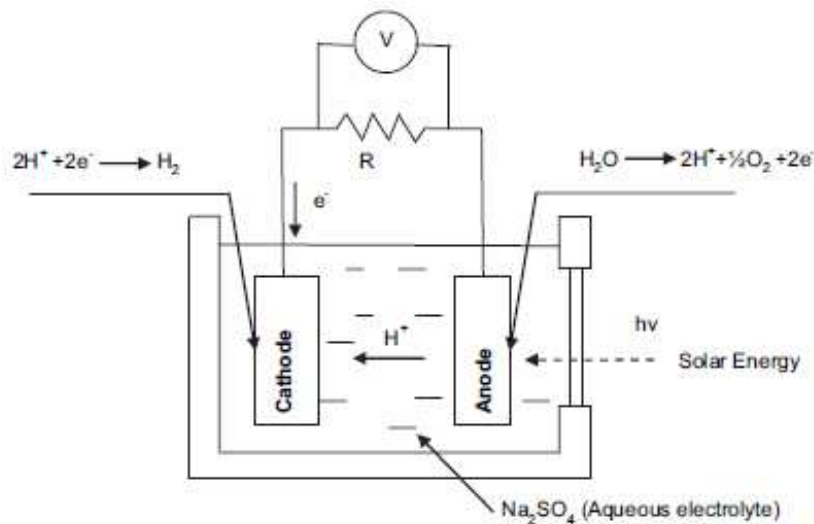


Figure 6: Schematic diagram of solar photo-electrolysis

Solar photo-biological hydrogen production

Photo-biological hydrogen production uses the processes same as plant and algal photosynthesis, for hydrogen production. The biological hydrogen production can be classified into:

- (1) Light dependent, and
- (2) Light independent process.

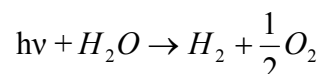
First processes, that is light dependent process, includes direct or indirect biophotolysis and photo-fermentation whereas the second one, light independent process includes dark fermentation [17]. Plant and algal photosynthesis results in the splitting of water into oxygen and a reducing agent strong enough to reduce CO₂ or protons in to carbohydrates or hydrogen respectively. One advantage of biological processes is to be catalyzed by microorganisms in an aqueous environment at ambient temperature and pressure [10]. Biological methods for solar hydrogen production have not yet been developed for commercial use, except for the laboratory stage and small (<10m²) out door demonstration scale systems [18]. This technology is still under development because of relatively low efficiency of photosynthesis as trees and agricultural crops convert sunlight at efficiencies less than 1% [19].

Concentrated solar thermal energy based hydrogen production

Various thermo-chemical methods are used for solar hydrogen production. Since all these methods involve endothermic reactions, they make use of thermal energy of concentrated solar radiation [21].

Solar thermolysis

The single-step thermal dissociation of water is known as water thermolysis and is represented by:

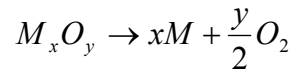


This reaction requires 1) a high temperature at above 2500 K to have a reasonable degree of dissociation, 2) an efficient technique for separating H₂ and O₂ to avoid ending up with an explosive mixture. Very high temperature required by the process poses severe material problems and can lead to significant re-radiation from the reactor, thereby lowering the absorption efficiency [21].

Solar thermo-chemical cycles

They do not have the H₂/O₂ separation problem and further allow operating at relatively moderate upper temperatures (1200 K) [21]. An efficient 2-step thermo-chemical cycle using metal oxide redox reactions is represented by [22, 23]

1st step (solar):



2nd step (non-solar):



Where M denotes a metal and M_xO_y the corresponding metal oxide. The first, endothermic step is the solar thermal dissociation of the metal oxide to the metal or the lower valence metal oxide. The second, non-solar, exothermic step is the hydrolysis of the metal to form H₂ and the corresponding metal oxide. The net reaction is (H₂O = H₂ + 0.5O₂), but since H₂ and O₂ are formed in different steps, the need for high temperature gas separation is thereby eliminated [20].

Concentrated solar thermal based electrolysis

The thermal energy coming from concentrating solar radiations (Fig. 7) can be applied to heat a specific fluid (phase change materials, molten salt mixtures [24]) at mid or high temperature, and then using that fluid to produce steams and consequently electricity. The phase change materials or molten salt mixtures can store thermal energy at about 500⁰C. These plants are known as thermodynamic solar plants. The electricity produced by these plants can be utilized for hydrogen production via electrolysis. In this route, the concentrated thermal energy can directly be used to produce steam and then using some steam turbine/engine the thermal energy can be converted to mechanical energy (rotary

motion) and then by coupling an electrical generator to it, electricity can be produced. Thermal energy can also be stored in molten salt mixtures that can be utilized to produce steam for off sunshine periods.

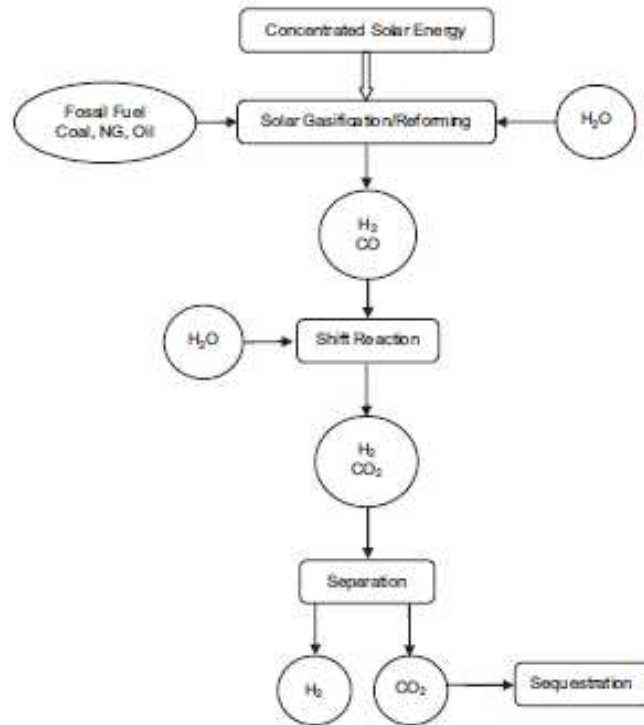


Figure 7: Schematic diagram of solar gasification/reforming

1.6 Different ways to harvest solar energy.

Harnessing solar energy involves both the direct use of the radiated heat as well as its conversion to electricity in the most efficient way possible. There are three categories that define solar energy technology:

1. Passive solar collection begins with the design of the buildings that includes optimal location, windows facing south, walls that absorb heat and light, and plenty of insulation. The heat or light that is collected is used in its original form of heat or light such as in a greenhouse.

2. Active solar collection implies converting solar energy to a more usable form of heat or electricity. Thermal applications include heat collection and heat-driven mechanisms, such as converting water to steam to power a steam engine that generates electricity. Electric processes use photovoltaic cells that create a moving electric charge that produces a direct electric current.
3. Finally, a third distinction in solar energy is related to the degree of concentration of the sun's energy. Concentrating systems engage mirrors and lenses to direct the sunlight to the area of collection. In some systems, parabolic trough-shaped structures of photovoltaic cells can even be powered to follow the motion of the sun to increased electricity generation [25].

1.7 Solar Power concentrator: Efficient way to utilize more solar energy

Concentrating Solar Power:

Concentrating solar power (CSP) technologies use mirrors to reflect and concentrate sunlight onto receivers that collect the solar energy and convert it to heat. This thermal energy can then be used to produce electricity via a steam turbine or heat engine driving a generator.

One way to classify concentrating solar power technologies is by how the various systems collect solar energy.

The following are three basic CSP technology systems:

- a) Linear Concentrator Systems
- b) Dish/Engine Systems
- c) Power Tower Systems

a) Linear Concentrator Systems

Linear CSP collectors capture the sun's energy with large mirrors that reflect and focus the sunlight onto a linear receiver tube. The receiver contains a fluid that is heated by the sunlight and then used to create superheated steam that spins a turbine that drives a

generator to produce electricity. Alternatively, steam can be generated directly in the solar field, eliminating the need for costly heat exchangers.

Linear concentrating collector fields consist of a large number of collectors in parallel rows that are typically aligned in a north-south orientation to maximize both annual and summertime energy collection. With a single-axis sun-tracking system, this configuration enables the mirrors to track the sun from east to west during the day, ensuring that the sun reflects continuously onto the receiver tubes.

Parabolic Trough Systems

The predominant CSP systems are linear concentrators using parabolic trough collectors (Fig.8). In such a system, the receiver tube is positioned along the focal line of each parabola-shaped reflector. The tube is fixed to the mirror structure and the heated fluid—either a heat-transfer fluid or water/steam—flows through and out of the field of solar mirrors where it is used to create steam (or, for the case of a water/steam receiver, it is sent directly to the turbine).

Currently, the largest individual trough systems generate 80 megawatts of electricity. However, individual systems being developed will generate 250 megawatts. In addition, individual systems can be collocated in power parks. This capacity would be constrained only by transmission capacity and availability of contiguous land area. Trough designs can incorporate thermal storage. In such systems, the collector field is oversized to heat a storage system during the day that can be used in the evening or during cloudy weather to generate additional steam to produce electricity. Parabolic trough plants can also be designed as hybrids, meaning that they use fossil fuel to supplement the solar output during periods of low solar radiation. In such a design, a natural-gas-fired heater or gas-steam boiler/re-heater is used. In the future, troughs may be integrated with existing or new combined-cycle natural-gas- and coal-fired plants.

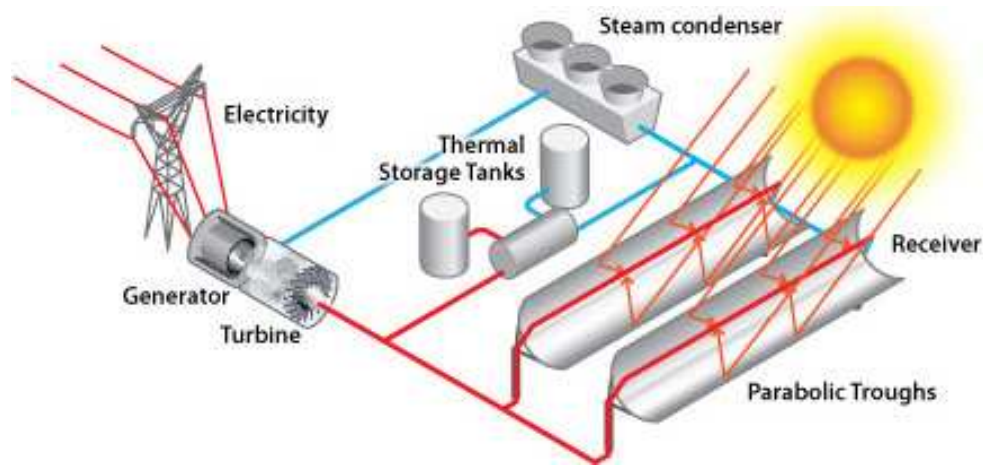


Figure 8: A linear concentrator power plant using parabolic trough collectors.

Linear Fresnel Reflector Systems

A second linear concentrator technology is the linear Fresnel reflector system (Fig.9). Flat or slightly curved mirrors mounted on trackers on the ground are configured to reflect sunlight onto a receiver tube fixed in space above these mirrors. A small parabolic mirror is sometimes added atop the receiver to further focus the sunlight.

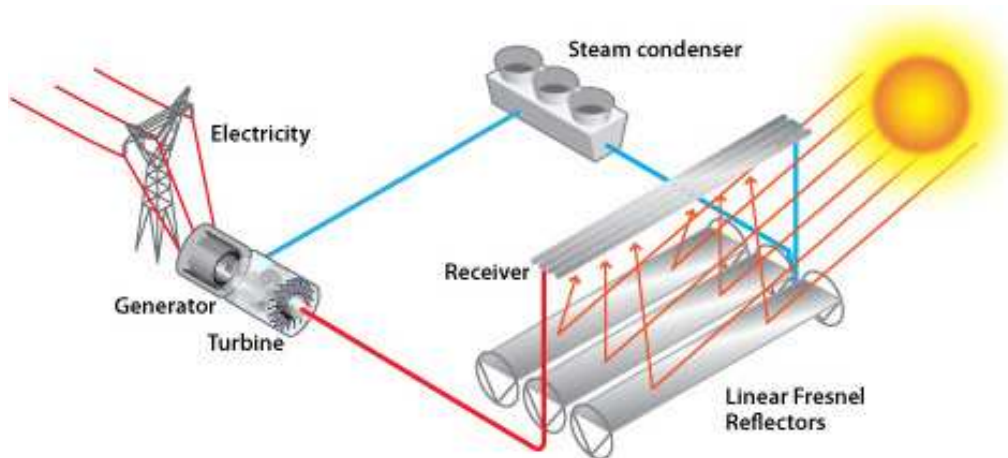


Figure 9: A linear Fresnel reflector power plant.

b) Dish/Engine Systems

The dish/engine system is a concentrating solar power (CSP) technology (Fig.10) that produces relatively small amounts of electricity compared to other CSP technologies

typically in the range of 3 to 25 kilowatts. A parabolic dish of mirrors directs and concentrates sunlight onto a central engine that produces electricity. The two major parts of the system are the solar concentrator and the power conversion unit.

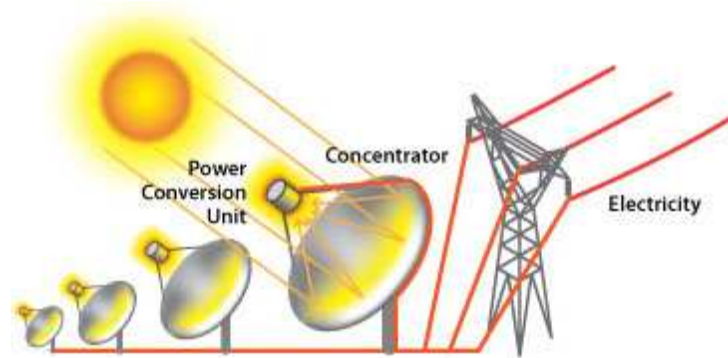


Figure 10: A dish/engine power plant.

Solar Concentrator

The solar concentrator, or dish, gathers the solar energy coming directly from the sun. The resulting beam of concentrated sunlight is reflected onto a thermal receiver that collects the solar heat. The dish is mounted on a structure that tracks the sun continuously throughout the day to reflect the highest percentage of sunlight possible onto the thermal receiver.

Power Conversion Unit

The power conversion unit includes the thermal receiver and the engine/generator. The thermal receiver is the interface between the dish and the engine/generator. It absorbs the concentrated beams of solar energy, converts them to heat, and transfers the heat to the engine/generator. A thermal receiver can be a bank of tubes with a cooling fluid—usually hydrogen or helium—that typically is the heat-transfer medium and also the working fluid for an engine. Alternate thermal receivers are heat pipes, where the boiling and condensing of an intermediate fluid transfers the heat to the engine.

The engine/generator system is the subsystem that takes the heat from the thermal receiver and uses it to produce electricity. Currently, the most common type of heat engine used in dish/engine systems is the Sterling engine. A Sterling engine uses the heated fluid to move

pistons and create mechanical power. The mechanical work, in the form of the rotation of the engine's crankshaft, drives a generator and produces electrical power.

c) Power Tower Systems

In this CSP technology, numerous large, flat, sun-tracking mirrors, known as heliostats, focus sunlight onto a receiver at the top of a tower (Fig.11). A heat-transfer fluid heated in the receiver is used to generate steam, which, in turn, is used in a conventional turbine generator to produce electricity. Some power towers use water/steam as the heat-transfer fluid. Other advanced designs are experimenting with molten nitrate salt because of its superior heat-transfer and energy-storage capabilities. Individual commercial plants can be sized to produce up to 200 megawatts of electricity.

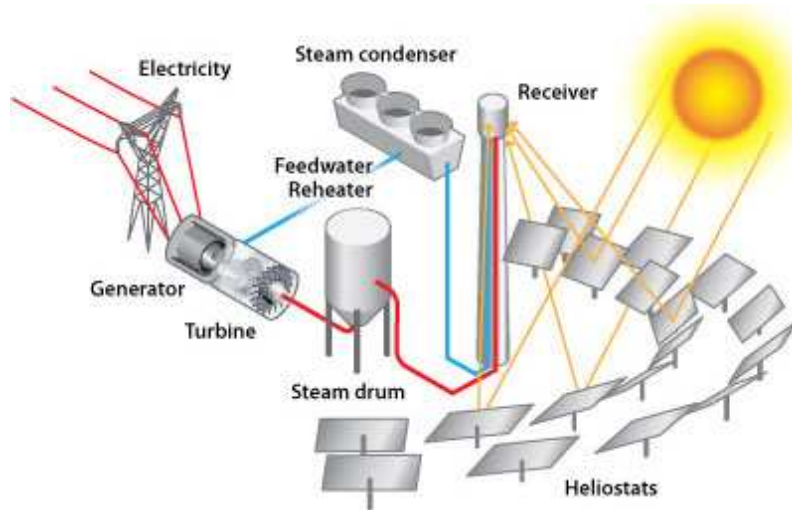


Figure 11: A power tower plant.

Power towers also offer good longer-term prospects because of the high solar-to-electrical conversion efficiency. Additionally, costs will likely drop as the technology matures [26].

1.8 Outline of Thesis :

All warning signs connected to the energy crisis, climate change, and water shortage force us to think about solution to utilize energy which comes from natural

resources. Therefore, the principal aim of this thesis, is to use renewable energy such as solar energy through collecting it with solar sensitive thin films. The body of thesis consists on four chapters including the present chapter 1. Chapter 2 presents the results on TiO₂ thin film photocatalyst for hydrogen production using water splitting. This chapter also briefly describes the backgrounds of the study, literature review, the objectives of the study, and the future works. Chapter 3 reports the synthesis and analysis of solar absorber in form of copper oxide thin film for water heating system using solar concentrator. This chapter also summarises the development of AR coating for the same system. Chapter 4 is devoted to the multilayered solar absorber thin film for high temperature application.

1.9 References

- [1] <http://www.roperld.com/science/Energy.htm>
- [2] Midilli, M. Aya, I. Dincer, M.A. Rosen On hydrogen and hydrogen energy strategies I: current status and needs. *International Journal of Hydrogen Energy* 2007 ; 32 : 1625-1637
- [3] Climate Change and Global Warming Introduction by Anup Shah August 10,2010
- [4] <http://timeforchange.org/cause-and-effect-for-global-warming>,
<http://timeforchange.org/CO2-cause-of-global-warming>
- [5] <http://www.nefl.org/ea/literacy.html>
- [6] U.S. energy information administration
http://www.eia.doe.gov/kids/energy.cfm?page=renewable_home-basics
- [7] <http://www.altenergy.org/renewables/renewables.html>
- [8] http://www.educapoles.org/multimedia/animation_detail/the_sun_a_form_of_energy_available_everywhere
- [9] <http://www.facts-about-solar-energy.com/solar-energy-advantages-disadvantages.html>
- [10] Yilanci A, Dincer I, Ozturk HK. A review on solar-hydrogen/ fuel cell hybrid energy systems for stationary applications. *Progress in Energy and Combustion Science* 2008;35(3):231–44
- [11] Hollmuller P, Joubert JM, Lachal B, Yvon K. Evaluation of a 5 kWp photovoltaic hydrogen production and storage installation for a residential home in Switzerland. *International Journal of Hydrogen Energy* 2000;25: 97–109.
- [12] Bilgen E. Solar hydrogen from photovoltaic-electrolyzer system. *Energy Conversion and Management* 2001;42:1047–57.
- [13] Lehman PA, Chamberlin CE, Pauletto G, Rocheleau MA. Operating experience with a Photo-voltaic hydrogen energy system. *International Journal of Hydrogen Energy* 1997;22(5):465-70
- [14] Rzaeva MP, Salamov OM, Kerimov MK. Modeling to get hydrogen and oxygen by solar water electrolysis. *International Journal of Hydrogen Energy* 2001;26:195–201.
- [15] Fujishima A, Honda K. Electrochemical photolysis of water at a semiconductor electrode. *Nature* 1972; 238: 37–8.

- [16] Nowotny J, Sorrell CC, Bak T, Sheppard LR. Solar-hydrogen: unresolved problems in Solid-state science. *Solar Energy* 2005; 78: 593–602.
- [17] Kotay SM, Das D. Biohydrogen as a renewable energy resource – prospects and potentials. *International Journal of Hydrogen Energy* 2008; 33: 258–63.
- [18] Luzzi A, Bonadio L, McCann M, editors. In pursuit of the future–25 years of IEA research towards the realisation of hydrogen energy systems. *International Energy Agency –Hydrogen Implementing Agreement*; 2004.
- [19] Benemann JR. Feasibility analysis of photobiological hydrogen production. *International Journal of Hydrogen Energy* 1997; 22: 979–87.
- [20] Steinfeld A, Meier A. Solar fuels and materials. In: *Encyclopedia of energy*. Cleveland:Elsevier 2004; p. 623–37.
- [21] Steinfeld A. Solar thermo-chemical production of hydrogen review. *Solar Energy* 2005; 78: 603–15.
- [22] Steinfeld A, Brack M, Meier A, Weidenkaff A, Wuillemin D. A solar chemical reactor for co- production of zinc and synthesis gas. *Energy* 1998; 23: 803–14.
- [23] Steinfeld A, Kuhn P, Reller A, Palumbo R, Murray JP, Tamaura Y. Solar-processed metals as clean energy carriers and water-splitters. *International Journal of Hydrogen Energy* 1998;23:767–74.
- [24] Zalba B, Marin JM, Cabeza LF, Mehling H. Review on thermal energy storage with phase change: materials, heat transfer analysis and applications. *Applied Thermal Engineering* 2003;23: 251–83.
- [25] http://synnoveenergy.com/about_solar_energy
- [26] <http://www1.eere.energy.gov/solar/csp.html>

Chapter 2

Solar sensitive TiO₂ thin film for hydrogen production by photocatalytic water splitting

This chapter presents a brief description of the Photo-electrolysis and development of solar sensitive thin films to split water molecules into hydrogen and oxygen. The chapter is divided into six sections. The first section introduces the basic mechanism of Photo-electrolysis and suitable photocatalyst for this kind of application. The section also introduces the essential parameters required by the semiconductor photo-electrode for efficient water splitting. By reading many literatures we found that TiO₂ is one of the most suitable candidate for water splitting application. Thus the second section shows the results on the synthesis of solar sensitive TiO₂ thin film photocatalyst by physics and chemical methods. The third section elucidates development of solar active Cr- or Fe-doped TiO₂ thin film to improve visible light absorption for water splitting. Improved photo-induced charge separation is achieved by deposition of efficient multilayer film for Cr- and V-doped TiO₂ film for water dissociation as reported in fourth and fifth section respectively. The sixth section describes the results on the implantation of ions such as Ar⁺, N⁺ in TiO₂ thin film in order to extend absorption in visible range of solar spectrum.

2.1 Introduction

Hydrogen is acclaimed to be an energy carrier of the future. It can be used as a media to store energy (example, metal hydrates). Currently, it is mainly produced by fossil fuels such as methane (CH_4), propane, coal and petroleum and biomass. Its "extraction" from certain compounds (e.g. methane and/or water) requires the use of energy from fossil fuel sources which release greenhouse gases (GHG) to the atmosphere. However, during usage, hydrogen burns very cleanly releasing very little GHGs emission to the atmosphere.

This problem of release of green house gases by use of fossil fuels to generate hydrogen could be solved by using electrolysis process. Water electrolysis decomposes H_2O into hydrogen and oxygen gas. Electrolytes dissolve and dissociate into cations and anions that carry the current; such processes can occur in an electrolysis cell, which consists of two electrodes, cathode and anode, where reduction and oxidation reactions simultaneously take place forming H_2 (at the cathode) and O_2 (at the anode). The fundamental problem in hydrogen production by water electrolysis is that today the electricity used to drive the process is primarily generated by the burning of fossil fuels [1]. The solution for this problem can be resolved by using photo-electrolysis.

Photo-electrolysis is generally carried out in cells having similar configuration as electrolysis cells with at least one of the two electrodes comprised of a semiconductor material. Upon exposure to sunlight the semiconductor electrode, called photo-electrode, immersed in an aqueous electrolyte solution generates, in an ideal case, enough electrical energy to drive the oxygen and hydrogen evolution reactions respectively at the interfaces of anode and cathode within the electrolyte. A necessary condition for such a spontaneous water splitting process upon illumination is that the semiconductor conduction band edge should lie at a position more negative (NHE as reference) relative to the reduction potential of water while the valence band edge should be more positive as compared to the oxidation potential. Photo-electrolysis integrates solar energy absorption and water electrolysis into a single photo-electrode. This method does not require a separate power generator.

2.1.1 Mechanism of hydrogen production in photo-electrochemical cell

The solar photo-electrochemical process is one of the most attractive methods for conversion of solar to chemical energy fuel(hydrogen) by means of water splitting. There are three possible ways to configure the electrodes in such systems: (1) Photo-anode made of n-type semiconductor and cathode made of metal. (2) Photo-anode made of n-type semiconductor and cathode made of p-type semiconductor. (3) Photocathode made of p-type semiconductor and anode made of metal. The simplest photo-electrochemical cell designed for such purpose consists of a semiconductor photo-electrode, or photo-anode and a metal counter electrode, or cathode, immersed in an electrolyte solution. With light incident upon the photo-anode, the photo-anode absorbs part of the light generating electron-hole pair which is then used for water splitting [1].

Photo-electrolysis of water involves several processes within a photo-anode, and at the photo-anode-electrolyte interface [2]. These are:

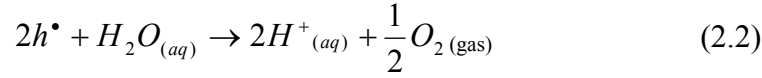
- (1) Absorption of light with energy exceeding the band gap.
- (2) Excitation of electrons from the valance band to the conduction band leaving holes behind in the valance band; that is to say, photo-generation of charge carriers (electron-hole pairs) due to light induced intrinsic ionization of the photo-anode.



where h is Planck's constant and ν is the frequency of light.

- (3) Charge separation and migration, at the same time; electrons passing through the photo-anode to the back-side electrical contact, and holes to the interface between the photo-anode and electrolyte.

(4) Oxidation of water at the photo-anode by holes.

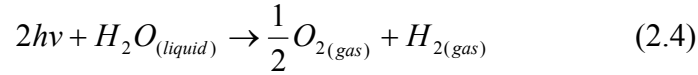


(5) The transport of H^{+} ions from the photo-anode to the cathode through the electrolyte.

(6) The transport of electrons from photo-anode to cathode through the external circuit, leading to the reduction of H^{+} ions into hydrogen gas at the cathode .



The overall reaction of the photo-electrochemical cell (PEC),



This reaction takes place when the energy of the photon absorbed by the photo-anode is equal to or larger than the threshold energy E_t ,

$$E_t = \frac{\Delta G^0}{2N_A} \quad (2.5)$$

Where ΔG^0 is standard free enthalpy (per mol) of reaction (2.4) = 237 kJ/mol and N_A is Avagadro's number = $6.022 \times 10^{23} \text{ mol}^{-1}$

Then we obtain

$$E = h\nu = 1.23 \text{ eV} \quad (2.6)$$

According to equation (2.6), electrochemical decomposition of water is possible when the electromotive force of the cell (EMF) is equal to or greater than 1.23 V .But sustained electrolysis generally requires $\sim 1.5 \text{ V}$ to overcome the impedance of the PEC.

Ideally, a photo-electrochemical cell should operate with no external bias so as to maximize efficiency and ease of construction. But practically it requires external bias to operate the splitting of water.

A common photoelectrolysis structure is that of a semiconductor photoanode and metal cathode, the band diagrams of which are illustrated in **Fig. 1** together with that of electrolyte redox couples [1].

In Fig.1(a) there is no contact between the semiconductor anode and metal cathode

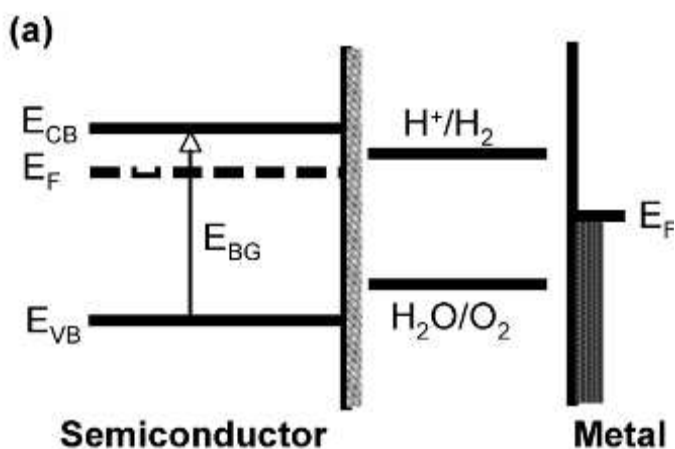


Figure 1(a): No contact and no chemical potential equilibrium.

As seen in **Fig.1(b)** contact between the two electrodes (no illumination) results in charge transfer from the semiconductor anode having a lower work function to the metal cathode having a higher work function until the work functions of both electrodes equilibrate. The result of this charge transfer is band bending by energy E_B. The energy levels of **Fig.1(b)** are not favorable for water decomposition since the H⁺/H₂ energy level is located above the cathode Fermi level.

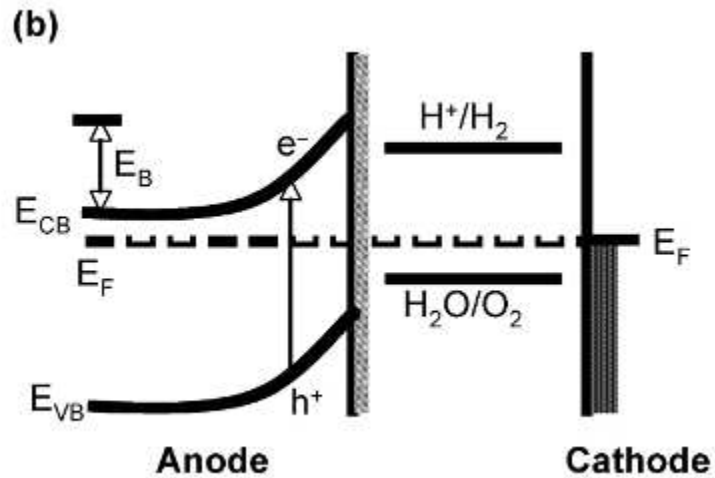


Figure 1(b): galvanic contact in dark.

Under illumination, **Fig. 1(c)**, both the photo-anode surface potential and the (H^+/H_2) water reduction potential are each lowered, but the (H^+/H_2) water reduction potential still remains above the cathode Fermi level.

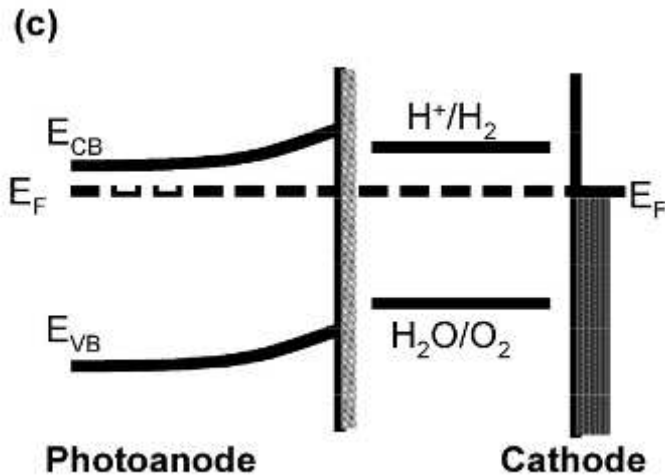


Figure 1(c): Energy diagram of PEC components after galvanic contact between anode and cathode

Anodic bias is thus needed to elevate the Fermi level of cathode above the water reduction potential, see **Fig.1(d)**, making the water splitting process feasible. This applied bias provides overvoltage at the metal cathode necessary to sustain the current flow, and increases the semiconductor band bending to maintain the required electric field.

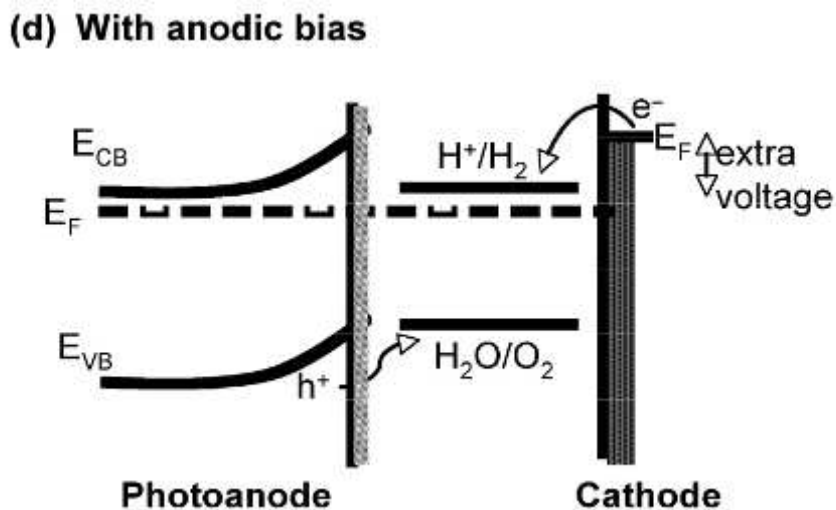


Figure 1(d): Effect of light on energy diagram of PEC with externally applied bias

2.1.2 Semiconductor photo-anode

The development of solar-hydrogen technology requires new photo-sensitive materials to be used as photo-electrodes for electrochemical devices converting solar energy into chemical energy. The photo-electrodes should be made of polycrystalline materials rather than single crystals (due to cost). The photo-sensitivity of polycrystalline materials must be approached using the influence of the local properties of interfaces, such as external surfaces and grain boundaries. Consequently, success in the development of novel photo-sensitive materials will be determined by progress in the science and engineering of materials interfaces. Specifically, more research is necessary to better understanding of the effects of interfacial properties, such as defect disorder, electronic structure, and related semi-conducting properties, on photo-electrochemical properties.

Semi-conducting oxides appear the most promising materials for photo-electrodes due to the fact that their properties may be modified by making changes in stoichiometry

and related semi-conducting properties [3]. Moreover, these materials are economically promising because their processing technologies are relatively simple.

Energetic and redox potentials of semiconductors

Semiconductor can absorb light with energy higher than certain energy threshold that is determined by band gaps (E_g) of semiconductors. Once photons are absorbed, photoelectrons and photo-holes are formed. The photo-generated electrons and holes quickly relax to the bottom of the conduction band and top of the valence band respectively by dissipating their kinetic energy. These electrons and holes can be used to drive redox reaction. Thermodynamically the energy level of conduction band edge (E_{cs}) measures the reduction strength of electron in the semiconductor, whereas valence band edge is a measure of oxidation power of holes in the semiconductor [4]. Figure 2 shows band edge energy levels of common semiconductors that are in contact with aqueous medium of pH 2.0 [5]

Different semiconductors possess different band energies. The higher the valence band edge potential, the higher the oxidizing power is. Small band gap semiconductors have a larger absorption spectrum. However, small band gap semiconductors normally do not have high valence band potential. In addition, many semiconductors, having small band gap, suffer serious chemical corrosion and photo corrosion when used as photocatalyst [6].

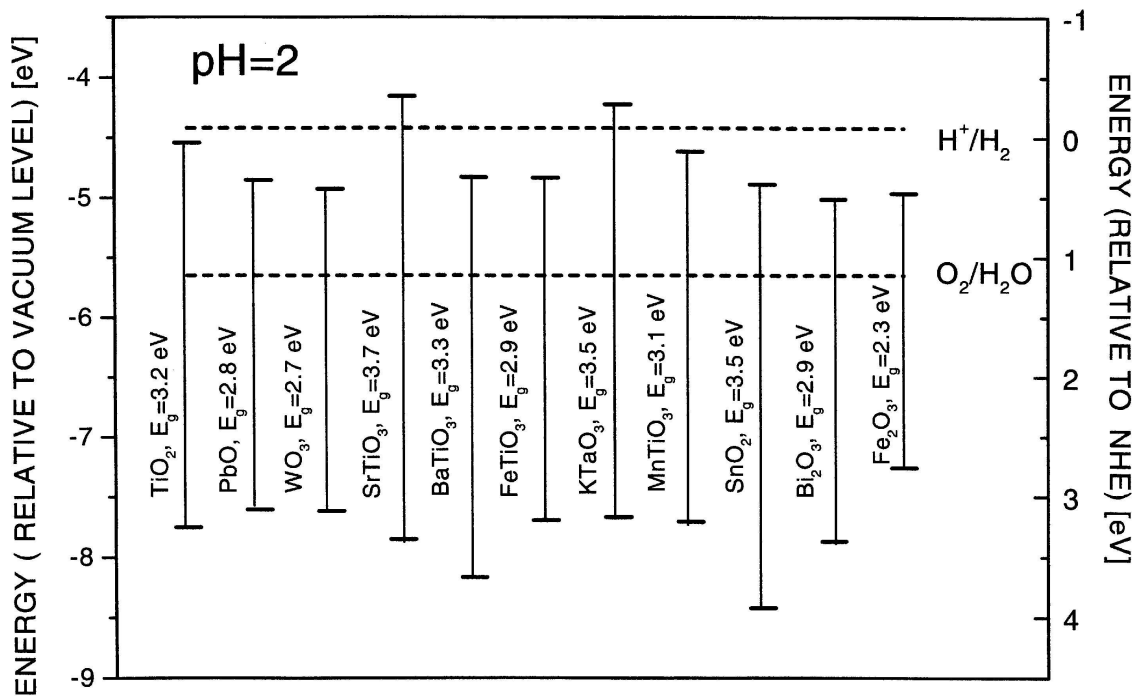


Figure 2: Band edge energy levels of common semiconductors that are in contact with aqueous medium of pH 2.0

Semiconductors suitable to serve as photo-anodes for solar water photo-electrolysis must have the following general properties [1]: (a) Chemical stability both under illumination and dark. (b) A band gap of approximately 2.0 eV to absorb maximum solar radiation. (c) Absence of charge recombination centers to prevent recombination of the photo-generated charge carriers. (d) Moderate conductivity. (e) Suitable band edge positioning with respect to the H^+/H_2 reduction potential and O_2/OH^- oxidation potential.

There are many semiconductors which possess one of the above properties such as WO_3 which is active in the visible wavelength range of the solar spectrum, but it is less stable in acidic medium. Fe_2O_3 has a smaller band gap and absorbs in the visible range, but it is also not very stable in acidic solutions. GaP ($E_g = 2.23$ eV) [66], and GaAs ($E_g = 1.4$ eV) are not stable in aqueous environments and exhibit indeed significant corrosion in water. Compounds such as CdTe or InP also have appropriate band gaps for efficient solar energy absorption, but these materials either corrode or become inert when used as photoelectrodes in aqueous solution[7]. The most promising oxide materials such as TiO_2

and CaTiO_3 and SrTiO_3 are resistant to corrosion and photo-corrosion in aqueous environment.

Unlike other materials, TiO_2 exhibits outstanding resistance to corrosion and photo-corrosion in aqueous environments. TiO_2 is one of the most promising candidates for a commercial photo-electrode for photo-electrochemical cell (PEC) for production of solar-hydrogen, due to the following reasons:

- Good chemical/photochemical stability and high oxidation power ($E=3.1\text{eV}$ Vs Standard Hydrogen Electrode (SHE)).
- The properties of TiO_2 can be widely altered by varying the defect chemistry and related electronic structure through change of the oxygen nonstoichiometry .[3,7-10]
- TiO_2 exhibits outstanding resistance to corrosion and photocorrosion in aqueous environments.[11]
- TiO_2 is reactive with both light and water [12]
- TiO_2 is substantially less expensive than other photosensitive materials and so it may also be a candidate to replace silicon in photovoltaic (PV) cells if its photosensitivity can be increased sufficiently.
- TiO_2 with enhanced photosensitivity has many supplementary applications that are environmentally friendly.[13]
- TiO_2 is abundant.

Presently, the energy conversion efficiency from solar to hydrogen by TiO_2 photocatalytic water-splitting is still low, mainly due to the following reasons:

(1) ***Recombination of photo-generated electron/hole pairs:***

Fig. 3 shows a schematic of the photoexcitation of a semiconductor solid particle by exposure to radiation with energy above the bandgap energy [14]. An exciton, produced by the absorption of a photon is shown by the star symbol. This is followed by charge separation – the production of an electron–hole pair. Charge transport to the particle

surface by processes C and D lead respectively to desirable reduction and oxidation reactions at the surface. Processes A and B represent electron–hole pair recombination processes at the surface and in the bulk, respectively.

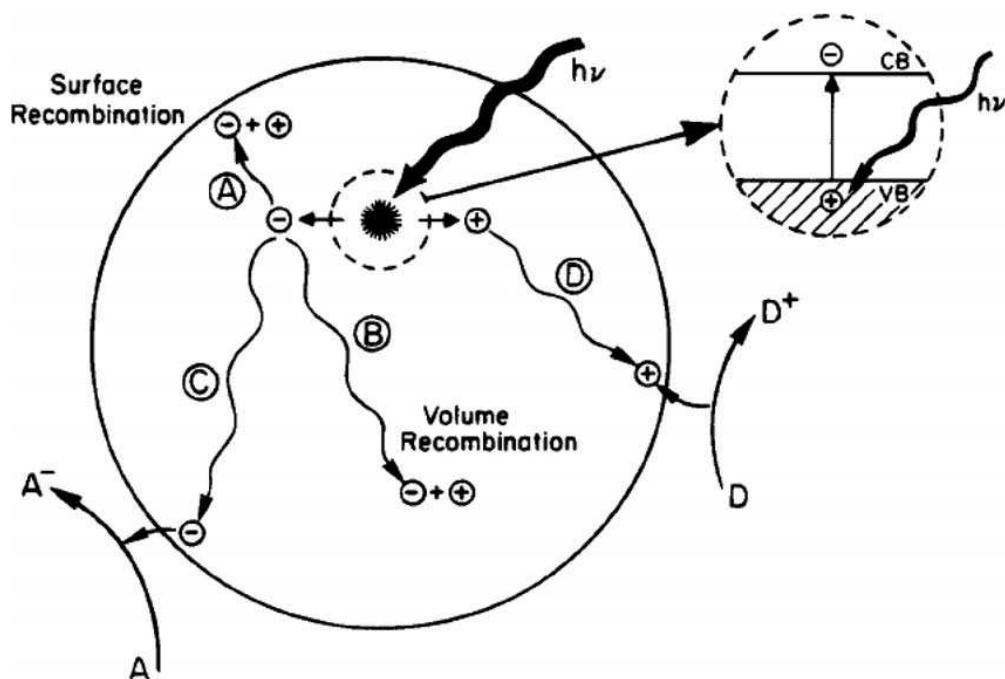


Figure 3: Schematic photoexcitation in a semiconductor particle followed by later events [14].

Fig. 4 shows a schematic energetic picture of surface or bulk electron trap states. These states exist in crystalline and colloidal TiO_2 where surface oxygen vacancy defects and defects in the crystalline lattice provide new localized energy states not available in the perfect crystal. In addition, since the perfect surface represents an abrupt discontinuity from the lattice, it too provides a high density of energy states in the surface region. These energy states differ in their energy from the energy bands present in the perfect solid and can act as traps for electrons, enhancing the recombination process and producing shorter hole lifetimes, which is detrimental to the efficiency of surface photochemistry driven by hole production.

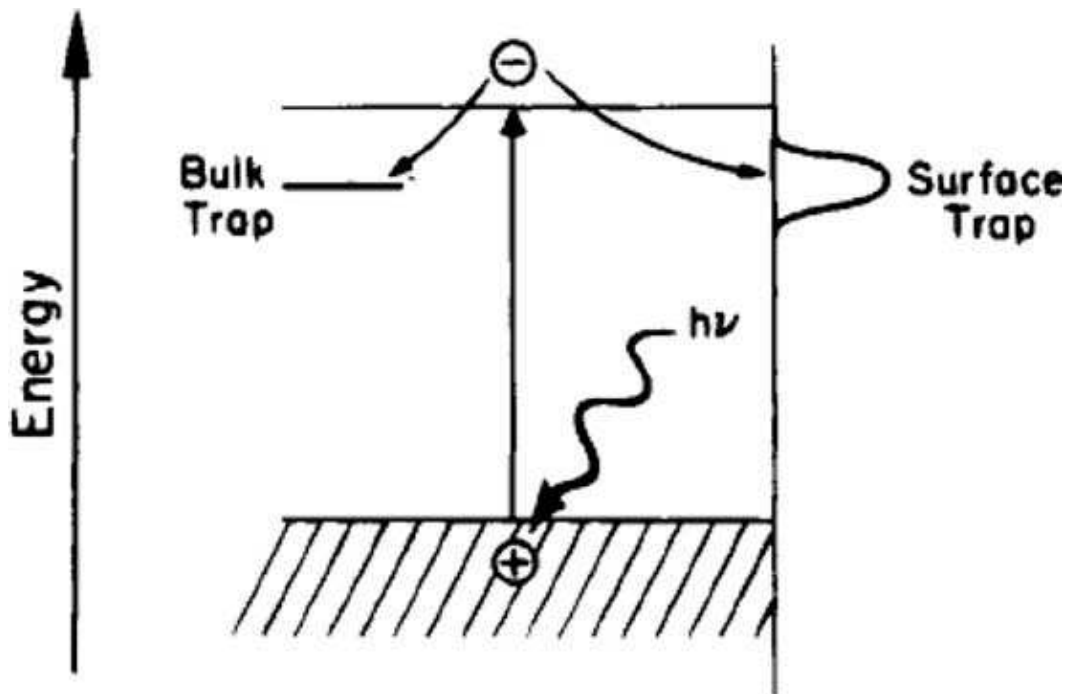


Figure 4: Surface and bulk electron carrier trapping leading to an enhanced charge carrier recombination rate and shorter hole lifetimes [14].

(2) Fast backward reaction:

Decomposition of water into hydrogen and oxygen is an energy increasing process, thus backward reaction (recombination of hydrogen and oxygen into water) easily proceeds. In the pioneering work of Fujishima and Honda [15], UV light irradiation of a TiO₂ photoelectrode in aqueous solution led to the production of H₂ and O₂ on a Pt electrode and TiO₂ photoelectrode, respectively. The reaction yields were, however, rather low, due in part to the recombination of the liberated gases at the surface of the Pt particles [16].

(3) Inability to utilize visible light:

The visible light absorption ability of the photo-electrode has a critical impact on the energy conversion of photons [17,18]. The band gap, E_g , is an important quantity for materials that are candidates for photo-electrodes. Indeed only the photons of energy equal to or larger than that of the band gap may be absorbed and used for conversion. The band gap of TiO₂ is about 3.2 eV and only UV light can be utilized for hydrogen production. Since the UV light only accounts for about 4% of the solar radiation energy

while the visible light contributes about 50%, the inability to utilize visible light limits the efficiency of solar photocatalytic hydrogen production.

The above mentioned problems can be solved using following solutions

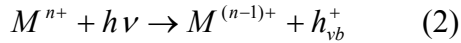
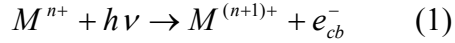
A) The rapid recombination of photo-generated CB electrons and VB holes can be reduced by adding electron donors which react irreversibly with the photo-generated VB holes thus enhance the photocatalytic electron/hole separation. Since electron donors are consumed in photocatalytic reaction, continual addition of electron donors is required to sustain hydrogen production.

Organic compounds (hydrocarbons) are widely used as electron donors for photocatalytic hydrogen production as they can be oxidized by VB holes. The remaining strong reducing CB electrons can reduce protons to hydrogen molecules. Ethylenediaminetetraacetic acid (EDTA), methanol, ethanol, lactic acid and formaldehyde have been tested and proved to be efficient to enhance hydrogen production [19–26]. Nada et al. [25] carried out a qualitative investigation to study the effects of different electron donors on hydrogen production. It should be noted that the decomposition of these hydrocarbons could also contribute to a higher hydrogen yield since hydrogen is one of their decomposed products.

B) Fast backward reaction of hydrogen and oxygen can be prevented by separating evolution of hydrogen and oxygen. Matsumura et al.[27] have reported that the separate evolution of H₂ and O₂ could be achieved by combining two photocatalytic reactions on suspended TiO₂ powders using a two-compartment cell equipped with platinum electrodes and a cation-exchange membrane. Recently, Anpo et al. succeeded in the preparation of visible light-responsive TiO₂ thin films by RF-magnetron sputtering (RF-MS) method for the separate evolution of H₂ and O₂ from water under visible light irradiation [28-36]. The backward reaction can also be suppressed by addition of carbonate salts. Sayama et al. [37–43] reported that addition of carbonate salts could significantly enhance hydrogen and oxygen production stoichiometrically. Addition of Na₂CO₃ was found to be efficient for enhancement of hydrogen and oxygen production using Pt loaded TiO₂ (Pt-TiO₂) [37]. However the production of hydrogen and oxygen was enhanced very significantly. The addition of too much carbonate salt or iodide anion beyond optimum level could reduce the

beneficial effects since these species adsorbed onto the catalyst surface could decrease light harvesting [39].

C) Transition metal ion doping and rare earth metal ion doping have been extensively investigated for enhancing the TiO₂ photocatalytic activities under visible light irradiation [44–59]. Choi et al. [44] carried out a systematic investigation to study the photoreactivity of 21 metal ions into TiO₂. It was found that doping with metal ions could expand the photo-response of TiO₂ into visible spectrum. As metal ions are incorporated into the TiO₂ lattice, impurity energy levels in the band gap of TiO₂ are formed, as indicated below:



where Mⁿ⁺ represent the metal ion dopant.

Furthermore, there exists an optimum concentration of doping metal ion, above which the photocatalytic activity decreases due to the increase in recombination. Among the 21 metal ions studied, Fe, Mo, Ru, Os, Re, V, and Rh ions can increase photocatalytic activity, while Co and Al ions cause detrimental effects [44]. The different effects of metal ions result from their abilities to trap and transfer electrons/holes. For example, Cu and Fe ions can trap not only electrons but also holes, and the impurity energy levels introduced are near to CB as well as to VB edges of TiO₂. Therefore, doping with either Cu or Fe ions could be recommended for enhancement of photocatalytic activity [44,45,53,55,56].

A qualitative analysis in investigating the effects of doping transition metal ions (Cr, Mn, Fe, Co, Ni, and Cu) on photocatalytic activity of TiO₂ was carried out by Wu et al. [52]. As Cu, Mn and Fe ions can trap both electrons and holes, doping with these metal ions may work better than doping with Cr, Co and Ni ions, as the latter metal ions can only trap one type of charge carrier.

Extensive research on metal ion doping method for enhancement of TiO₂ photocatalytic activities has been carried out especially for water/air cleaning applications. Organic compounds adsorbed by the photo-catalysts are decomposed mainly by the VB holes and radicals induced by holes. Therefore, the mechanism involved in transferring these photo-generated holes to the interface is of paramount importance. On the other hand, for photocatalytic hydrogen production, the transfer of CB electrons to the interface and

their energy are the most important factors that affect the hydrogen production rate. Hence, the results based on water/air cleaning applications cannot be directly applied to hydrogen production. Besides, the TiO₂ photocatalytic effect is very sensitive to the metal ion doping methods, doping content and depth. Therefore, a systematic, comparative investigation is needed in order to characterize photocatalytic hydrogen production enhanced by metal ion doping.

2.1.3 Brief Overview of Titanium Dioxide

Physical and Chemical Properties of TiO₂

Titanium dioxide, a natural oxide of titanium, exists in three different polymorphs: anatase, rutile, and brookite. TiO₂ has been widely studied in the past few decades due to its remarkable electric, magnetic, and catalytic activities [60]. The crystal structure data of the three different polymorphs phases of TiO₂ are summarized in table 1. Figure 5 represents the crystal structures of the three different phases of TiO₂ [60].

	Rutile ^a	Anatase ^a	Brookite ^b
Crystal structure	tetragonal	tetragonal	orthorhombic
Lattice constants (Å)	$a=4.5936$ $c=2.9587$	$a=3.784$ $c=9.515$	$a=9.184$ $b=5.447$ $c=5.145$
Space group	$P4_2/mnm$	$I4_1/amd$	$Pbca$
Molecule/cell	2	4	8
Volume/molecule (Å ³)	31.2160	34.061	32.172
Density (g/cm ³)	4.13	3.79	3.99
Ti—O bond length (Å)	1.949(4)	1.937(4)	1.87~2.04
O—Ti—O bond angle	81.2° 90.0°	77.7° 92.6°	77.0°~105°

Table 1: The crystal structure data of Titanium dioxide

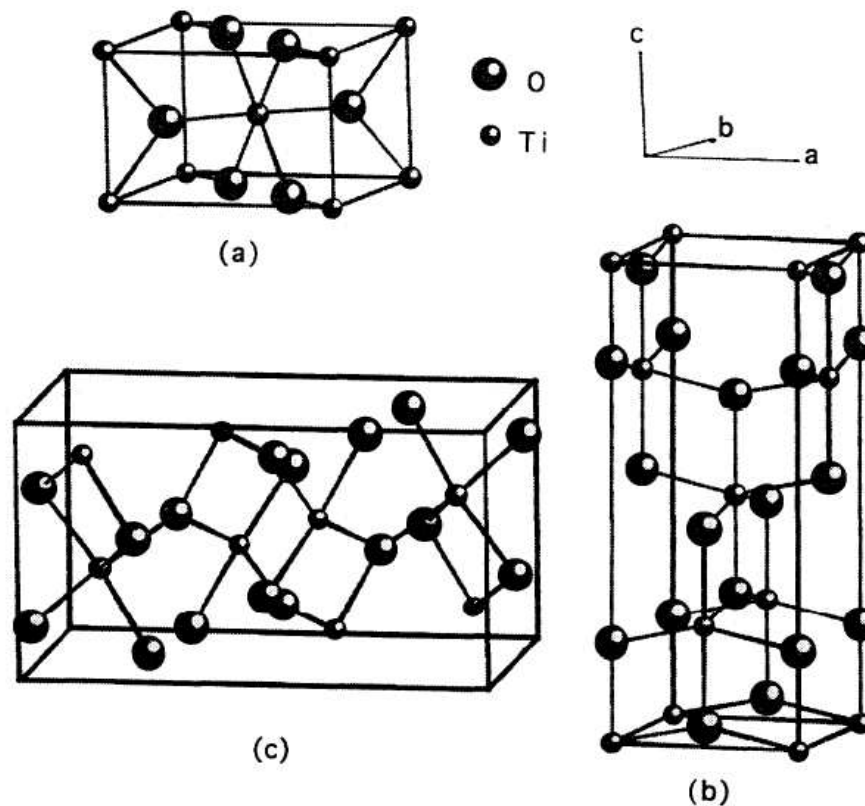


Figure 5: Crystal structures of titanium dioxide. (a) Rutile (b) Anatase and (c) Brookite

Rutile is the most extensively studied phase of titanium dioxide and contains six atoms per unit cell. Anatase contains twelve atoms per unit cell. In both phases, for a perfect crystal, every Ti atom is attached to six O atoms[60]. Since the flat-band potential of rutile is faintly more positive than that of the Standard Hydrogen Electrode(SHE) and the flat-band potential of anatase is more negative to SHE, the reduction of water molecules to hydrogen by photo-excited conduction band electrons takes place more easily on anatase polymorphs than on rutile. On the other hand, O₂ evolution occurs at similar rates both on anatase and rutile since the potential of the photo-generated holes is above the potential of oxygen evolution. These two characteristics make anatase the only crystalline titania phase where photo-dissociation of water molecules can take place without an external applied voltage. In addition, the enhanced photo-activity of anatase with respect to rutile is attributed to the larger band gap of the former (3.2 eV versus 3.0 eV) which helps in

increasing the surface redox potentials and prolonging the electron/hole lifetime [61]. Furthermore, Tang *et al.* reported that anatase thin film has a wider optical absorption edge than rutile resulting in higher photoconductivity threshold energy [62]. The value of the absorption edge of anatase is equal to 387 nm and that for rutile is equal to 418 nm [63] .

2.1.4 Other application of TiO₂

The produced TiO₂ films are applicable not only for photo-electrochemical solar-hydrogen production but also they could be efficient for following applications

- Decontamination of water from bacteria, viruses and organic compounds [64,65].
- Self-cleaning building materials [64].
- Paving materials leading to reduction of air pollution [66].
- Antiseptic paints and coatings [64].
- Chemical gas sensors [67].
- Skin and stomach anticancer treatments [65].
- Antifogging mirror and glass coatings [66].
- Generation of PV electricity [68].
- Purification of air [64].

2.1.5 References

- [1] Grimes CA, Varghese OK, Ranjan S. Light, Water, Hydrogen The Solar Generation of Hydrogen by Water Photoelectrolysis. Springer May 2007
- [2] Bak T, Nowotny J, Rekas M and Sorrell CC. Photo-electrochemical hydrogen Generation from water using solar energy. Materials-related perspective. Int J Hydrogen Energy 2002; **27** : 991–1022.
- [3] P. Kofstad. Nonstoichiometry, electrical conductivity and diffusion in binary metal oxides, Wiley, New York 1972.
- [4] Hoffmann MR, Martin ST, Choi W, Bahnemann DW. Environmental Applications of Semiconductor Photocatalysis .Chemical review 1995,95,69-95
- [5] John Willey and Sons photocatalysis ,fundamentals and application. New York, Brisbane 1989
- [6] Pleskov YV ,Gurevich YY. Semiconductor photo-electrochemistry consultants bureau, New York, London 1986
- [7] Bak T, Nowotny J, Rekas M, Sorrell CC. Defect chemistry and semiconducting properties of titanium dioxide. I. Intrinsic equilibrium constant. J Phys Chem Solids 2003; 64: 1043–56.
- [8] Bak T, Nowotny J, Rekas M, Sorrell CC. Defect chemistry and semiconducting properties of Titanium dioxide. II. Defect diagrams. J Phys Chem Solids 2003; 64:1057–67.
- [9] Bak T, Nowotny J, Rekas M, Sorrell CC. Defect chemistry and semiconducting properties of Titanium dioxide. III. Mobility of electronic charge carriers. J Phys Chem Solids 2003; 64: 1069–87.
- [10] Nowotny J, Sorrell CC, Sheppard LR. In: Materials for energy conversion devices. Cambridge: Woodhead 2005; 84–116.
- [11] Reiche P. A survey of weathering processes and products. The University of New Mexico Press; 1950; 55.
- [12] Nowotny J, Sorrell CC, Sheppard LR, Bak T. Solar-hydrogen: environmentally safe fuel for the future. Int J Hydrogen Energy 2005; 30: 521–44.
- [13] Fujishima A, Hashimoto K, Watanabe T. TiO₂ Photo-catalysis. Fundamentals and Applications. Tokyo: BKC 1999; 14–176.

- [14] Linsebigler AL, Lu G, Jr. Yates JT. Photocatalysis on TiO₂ Surfaces: Principles, Mechanisms, and Selected Results. *Chem. Rev.* 1995;95: 735.
- [15] Fujishima A, Honda K. Electrochemical Photolysis of Water at a Semiconductor Electrode. *Nature* 1972;238: 37.
- [16] Tabata S, Nishida N, Masaki Y, Tabata K. Stoichiometric photocatalytic decomposition of pure water in Pt/TiO₂ aqueous suspension system. *Catal. Lett.* 34 (1995) 245.
- [17] Oriel-Instruments. *Book of Photon Tools*, 1999. p. 1–3.
- [18] Wenham SR, Green MA, Watt ME. *Applied photovoltaics*, Centre for Photovoltaic Devices and Systems, Sydney, 1994. p. 239-46.
- [19] Bamwenda GR, Tsubota S, Nakamura T, Haruta M. Photoassisted hydrogen production from a water/ethanol solution: a comparison of activities of Au-TiO₂ and Pt-TiO₂. *J Photochem Photobiol A: Chem* 1995;89(2):177–89.
- [20] Gurunathan K, Maruthamuthu P, Sastri VC. Photocatalytic hydrogen production by dye-sensitized Pt=SnO₂ and Pt=SnO₂=RuO₂ in aqueous methyl viologen solution. *Int J Hydrogen Energy* 1997;22(1):57–62.
- [21] Lee SG, Lee SW, Lee HI. Photocatalytic production of hydrogen from aqueous solution containing CN⁻ as a hole scavenger. *Appl Catal A: Gen* 2001;207(1–2):173–81.
- [22] Li YX, Lu GX, Li SB. Photocatalytic production of hydrogen in single component and mixture systems of electron donors and monitoring adsorption of donors by in situ infrared spectroscopy. *Chemosphere* 2003;52(5):843–50.
- [23] Kida T, Guan GQ, Yamada N, Ma T, Kimura K, Yoshida A. Hydrogen production from sewage sludge solubilized in hot-compressed water using photocatalyst under light irradiation. *Int J Hydrogen Energy* 2004;29(3):269–74.
- [24] Wu NL, Lee MS. Enhanced TiO₂ photocatalysis by Cu in hydrogen production from aqueous methanol solution. *Int J Hydrogen Energy* 2004;29(15):1601–5.
- [25] Nada AA, Barakat MH, Hamed HA, Mohamed NR, Veziroglu TN. Studies on the Photocatalytic hydrogen production using suspended modified TiO₂ photocatalysts. *J Hydrogen Energy* 2005;30(7): 687–691.
- [26] Peng SQ, Li YX, Jiang FY, Lu GX, Li SB. Effect of Be²⁺ doping TiO₂ on its photocatalytic activity. *Chem Phys Lett* 2004;398(1–3):235–9.

- [27] Fujihara K, Ohno T, Matsumura M. Splitting of water by electrochemical combination of two photocatalytic reactions on TiO₂ particles. *J. Chem. Soc. Faraday Trans.* 1998; 94: 3705.
- [28] Moon SC, Matsumura Y, Kitano M, Matsuoka M, Anpo M. Hydrogen production using semiconducting oxide photo-catalysts *Res. Chem. Intermed.* 2003;29: 233.
- [29] Anpo M. Bull. Preparation, Characterization, and Reactivities of Highly Functional Titanium Oxide-Based Photocatalysts Able to Operate under UV–Visible Light Irradiation: Approaches in Realizing High Efficiency in the Use of Visible Light *Chem. Soc. Jpn.* 2004;77 :1427.
- [30] Anpo M, Dohshi S, Kitano M, Hu Y, Takeuchi M, Matsuoka M. The preparation and characterization of highly efficient titanium oxide-based photofunctional materials. *Annu. Rev. Mater. Res.* 2005;35 : 1.
- [31] Matsuoka M, Kitano M, Takeuchi M, Anpo M, Thomas JM. *Mater. Sci. Forum* 2005; 81:486–487 .
- [32] Takeuchi M, Anpo M, Hirao T, Itoh N, Iwamoto N. Preparation of TiO₂ Thin Film Photocatalysts Working under Visible Light Irradiation by Applying a RF Magnetron Sputtering Deposition Method *Surf. Sci. Jpn.* 2001;22: 561.
- [33] Kitano M, Takeuchi M, Matsuoka M, Thomas JM, Anpo M. Preparation of Visible Light-responsive TiO₂ Thin Film Photocatalysts by an RF Magnetron Sputtering Deposition Method and Their Photocatalytic Reactivity. *Chem. Lett.* 2005;34 : 616.
- [34] Matsuoka M, Kitano M, Takeuchi M, Anpo M, Thomas JM. Photocatalytic Water Splitting on Visible Light-responsive TiO₂ Thin Films Prepared by a RF Magnetron Sputtering Deposition Method *Top. Catal.* 2005;35: 305.
- [35] Kitano M, Kikuchi H, Hosoda T, Takeuchi M, Matsuoka M, Eura T, Anpo M, Thomas JM. The Preparation of Visible Light-Responsive TiO₂ Thin Films by Applying a RF-Magnetron Sputtering Deposition Method and Their Photocatalytic Reactivity for the Decomposition of Water with a Separate Evolution of H₂ and O₂ *Key Eng. Mater.* 2006; 317–318:823.

- [36] Kikuchi H, Kitano M, Takeuchi M, Matsuoka M, Anpo M, Kamat PV. Extending the Photoresponse of TiO₂ to the Visible Light Region: Photoelectrochemical Behavior of TiO₂ Thin Films Prepared by the Radio Frequency Magnetron Sputtering Deposition Method. *J. Phys. Chem. B* 2006;110: 5537.
- [37] Sayama K, Arakawa H. Significant effect of carbonate addition on stoichiometric photodecomposition of liquid water into hydrogen and oxygen from platinum-titanium (IV) oxide suspension. *J Chem Soc, Chem Commun* 1992;2:150–2.
- [38] Sayama K, Arakawa H. Effect of Na₂CO₃ addition on photocatalytic decomposition of liquid water over various semiconductors catalysis. *J Photochem Photobiol A: Chem* 1994;77(2–3):243–7.
- [39] Sayama K, Arakawa H. Effect of carbonate addition on the photocatalytic decomposition of liquid water over a ZrO₂ catalyst. *J Photochem Photobiol A: Chem* 1996;94:67–76.
- [40] Sayama K, Arakawa H, Domen K. Photocatalytic water splitting on nickel intercalated A₄TaxNb₆O₁₇ (A = K; Rb). *Catal Today* 1996;28:175–82.
- [41] Sayama K, Yase K, Arakawa H, Asakura K, Tanaka A, Domen K, et al. Photocatalytic activity and reaction mechanism of Pt-intercalated K₄Nb₆O₁₇ catalyst on the water-splitting in carbonate salt aqueous solution. *J Photochem Photobiol A: Chem* 1998;114:125–35.
- [42] Arakawa H, Sayama K. Oxide semiconductor materials for solar light energy utilization. *Res Chem Intermed* 2000;26(2):145–52.
- [43] Arakawa H, Sayama K. Solar hydrogen production: significant effect of Na₂CO₃ addition on water splitting using simple oxide semiconductor photocatalysts. *Catal Surv Jpn* 2000;4:75–80.
- [44] Choi WY, Termin A, Hoffmann MR. The role of metal ion dopants in quantum-sized TiO₂: correlation between photoreactivity and charge carrier recombination dynamics. *J Phys Chem* 1994;84:13669–79.
- [45] Litter MI. Heterogeneous photocatalysis transition metal ions in photocatalytic systems. *Appl Catal B: Environ* 1999;23:89–114.
- [46] Dvoranova D, Brezova V, Mazur M, Malati M. Investigations of metal-doped titanium dioxide photocatalysts. *Appl Catal B: Environ* 2002;37:91–105.
- [47] Hameed A, Gondal MA, Yamani ZH. Effect of transition metal doping on

- photocatalytic activity of WO₃ for water splitting under laser illumination: role of 3d-orbitals. *Catal Commun* 2004;5:715–9.
- [48] Xu AW, Gao Y, Liu HQ. The preparation characterization and their photocatalytic activities of rareearthdoped TiO₂ nanoparticles. *J Catal* 2002;207:151–7.
- [49] Paola AD, Marci G, Palmisano L, Schiavello M, Uosaki K, Ikeda S, et al. Preparation of polycrystalline TiO₂ photocatalysts impregnated with various transition metal ions: characterization and photocatalytic activity for degradation of 4-nitrophenol. *J Phys Chem B* 2002;106:637–45.
- [50] Wu XS, Ma Z, Qin YN, Qi XZ, Liang ZC. Photocatalytic redox activity of doped nanocrystalline TiO₂. *Wuli Huaxue Xuebao* [in Chinese] 2004;20(2):138–43.
- [51] Zou XH, Qi SX, He HJ, An LD, Duan X. Preparation and photo-catalytic activity of TiO₂ films doped with metal ions. *J Mol Catal* [in Chinese] 2003;17(6):456–60.
- [52] Yuan WH, Bi HQ, Wei CH. Effect of Zn doping on the photocatalytic activity of nano-sized TiO₂. *J S China Univ Technol (Nature Science Edition)* 2004;32(3):29–32.
- [53] Zhou L, Guo XS. Preparation and photocatalytic activity of nanoparticle TiO₂ doped with iron. *Ind Catal* [in Chinese] 2004;12(4):38–41.
- [54] Hou MF, Li FB, Li RF, Wan HF, Zhou GY, Xie KC. Enhancement of photocatalytic properties and activity of Nd³⁺-doped TiO₂ powders. *J Chinese Rare Earth Soc* [in Chinese] 2004;22(1):75–80.
- [55] Feng LR, Lu SJ, Qiu FL. Influence of transition elements dopant on the photocatalytic activities of nanometer TiO₂. *Acta Chimica Sinica* [in Chinese] 2002;60(3):463–7.
- [56] Zhao DM, Wang DH, Shi HX, Yan XL. Study on photocatalytic oxidation of p-chlorophenol with transition metal-doped TiO₂ nanoparticles. *Environ Prot Chem Ind* [in Chinese] 2003;23(2):75–8.
- [57] Wilke K, Breuer HD. The influence of transition metal doping on the physical and photocatalytic properties of titania. *J Photochem Photobiol A: Chem* 1999;121(1):49–53.
- [58] Wang RH, Xin JHZ, Yang Y, Liu HF, Xu LM, Hu JH. The characteristics and photocatalytic activities of silver doped ZnO nanocrystallites. *Appl Surf Sci* 2004;227:312–7.

- [59] Xu JC, Shi YL, Huang JE, Wang B, Li HL. Doping metal ions only onto the catalyst surface. *J Mol Catal A: Chem* 2004;219:351–5.
- [60] Mo S and Ching WY. Electronic and Optical Properties of Three Phase Titanium Dioxide: Rutile, Anatase, and Brookite. *Phys. Rev. B* 1995; 51: 13023-13032.
- [61] Sumita T, Yamaki T, Yamamoto S, and Miyashita A. Photo-Induced Surface Charge Separation of Highly Oriented TiO₂ Anatase and Rutile. *Thin Surf. Sci.* 2000; 200: 21-26
- [62] Tang H, Prasad K, Sanjinèz R, Schmid PE, and Lévy F. Electrical and Optical Properties of TiO₂ Anatase Thin Films. *J. Appl. Phys.* 1994; 75: 2042-2047.
- [63] Tian B, Zhang J, Tong T and Chen F. Preparation of Au/TiO₂ Catalysts From Au(I)-Thiosulfate Complex and Study of Their Photocatalytic Activity for the Degradation of Methyl Orange, *Appl. Catal. B* 2008; 79: 394-401
- [64] Fujishima A, Hashimoto K, Watanabe T. *TiO₂ Photocatalysis. Fundamentals and Applications.* Tokyo: BKC; 1999. p. 14–176.
- [65] Fujishima A, Rao TN, Tryk DA. Titanium dioxide photocatalysis. *J Photochem Photobiol C: Photochem Rev* 2000;1:1–21.
- [66] Wang L. Paving out pollution, *Sci Am* February 2002; 20.
- [67] Sharma RK, Bhatnagar MC, Sharma GL. Mechanism of highly sensitive and fast response Cr doped TiO₂ oxygen gas sensor. *Sens Actuators B* 1997;45: 209–15.
- [68] Grätzel M. Nanocrystalline ceramic films for efficient conversion of light into electricity. *J Sol–Gel Sci Technol* 1994;2:673–7.

2.2 Physically and chemically prepared TiO₂ thin film for Hydrogen production.

TiO₂ electrode preparation and characterization are of paramount importance for success of the present study since the photocatalytic activities of these electrodes depend on the crystalline structure of TiO₂ and control synthesis technique. Thus this chapter is devoted to this important topic which deals with the synthesis of photo-catalyst in the form of thin films for hydrogen production from water splitting. TiO₂ can be synthesized by several different methods including metal organic chemical vapor deposition (MOCVD) [1], sol-gel [2], electrophoretic deposition [3], reactive RF sputtering [4], and pulsed laser deposition (PLD) [5]. In the present work, TiO₂ thin films are synthesized by using Vapor Phase Deposition (VPD) such as RF magnetron sputtering and spin coating technique in order to study the difference between physical and chemical deposited samples.

2.2.1 Experimental methods

Material and chemicals:

Indium Tin Oxide (ITO) (99.99%) target purchased from supplier named as “Thin films materials process solutions” and TiO₂ (99.99%) targets commercially supplied by “Goodfellow” Cambridge Ltd. Titanium butoxide [Ti(OC₄H₉)₄], Ethanol (C₂H₅OH) and Nitric Acid (HNO₃) were used as received. These chemicals were of analytical grade and purchased from “Sigma Aldrich”. All solutions were prepared using high purity deionized water.

Synthesis of ITO conducting thin film photocatalyst by using RF magnetron sputtering:

To measure photocatalytic activity, TiO₂ films were deposited on the conducting indium tin oxide (ITO) layer because ITO has two chief properties, namely electrical conductivity and optical transparency. A high electrical conductivity facilitated the separation of photogenerated electrons and holes, preserving the photocurrents of the electrodes. ITO layer was deposited on the glass slide by magnetron sputtering using RF

power of 100W and working Ar gas pressure of 0.8 Pa. Pre-sputtering of the ITO target was also conducted in order to remove the surface contamination. The sample and target distance was kept constant at 5 cm for all the samples.

Synthesis of TiO₂ thin film by using RF magnetron sputtering:

For sputter deposition, TiO₂ disc (99.99%) and pure Ar (99.99%) were used as sputtering target and working gas, respectively. High vacuum (HV) with base pressure $<3 \times 10^{-5}$ Pa and working Ar pressure of 0.8 Pa were used for the deposition. Before sample deposition, the TiO₂ target was pre-sputtered for 20 min in order to remove any surface contamination. TiO₂ target was sputtered on both glass and Si (100) substrates at room temperature using RF power of 150 W. The sample and target distance was kept constant at 5 cm for all the samples. After deposition, no post annealing was performed.

A sputter deposited photocatalytic ITO/TiO₂ composite films were deposited in-situ in the same chamber.

Synthesis of TiO₂ thin film t by Sol-gel method:

In sol-gel method, TiO₂ thin film was deposited by spin coating. TiO₂ sol was prepared by hydrolysis reaction of titanium butoxide [Ti(OC₄H₉)₄] as precursor and nitric acid as catalyst. The molar composition of Ti(OC₄H₉)₄/H₂O/C₂H₅OH/HNO₃ for sol were 1:0.5:20:0.1. Ti (OC₄H₉)₄ was mixed with ethanol (half the amount) and constantly stirred for 1 h at room temperature. Further mixture of water, ethanol (remaining half) and HNO₃ was added drop wise under a vigorous stirring to the above mixture for 1 h. The resultant solution was stirred for further 1 h at room temperature to increase homogeneity before spin coating. TiO₂ sol was spun for 40 sec at 3000 rpm on glass and Si (100) substrate to obtain TiO₂ thin film which was further baked at 125 °C for 1 h. Obtained samples were thermally treated in static air at 500 °C for 2 h with a heating rate of 1 °C min⁻¹. The flow chart of sample preparation is shown in Fig 1.

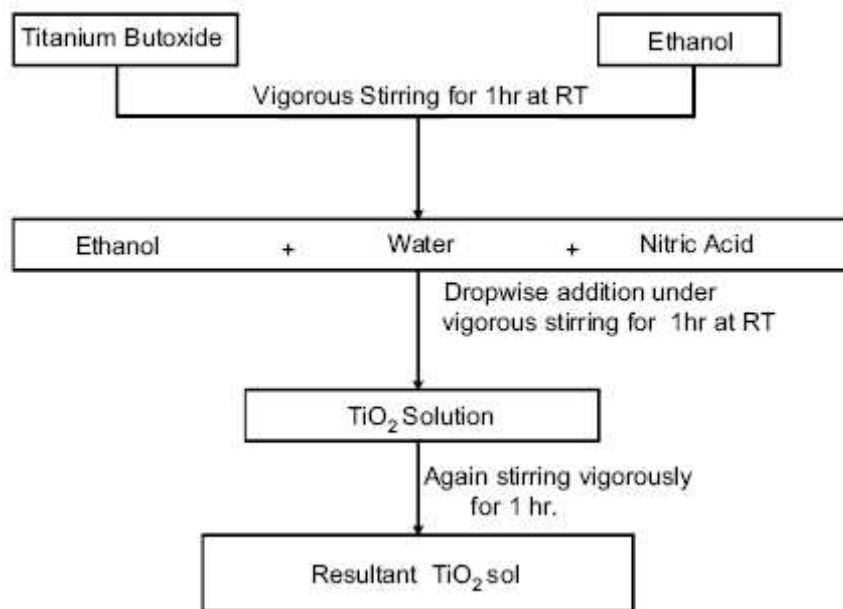


Figure 1: Schematic diagram of preparation process of TiO_2 sol by sol-gel method.

The structural characterization of photocatalyst films produced by sputtering was carried out using X-ray diffraction (XRD) technique (Cu K α radiation, $\lambda = 1.5414\text{\AA}$) in Bragg-Brentano (θ - 2θ) configuration. However, TiO_2 films synthesized by sol-gel method were structurally characterized by Fourier Transform Infrared Spectroscopy (FTIR) because of the low thickness achieved. FTIR measurements were carried out in transmission mode at normal incidence in the spectral range between 4000 and 400 cm^{-1} using a Bruker (Equinox 55) spectrometer at room temperature. Optical measurements in the Ultraviolet (UV) and visible range were performed in a Bruker IFS66 spectrometer equipped with a reflection and transmission unit with near normal incidence of the incoming beam. The wavelength range of 250–750 nm was used to obtain the absorbance spectra. The sample deposited on the glass slide was used for this measurement. The surface morphology of the TiO_2 samples was detected by using scanning electron microscope (SEM-FEG, JSM-7001F, JEOL) and atomic composition was analyzed by energy dispersive spectroscopy (EDS, INCA PentaFET-x3) attached to SEM.

Photocatalytic activities of the TiO_2 films were tested by producing hydrogen from water splitting. Two photo-electrochemical cells were developed having TiO_2 as

photo-anode, Pt mesh as cathode, and aqueous electrolytes. The first photocell was formed with both electrodes in contact with the same electrolyte in form of distilled water solution. In order to have chemical bias, two different electrolytes of different pH in two chambers were used in the second cell. The TiO₂ photo-anode was in contact with the solution of NaOH (1M), while the cathode was immersed in solution of H₂SO₄ (1 M). Salt bridge containing 1M of NaCl was used to provide the path for the ion conduction between two solutions. Photo-anode was exposed to light by using 250W tungsten halogen lamp and open-circuit photo-voltage was measured during successive light-off and light-on regimes. Reactor is made of borosilicate glass, thus no UV filter was used and reactant water solution acts as filter for the IR irradiation. Oxygen from the reaction chamber was completely removed by purging the chamber with pure Ar gas (99.9%) for 1 h before measurement. The separate evolution of H₂ originated by the water splitting on the cathode side was measured online as function of time by gas chromatographer (GC, Agilent MIRCOGC-3000A). Hydrogen evolution was measured in both ON/OFF light regime.

2.2.2. Results and Discussion

A. X-Ray Diffraction:

Figure 2 shows the XRD spectra of the TiO₂ film on amorphous glass synthesized by sputter deposition. The peaks observed in the spectra of TiO₂ thin film are mainly due to the anatase phase while some weak additional reflexes of rutile phase could be identified in form of broad peak. The crystal size D_{hkl} of 6 and 45 nm was calculated by Debye–Scherrer equation (2.7) from most intense (110) and (101) peaks of rutile and anatase phase respectively.

$$D_{hkl} = \frac{0.9\lambda}{\beta \cos \theta_B} \quad (2.7)$$

Where λ is the wavelength of the x-rays, β is the full width half maxima (FWHM) in radians. θ_B is the position of the maximum diffraction.

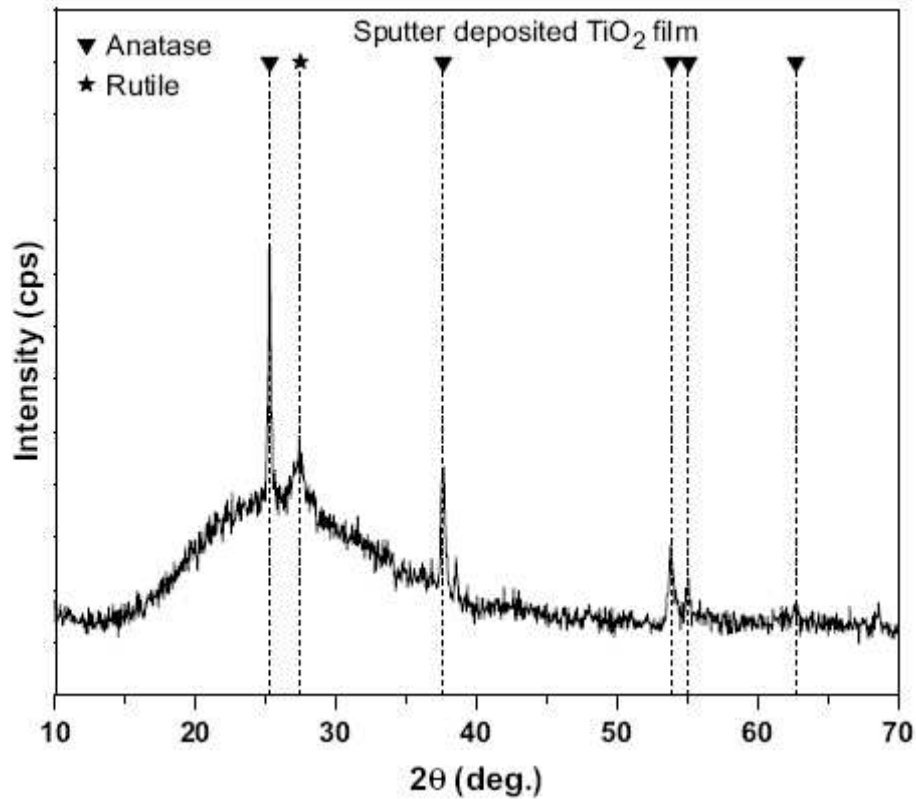


Figure 2: XRD pattern of TiO₂ film deposited on amorphous glass slide by RF magnetron Sputtering

This means that rutile phase is almost amorphous with very finely dispersed grains while, on the contrary, anatase phase is in crystallized form. However, anatase phase is most favourable for the photocatalytic reaction [6]. TiO₂ films synthesized by sol-gel method were structurally characterized by FTIR due to the low thickness achieved.

B. Fourier Transform Infrared Spectroscopy (FTIR):

Essentially, we see no distinct peaks in IR spectra (Fig. 3) for the as deposited TiO₂ thin film (note that in FTIR spectra, the TiO₂ vibrations are normally observed in the range between 800 and 350 cm⁻¹) but, after heat-treatment at 500 °C, there is formation of a broad peak centred at 433 cm⁻¹ which corresponds to the vibration of the TiO₂ units of the anatase phase [7]. No indication of rutile phase formation was observed and so, our sol-gel deposited TiO₂ films possess only anatase phase with low crystalline degree.

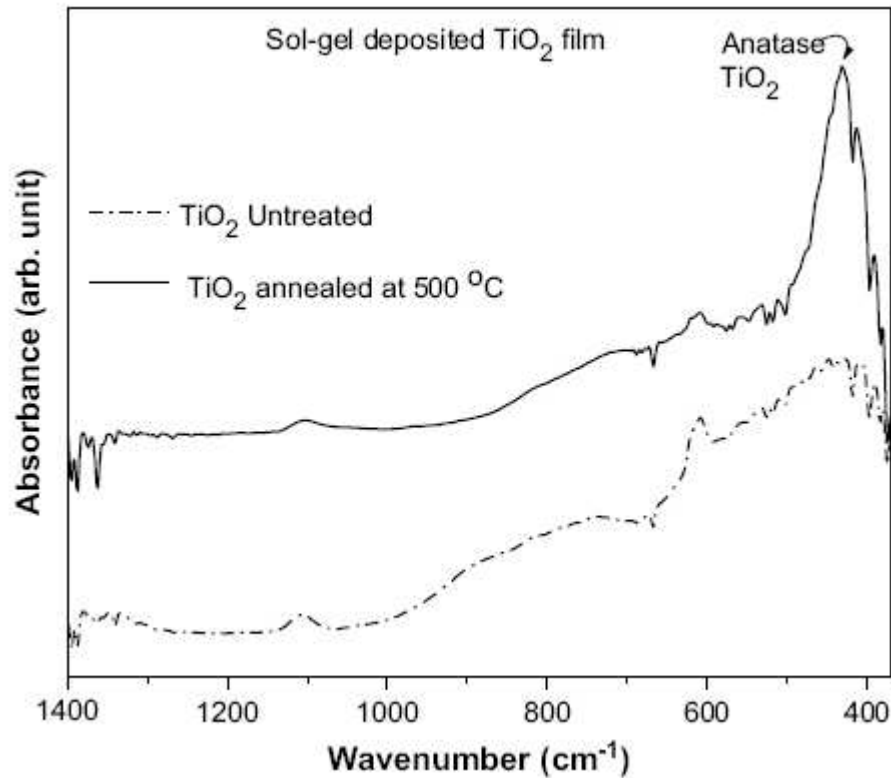


Figure 3: FTIR spectra of TiO_2 film deposited on amorphous glass slide by sol-gel method.

C. Scanning Electron Microscopy (SEM)

Surface morphology, observed by SEM, of the TiO_2 films deposited by both the methods was quite flat, smooth and without major defects. SEM cross-section micrographs of TiO_2 thin films are reported in Fig. 4. Sol-gel prepared films (Fig. 4a) are quite compact with thickness of about 135 nm which is confirmed by the profilometry measurement. On the contrary, typical dense columnar structure is observed in TiO_2 film deposited by sputtering (Fig. 4b) with average diameter of around 30–50 nm.

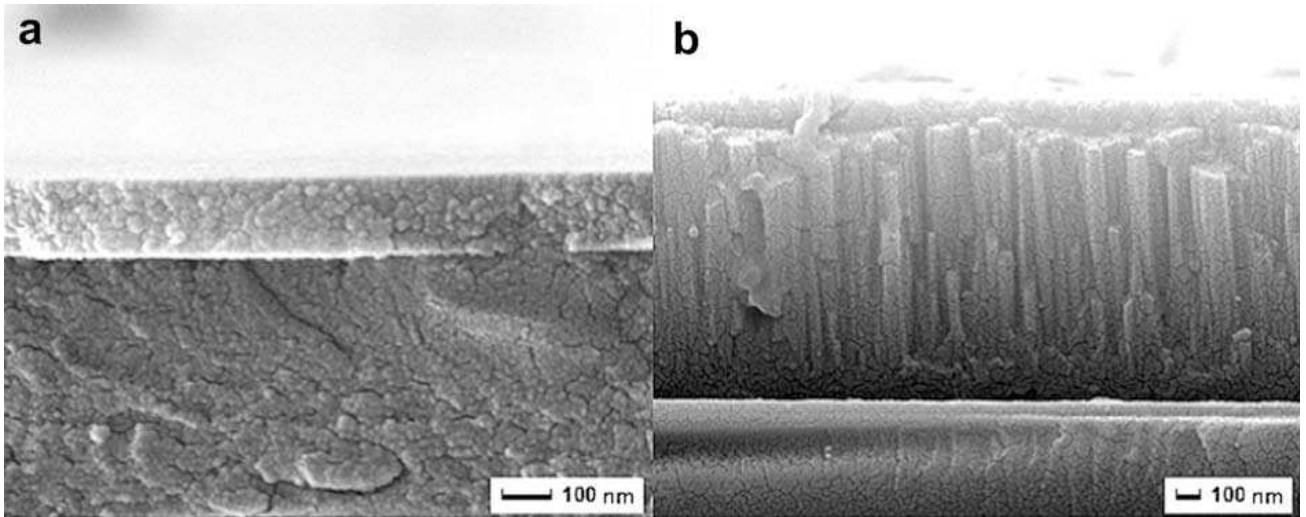


Figure 4: Cross-section SEM micrographs of TiO₂ films deposited by (a) sol–gel method and (b) RF magnetron sputtering technique

D. UV-Visible spectroscopy

Transmission spectra of the TiO₂ thin films deposited by sputtering and sol–gel on glass substrate are presented in Fig. 5 in the UV–visible range (250–600 nm). The absorbance edge of TiO₂ film deposited by sputtering is at the higher wavelength (~388 nm) as compared to the sol–gel derived film (~370 nm).

Band gap is obtained by fitting the absorption edge of UV–Visible spectra by using the following equation [8]:

$$\ln T = \ln T_0 - C \frac{(\hbar\omega - E_g)^\nu}{\hbar\omega} \quad (2.8)$$

Where E_g is the band gap, C is a constant, and T_0 is the transmission of the substrate. Depending on the type of transition, ν assumes different values: for direct, allowed (forbidden) transitions $\nu = 1/2$ ($\nu = 3/2$) and for indirect, allowed (forbidden) transitions $\nu = 2$ ($\nu = 3$). For our nano crystalline or amorphous films $\nu = 2$ is used, according to Ref. [9]. Near the absorption edge, T_0 and C are approximately constant and fitting the absorption edge with Eq. (2.8) gives E_g for the TiO₂ samples. The energy band

gap of 3.4 eV is obtained for the chemically prepared samples which is higher than the theoretical value for the anatase ($E_g = 3.2$ eV) and rutile ($E_g = 3.0$ eV) phase of TiO_2 [10]. Note that these values are obtained in the single or proper crystallized samples while, in the present case, higher band gap is due to the low crystallization degree as observed in the IR spectra. Similar high values are reported for the nano crystallized TiO_2 film [11,12] and powder [13,14]. In case of sputter-deposited TiO_2 a band gap of 3.21 eV is obtained, signalling the presence of a well crystallized anatase phase. Absorption edge also contains shoulder which is fitted thus obtaining the value of 2.85 eV indicating the presence of defect energy levels in the band gap. Interference fringes are observed in the visible range for the sputter-deposited TiO_2 suggesting thickness uniformity in the film. This effect is absent in sol-gel deposited films because of their low and non-uniform thickness achieved by spin coating [15].

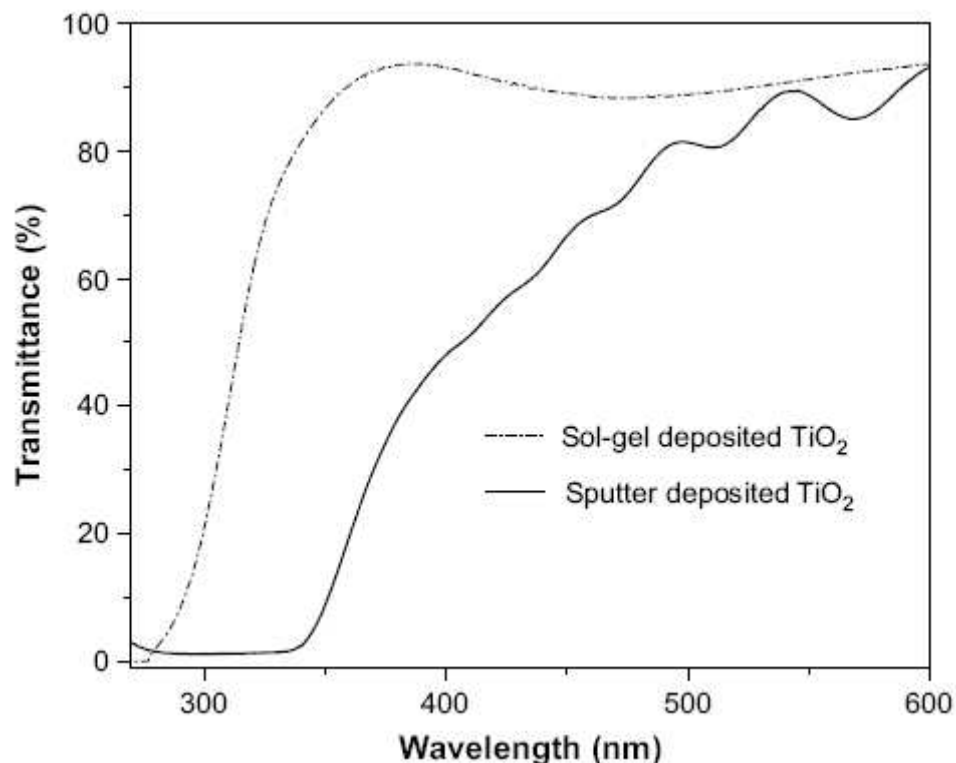


Figure 5: UV-Vis transmission spectra of TiO_2 films deposited by sol-gel method and RF magnetron sputtering technique.

E. Hydrogen Measurement

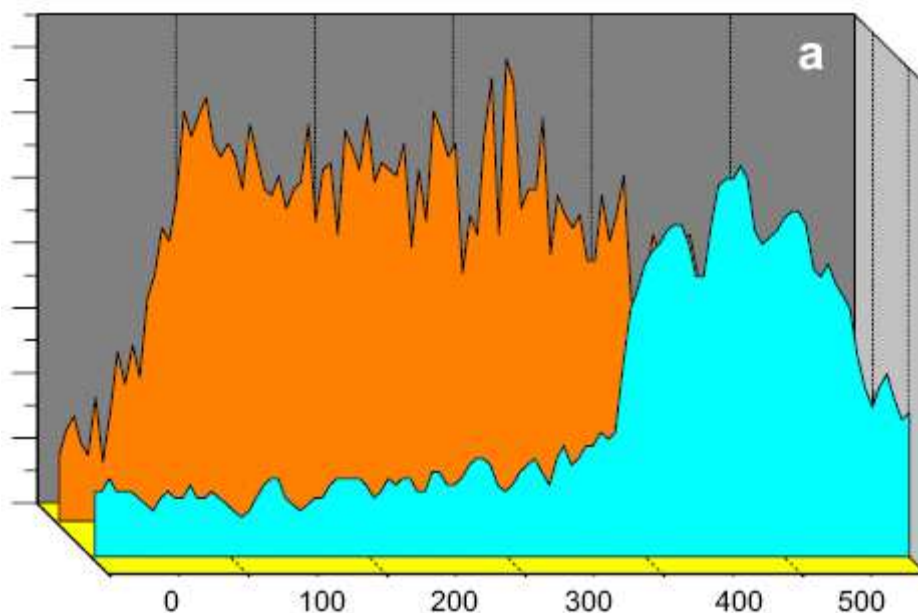
To split water using TiO_2 as photo-anode it is necessary to attain a voltage value of 1.23 V in the photo-electrochemical cell. Thus the open-circuit voltage (V_{oc}) was measured in ON/ OFF light regime for the first cell in which both cathode (Pt mesh) and photo-anode (TiO_2 thin film deposited on conducting ITO layer) were immersed into the single electrolyte in form of distilled water. Table 1 shows the V_{oc} measured for the TiO_2 films deposited by sputtering and sol-gel method on ITO of different thickness to study the effect of the conducting layer.

Table 1 - Open-circuit photo-voltage (V_{oc}) measured across TiO_2 films deposited by sputtering and sol-gel method on different thickness of ITO immersed in single electrolyte (distilled water) with Pt cathode in photoelectrochemical cell				
Different thickness of ITO (nm)	Open-circuit photo-voltage measured in distilled water (V)			
	Sputter-deposited TiO_2 (Film Thickness = 1000 nm)		Sol-gel deposited TiO_2 (Film Thickness = 100 nm)	
	light off	light on	light off	light on
30	0.130	0.686	-	-
50	0.170	0.720	0.122	0.558
100	0.196	0.583	-	-
150	0.146	0.577	0.170	0.553
250	0.140	0.543	0.159	0.649
350	-	-	0.134	0.707

As seen from the table, V_{oc} is less than 0.2 V in light OFF regime for all the TiO_2 films while it increases to about ~ 0.7 V in light ON regime. However, in case of sputter deposited TiO_2 film, V_{oc} shows maximum value when placed on thinner ITO films (30 and 50 nm) as compared to thicker ones (150 and 250 nm). This can be explained in terms of resistance offered by the electrical contact layer which is one of the key factor for loss of absorbed photon energy [16]. Since the conductivity is inversely proportional to the thickness of ITO film, thus by depositing TiO_2 on thinner ITO will help to obtain better electrical contact which in turn reduces the absorbed photon energy losses thus favouring better photo-voltage. Thickness of ITO film can be further decreased to enhance the photo-voltage value but this will result on the incomplete coverage of the substrate. Reverse behaviour is observed for the sol-gel deposited TiO_2 film which showed increase in the V_{oc} by increasing the ITO thickness up to certain value. To better understand this behaviour,

elemental composition line scan was conducted by EDS along the cross-section of the sol-gel deposited films, before and after heat treatment at 500⁰C.

Two distinct layers of tin and titanium, from ITO and TiO₂ layer respectively, can be clearly visualized for the as deposited film (Fig. 6). Heat-treatment at 500⁰C causes the diffusion of titanium atoms into ITO layer up to depth of 120–150 nm. In case of the thin ITO layer (50 and 150 nm), there would be a full mixing of Ti with ITO that will change the peculiar properties of ITO thus explain the lower V_{oc} values. For thicker ITO film (250 and 350 nm) the Ti atoms would have only partially diffused into the ITO film thus preserving its properties. The above result shows that conductivity of the electrical contact layer is an important factor to be considered to acquire better photo-voltage. Another fact to be possibly considered is that conductance of annealed TiO₂ film is often low and depends on annealing condition. Hence in future activity, electrochemical pre-treatment process will be considered for sol-gel derived film before annealing to modify carrier density and increase surface area as reported by Hepel et al. [17]. Nevertheless, the voltage attained by the first cell (0.7 V) is not enough for water decomposition (1.23 V).



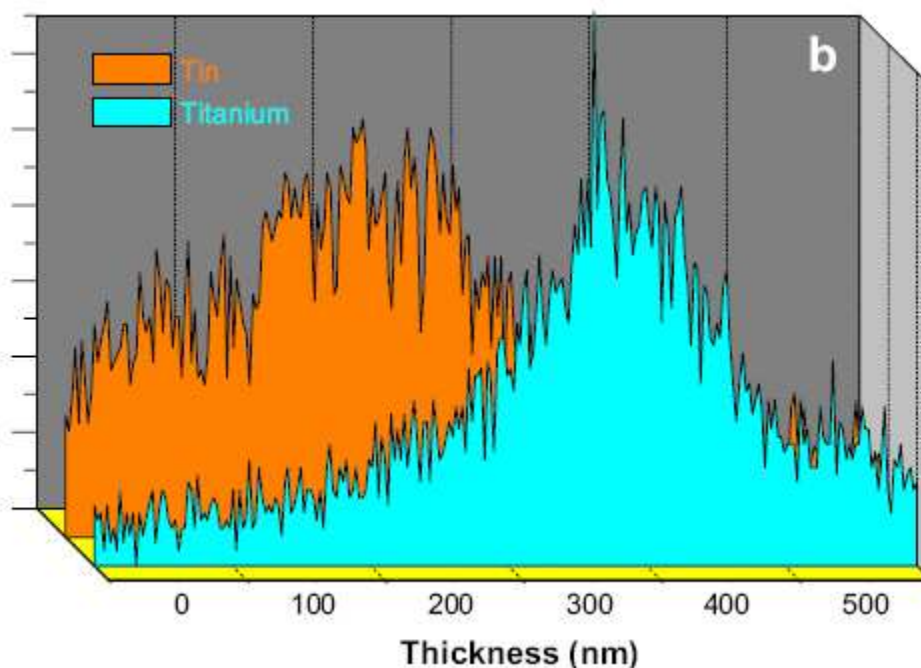


Figure 6: Composition analysis along the cross-section of the sol-gel deposited TiO_2 thin films (a) before and (b) after heat-treatment at 500°C .

In the second cell as shown in Fig. 7, chemical bias with high pH difference ($\Delta\text{pH} = 14$) was applied to reach the required voltage for the water splitting. TiO_2 photo-anode and Pt cathode were immersed into basic and acidic solution respectively ($\Delta\text{pH} = 14$), to provide electrical driving force for electron transfer from TiO_2 to Pt side. As observed earlier, sputter deposited TiO_2 film acts as a better photocatalyst when deposited on low thickness (50 nm) ITO film (denoted as sample A hence after). On the contrary, the sol-gel deposited TiO_2 film showed enhanced performance with thicker (on the order of 350 nm) ITO film (denoted as sample B hence after). The open-circuit voltage characteristics of samples A and B, as function of time during the light ON/OFF regime are reported in Figs. 8 and 9, respectively, for chemically biased cell.

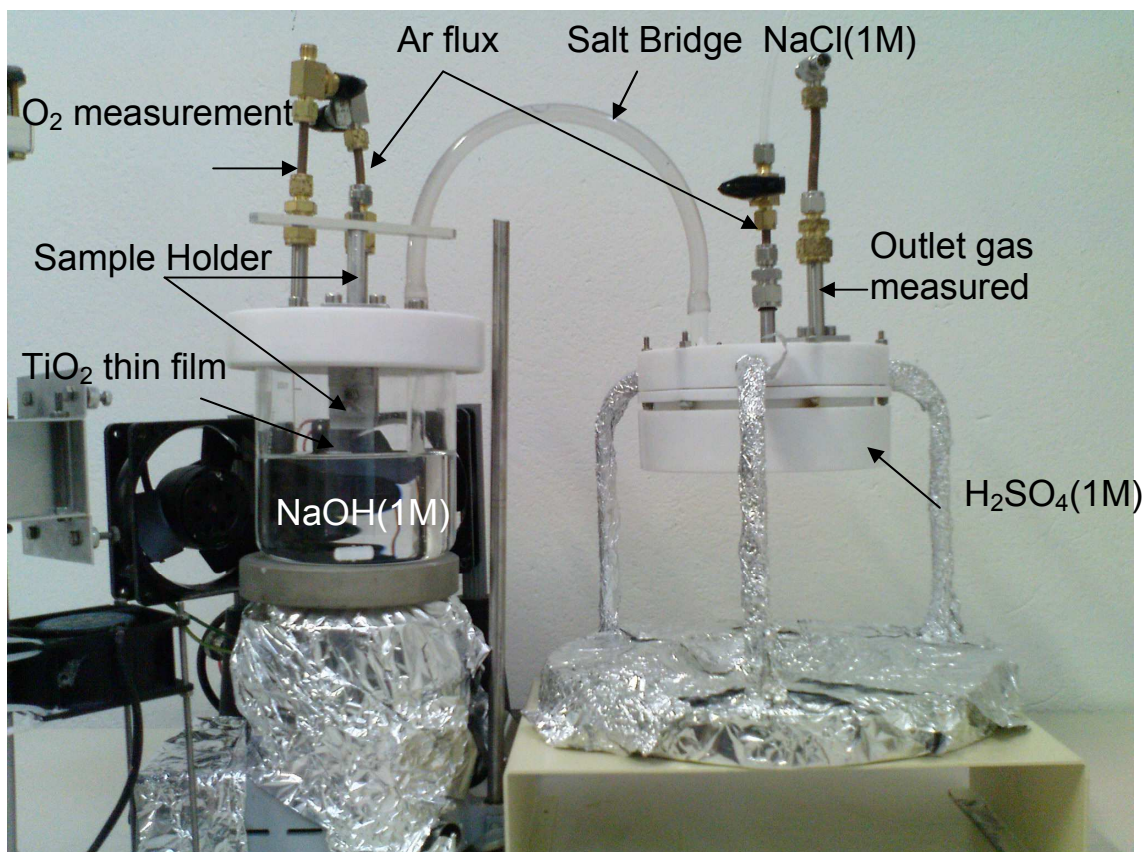


Figure 7: The photo-electrochemical cell

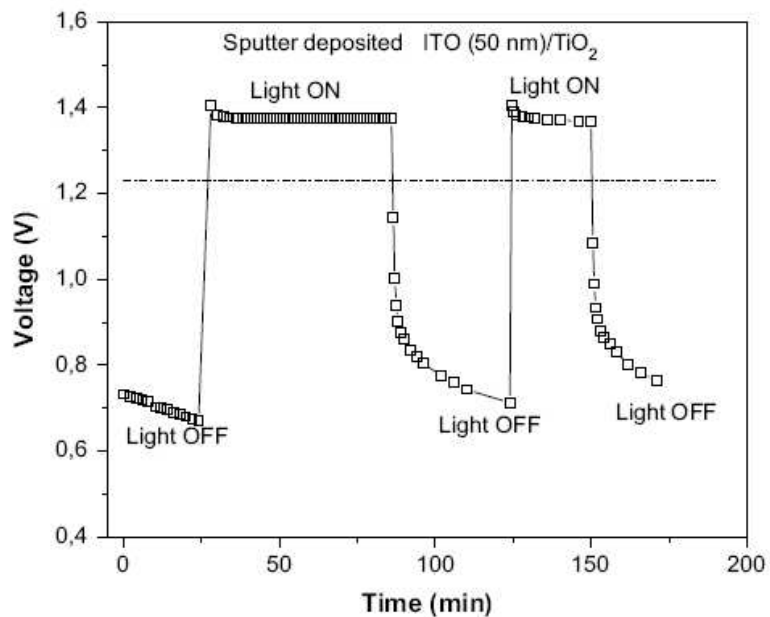


Figure 8: Open-circuit photo-voltage (V_{oc}) measured during the light ON and OFF regime as function of time for the sample A using photo-electrochemical cell containing two electrolytes of different pH.

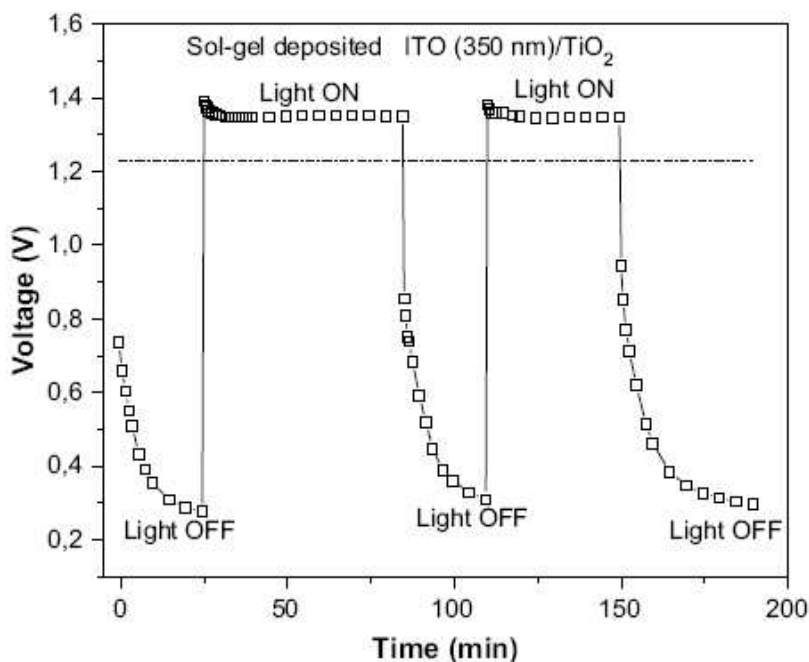


Figure 9: Open-circuit photo-voltage (V_{oc}) measured during the light ON and OFF regime as function of time for the sample B using photo-electrochemical cell containing two electrolytes of different pH.

In the initial light OFF interval, the V_{oc} value measured across samples A and B is about 0.7 V which decreases with time up to ~0.65 V and ~0.3 V respectively. Exposure to light results in the increase of photo-voltage to the level of about ~1.4 V for both samples and this voltage value is achieved in 30 s. These results indicate that by using the present photo-electrochemical cell with TiO_2 photocatalyst, the required voltage for the water decomposition (1.23 V) is attained. The photo-voltage (~1.4 V) remains almost constant for period of 60 min in the ON light regime as shown in figures. The light OFF regime causes the voltage to drop to about the same initial values but the sample A takes about twice the time (40 min) as compared to sample B (20 min). Re-exposure of light again leads to the increase in the photo-voltage to previous level. After 45 days, similar results are obtained in light ON/OFF regime by using same samples thus proving the stability of our samples for photocatalytic activity.

Photocatalytic activity of the TiO_2 films produced by sputtering and sol-gel has been tested by measuring H_2 generated by water splitting.

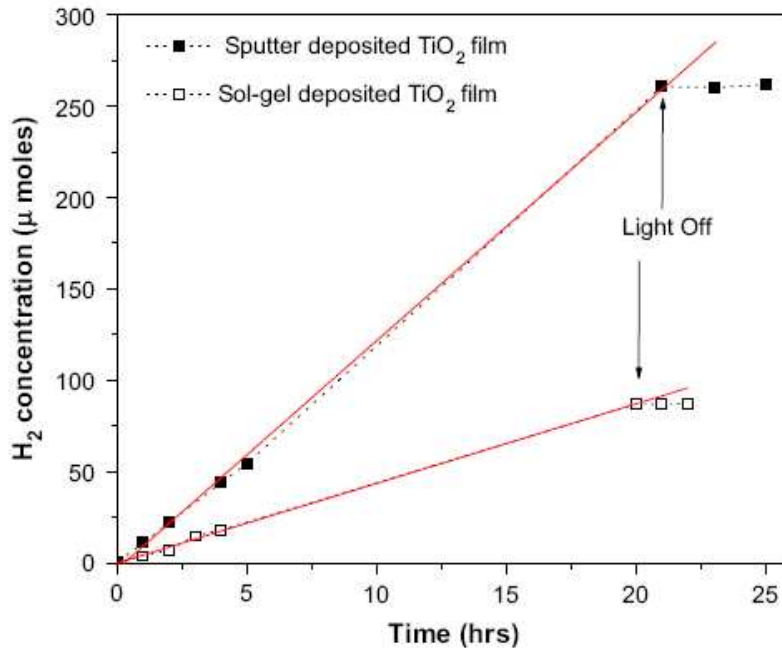


Figure 10: Hydrogen evolution as a function of time measured through water splitting by using magnetron sputter and sol-gel deposited TiO₂ photo-anode films in photo-electrochemical cell containing two electrolytes of different pH. The red line in the figure demonstrates the linear trend of the experimental points.

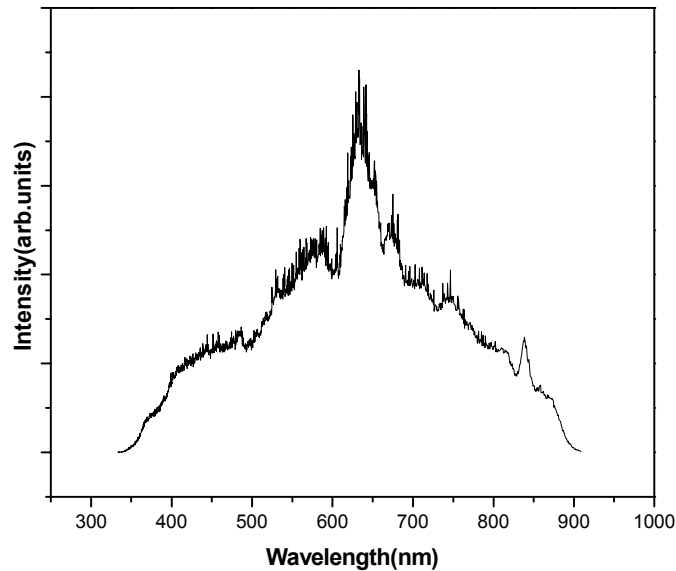


Figure 11: Spectral photon flux for tungsten halogen lamp.

Fig. 10 shows the H₂ evolution as function of time by irradiating the TiO₂ films with the light (250W tungsten halogen lamp) which contains mostly visible light with small portion of UV light (0.5%) as shown in Fig.11. Photocatalytic H₂ evolution increases linearly with the exposure time and even after 20 and 21 h the H₂ production rate (obtained with linear fitting of the experimental data points having R² = 0.999) is constant for sputter and sol-gel deposited TiO₂ films respectively. The H₂ evolution completely stopped after termination of the light irradiation thus showing that H₂ is produced only photocatalytically. The constant rate production observed in the present case is simply due to the employ of TiO₂ photocatalyst in form of thin film in a system where the H₂ and O₂ evolve separately. Thus the present protocol provides a better option than the Pt-loaded TiO₂ powder where H₂ production rate decreases with time because of the back-reaction with O₂ produced in the same chamber. By adding redox mediator like Na₂CO₃, NaI, and NaOH in the solution to stop the back reaction in the Pt-loaded TiO₂ powder, the H₂ production rate does not remain constant along the time [18,19]. The H₂ generation rate was measured to be 12.5± 0.1 and 4.3 ± 0.1 μmole/h for the sputter (sample A) and sol-gel (sample B) deposited TiO₂ films, respectively. During the measurement, the same surface area (13.75 cm²) was exposed to the light for both films. Lower production rate observed for sample B is also connected to the absorption band which extends towards the lower wavelength as compared to the sample A. However in sample A, along with the band gap of 3.2 eV of the anatase phase, there are also the energy levels in the band gap contributed by either rutile phase or stoichiometric defects leading to greater absorption of the visible light. Defects are produced by the sputter deposition process during which energetic ions, at low Ar gas deposition pressure, create oxygen vacancies in the deposited film. Another possible proof for the role of the oxygen vacancies can be obtained on the basis of morphological variation observed in sputter and sol-gel deposited films. During sputter deposition, a proper columnar structure perpendicular to the substrate is observed by SEM. In agreement with the experimental evidence reported by Matsuoka et al. [26], in this kind of columnar crystals the surface is covered with a stoichiometric TiO₂ phase (O/Ti = 2.00) while moving inside the bulk and near the interface with the substrate, the oxygen concentration slightly decreases (O/ Ti = 1.93). On the contrary, in sol-gel-synthesized film a compact and uniform film is formed throughout. The oxygen vacancies created in film during sputtering process produce the impurity energy levels into the band gap leading to the

higher visible light absorption. Similar results have been reported by Kitano et al. [33] who showed the increase in the light absorbance by decreasing the deposition gas pressure. The recombination of the photo-generated electron–hole pairs is one of the important factors in the efficient solar energy conversion. However in present ITO/TiO₂ stack film, conduction band edge of ITO (~-4.5 eV) is at lower energy level than that of TiO₂ (~-4.0 eV) thus creating favourable situation for later to inject electrons [46]. In addition, external chemical bias would create downward band bending of the conduction and valence bands at the interface between the TiO₂ film and ITO substrate [47]. Hence, photo-excited electrons in the conduction band of TiO₂ can effortlessly flow to the conduction band of ITO leaving back the holes in the valence band of former, thus efficiently separating the photo-generated charges. Similar behaviour is visualized for WO₃/TiO₂ bi-layers semiconductor photo-anodes where the conduction band electron from TiO₂ as an external film were driven to the internal WO₃ film due to the lower level of conduction band edge in WO₃ [48]. The holes on TiO₂ surface then oxidize the water molecule to produce O₂ gas while electrons collected on Pt, transferred by ITO, reduce the H⁺ ions to evolve H₂ gas.

2.2.3 Conclusion:

We reported hereby on hydrogen production by water splitting in photo-electrochemical cells prepared by using photo-anodes made by two different kinds of TiO₂: one deposited by RF sputtering and the other one by sol–gel method. Depositions were performed on electrical conducting ITO whose electrical properties play vital role to reduce the photon energy loss. The photo-anodes have been characterized by several techniques to infer on their optical and compositional properties. The observed differences in hydrogen production have been attributed to the peculiarities in absorption properties of the two TiO₂ films that in the case of sputter-deposited films are more prone to absorb radiation also because of the produced defects during the deposition process.

2.2.4 References

- [1] Rausch N, Burte EP. Thin TiO₂ films prepared by low pressure chemical vapor deposition. *J Electrochem Soc* 1993;140(1): 145–9.
- [2] Ozer N, Demiryont H, Simmons JH. Optical properties of sol– gel spin-coated TiO₂ films and comparison of the properties with ion-beam-sputtered films. *Appl Opt* 1991; 30(25): 3661–6.
- [3] Byrne JA, Eggins BR, Linquette-Mailley S, Dunlop PSM. The effect of hole acceptors on the photocurrent response of particulate titanium dioxide. *Analyst* 1998; 123: 2007–12.
- [4] Kikuchi H, Kitano M, Takeuchi M, Matsuoka M, Anpo M, Kamat PV. Extending the photoresponse of TiO₂ to the visible light region: photo-electrochemical behavior of TiO₂ thin films prepared by the radio frequency magnetron sputtering deposition method. *J Phys Chem B* 2006;110(11):5537–41.
- [5] Kim JH, Lee S, Im HS. The effect of target density and its morphology on TiO₂ thin films grown on Si(100) by PLD. *Appl Surf Sci* 1999; 151:6–16.
- [6] Fujishima A, Hashimoto K, Watanabe T. TiO₂ photocatalysis: fundamentals and applications. BKC Inc.; 1999; 123.
- [7] Djaoued Y, Badilescu S, Ashrit PV, Bersani D, Lottici PP, Robichaud J. Study of anatase to rutile phase transition in nanocrystalline titania films. *J Sol–Gel Sci Tech* 2002; 24(3): 255-64.
- [8] Lohstroh W, Westerwaal RJ, Van Mechelen JLM, Chacon C, Johansson E, Dam B, et al. Structural and optical properties of Mg₂NiH_x switchable mirrors upon hydrogen loading. *Phys Rev B* 2004; 70(16): 165411
- [9] Davis EA, Mott NF. Conduction in non-crystalline systems V. Conductivity, optical absorption and photoconductivity in amorphous semiconductors. *Philos Mag* 1970; 22(179): 903–22.
- [10] Radecka M, Zakrewska K, Wierzbicka M, Gorzkowska A, Komornicki S. Study of the TiO₂-Cr₂O₃ system for photoelectrolytic decomposition of water. *Solid State Ionics* 2003; 157(1–4): 379–86.
- [11] Halley JW, Kozlowski M, Michalewicz M, Smyrl W, Tit N. Photoelectrochemical

- spectroscopy studies of titanium dioxide surfaces: theory and experiment. *Surf Sci* 1991; 256(3): 397–408.
- [12] Radecka M, Zakrzewska K, Czternastek H, Stapiński T, Debrus S. The influence of thermal annealing on the structural, electrical and optical properties of TiO_{2-x} thin films. *Appl Surf Sci* 1993; 65/66: 227–34.
- [13] Madhusudan Reddy K, Gopal Reddy CV, Manorama SV. Preparation, characterization and spectral studies on nanocrystalline anatase TiO₂. *J Solid State Chem* 2001; 158(2): 180–6.
- [14] Kumar PM, Badrinarayanan S, Sastry M. Nanocrystalline TiO₂ studied by optical, FTIR and X-ray photoelectron spectroscopy: correlation to presence of surface states. *Thin Solid Films* 2000; 358(1–2): 122–30.
- [15] Matsuoka M, Kitano M, Takeuchi M, Anpo M, Thomas JM. Photocatalytic water splitting on visible light responsive TiO₂ thin films prepared by a RF magnetron sputtering deposition method. *Topics Catal* 2005; 35(3–4): 305–10.
- [16] Bak T, Nowotny J, Rekas M, Sorrell CC. Photo-electrochemical hydrogen generation from water using solar energy. Materials-related aspects. *Int J Hydrogen Energy* 2002; 27(10): 991–1022.
- [17] Hepel M, Dela I, Hepel T, Luo J, Zhong CJ. Novel dynamic effects in electrocatalysis of methanol oxidation on supported nanoporous TiO₂ bimetallic nanocatalysts. *Electrochim Acta* 2007; 52(16): 5529–47.
- [18] Kudo A. Recent progress in the development of visible light driven powdered photocatalysts for water splitting. *Int J Hydrogen Energy* 2007; 32(14): 2673–8.
- [19] Sato S, White JM. Photodecomposition of water over Pt/TiO₂ catalysts. *Chem Phys Lett* 1980; 72(1): 83–6.
- [20] Matsuoka M, Kitano M, Takeuchi M, Tsujimaru K, Anpo M, Thomas JM. Photocatalysis for new energy production recent advances in photocatalytic water splitting reactions for hydrogen production. *Catal Today* 2007; 122(1–2): 51–61.
- [21] Kitano M, Matsuoka M, Ueshima M, Anpo M. Recent developments in titanium oxide-based photocatalysts. *Appl Catal A Gen* 2007; 325(1): 1–14.
- [22] Salafsky JS. Exciton dissociation, charge transport, and recombination in ultrathin, conjugated polymer-TiO₂ nanocrystal intermixed composites. *Phys Rev B* 1999; 59(16) 10885–94.

- [23] Ma Y, Qiu J, Cao Y, Guan Z, Yao J. Photocatalytic activity of TiO_2 films grown on different substrates. *Chemosphere* 2001; 44(5):1087–92.
- [24] Shiyanskaya I, Hepel M. Decrease of recombination losses in bicomponent WO_3/TiO_2 films photosensitized with cresyl violet and thionine. *J Electrochem Soc* 1998; 145: 3981–5.

2.3 Visible light active Cr-Fe doped TiO₂ thin film for water splitting.

The last section (2.2) compares the physical and chemical methods to synthesize TiO₂ thin film and development of photochemical cell was also mentioned. This section elucidates the improvement of TiO₂ thin film to absorb visible part of solar light by modification of its optical properties. The most popular dopants for modification of the optical and photo-electrochemical properties of TiO₂ are transition metals such as Cr, Fe, Ni, V, Mn, and Cu. Choi et al. [5] carried out a systematic investigation of the photocatalytic activity of TiO₂ doped with 21 different metal ions. It was found that doping with metal ions may extend the photo-response of TiO₂ into the visible spectrum by introducing additional energy levels in the band gap of TiO₂. Among this transition metals we selected two transition metals, namely Cr and Fe, for doping TiO₂ to make it sensitive to visible light and to split water efficiently in hydrogen and oxygen. Investigations of the doping methods, dopant concentration, charge transfer from metal dopants to TiO₂, and type of dopants were carried out in an attempt to enhance photocatalytic activity.

2.3.1 Experiment

Material and chemicals:

Indium Tin Oxide (ITO) (99.99%) bought from supplier “Thin Films materials process solutions” and TiO₂ (99.99%) targets was commercially supplied by “Goodfellow Cambridge Ltd.”. Metal pieces of Chromium and iron acquire from “Balzers coating materials” and “Cerac coating materials” respectively. Titanium butoxide [Ti(OC₄H₉)₄], Ethanol (C₂H₅OH) and Nitric Acid (HNO₃) were used as received. To doped TiO₂ film chemical salts such as Cr(NO₃)₃ or Fe(NO₃)₃ used as source of Cr and Fe metal respectively. These chemicals were of analytical grade and purchased from “Sigma Aldrich”. All solutions were prepared using high purity deionized water.

Synthesis of ITO conducting thin film by using RF magnetron sputtering:

To measure photocatalytic activity, TiO₂ films were deposited on the conducting indium tin oxide (ITO) layer because ITO has two chief properties, namely electrical conductivity and optical transparency. A high electrical conductivity facilitated the separation of photogenerated electrons and holes, preserving the photocurrents of the electrodes. ITO layer was deposited on the glass slide by magnetron sputtering by using RF power of 100W and working Ar gas pressure of 0.8 Pa. Pre-sputtering of the ITO target was also conducted in order to remove the surface contamination. The sample and target distance was kept constant at 5 cm for all the samples.

Synthesis of metal doped TiO₂ solar sensitive thin film photocatalyst by using RF magnetron sputtering:

Metal-doped TiO₂ films were synthesized by partially covering the TiO₂ target surface with small Cr- or Fe metal discs. The number of discs on the TiO₂ target was varied in order to obtain metal-doped films of several different atomic concentrations of Cr or Fe, up to a maximum value of 5 at.%. High vacuum (HV) with base pressure $< 3 \times 10^{-5}$ Pa and working Ar pressure of 0.8 Pa were used in the deposition chamber. Before film deposition, the TiO₂ target was pre-sputtered for 20 min in order to remove any surface contamination. The TiO₂ films were sputter-deposited on both glass and Si (100) substrates at room temperature using RF power of 150 W. The sample-target distance was kept constant at 6cm for deposition of all the samples. After deposition, no post annealing was performed.

The molar compositions of [Ti(OC₄H₉)₄]/H₂O/C₂H₅OH/HNO₃/Cr(NO₃)₃ or Fe(NO₃)₃ for sol were: 1:0.5:20:0.1:x. Here, x was set at several different molar values, namely: 0.03, 0.06, 0.158, and 0.260, to obtain metal at.% values of: 0.5, 1, 2, and 5, respectively, in the final metal-doped TiO₂ films. The mixture of Ti (OC₄H₉)₄, ethanol (half the amount), and metal salts was vigorously stirred for 1 h at room temperature. Another mixture of water, ethanol (remaining half), and HNO₃ was added drop wise to the original mixture under vigorous stirring for 1 h. The resultant solution was stirred for an additional

1 h at room temperature to increase its homogeneity before spin coating. Metal-doped TiO₂ sol was spun for 40 s at 3000 rpm on both glass and Si (100) substrates to obtain thin films which were further baked at 125 °C for 1 h. The samples thus obtained were thermally treated in static air at 500 °C for 2 h. The heating rate was about 1 °C min⁻¹. Flowchart of experimental procedure is shown in Fig.1.

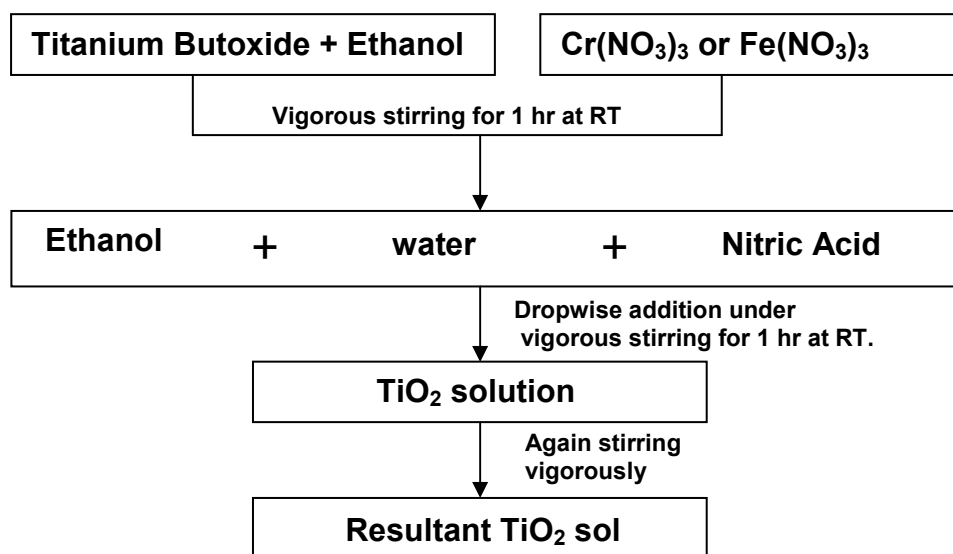


Figure 1: Schematic diagram of preparation process of metal doped TiO₂ sol by sol–gel method.

The structural characterization of the sputter-deposited TiO₂ films was carried out by an X-ray diffraction (XRD) technique (Cu K α radiation, $\lambda = 1.5414 \text{ \AA}$) in Bragg–Brentano ($\theta - 2\theta$) configuration. Fourier Transform Infrared Spectroscopy (FTIR) was used to determine the phase of the TiO₂ films because the thickness of the sol–gel films was too thin to be analyzed with our XRD set-up. The measurements were conducted in absorbance mode at normal incidence within the spectral range of 4000–400 cm⁻¹ using a Bruker (Equinox 55) spectrometer at room temperature. Optical measurements in the Ultraviolet (UV) and visible range were performed using a Bruker IFS66 spectrometer equipped with reflection and transmission units while the incoming beam was incident near to the surface normal. To obtain the absorbance spectra of samples deposited on glass slides, the measurements were performed in the wavelength range between 250 nm and 750 nm. The surface morphology of the TiO₂ samples was analyzed by means of a scanning

electron microscope (SEM, JEOL) equipped with Energy Dispersive Spectroscopy (EDS) which permitted compositional studies of the films.

To measure their photocatalytic activity, metal doped TiO₂ thin films were deposited on a conducting indium tin oxide (ITO) layer. The performance of metal-doped TiO₂ films in photocatalytic water-splitting was tested by measuring both photo-current and hydrogen production rates. The photo-electrochemical cell used TiO₂ as the photo-anode, Pt mesh as the cathode, and aqueous electrolytes. In order to establish a chemical bias we used two chambers containing electrolytes with different pH values. The TiO₂ photo-anode was kept in contact with an NaOH (1 M) solution, while the cathode was immersed in a H₂SO₄ (1 M) solution. A salt bridge containing NaCl (1 M) was used to provide a path for ion conduction between the two chambers. The photo-anode was exposed to visible light from a 250-W tungsten halogen lamp to measure open-circuit photo-voltage and closed-circuit photo-current. The reactor for water-splitting tests was prepared with borosilicate glass that acts as a UV filter, while the reactant water solution is a filter for IR radiation. Oxygen from the reaction chamber was completely removed by purging the chamber with pure Ar gas (99.9%) for 1 h before performing measurements. The evolution of H₂ originated by the water-splitting process at the cathode was measured on-line, as a function of time, by using a gas chromatographer (GC, Agilent MIRCOGC- 3000A). Finally, the hydrogen evolution was measured in both light-ON and light-OFF regimes.

2.3.2 Results and discussion

A. X-Ray Diffraction:

The Cr- and Fe-doped TiO₂ films were greenish and reddish in color, respectively. Fig. 2 shows the XRD spectra of the metal-doped-TiO₂ films deposited by RF-magnetron sputtering on amorphous glass. The peaks of pure TiO₂ are mainly due to the anatase phase while some weak additional reflexes are attributed to the rutile phase. The crystal grain size of the rutile and anatase phase is about 6 nm and 45 nm, respectively, as calculated by using the Debye–Scherrer equation. This means that the rutile phase is almost amorphous with very finely dispersed grains while, on the other hand, the anatase phase is in nano

crystalline form and just this phase is most suitable for the photocatalytic reaction [2]. The TiO₂ films doped with low concentrations of Cr (0.8 and 1.2 at.%) and Fe (0.4 and 1.1 at.%) exhibit peaks which are similar to that of the un-doped films. However, when TiO₂ is doped with 3.8 at.% of Cr, the rutile phase, with crystal grain size of about 30 nm, prevails over the anatase phase. The reflexes of the rutile phase are now shifted to lower 2θ values, as compared to those of pure TiO₂ film. This indicates a slight increase in the spacing value between the lattice planes which might be caused due to insertion of Cr in the lattice. A complete amorphization of the TiO₂ films is observed at high dopant concentration of both Cr (5.2 at.%) and Fe (4.9 at.%), while metal oxides (Fe₂O₃ or Cr₂O₃) formation is not detected by XRD. Cr³⁺ and Fe³⁺ metal ions have an effective diameter comparable to that of Ti⁴⁺ ions. Thus, during sputter deposition, the metal ions emitted from the target with kinetic energy of some 10 eV might be able to replace the Ti⁴⁺ ions in the lattice of TiO₂ without changing the crystal structure, at least for low doping concentration. However, high metal acceptor dopant concentration (on the order of 4 at.%) causes the formation of oxygen vacancies whose mobility may account for anatase to rutile phase transformation [3] in the TiO₂ film. If the concentration of these metal ions exceeds the solubility limit, the TiO₂ cannot crystallize in any particular phase [4].

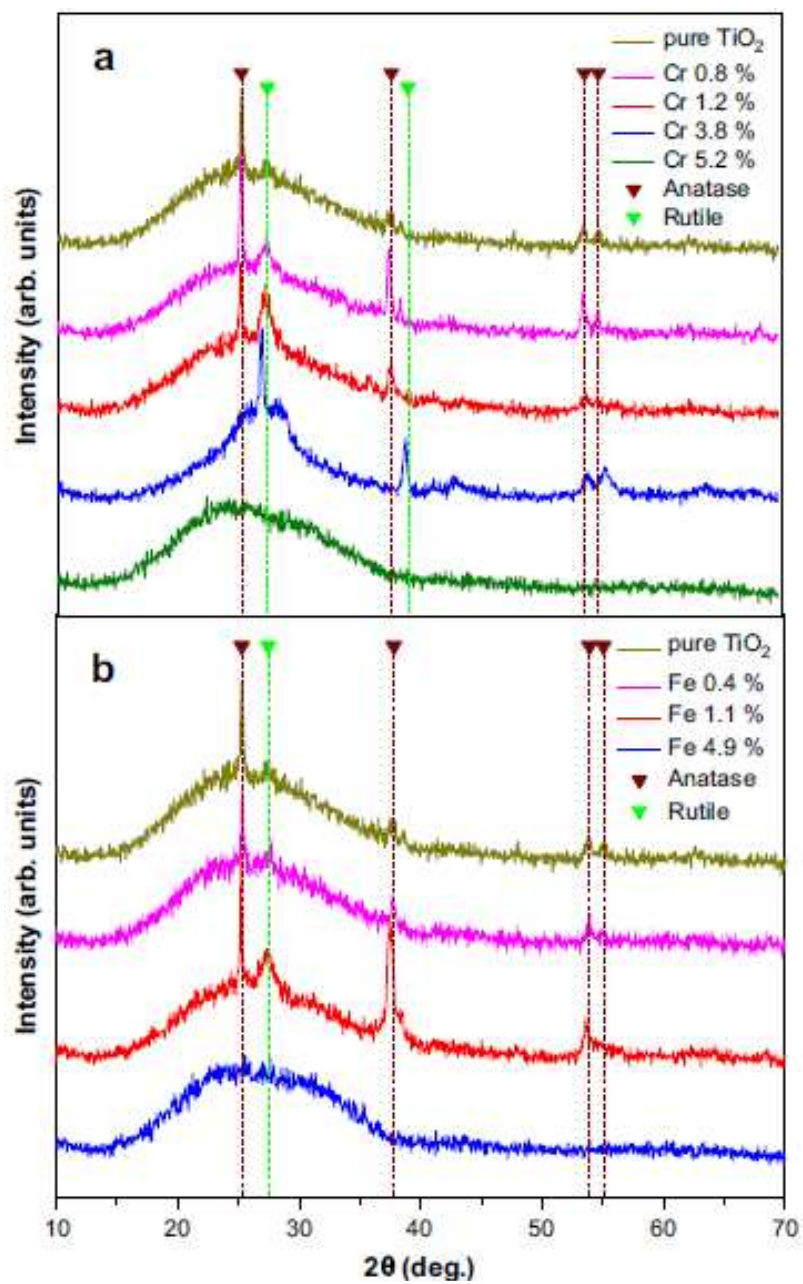


Figure 2: XRD spectra of (a) Cr- and (b) Fe-doped TiO_2 thin films with different dopants concentration deposited by RF-magnetron sputtering.

B. Fourier Transform Infrared Spectroscopy (FTIR)

The IR spectra (Fig. 3) of pure TiO₂ films prepared by sol-gel method show one distinct peak at ~433 cm⁻¹ which is attributed to the vibration of the TiO₂ units in anatase phase [5]. The same peak, with more broadening, also appears in low concentration (0.5–1 at.%) Cr- (Fig. 3a) or Fe- (Fig. 3b) doped TiO₂ films. This proves that after metal doping at low concentration, the TiO₂ anatase phase still exists, but having a low crystalline degree. The vibration peak of the anatase phase disappears in Cr-doped (2 at.%) TiO₂ film, while it appears very broadened in the case of Fe-doped films with similar concentration. However, by increasing the dopant concentration up to 5 at.% for both the metal ions doping, the anatase phase related vibration peak disappears while a new peak at ~490 cm⁻¹ emerges. This band has been assigned to the Ti–O–Ti stretching vibration in the rutile phase [5]. Thermal annealing at 500⁰C of sol-gel-TiO₂, doped with Cr or Fe at concentration similar to 5 at.%, causes phase transformation from anatase to rutile. As explained above, doping TiO₂ with acceptor impurities like chromium or iron, causes oxygen vacancies formation favoring the rearrangement of Ti⁴⁺ and O²⁻ ions in the lattice and finally the anatase to rutile phase transformation [3].

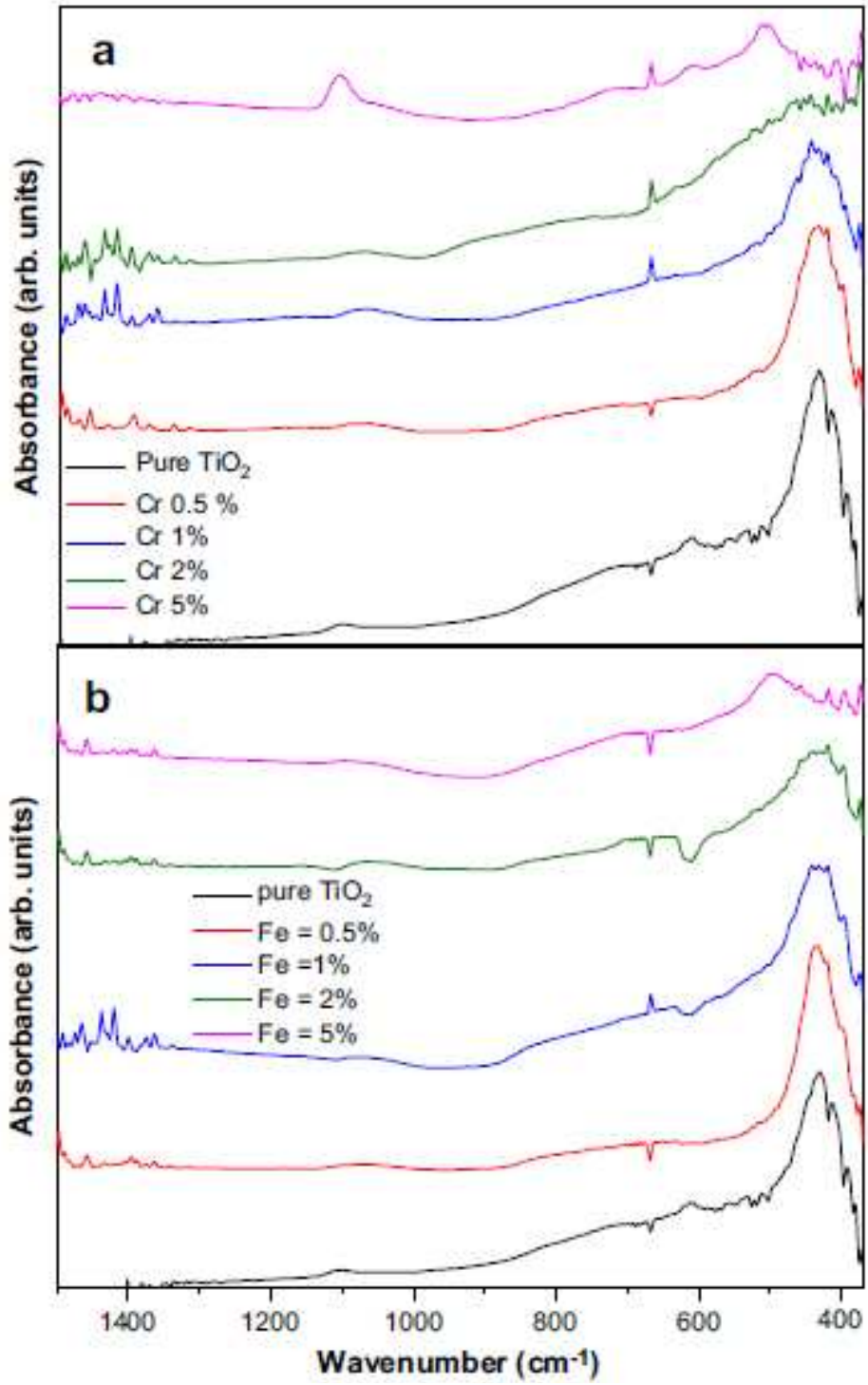


Figure 3: FTIR spectra of (a) Cr- and (b) Fe-doped TiO₂ thin films with different dopants concentration deposited by sol-gel technique.

C. Scanning Electron Microscopy (SEM):

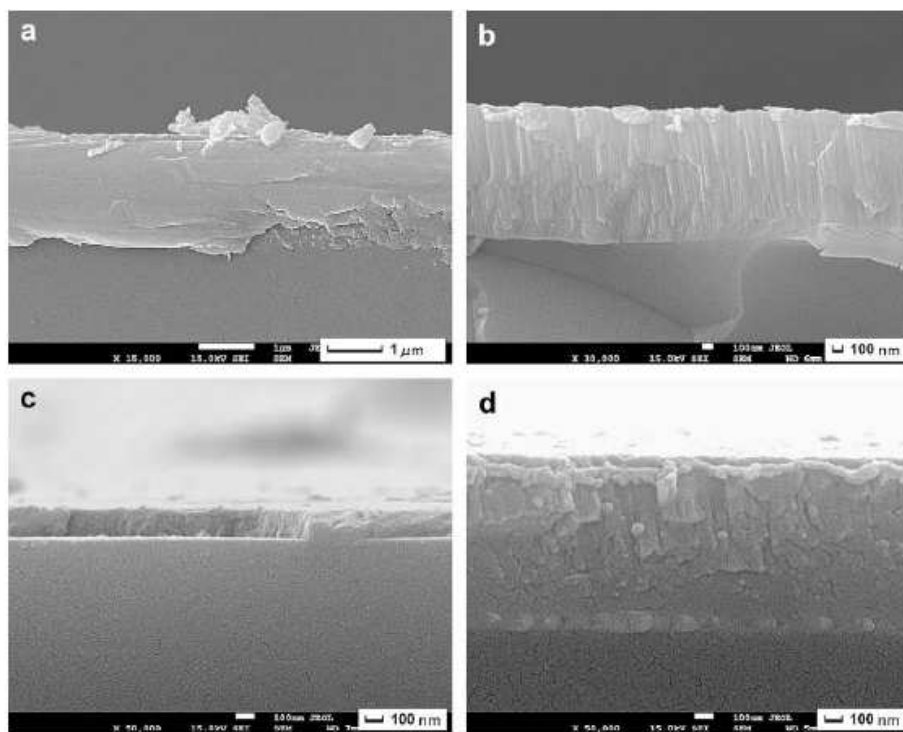


Figure 4: SEM images of (a) Cr- and (c) Fe-doped TiO_2 films prepared by sol-gel method, and (b) Cr- and (d) Fe-doped TiO_2 films prepared by RF-magnetron sputtering.

As observed by SEM, the surface morphology of the metal doped TiO_2 films, deposited by both methods, appears quite flat, smooth, and without major defects. In Fig. 4 we report SEM cross-section micrographs of the metal doped TiO_2 thin films (concentration similar to 1 at.%) deposited by both methods. The sol-gel- TiO_2 films, doped with Cr or Fe, result quite compact as observed in Fig. 4a and Fig4c.

A dense columnar structure is typically observed in Cr-doped TiO_2 film deposited by sputtering (Fig. 4b). On the other hand, Fe-doped TiO_2 film produced by sputtering shows a compact structure rather than a columnar one (Fig. 4d). In addition, SEM images obtained in back scattering mode, show uniform distribution of metal ions in the TiO_2 film. This feature is also confirmed, in the sampled volume, by compositional line scan using

EDS. The dopant concentration uniformity is clearly connected to the adopted co-deposition procedure.

D. UV-Visible Spectroscopy:

The optical properties of the pure and metal-doped TiO₂ were studied by measuring the absorption spectra ranging from UV (250 nm) to visible (750 nm) wavelengths. The results are presented in Figs. 5 and 6 for TiO₂ samples doped with Cr and Fe, respectively. The figures clearly show a shift in the absorption band edge towards longer wavelength when increasing the metal concentration in the TiO₂ film. This shift is more prominent for the sputter-deposited films. The band gap value is obtained by fitting the absorption edge of UV– Visible spectra by using the following equation [6]:

$$\ln T = \ln T_0 - C \frac{(\hbar\omega - E_g)^n}{\hbar\omega} \quad (2.9)$$

where E_g is the band gap, C is a constant, and T_0 is the optical transmission of the substrate. Depending on the type of transition, n assumes different values: for direct, allowed (forbidden) transitions $n = 1/2$ ($n = 3/2$) and for indirect, allowed (forbidden) transitions $n = 2$ ($n = 3$). We used $n = 2$ for the present nano crystalline or amorphous films according to Ref. [7]. Near the absorption edge, T_0 and C are approximately constant and the E_g value of all the TiO₂ samples is obtained (see Table 1) by fitting the absorption edge with Eq. (2.9).

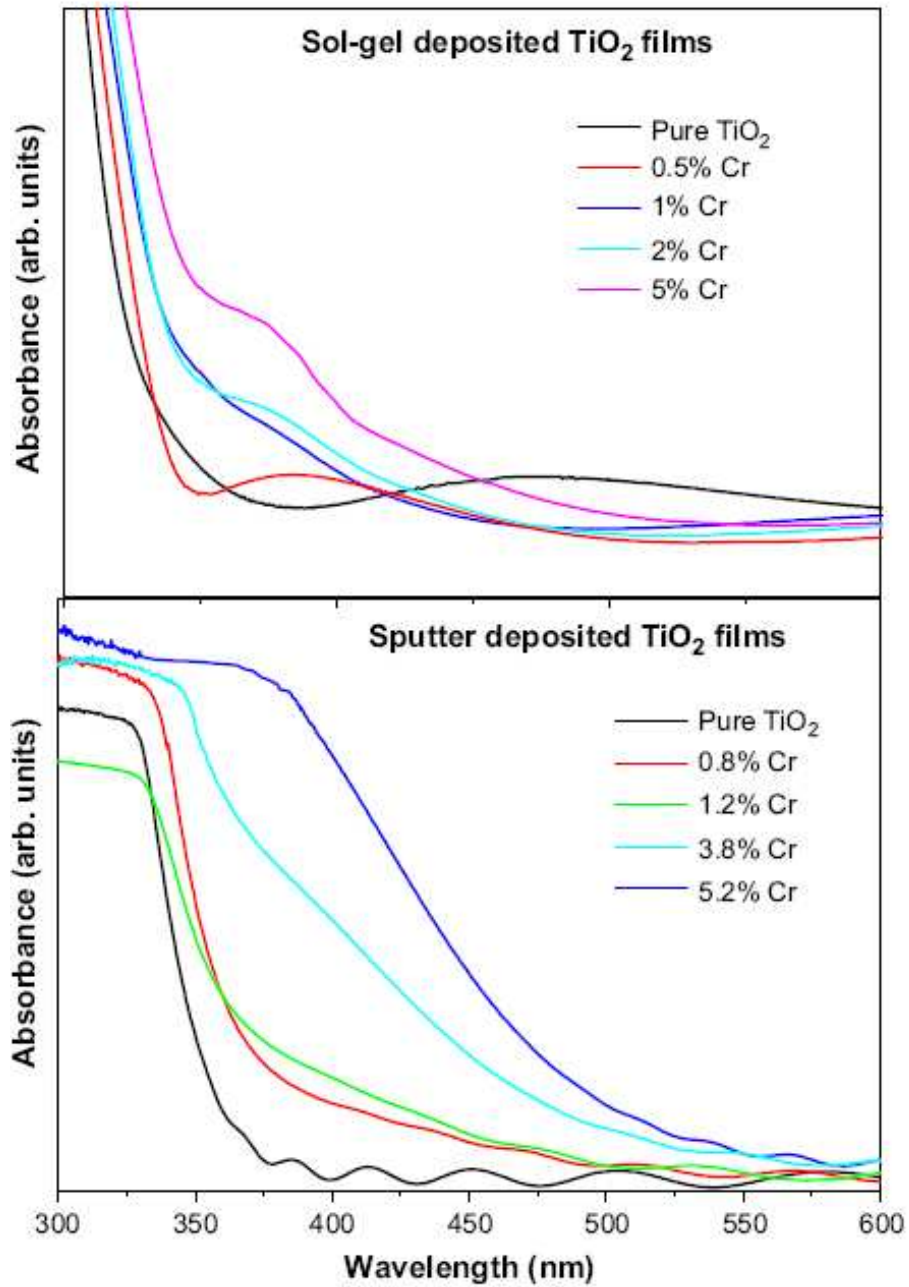


Figure 5: UV-Visible absorption spectra of TiO₂ doped with different concentrations of Cr by using sol-gel and sputtering techniques.

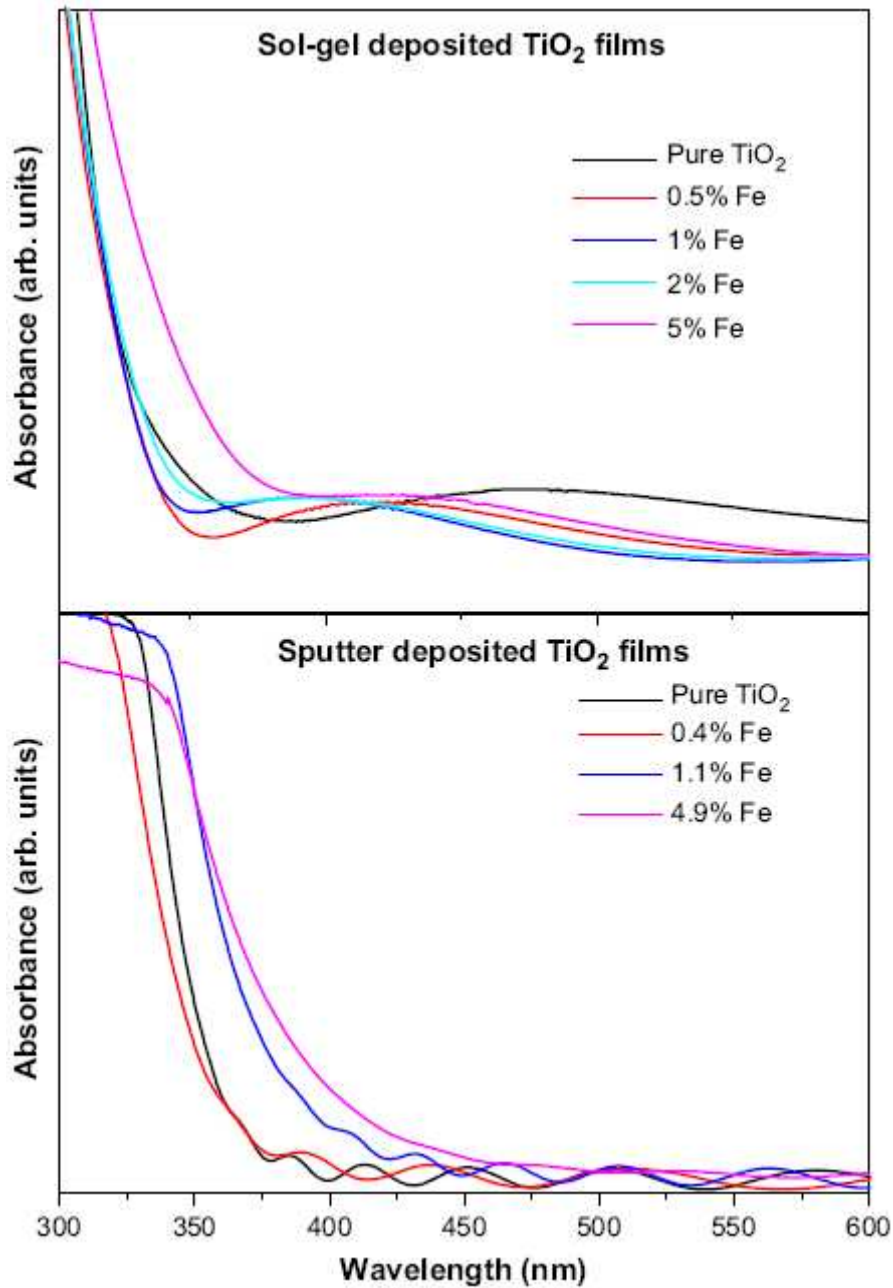


Figure 6: UV-Visible absorption spectra of TiO_2 doped with different concentrations of Fe by using sol-gel and sputtering techniques.

$E_g = 3.4$ eV is obtained for pure sol-gel samples: this value is greater than the theoretical value of both anatase ($E_g = 3.2$ eV) and rutile ($E_g = 3.0$ eV) phase of TiO_2 [24]. However, note that the literature values [8] are related to single crystal or proper crystallized samples, while our IR spectra indicate a low crystallization degree for the

present films. High values, similar to ours, are reported for nano crystallized TiO₂ film [9] and powder [10]. There is no much change in the TiO₂ electronic band gap after chemical doping with Cr at low concentration (0.5 at.%). On the other hand, doping with 1, 2, and 5 at.% of Cr causes a slight narrowing of the band gap and the lower value of 3.2 eV is observed at the highest concentration (5 at.%). This narrowing might be due to the formation of the rutile phase which is here detected by the FTIR analysis. Indeed, the theoretical band gap of the rutile phase is lower than that of the anatase phase [8]. The absorption edge of the Cr-doped samples also possesses a shoulder: its value, after fitting, lies in the range between 2.5 and 2.2 eV. This suggests the presence of new electronic energy levels, within the energy band gap, which are related to the presence of Cr ions into TiO₂. On the contrary, chemical doping of TiO₂ with Fe (0.5, 1, and 2 at.%) does not show any formation of defect energy levels. However, when the Fe dopant concentration is of 5 at.%, a slight narrowing of the band gap (3.2 eV) is observed after heat treatment because of the rutile phase formation.

Table 1 – The energy values of the fundamental band gap and impurity levels obtained after doping TiO₂ films, synthesized with sputtering and sol-gel methods, with Cr and Fe at different atomic concentration. R = fitting coefficient.

Sputter-deposited TiO ₂ films			Sol-gel deposited TiO ₂ films		
Metal concentration (at.%)	TiO ₂ optical band gap (eV)	Impurity energy level (eV)	Metal concentration (at.%)	TiO ₂ optical band gap (eV)	Impurity energy level (eV)
Pure TiO ₂	3.21 (R ² = 0.999)	2.85 (R ² = 0.997)	Pure TiO ₂	3.41 (R ² = 0.994)	–
0.8 Cr%	3.01 (R ² = 0.996)	–	0.5 Cr%	3.38 (R ² = 0.998)	–
1.2 Cr%	2.38 (R ² = 0.991)	–	1 Cr%	3.32 (R ² = 0.996)	2.51 (R ² = 0.999)
3.8 Cr%	2.24 (R ² = 0.999)	–	2 Cr%	3.31 (R ² = 0.995)	2.39 (R ² = 0.999)
5.2 Cr%	2.19 (R ² = 0.999)	–	5 Cr%	3.19 (R ² = 0.994)	2.21 (R ² = 0.998)
0.4 Fe%	3.13 (R ² = 0.996)	–	0.5 Fe%	3.45 (R ² = 0.998)	–
1.1 Fe%	3.02 (R ² = 0.994)	–	1 Fe%	3.44 (R ² = 0.999)	–
4.9 Fe%	2.83 (R ² = 0.999)	–	2 Fe%	3.43 (R ² = 0.999)	–
			5 Fe%	3.22 (R ² = 0.998)	–

In the case of sputter-deposited pure TiO₂ films a band gap of 3.21 eV is obtained: it signals the presence of a well crystallized anatase phase. The absorption edge now contains a shoulder which was fitted with an energy value of 2.85 eV (Table 1) signalling the presence of a new electronic energy level in the band gap. This energy level could be connected to the stoichiometric defects produced by the sputter deposition process where energetic ions at low Ar gas deposition pressure, create oxygen vacancies in the deposited film [11]. Non-stoichiometric TiO₂ plays a significant role in enhancement of

photocatalytic activity. Sputter-deposited TiO₂ film showed indeed higher photocatalytic activity as compared to sol–gel synthesized TiO₂ [11].

In case of metal-doped TiO₂ films produced by sputtering, we note a red shift of the absorption edge irrespective of the metal (Cr or Fe) dopant used. In 5.2 at.% Cr-doped TiO₂, a relevant narrowing of the band gap, from 3.2 eV (pure TiO₂) to 2.2 eV, is observed. On the other hand, the decrement in the energy band gap value of Fe-doped TiO₂ is not as pronounced as in case of the Cr-doped TiO₂. In any case, a band gap value of 2.8 eV is measured in 4.9 at.% Fe-doped TiO₂. Finally, no shoulder is observed in the absorption edge of the Fe- or Cr doped TiO₂ films synthesized by sputtering. The results shown above definitely prove that we were able to sensitize TiO₂ in visible light range by doping with metal ions. We also infer that the metal doping of TiO₂ by sputtering is able to narrow the band gap while the chemical metal doping only forms impurity energy levels into the band gap. To explain these finds, we're going to stress some considerations on the two deposition techniques adopted. During sputter deposition, Cr or Fe ions may have enough energy to displace the Ti ions from their lattice positions thus creating lattice vacancies where the impurity metal ions get incorporated into the TiO₂ films. This incorporation leads to the transfer of 3d electrons from Fe³⁺ or Cr³⁺ to the conduction band of TiO₂ thus causing the narrowing of the band gap [12]. In sol–gel method, the metal-doped TiO₂ sol is deposited on substrate by spinning where the involved kinetic energy is not sufficient to induce lattice atomic relocation. Here the metal-dopant ions could only form aggregate oxides. The formation of impurity energy levels within the band gap is due to these metal oxides [13]. In conclusion, the substitution of Ti with metal ions in the TiO₂ lattice is essential to shrink the TiO₂ band gap.

The above explanation was experimentally proved by Anpo et al. [15]. The authors conducted Extended X-ray Absorption Fine Structure (EXAFS) measurements on Cr-doped TiO₂ produced by ion implantation (physical procedure) and chemical impregnated method. The analysis of EXAFS spectra indicates that, in ion-implanted TiO₂, isolated Cr ions substitute Ti in the lattice position. On the other hand, the chemically Cr doped TiO₂ contains a mixture of aggregated Cr-oxides having tetrahedral and octahedral coordination similar to CrO₃ and Cr₂O₃, respectively. In addition, the results obtained by Anpo et al. [15]

show that the metal-doped TiO₂ synthesized through the physical method is much more efficient to absorb visible light than the chemically doped TiO₂. Considering the above results, we performed the photocatalytic activity measurements only with sputter-deposited metal-doped films.

E. Open Circuit Photo-voltage and photocurrent measurement:

Metal-doped TiO₂ (about 1000 nm thick) was deposited on an ITO layer (50 nm), previously deposited on glass substrate, and the obtained bi-layer was used as photocatalyst for water splitting experiments. This ITO/TiO₂ stack film is able to partially limit the recombination of photo-generated holes and electrons (h⁺ and e⁻) because the conduction band edge of ITO (~-4.5 eV) is at an energy value lower than that of TiO₂ (~- 4.0 eV) thus making favourable the electrons injection for the latter into the former. In addition, the external chemical bias applied to the photo-electrochemical cell creates a downward band bending of both conduction and valence band near the interface between TiO₂ and ITO film substrate [30]. Hence the photo-generated electrons in the conduction band of TiO₂ can effortlessly flow to the conduction band of ITO leaving back the holes in the valence band of the former: this process finally separates the photo-generated charges.

To split water using TiO₂ as photo-anode, a voltage value of 1.23 V in the photo-electrochemical cell is required [2]. Thus the open-circuit photo-voltage, (V_{oc}), was measured in light- ON and light-OFF regimes in photo-electrochemical cell by using Cr- or Fe-doped TiO₂ films as photo-electrode: results are reported in Table 2.

In the initial light-OFF regime, the V_{oc} value measured across all the TiO₂ samples is about 0.7 V and it is due to the chemical bias (details on the adopted procedure are reported in our previous paper [27]). In light-ON regime the photo-voltage value increases to about ~1.4 V for pure TiO₂ samples. This voltage value is achieved in 30 s and remains constant for longer period of time.

Table 2 – Open-circuit photo-voltage (V_{oc}) measured in ON/OFF light regime using Cr- or Fe-doped TiO_2 films, synthesized by sputtering, as photo-anode.

Sample ITO/metal-doped TiO_2	Open-circuit photo-voltage (V_{oc})	
	Light-OFF (V)	Light-ON (V)
Fe = 0.4 at. %	0.73	1.10
Fe = 1.1 at. %	0.74	1.08
Fe = 4.9 at. %	0.71	1.01
Cr = 0.8 at. %	0.72	1.22
Cr = 1.2 at. %	0.75	1.10
Cr = 3.8 at. %	0.75	0.79
Cr = 5.2 at. %	0.76	1.04
Pure TiO_2	0.73	1.44

However, none of the metal-doped TiO_2 samples was able to reach the minimum photo-voltage value (1.23 eV) required for water-splitting. We suppose two possible reasons for the metal-doped TiO_2 inability to produce the appropriate photo-voltage value:

- 1) Recombination of the photo-generated charges on defects associated to the metal ions, and/or
- 2) Battery effect caused under chemical bias [4] by the metal ions which may be leached out in the aqueous medium from the surface of the metal-doped TiO_2 .

To overcome the problem of battery effect, one more layer of non-conducting pure TiO_2 , about 1000 nm thick, was deposited on metal-doped TiO_2 layer. The photo-induced voltage and current were measured in light-ON regime in photo-electrochemical cell with open- and closed-circuit, respectively. The open-circuit photo-voltage value was measured around 1.4 V: this means that the additional TiO_2 top layer was really able to remove the battery effect. However, the problem of recombination centres formed by the dopant metal ions still remains: this is proved by the very low photo-current values measured in the light-ON regime. As seen in Table 3, the value of photo-current is negligible for all the metal-doped TiO_2 samples as compared to the pure TiO_2 films. This clearly shows that doping TiO_2 with metal ions has two effects: 1) titania is sensitized to the visible light range, 2)

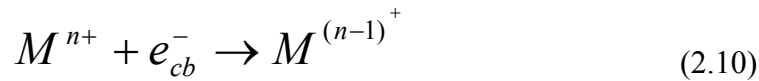
recombination centres are formed where the photo-generated electrons and holes recombine by limiting the photocatalytic activity.

Table 3 – Open-circuit photo-current (I_{oc}) measured in light-ON regime using Cr- or Fe-doped TiO₂ films with pure TiO₂ layer on the top. The three-layer structure was synthesized by sputtering.

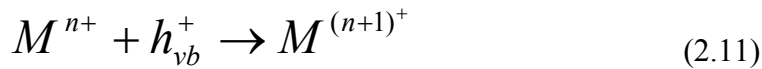
Sample ITO/metal-doped TiO ₂ /pure TiO ₂	Open-circuit photo-current (μ A) (I_{oc})
Metal concentration	Light-ON regime
Cr = 0.8%	26.4
Cr = 1.2%	3
Cr = 3.8%	0.8
Cr = 5.2%	12.5
Fe = 0.4%	3.2
Fe = 1.1%	5.2
Fe = 4.9%	0.2
Pure TiO ₂	290

The concentration of metal-dopant ions plays a very important role in photocatalytic activity. Ideally, metal ions, at low concentration, act as trapping centres for photo-generated electron (e^-) and/or hole (h^+) within the titania band gap thus increasing the recombination time of e^-/h^+ pairs.

Electron trap:

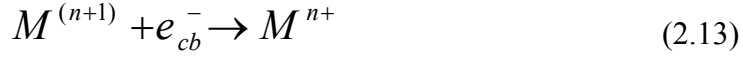
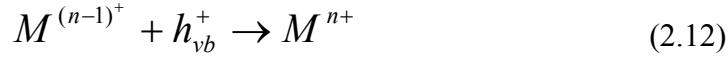


Hole trap:



These initially trapped charges may then migrate, before recombination, towards the interface of the semiconductor where further redox reaction occurs, thus increasing the photocatalytic activity. However, a high concentration of metal ions leads to the recombination of the photo-generated e^- and h^+ accordingly to the following equations:

Recombination trap :



There exists an optimum concentration value of metal dopant ions at which the maximum amount of e^- and/or h^+ are trapped without recombination; above this amount the photocatalytic activity decreases because of the increasing recombination rate. Choi et al. [5] investigated 21 different metal-dopant ions in TiO_2 used for photocatalytic degradation of chemicals. The authors found that the dopant concentration value is a key factor in photocatalytic activity. In addition, a well-defined concentration of Fe^{3+} in TiO_2 is required to gain good photocatalytic activity for water-splitting in aqueous methanol under visible light irradiation [7].

In photocatalytic reaction, with low concentration of dopant ions, charge transfer process is as important as charge trapping. In TiO_2 powders, the trapped electrons and holes must be transferred to the TiO_2 surface where photocatalytic reaction takes place. Therefore, in TiO_2 powders, metal ions should be injected near the surface to have the best conditions for the charge transfer. In case of doping at the major depth below the surface, metal ions likely behave as recombination centres since electron/hole transfer is more difficult. Peng et al. [31] found that the Be dopant ions near the TiO_2 powders surface are efficient for charge carrier transfer, while dopant ions at major depth led to poor performance in photocatalytic activity. A similar finding was reported in Ref. [5].

In our photo-electrochemical cells the TiO_2 photocatalyst is used in form of thin film photo-anode and photo-generated electrons take part in hydrogen generation through H^+ neutralization at the cathode. Thus, before recombination, photo-electrons must be transferred from TiO_2 photocatalyst to the Pt electrode, via ITO. To favour the role of the photo-electrons, they must be efficiently transferred from TiO_2 to the ITO.

According to our previous considerations, in order to reduce the recombination rate of electrons and holes and to improve the efficiency of the hydrogen production, two samples of thin Cr- or Fe-doped TiO₂ layer of about 200 nm were deposited on the surface of ITO. The concentration of Fe or Cr was kept low (about 1 at.%) in the metal-doped TiO₂ layer. One more layer of pure TiO₂ of about 800 nm was deposited on the top of metal-doped thin TiO₂ layer to remove the battery effect as well. Henceforth these Cr- and Fe-doped TiO₂ samples are designated as sample A and B, respectively. The open-circuit voltage and the closed-circuit current were measured with these samples in light-ON regime by using our photo-electrochemical cell. A photo-voltage value of about 1.45 V is measured with both samples A and B: such a value is greater than the required photo-voltage value (1.23 V) to split water. A significant enhancement in the photo-current is also observed with these thin samples as compared to previous thick metal-doped TiO₂ samples.

In Cr-doped samples the photo-current is increased from 3 to 150 μ A with same Cr concentration (about 1 at.%) but with thinner layer (about 200 nm) over ITO. Among all samples, Fe doped TiO₂ thin films showed the highest photo-current value, 350 μ A, better than that of pure TiO₂ samples (290 μ A).

F: Hydrogen measurement

The photocatalytic activity of the three ITO/TiO₂ stacks (pure TiO₂, sample A, and sample B) was tested by measuring the amount of H₂ generated by water-splitting.

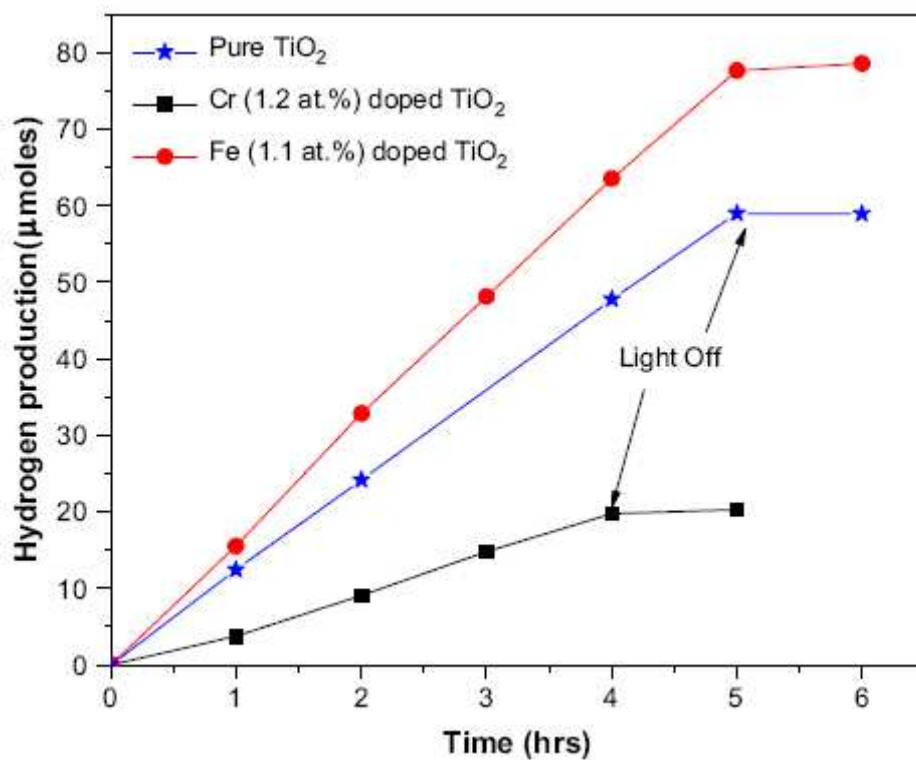


Figure 7: Hydrogen evolution, as a function of time, from water-splitting by using sputter-deposited, pure and Cr- or Fe-doped TiO₂ photo-anode films in photo-electrochemical cell containing two electrolytes of different pH (see procedure in Ref. [11]).

Fig. 7 shows the H₂ evolution, as function of time, from water-splitting by irradiating the TiO₂ films with light (250W tungsten halogen lamp) which contains mostly visible light and includes a very small portion of UV light (0.5%). The amount of the photo-catalytically produced H₂ increases linearly with the exposure time. The H₂ production completely stops after termination of light irradiation: this proves that H₂ is produced photo-catalytically only. The constant production rate observed in the present case is simply due to the employ of TiO₂ photocatalyst in form of thin film in an apparatus [27] where H₂ and O₂ evolve separately. During the measurement, the same amount of surface area (13.75 cm²) is exposed to the light for all the three films. The H₂ generation rate was measured to be 5.3 ± 0.1 , 15.5 ± 0.1 , and 12.5 ± 0.1 μmol/h for sample A, sample B, and pure TiO₂ film, respectively. As expected, the H₂ production rate is higher with Fe-doped TiO₂ than both pure and Cr-doped TiO₂. The photocatalytic activity not only

depends on the concentration of the dopants but it is also affected by type of metal used for the doping. A qualitative analysis on the effects of transition metal ions (Cr, Mn, Fe, Co, Ni, and Cu) on photocatalytic activity of TiO₂ was carried out for photocatalytic oxidation of acetic acid [4]. The results showed that Cu, Mn, and Fe ions can trap both electrons and holes thus avoiding their recombination: thus, doping TiO₂ with these metal ions may contribute to a better activity than doping with Cr, Co, and Ni ions. Indeed, the latter metal ions can only trap one type of charge carrier. In Fe-doped TiO₂, the electrons trapped by Fe³⁺ could readily transit to sideward Ti⁴⁺ due to the similar energy level of Fe²⁺/Fe³⁺ and Ti³⁺/Ti⁴⁺ thus improving the separation of photo-generated electron– hole pairs [32]. This was experimentally proved by Murakami et al. [33] using photo-acoustic spectroscopy to measure the amount of electrons injected from the metal into TiO₂ as function of time under visible light irradiation. The rate of electron injection from Fe³⁺ ions to TiO₂ is far better than that from Cr³⁺ ions. This result has clear connections with the photocatalytic activity of our samples even if Cr-doped TiO₂ absorbs more visible light than Fe-doped TiO₂. Thus, the difference observed in H₂ production rate between Cr- and Fe doped TiO₂ is easily understood in the framework of literature results.

Let us now summarize the mechanisms involved in photocatalytic activity of our samples. In sputter-deposited pure TiO₂, as previously noted [27], oxygen vacancies created in film by the energetic target ions during deposition in pure Ar gas pressure are mainly responsible for creating defect energy levels, in the band gap, which enhance the visible light absorption. The higher H₂ production rate obtained with Fe doped TiO₂, as compared to pure TiO₂, is connected to the shift of the absorbance band towards higher wavelength. In addition, although Cr-doped TiO₂ better absorbs visible light than all the other samples, it however forms recombination sites that reduce the photocatalytic activity.

2.3.4 Conclusion

RF-magnetron sputtering and sol-gel methods were used to synthesize Cr- and Fe-doped TiO₂ thin films to study the hydrogen generation by photocatalytic water-splitting under visible light irradiation in photo-electrochemical cells which eliminate back-reaction effects. UV-Visible spectra show that the sputter-metal-doped-TiO₂ films are much more efficient than the chemically prepared samples to induce red shift of the absorption edge for absorbing visible light. In addition, we proved that dopant atoms must be located, at low concentration, near the ITO-TiO₂ interface to avoid the formation of recombination centres for photo-generated electron-hole pairs. H₂ production rate is higher with Fe-doped TiO₂ (15.5 μmol/h) than with Cr-doped TiO₂ (5.3 μmol/h) because Fe ions trap both electrons and holes thus avoiding recombination. On the other hand, Cr can only trap one type of charge carrier.

2.3.5 References

- [1] Choi WY, Termin A, Hoffmann MR. The role of metal ion dopants in quantum-sized TiO₂: correlation between photoreactivity and charge carrier recombination dynamics. *J Phys Chem* 1994;84:13669–79.
- [2] Kitano M, Matsuoka M, Ueshima M, Anpo M. Recent developments in titanium oxide-based photocatalysts. *Appl Catal A Gen* 2007;325(1):1–14.
- [3] Gennari FC, Pasquevich DM. Enhancing effect of iron chlorides on the anatase-rutile transition in titanium dioxide. *J Am Ceram Soc* 1999;82(7):1915–21.
- [4] Zhang W, Li Y, Zhu S, Wang F. Surface modification of TiO₂ film by iron doping using reactive magnetron sputtering. *Chem Phys Lett* 2003;373:333–7.
- [5] Djaoued Y, Badilescu S, Ashrit PV, Bersani D, Lottici PP, Robichaud J. Study of anatase to rutile phase transition in nanocrystalline titania films. *J Sol-Gel Sci Tech* 2002;24(3): 255–64.
- [6] Lohstroh W, Westerwaal RJ, Van Mechelen JLM, Chacon C, Johansson E, Dam B, et al. Structural and optical properties of Mg₂NiH_x switchable mirrors upon hydrogen loading. *Phys Rev B* 2004;70(16):165411.
- [7] Davis EA, Mott NF. Conduction in non-crystalline systems V. Conductivity, optical absorption and photoconductivity in amorphous semiconductors. *Philos Mag* 1970;22(179): 903–22.
- [8] Radecka M, Zakrewska K, Wierzbicka M, Gorzkowska A, Komornicki S. Study of the TiO₂–Cr₂O₃ system for photoelectrolytic decomposition of water. *Solid State Ionics* 2003;157(1–4):379–86.
- [9] Halley JW, Kozlowski M, Michalewicz M, Smyrl W, Tit N. Photoelectrochemical spectroscopy studies of titanium dioxide surfaces: theory and experiment. *Surf Sci* 1991;256(3): 397–408.
- [10] Madhusudan Reddy K, Gopal Reddy CV, Manorama SV. Preparation, characterization and spectral studies on nanocrystalline anatase TiO₂. *J Solid State Chem* 2001;158(2): 180–6.
- [11] Dholam R, Patel N, Adami M, Miotello A. Physically and chemically synthesized TiO₂ composite thin films for hydrogen production by photocatalytic water splitting. *Int J Hydrogen Energy* 2008;33:6896–903.

- [12] Singh AP, Kumari S, Shrivastav R, Dass S, Satsangi VR. Iron doped nanostructured TiO₂ for photoelectrochemical generation of hydrogen. *Int J Hydrogen Energy* 2008;33: 5363–8.
- [13] Yamashita H, Harada M, Misaka J, Takeuchi M, Ichihashi Y, Goto F, et al. Application of ion beam techniques for preparation of metal ion-implanted TiO₂ thin film.
- [14] Anpo M, Takeuchi M, Ikeue K, Dohshi S. Design and development of titanium oxide photocatalysts operating under visible and UV light irradiation: the applications of metal ion-implantation techniques to semiconducting TiO₂ and Ti/zeolite catalysts. *Curr Opin Solid State Mater Sci* 2002; 6(5):381–8.
- [15] Ma Y, Qiu J, Cao Y, Guan Z, Yao J. Photocatalytic activity of TiO₂ films grown on different substrates. *Chemosphere* 2001; 44(5):1087–92.
- [16] Bak T, Nowotny J, Rekas M, Sorrell CC. Photo-electrochemical hydrogen generation from water using solar energy. Materials-related aspects. *Int J Hydrogen Energy* 2002;27(10):991–1022.
- [17] Ni M, Leung MKH, Leung DYC, Sumathy K. A review and recent developments in photocatalytic water-splitting using TiO₂ for hydrogen production. *Renew Sustain Energy Rev* 2007;11:401–25.
- [18] Khan MA, Woo SI, Yang OB. Hydrothermally stabilized Fe(III) doped titania active under visible light for water splitting reaction. *Int J Hydrogen Energy* 2008;33:5345.
- [19] Peng S, Li Y, Jiang F, Lu G, Li S. Effect of Be²⁺ doping TiO₂ on its photocatalytic activity. *Chem Phys Lett* 2004;398:235–9.
- [20] Yuan Z, Zhang J, Li B, Li J. Effect of metal ion dopants on photochemical properties of anatase TiO₂ films synthesized by a modified sol–gel method. *Thin Solid Films* 2007;515: 7091–5.
- [21] Murakami N, Chiyoya T, Tsubota T, Ohno T. Switching redox site of photocatalytic reaction on titanium(IV) oxide particles modified with transition-metal ion controlled by irradiation wavelength. *Appl Catal A Gen* 2008;348:148–52.

2.4 Efficient solar sensitized multilayer Cr doped TiO₂ thin film for water splitting

The last section showed how doping TiO₂ with transition metals like Cr and Fe leads to better absorption in visible light. The TiO₂ doped with Fe shows higher hydrogen production rate than Cr doped TiO₂ because Fe ions trap both electrons and holes which help to reduce recombination rate while Cr ions trap only one type of charge carrier. By increasing the Cr concentration creates major narrowing of band-gap of TiO₂ but at the same time forms a recombination center for the charge carriers to recombine. From this consideration, it becomes important to solve the problem of recombination for this metal doped TiO₂. The best way to suppress the recombination processes is to produce specific charge states to favour electrons and holes trapping while having appropriate spatial separation. This can be achieved by using coupled semiconductor layers having appropriate electron energy levels where the edge of the conduction band of the first semiconductor is lower than that of the second one. If the semiconductor layers are not much thick, then the photo-generated electrons in one layer are easily injected into the second one [1]. In addition, a thin space charge layer of a few tens of nanometres is formed near the interface of the semiconductors to make their Fermi level equal [2]. The junction electric field is built up in this space charge layer of the electrode and is able to provide the driving force to the photo-generated electrons to move from one semiconductor to another thus favouring the electron-hole separation. Therefore, the development of a number of interfaces in the photo-electrode creates an ideal scenario to reduce the recombination rate. Many TiO₂-based coupled systems such as CdS/TiO₂ [3], WO₃/TiO₂ [4], SnO₂/TiO₂ [5,6], SiO₂/TiO₂ [7] etc., have been used in the past as photo-catalysts. But none was reported using transition metal -doped-TiO₂ in the coupled system where the recombination rates are much higher.

The aim of the present work is to enhance the visible light absorption efficiency of TiO₂ films by doping with Cr metal, using co-sputtering deposition technique, and by also depositing ITO/TiO₂ multilayer to reduce the recombination rates. The photocatalytic efficiency of the multilayer-based TiO₂ photo-electrode was tested by measuring hydrogen production through water spitting in photo-electrochemical cell.

2.4.1 Experiment

Material and chemicals:

Indium Tin Oxide (ITO) (99.99%) bought from supplier “Thin Films materials process solutions” and TiO₂ (99.99%) target was commercially supplied by “Goodfellow Cambridge Ltd.”. Metal pieces of Chromium acquire from “Balzers coating materials”.

Synthesis of Cr doped TiO₂ Multilayer films

Un-doped and Cr-doped-TiO₂ thin films were synthesized by RF-magnetron sputtering using TiO₂ disc (purity equal to 99.99%) and Ar gas (purity equal to 99.99%) as sputtering target and working gas, respectively. Cr-doped TiO₂ films were synthesized by partially covering the TiO₂ target surface with small Cr-metal discs. The number of discs on the TiO₂ target was varied in order to obtain Cr-doped films of three different atomic concentrations. High vacuum (HV) with base pressure $<3 \times 10^{-5}$ Pa and working Ar pressure of 0.8 Pa were used in the deposition chamber. Before film deposition, the TiO₂ target was pre-sputtered for 20 min in order to remove any surface contamination. The TiO₂ films were sputter-deposited on both glass and Si (100) substrates at room temperature using RF power of 150 W. The sample-target distance was kept constant at 5.5 cm for deposition of all the samples. After deposition, no post annealing was performed.

To test photocatalytic activity, TiO₂ thin films were deposited on a conducting indium tin oxide (ITO) layer. The ITO layer, of about 80 nm, was deposited on the glass slide using magnetron sputtering with RF power of 100 W and working Ar gas pressure of 0.8 Pa. Pre-sputtering of the ITO target was also conducted to remove possible surface contamination. Multilayer coating was prepared by sequential in-situ sputtering, firstly of the ITO layer and then of Cr-doped TiO₂: this forms a single bi-layer. Similarly, several numbers of bi-layers (3-, 4-, 5-, 6- and 7-bilayers) were deposited in order to study the efficiency of the adopted multilayer structure to reduce the recombination process of holes

and electrons. The total thickness of Cr-doped TiO₂ was kept constant, about 750 nm, in all the multilayer films by controlling the sputtering deposition time. Thus, as the bi-layers number increases, the thickness of the Cr-doped TiO₂ decreases in each bi-layer to maintain constant the total thickness of TiO₂ in all films. The thickness of ITO (~80 nm) was kept constant in all the multilayer films irrespective of number of bi-layers. The top surface of all the films was always covered with pure TiO₂ of ~100 nm to protect the metal ions from leaching out in the electrolyte.

The structural characterization of the sputter-deposited TiO₂ films was carried out by X-ray diffraction (XRD) technique (Cu K α radiation, $\lambda = 1.5414 \text{ \AA}$) in Bragg-Brentano (θ - 2θ) configuration. Surface electronic states of the photo-catalysts were established by using X-ray photoelectron spectroscopy (XPS). X-ray photoelectrons spectra were acquired using a SCIENTA ESCA200 instrument equipped with a monochromatic Al K α (1486.6eV) X-Ray source and a hemispherical analyzer. No electrical charge compensation was required to perform XPS analysis. Optical measurements in the Ultraviolet (UV) and visible range were performed using a Bruker IFS66 spectrometer equipped with reflection and transmission units while the incoming beam was incident near to the surface normal. The measurements were performed in the wavelength range between 250 nm and 750 nm to obtain the absorbance spectra of samples deposited on glass slides. The surface morphology of the TiO₂ samples was analyzed by means of a scanning electron microscope (SEM, JEOL) equipped with Energy Dispersive Spectroscopy (EDS) which permitted compositional studies of the films.

The performance of multilayer-Cr-doped TiO₂ films in photocatalytic water-splitting was tested by measuring both photocurrent and hydrogen production rates in photo-electrochemical cell which consists of TiO₂ as photo-anode, Pt mesh as cathode, and aqueous electrolytes. In order to establish a chemical bias we used two chambers containing electrolytes with different pH values. The TiO₂ photo-anode was kept in contact with a NaOH (1 M) solution, while the cathode was immersed in a H₂SO₄ (1 M) solution. A salt bridge containing NaCl (1 M) was used to provide a path for ion conduction between the two chambers. The photo-anode was exposed to visible light, generated by a 250-W tungsten halogen lamp, to measure both open-circuit photo-voltage and closed-circuit

photocurrent. The reactor for water-splitting tests was prepared with borosilicate glass that acts as a UV filter, while the reactant water solution is a filter for IR radiation. Oxygen from the reaction chamber was completely removed by purging the chamber with pure Ar gas (99.9%) for 1 h before performing measurements. The evolution of H₂ originated by the water-splitting process at the cathode was measured on-line, as a function of time, by using a gas chromatographer (GC, Agilent MIRCOGC-3000A). Finally, the hydrogen evolution was measured in both ON- and OFF- light regimes.

2.4.2 Results and discussion

A. X-Ray Diffraction:

As observed by SEM, the surface morphology of the Cr-doped TiO₂ films appears quite flat, smooth, and without major defects, while the cross-section of the Cr-doped films showed a dense columnar structure (Fig. 4 of section 2.3.2)[8]. In addition, SEM images obtained in back scattering mode, show uniform distribution of Cr-ions in the TiO₂ film (figure not shown). The dopant concentration uniformity is clearly connected to the adopted co-deposition procedure. This feature was also confirmed, in the sampled volume, by compositional line scan using EDS. The Cr concentration of about 2 ± 0.2 , 5.5 ± 0.2 , and 9 ± 0.3 at.% was obtained in three different TiO₂ films as confirmed by EDS. Fig. 1 shows the XRD spectra of the Cr-doped-TiO₂ films, of several concentrations, deposited by RF-magnetron sputtering on amorphous glass.

The XRD peaks of pure TiO₂ are mainly due to the anatase phase while some weak additional reflexes are attributed to the rutile phase. The crystal grain sizes of the rutile and anatase phase are about 6 nm and 45 nm, respectively, as calculated by using the Debye-Scherrer equation. This means that the rutile phase is almost amorphous with very finely dispersed grains while, on the other hand, the anatase phase is in nano crystalline form.

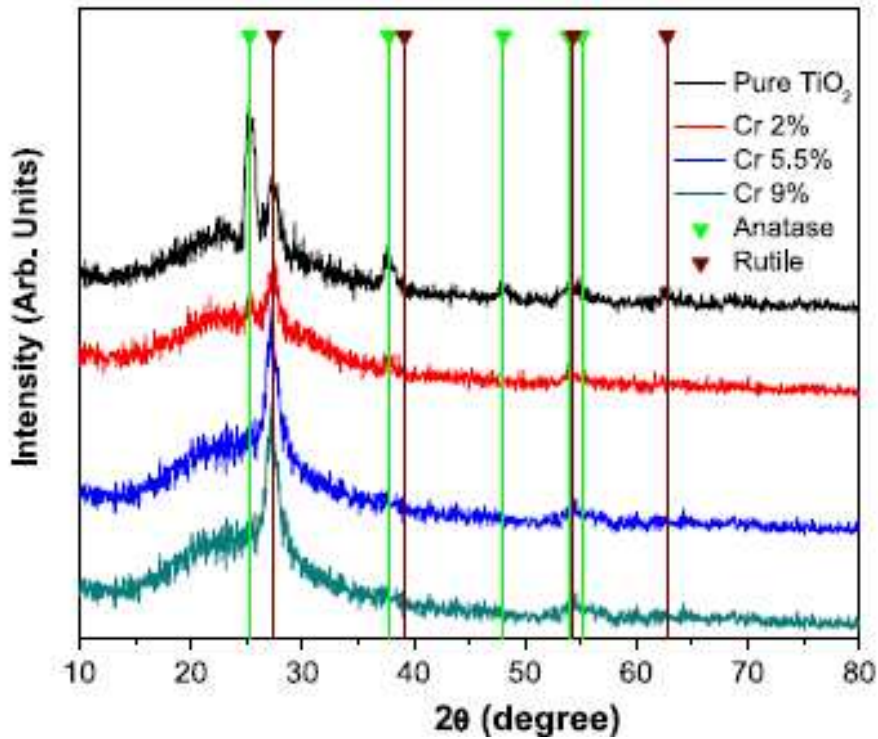


Figure 1: XRD spectra of un-doped and Cr-doped TiO_2 films deposited by RF-magnetron sputtering with different dopants concentration.

The peaks due to rutile phase, with crystal grain size of about 35 nm, prevail over the anatase phase for TiO_2 films doped with low concentrations of Cr (~2 at.%). The reflexes of the rutile phase are now shifted to lower 2θ values, as compared to those of pure TiO_2 film. This indicates a slight increase in the spacing value between the lattice planes which might be caused by the insertion of Cr in the lattice. Complete transformation from anatase to rutile phase is observed in XRD pattern for higher concentration of Cr-doped TiO_2 (5.5 and 9 at. %) films. The peaks due to Cr oxides (Cr_2O_3 or CrO) formation were not detected by XRD. Cr^{3+} metal ions have an effective diameter comparable to that of Ti^{4+} ions thus, during deposition, the metal ions sputtered from the target with kinetic energy of some 10 eVs might be able to replace the Ti^{4+} ions in the lattice of TiO_2 without major variation in the crystal structure, at least for low doping concentration. However, high metal-acceptor dopant concentration causes the formation of oxygen vacancies whose mobility may account for the rearrangement of Ti^{4+} and O^{2-} ions in the lattice and finally favouring the anatase to rutile phase transformation [9] in the TiO_2 film.

B. X-ray Photo-electron Spectroscopy:

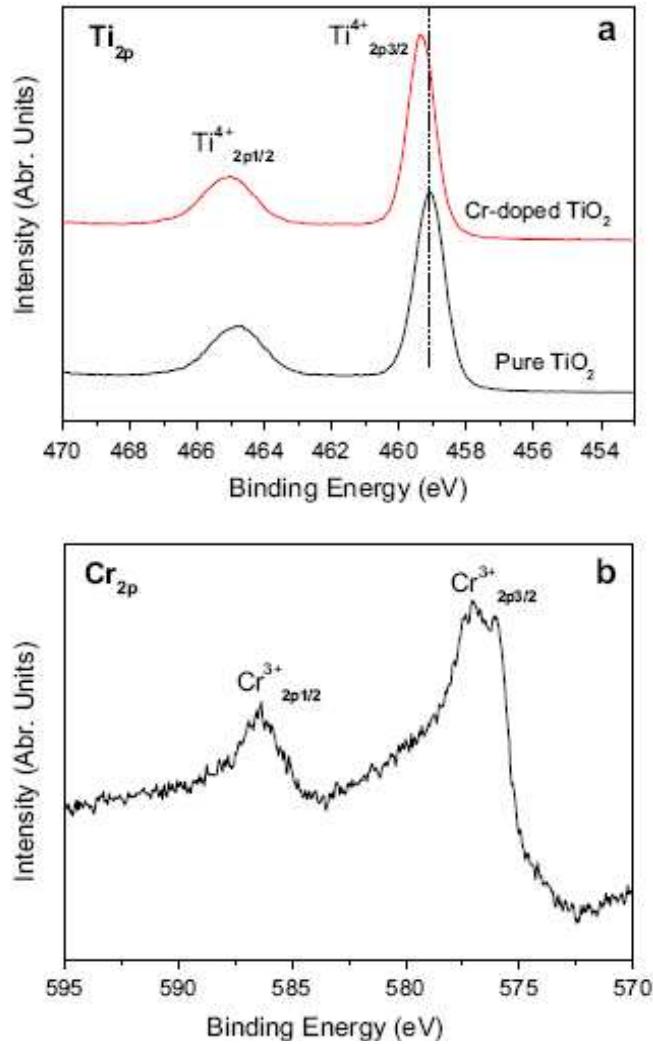


Figure 2: X-ray photoelectrons spectra of (a) Ti_{2p} and (b) Cr_{2p} levels for pure TiO₂ and Cr-doped TiO₂ (9 at.%)

Figs. 2a and b show the XPS spectra of Ti_{2p} and Cr_{2p} electronic levels, respectively, for pure TiO₂ and Cr-doped TiO₂ (9 at.%). For pure TiO₂, two peaks appear at 459.1 and 464.7 eV that corresponds to Ti⁴⁺2p_{3/2} and Ti⁴⁺2p_{1/2} electronic levels, respectively.

For Cr-doped TiO₂, the Ti_{2p} peaks position shows slight shifts of about 0.3 eV towards higher energy side. This indicates that Cr³⁺ ions are incorporated into TiO₂ lattice thus influencing the local chemical state of Ti⁴⁺ ions. To achieve local charge balance in the TiO₂ lattice, some of the Ti ions may acquire higher oxidation state by releasing electrons, a process that explains the XPS peak shift for Cr-doped TiO₂. The XPS spectra

of Cr2p (Fig. 2b) show two peaks at 576.7 and 586.5 eV that are assigned to 2p_{3/2} and 2p_{1/2} of Cr³⁺ species, respectively. This indicates that Cr atoms are incorporated into TiO₂ lattice in form of Cr³⁺ ion

C. UV-Visible Spectroscopy

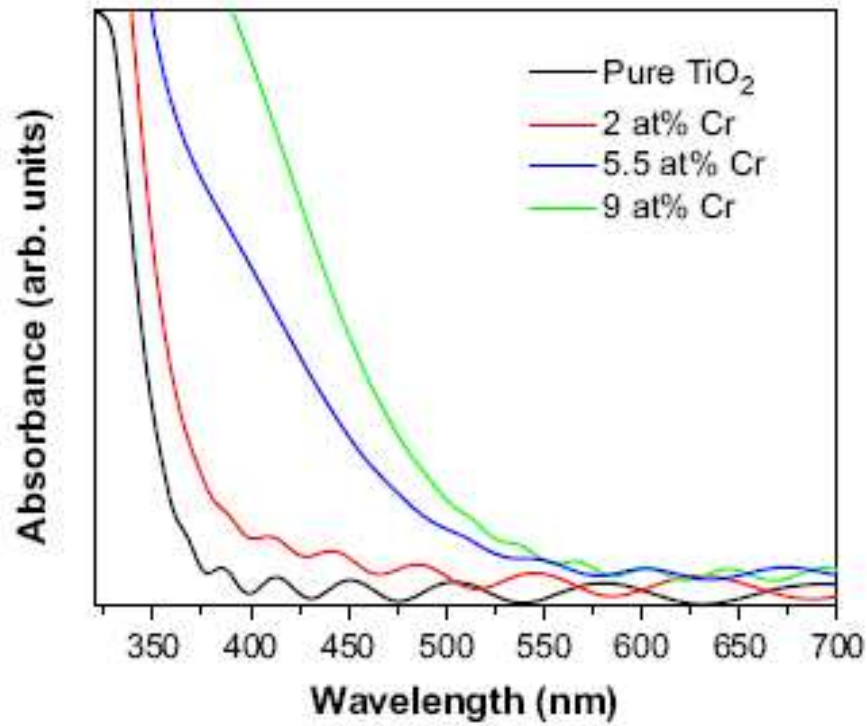


Figure 3: UV-VIS absorption spectra of un-doped and Cr doped TiO₂ films deposited by RF-magnetron sputtering with different dopants concentration.

The optical properties of the pure and Cr-doped TiO₂ were studied by measuring the absorption spectra ranging from UV (250 nm) to visible (750 nm) wavelengths and presented in Fig. 3. The figures clearly show a shift in the absorption band edge towards longer wavelengths when increasing the Cr concentration in the TiO₂ film.

The band gap value is obtained by using the following equation [10]:

$$\alpha h\nu = \alpha_0 (h\nu - E_g)^\gamma \quad (2.14)$$

where E_g is the optical band gap, $h\nu$ is the photon energy, α_0 is a constant which does not depend on $h\nu$, and α is the absorption coefficient which is obtained from the measured absorbance (A) and thickness (t) of the TiO_2 film through the relation: $\alpha = A/t$. Depending on the type of transition, g assumes different values: for direct, allowed (forbidden) transitions $\gamma = 1/2$ ($\gamma = 3/2$) and for indirect, allowed (forbidden) transitions $\gamma = 2$ ($\gamma = 3$). We used $\gamma = 2$ for the present nano crystalline or amorphous films according to Ref. [11]. Using Tauc plot (Fig. 4), i.e. $(\alpha h\nu)^{1/2}$ versus $(h\nu)$, the band gap energies were deduced by extrapolating the linear region of the plot to intersect the photon energy axis: the obtained values are reported in Table 1.

Table 1 – TiO_2 optical band gap and doping energy level values for undoped and Cr-doped TiO_2 films deposited by RF-magnetron sputtering with several Cr concentration.		
Cr concentration in TiO_2 film (at.%)	TiO_2 optical band gap values (eV)	Doping energy level values (eV)
Pure TiO_2	3.25 ± 0.2	–
2 at.%	3.17 ± 0.2	2.85 ± 0.2
5.5 at.%	2.63 ± 0.2	2.1 ± 0.2
9 at.%	2.1 ± 0.2	–

For sputter-deposited pure TiO_2 films a band gap of 3.25 eV is obtained: it signals the presence of a well-crystallized anatase phase. In case of Cr-doped TiO_2 films, by increasing the Cr concentration a red shift of the absorption edge is noticed. In 9 at.% Cr-doped TiO_2 , a relevant lowering of the photon-absorbed energy from ~ 3.2 eV (pure TiO_2) to ~ 2.1 eV, is observed. During sputter deposition, Cr^{3+} ions may have enough energy to displace the Ti^{4+} ions from their lattice positions thus creating lattice vacancies where the impurity metal ions get incorporated into the TiO_2 films. This incorporation leads to formation of new energy levels, due to Cr^{3+} , at ~ 1 eV above the valence band of the TiO_2 [12]. When excited with visible light 3d-electrons are transferred from Cr^{3+} to the conduction band of TiO_2 : this explains the observed increased absorption [12]. In addition, a characteristic bend of the linear part in the experimental plot can be recognized (Fig. 4) whose extrapolation establishes the doping energy level in the band gap [10]. This feature is mainly observed in TiO_2 doped with low Cr concentration (2 at.%) showing energy level

at 2.85 eV (Table 1). However at high Cr concentration, the density of the doping energy level causes the definite narrowing of the band gap as shown in the UV-visible spectra. These results definitely prove that we were able to sensitize TiO₂ in visible light range by doping with Cr³⁺ ions.

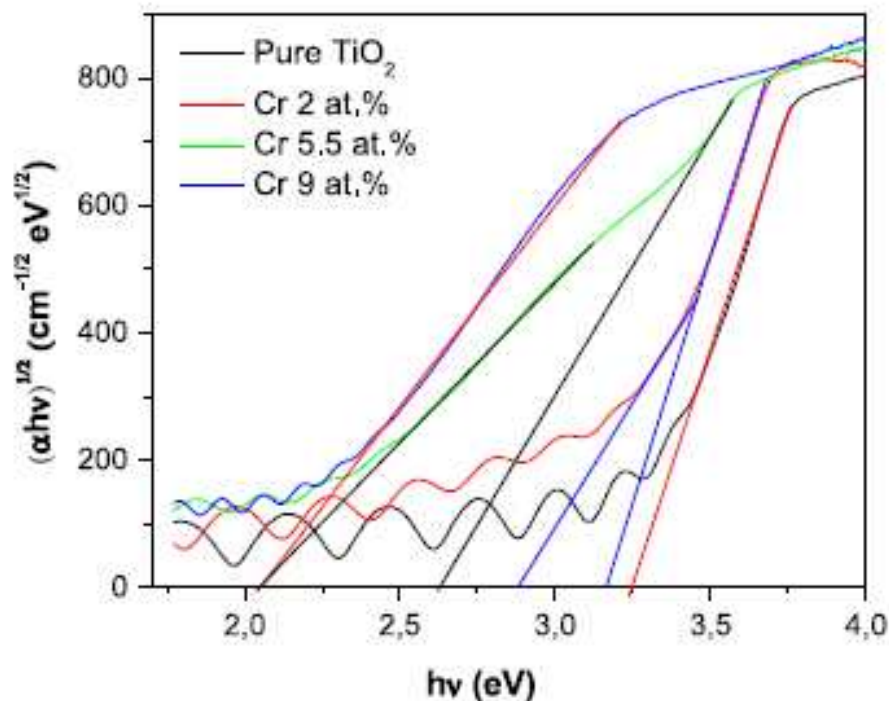


Figure 4: Tauc plot of undoped and Cr-doped TiO₂ films deposited by RF-magnetron sputtering with different dopants concentration.

As seen from the above results, Cr-doped TiO₂ with 9 at.%, shows the maximum lowering of the photon-absorbed energy and thus we preferred to perform the photocatalytic activity measurements only with these doped-films by making comparison with un-doped TiO₂. Henceforth, 9 at.% Cr-doped TiO₂ film will be designated as Cr9-doped TiO₂ film.

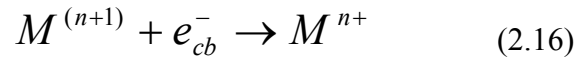
D. Open circuit Voltage-Current Measurement:

Cr9-doped TiO₂ film (about 750 nm thick) was deposited on an ITO layer (80 nm), previously deposited on glass substrate, and the obtained bi-layer was covered with thin

layer of pure TiO₂ to protect the film from possible corrosion induced by contact with the electrolyte. This single bi-layer film was used as photocatalyst for water-splitting experiments. The ITO/ TiO₂ stack film is able to partially limit the recombination of photo-generated holes and electrons (h⁺ and e⁻) because the conduction band edge of ITO (~-4.5 eV) is at an energy value lower than that of TiO₂ (~-4.0 eV) thus making favourable for the electrons injection from the later into the former.

The open-circuit photo-voltage (V_{oc}) was first measured in light-ON regime in photo-electrochemical cell by using Cr9-doped and un-doped TiO₂ films as photo-electrode. Both these films show a photo-voltage value of about 1.45 V which is greater than the required voltage (1.23 V) to break the water molecule. However, the photocurrent measured using Cr9- doped TiO₂ (~14 μA) is negligible as compared to pure TiO₂ films (~290 μA). This is mainly due to recombination of the photo-generated charges on defects associated to the Cr³⁺ ions. High concentration of metal ions leads to the recombination of the photo-generated e⁻ and h⁺ accordingly to the following equations:

Recombination centre:



This means that doping TiO₂ with 9 at.% of Cr has two effects:1) titania is sensitized to the visible light range, and 2) recombination centres are formed where the photo-generated electrons and holes recombine by limiting the photocatalytic activity.

To avoid the recombination problem we may lower the concentration of Cr in the TiO₂ film. But this will cause lower absorption of the visible light. In addition, the low concentration of Cr in TiO₂ is unable to completely solve the problem of recombination as reported in our previous work [8]. A simple and efficient route to suppress the recombination of charge carriers is by immediately removing the photoelectron from the generation site before it recombines with the holes through radiative or non-radiative processes. This fast separation can be achieved through the use of coupled semiconductors with appropriate conduction energy levels. For instance, as mentioned previously, in the ITO/TiO₂ coupled system, the conduction band edge of ITO (~-4.5 eV) is at an energy

value lower than that of TiO_2 (~ 4.0 eV) thus making favourable for the electrons injection from the later into the former. Once the photoelectron from TiO_2 is injected in ITO, it has a very low probability of back transfer and, as a result, electrons and holes are definitely separated. However, to be efficient, ITO should be located near the electron generation site to provide the driving force for the photoelectron transfer.

Having this in mind, we have deposited multilayer films with different numbers (3-, 4-, 5-, 6- and 7-bilayers) of ITO/Cr9-doped TiO_2 bi-layers and finally covering with thin layer of pure TiO_2 (100 nm) the surface layer that will be in contact with the electrolyte. The bottom portion of the overall multilayer is also in contact with the electrolyte through the pure TiO_2 (100 nm) layer (while the corresponding top portion is electrically connected to cathode of the photo-electrochemical cell). The total thickness of Cr9-doped TiO_2 was kept constant, about 750 nm, in all the multilayer films by decreasing the thickness of each Cr9-doped TiO_2 layer when increasing the number of the bi-layers. The thickness of ITO (~ 80 nm) was kept constant in all the multilayer films irrespective of number of bi-layers. In our previous work [13], the effect of conducting ITO layer on photocatalytic activity was studied by varying the thickness of the ITO films and we found that ITO layers having thickness in the range of 50-100 nm offer the best conditions to have low losses of absorbed photon energy thus favouring better photo-voltage.

In Fig. 5 we present the cross-section SEM images, in back scattering mode, of multilayer films with 1-, 3-, 4-, 5-, 6- and 7- bi-layers of ITO/Cr9-doped TiO_2 .

The white layer of ITO can be easily distinguished from the dark layer of Cr9-doped TiO_2 and for this reason both the periodicity and continuity of the layers are clearly visible. The images clearly show that along with the increase of bilayers number, the thickness of single Cr9-doped TiO_2 layer decreases (see Fig. 6).

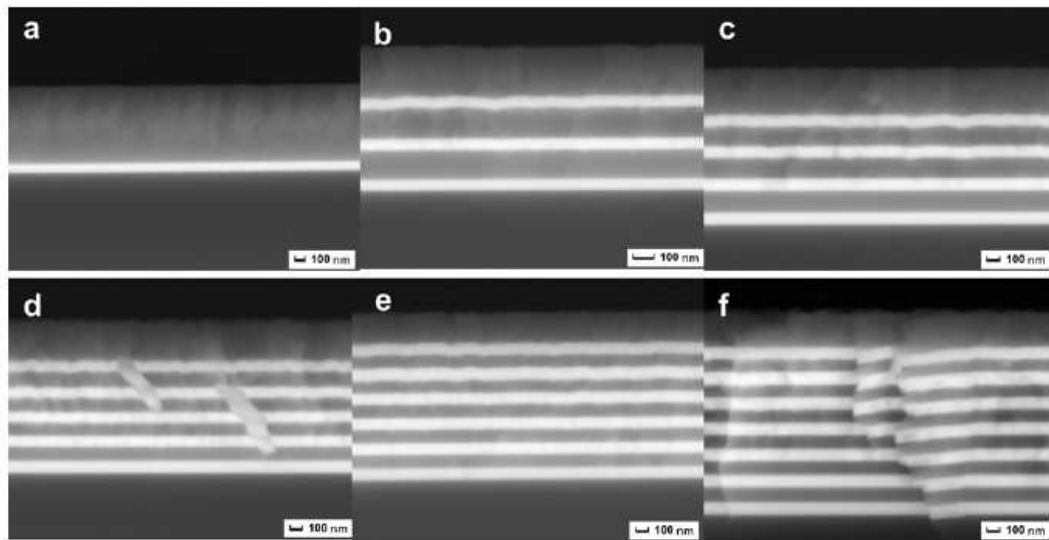


Figure 5: SEM Images, in back scattering mode, of ITO/Cr9-doped TiO_2 multilayer films: (a) single bilayer, (b) 3-bilayers, (c) 4- bilayers, (d) 5-bilayers, (e) 6-bilayers, and (f) 7-bilayers.

Here we want to note that ITO deposited on the top of TiO_2 layer does not affect the amount of photons reaching the TiO_2 layer because ITO is a transparent conducting oxide with a direct band gap in the range of 3.9-4.2 eV which is significantly higher than the absorption edge of Cr9-doped TiO_2 layer (2.1 eV). This feature was experimentally confirmed by measuring the absorbance of the Cr9-doped TiO_2 -ITO bi-layers, with ITO on top, in the UV-Visible range: the spectra showed similar red shift in the band edge as that observed with single layer.

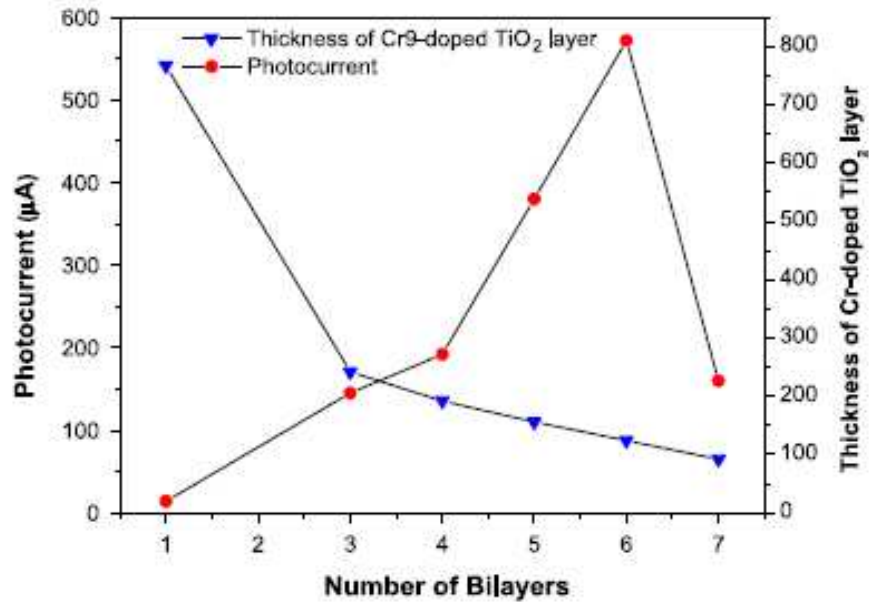


Figure 6: Photocurrent and thickness of each Cr9-doped TiO₂ layer as a function of number of bilayers.

To check the photocatalytic activity of the multilayer films we measured photo-voltage and photocurrent for light-ON regime in photo-electrochemical cell by using ITO/Cr9-dopedTiO₂ multilayer films as photo-anode. Each ITO layer in the multilayer films is directly connected to the platinum cathode and so as soon as the electrons are injected from the Cr9- doped TiO₂ layers into the ITO layers, they are immediately transferred to the cathode. The photo-voltage measured on all the multilayer films (about 1.4-1.5 V) is greater than that required to split the water molecule. The measured photocurrent as a function of number of bi-layers is reported in Fig. 6. As the number of ITO/Cr9-doped TiO₂ bi-layers increases the photocurrent increases and reaches the maximum value with 6-bilayers (572 µA). However, with 7-bilayers the photocurrent decreases to the value of 160 µA. The photocurrent value measured with 6-bilayers Cr9-doped TiO₂ film (572 µA) is about two times higher than that obtained with pure TiO₂ (290 µA) with same total thickness of TiO₂.

When semiconductors having different energy bands are brought in contact with each other, a band bending occurs near the interface to make Fermi level equal on both sides. This band bending generates an interface space charge layer, having thickness of several tens of nanometer, where a large electric field is developed. When photoelectrons

are generated in this interface region (or very near) they are instantaneously pushed out to the adjacent semiconductor due to the driving force provided by the electric field and the electron-hole separation is definitely obtained, a process well known in p-n semiconductor junctions. In the present ITO/TiO₂ system, the interface region presents electrical features that are similar to previously described p-n junction thus providing an efficient route for the e⁻ - h⁺ separation. Hence by adopting a multilayer structure, we are able to produce many interfaces of ITO/TiO₂ which establish fast transport channels along with efficient e-h separation.

Now let's understand in detail the mechanism of the electron flow in the multilayer films and how the number of bi-layers affects the generation of the photocurrent. Our results show that the photocurrent obtained with single bilayer of ITO/Cr9-doped TiO₂ is very low. In this single bi-layer film there is only one interface of ITO/Cr9-doped TiO₂ at the bottom with the thick layer of Cr9-doped TiO₂ (750 nm) over it. Most of the photoelectrons are generated in the bulk of the doped-TiO₂ where they have to travel some distance within the TiO₂ itself before entering the space charge region of the interface to feel the driving field for final injection into ITO. In Cr9-doped TiO₂ the probability of e⁻-h⁺ recombination is much higher because of the presence of recombination sites associated to the Cr³⁺ ions. By depositing 3-bilayers film the photocurrent increases significantly from 14 μA (for single bi-layer film) to 145 μA. In this film, the previous Cr9-doped TiO₂ layer having thickness of 750 nm was divided into three layers of 250 nm by introducing two more ITO layers. The resulting film now contains five ITO/TiO₂ interfaces where space charge layer is formed and the decreased thickness of the Cr9-doped TiO₂ layers assures that the photo-generated electrons have to travel a short distance into TiO₂ (the unshielded region) before being injected into the ITO layer where recombination is definitely hindered. Another relevant point to be considered is that in single bi-layer film the photoelectrons, generated in the Cr9-doped TiO₂ layer, to avoid recombination have to move only along one direction towards the ITO layer placed at the bottom of the layered structure. On the contrary, in 3-bilayers film the Cr9-doped TiO₂ layer is sandwiched between the two ITO layers and so the photoelectrons can move along either of two directions to avoid recombination. All these reasons favour the increment of the photocurrent in the 3-bilayers film.

In addition we observe that by increasing the bi-layers number there is an almost linear increment in the photocurrent, mainly attributed to the better conditions for charge separation and transport with reduced number of recombination processes: here we have to further underline the key role of number of ITO/TiO₂ interfaces. The measured photocurrent reaches the maximum value (572 μ A) with 6-bilayers film; the measured photocurrent is significantly higher than that measured with single bi-layer film (14 μ A). For 6-bilayers film, the thickness of Cr⁹-doped TiO₂ layer (125 nm) in each bi-layer may be lower than the total thickness of the space charge layer of the pertinent interface. Thus photoelectrons generated in the Cr⁹-doped TiO₂ are already in space charge region where the electric field provides them the driving force to instantaneously inject into the ITO layers: this means that the 6-bilayers film creates the best conditions for charge separation. In addition, this film is able to absorb more visible light than pure TiO₂ due to the band narrowing caused by Cr³⁺ energy levels, hence generating higher amount of photoelectrons. With 7-bilayers film the photocurrent decreases (Fig. 6); we suggest this might be due to the poor crystallinity of very thin films of TiO₂ (92 nm). Takahashi et al. [14] showed indeed that with sol-gel deposited TiO₂ film the photocurrent increases by decreasing the TiO₂ layer thickness and reaches maximum value at particular thickness. Below this thickness the photocurrent decreases drastically and, as indicated by the authors, this is attributed to the low crystallinity achieved with thinner films. Nasr et al. [1] also reported a similar trend in the photocurrent as a function of TiO₂ thickness but they did not explain the reason behind the reduced photocurrent with thinner TiO₂ layers. For the moment with our XRD setup it is difficult to acquire the spectra of such a thin layer of TiO₂. However, we will address this open problem with dedicated experiments in the future.

The reduced probability in charge recombination processes observed with multilayer films can be further analyzed by studying the photocurrent kinetics curve. Fig. 7A shows the schematic diagram of photocurrent transient curve.

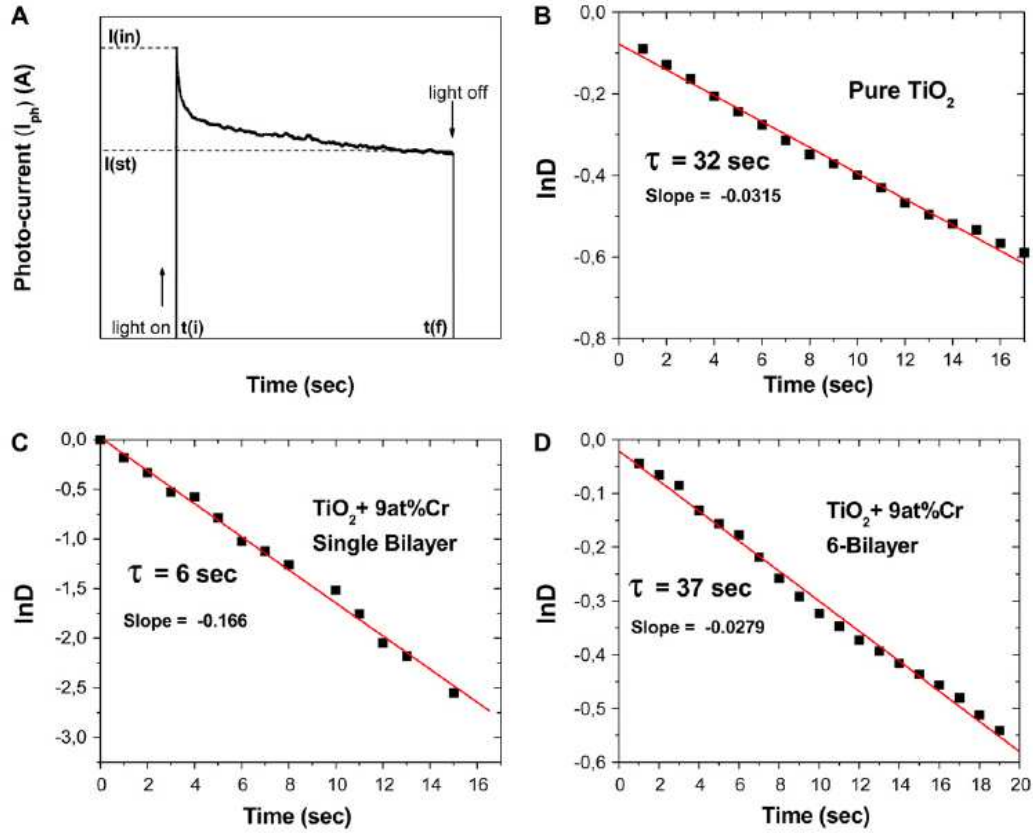


Figure 7: (A) Schematic representation of the photocurrent transient curve. Normalized plot of current-time dependence for: (B) pure TiO_2 , (C) single bi-layer, and (D) 6-bilayers of ITO/Cr9-doped TiO_2 multilayer film.

The initial anodic photocurrent spike is denoted by $I(i)$. This current signals the separation of the electron-hole pairs by movement of holes towards the semiconductor surface where they are trapped or reduced by the species in the electrolyte, while the electrons are transported to the back contact. After $I(i)$ has been attained, then a continuous decrease of the photocurrent with time is observed until a steady-state photocurrent, $I(st)$, is reached. The photocurrent decay indicates that charge recombination processes are occurring. The holes reaching the semiconductor surface may, instead of capturing electrons from the electrolyte, accumulate at the surface and recombine with electrons from the conduction band, i.e. the decay is determined by the rate at which minority carriers trapped at surface states capture majority carriers [15].

The photocurrent transient can be defined by the following kinetic equation [16]:

$$D = \exp\left(-\frac{t}{\tau}\right) \quad (2.17)$$

Where D is defined as

$$D = \frac{I(t) - I(st)}{I(in) - I(st)} \quad (2.18)$$

Here, τ is the transient time constant, $I(t)$ is the current at time t , $I(in)$ is the current at $t = 0$, and $I(st)$ the stationary current. Figs. 7B, C, and D illustrate the $\ln D$ vs. time plot for pure TiO_2 film, single bi-layer, and 6-bilayers of ITO/Cr9-doped TiO_2 films respectively. The slope of this plot provides τ which is related to the time for charge recombination processes in the films. The measured τ for Cr9-doped TiO_2 with single bi-layer film is about five times smaller than that for the un-doped TiO_2 .

Specifically, the photocurrent decays within a few seconds in Cr-doped TiO_2 is due to recombination of the photo-generated charges on defects associated to the Cr^{3+} ions. On the contrary, with 6-bilayers the transient time constant is about the same as for undoped TiO_2 film where there are no defect sites. This again proves that by introducing space charge regions in form of ITO/ TiO_2 interfaces and by decreasing the thickness of TiO_2 layer favours charge separation, and recombination processes are suppressed even if recombination sites such as Cr^{3+} are still present.

After optimizing the thickness of the Cr-doped TiO_2 in them multilayer films, it is necessary to study the effect of the number of bi-layers on the photocurrent. Thus we deposited different number of ITO/ TiO_2 bi-layers by keeping constant the thickness of Cr9-doped TiO_2 and ITO layers (125 and 80 nm respectively). The photo-voltage and photocurrent measured in light-ON regime with these multilayer films are reported in Table 2.

Table 2 – Photo-voltage and photocurrent measured for different numbers of ITO/TiO₂ bilayers by keeping constant the thickness of each single bilayer.

Number of ITO/TiO ₂ Bilayers	Photo-voltage (V)	Photocurrent (μA)
1	1.321	92
2	1.329	190
4	1.393	315
6	1.4	572
7	1.345	551

All the multilayer films were able to produce photo-voltage greater than 1.3 V irrespectively on the number of bi-layers. On the contrary, the photocurrent increases with the number of bi-layers and reaches an early constant value for the highest number of bi-layers (6 and 7). A saturation effect is clearly expected on physical basis but what is important here is that the photocurrent value depends not only on thickness but also on the number of bi-layers, i.e. on the ability of the multilayer structure to efficiently avoid charges recombination. Here, another important point is that with 7-bilayers there is not a dramatic decrease of the photocurrent as observed in Fig. 6. This supports the point that the low crystallinity achieved with very thin films is deleterious to photocurrent generation.

E. Hydrogen Measurement:

The photocatalytic activity of the 6-ITO/Cr9-doped TiO₂ bi-layers was finally tested by measuring the amount of H₂ generated by water-splitting in photo-electrochemical cell and compared to pure TiO₂. Fig. 8 shows the H₂ evolution, as function of time, from water-splitting by irradiating the multilayer and pure TiO₂ films with light (250 W tungsten halogen lamp) which contains mostly visible light and includes a very small portion of UV light (1%).

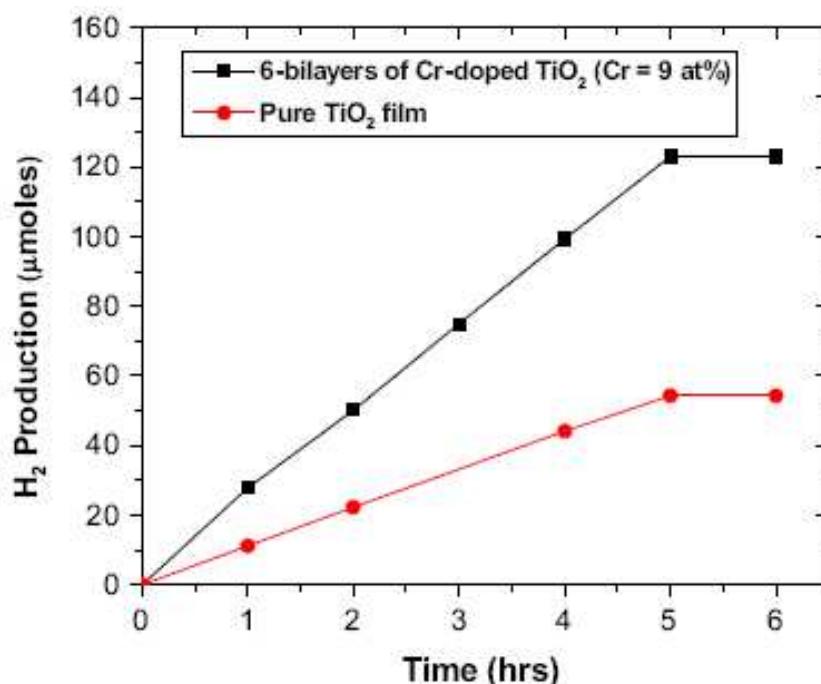


Figure 8: Hydrogen evolution, as a function of time, from water-splitting by using sputter-deposited pure TiO₂ and 6-bilayers of ITO/Cr9-doped TiO₂ multilayer film in photo-electrochemical cell containing two electrolytes of different pH (see procedure in Ref. [13]).

The amount of the photo-catalytically produced H₂ increases linearly with the exposure time. The H₂ production completely stops after termination of light irradiation: this proves that H₂ is only produced photo-catalytically. The constant production rate observed in the present case is simply due to the employ of TiO₂ photocatalyst in form of thin film in an apparatus [28] where H₂ and O₂ evolve separately. During the measurement, the same amount of surface area (13.75 cm²) is exposed to the light for both the films. The H₂ generation rate was measured to be 24.4 ± 0.1 μmol/h for 6-bi-layers based Cr9- doped TiO₂ multilayer film and is about two times higher than that measured with pure TiO₂ film (12.5 ± 0.1 μmol/h). The greater H₂ generation rate with Cr9-doped TiO₂ multilayer film is definitely attributed to an increased absorption of visible light, larger than pure TiO₂, and to reduced charge recombination processes because of the number of space charge ITO/TiO₂ interfaces in multilayer films. However, a comment must be included now to explain the hydrogen production results. Indeed, while the photo-generated electrons are easily

collected by the established electrical contact to produce the measured photocurrent, the positive holes that are produced inside the Cr-doped TiO₂ layers sandwiched by the ITO films, may arrive at the TiO₂ irradiated surface that is in contact with water. We suspect that holes migrate through the bottom deposited TiO₂ layer towards the irradiated front surface where H₂O molecules get oxidized. This holes mobility is a new aspect, regarding the photo-electrochemical cells, that should be further investigated.

Therefore the above results prove that:

1. There is an enhanced visible light absorption in Cr-doped TiO₂ because of the formation of wide Cr³⁺ energy levels into the band gap;
2. There is a better photo-generated charge separation by introducing space charge layers in form of ITO/TiO₂ interfaces;
3. Holes mobility towards the irradiated surface layer is a relevant new process that should be further investigated.

2.4.3 Conclusions

TiO₂ doped with Cr ions (9 at.%) shows an increase in the optical absorption efficiency and photons with energy as low as 2.1 eV are absorbed as compared to the lower limit of 3.2 eV for undoped TiO₂. However, in photo-electrochemical cell, negligible photocurrent is measured with ITO/Cr-doped-TiO₂ (9 at.%) single bilayer, a problem that we attribute to the increased recombination rate of the photo-generated charges. To reduce the charge recombination rate we prepared multilayer films with different numbers of ITO/Cr-doped-TiO₂ (9 at. %) bilayers (namely, 3-, 4-, 5-, 6- and 7-bilayers) by keeping the total thickness of TiO₂ constant. The reduced thickness of the Cr-doped TiO₂ film, deposited on ITO, significantly contributes to reduce the charge recombination rates. This is because the generated photoelectrons, travelling into TiO₂ film of limited thickness, rapidly enter the space charge interface of the ITO/TiO₂ films from where they are instantaneously injected into the ITO layer and then removed towards the cathode of the photo-electrochemical cell: here H⁺ reduction occurs. When the multilayer film is exposed to visible light, we observe that the photocurrent increases as function of the number of

bilayers. The maximum value of the photocurrent is obtained with 6-bilayers of ITO/Cr-doped-TiO₂. The enhanced photocurrent is attributed to both higher absorption of visible light by Cr-doped-TiO₂ and to the number of space charge ITO/TiO₂ interfaces in multilayer films. With six bilayers, the H₂ production rate obtained through water-splitting is about 24.4 μmol/h, a value about two times higher than that of pure TiO₂ (12.5 μmol/h).

2.4.4 References

- [1] Nasr C, Kamat PV, Hotchandani S. Photo-electrochemistry of composite semiconductor thin films. Photosensitization of the SnO₂/TiO₂ coupled system with a ruthenium polypyridyl complex. *J Phys Chem B* 1998; 102: 10047-56.
- [2] Morrison SR. *Electrochemistry at semiconductor and oxidized metal electrodes*. New York: Plenum Press; 1984.
- [3] Chi Y, Fu H, Qi L, Shi K, Zhang H, Yu H. Preparation and photoelectric performance of ITO/TiO₂/CdS composite thin films. *J Photochem Photobio A Chem* 2008;195: 357-63.
- [4] Akurati KK, Vital A, Dellemann JP, Michalow K, Graule T, Ferri D, et al. Flame-made WO₃/TiO₂ nanoparticles: relation between surface acidity, structure and photocatalytic activity. *Appl Catal B Environ* 2008; 79: 53-62.
- [5] Shang J, Yao W, Zhu Y, Wu N. Structure and photocatalytic performances of glass/SnO₂/TiO₂ interface composite film. *Appl Catal A Gen* 2004;257:25-32.
- [6] Sasikalaa R, Shirolea A, Sudarsana V, Sakuntalab T, Sudakarc C, Naikc R, et al. Highly dispersed phase of SnO₂ on TiO₂ nanoparticles synthesized by polyol-mediated route: photocatalytic activity for hydrogen generation. *Int J Hydrogen Energy* 2009;34:3621-30
- [7] Beyers E, Biermans E, Ribbens S, De Witte K, Mertens M, Meynen V, et al. Combined TiO₂/SiO₂ Mesoporous photocatalysts with location and phase controllable TiO₂ nanoparticles. *Appl Catal B Environ* 2009;88: 515-24.
- [8] Dholam R, Patel N, Adami M, Miotello A. Hydrogen production by photocatalytic water-splitting using Cr- or Fe doped TiO₂ composite thin films photocatalyst. *Int J Hydrogen Energy* 2009;34:5337-46.
- [9] Gennari FC, Pasquevich DM. Enhancing effect of iron chlorides on the anatase-rutile transition in titanium Dioxide. *J Am Ceram Soc* 1999;82: 1915-21.
- [10] Domaradzki J. Structural, optical and electrical properties of transparent V and Pd-doped TiO₂ thin films prepared by sputtering. *Thin Solid Films* 2006;497:243-8.
- [11] Djaoued Y, Badilescu S, Ashrit PV, Bersani D, Lottici PP, Robichaud J. Study of anatase to rutile phase transition in nanocrystalline titania films. *J Sol-Gel Sci Tech*

2002; 24: 255-64.

- [12] Umebayashi T, Yamaki T, Itoh H, Asai K. Analysis of electronic structures of 3d transition metal-doped TiO₂ based on band calculations. *J Phys Chem Solids* 2002;63: 1909-2002.
- [13] Dholam R, Patel N, Adami M, Miotello A. Physically and chemically synthesized TiO₂ composite thin films for hydrogen production by photocatalytic water splitting. *Int. J Hydrogen Energy* 2008;33:6896-903.
- [14] Takahashi M, Tsukigi K, Uchino T, Yoko T. Enhanced photocurrent in thin film TiO₂ electrodes prepared by sol-gel method. *Thin Solid Films* 2001; 388: 231-6.
- [15] Hagfeldt A, Lindstrom H, Sodergren S, Lindquist SE. Photo-electrochemical studies of colloidal TiO₂ films: the effect of oxygen studied by photocurrent transients. *J. Electroanal. Chem.* 1995; 381: 39-46.
- [16] Redecka M, Wierzbicka M, Komornicki S, Rekas M. Influence of Cr on photoelectrochemical properties of TiO₂ thin films. *Physica B* 2004; 348:160-8.

2.5 Efficient Hydrogen production using vanadium-doped TiO₂ thin film

In last section we successfully structured multilayer stacks of ITO/Cr doped TiO₂ film by which we have resolved the problem of visible light absorption and recombination of e⁻ and h⁺. To check and to be confident about this multilayer concept we doped TiO₂ with another transition metal dopant in the form of Vanadium ions which are more efficient to absorb visible light by forming impurity levels in mid-gap state.

Hence the aim of the present work is to enhance the visible light absorption efficiency of TiO₂ films by doping with vanadium metal, using co-sputtering deposition technique, and by also depositing ITO/TiO₂ multilayer to reduce the recombination rates. The photocatalytic efficiency of the multilayer-based TiO₂ photo-electrode was tested by measuring hydrogen production through water spitting in photo-electrochemical cell.

2.5.1 Experiment

Material and chemicals:

Indium Tin Oxide (ITO) (99.99%) bought from “Thin Films materials process solutions” and TiO₂ (99.99%) target was commercially supplied by “Goodfellow Cambridge Ltd.”. Metal pieces of Vanadium acquire from “Balzers coating materials”.

Synthesis of V- doped TiO₂ Multilayer films

Undoped and V-doped-TiO₂ thin films were synthesized by RF-magnetron sputtering. Pure TiO₂ disc (purity equal to 99.99%) and Ar gas (purity equal to 99.99%) were used as sputtering target and working gas for the deposition, respectively. Before deposition high vacuum with base pressure of 3×10^{-5} Pa was attained, while during deposition Ar pressure of 0.8 Pa was maintained in the chamber. V-doped TiO₂ films were synthesized by partially covering the TiO₂ target surface with small V-metal pellets. The number of pellets on the TiO₂ target was varied in order to obtain V-doped films of four different atomic concentrations. Before film deposition, the TiO₂ target was pre-sputtered

for 20 min in order to remove any surface contamination. The TiO₂ films were sputter-deposited on both glass and Si (100) substrates at room temperature using RF power of 150 W. The sample-target distance was kept constant at 5.5 cm for deposition of all the samples. After deposition, no post annealing was performed.

TiO₂ thin films were deposited on a conducting indium tin oxide (ITO) layer which provides electrical back contact to test photocatalytic activity. The ITO layer, of about 80 nm, was deposited on the glass slide before the deposition of TiO₂ film using magnetron sputtering with RF power of 100 W and working Ar gas pressure of 0.8 Pa. Pre-sputtering of the ITO target was also conducted to remove possible surface contamination. Multilayer coating was prepared by sequential in-situ sputtering, firstly of the ITO layer and then of V-doped TiO₂; this forms a single bilayer. Similarly, several numbers of bi-layers (2-, 3-, 4-, 5-, 6- and 7-bilayers) were deposited in order to study the efficiency of the adopted multilayer structure to reduce the recombination process of holes and electrons. The total thickness of V-doped TiO₂ was kept constant, about 750 nm, in all the multilayer films by controlling the sputtering deposition time. Thus, as the bilayer number increases, the thickness of the V-doped TiO₂ decreases in each bilayer to sustain total thickness of all TiO₂ films constant. The thickness of ITO (~80 nm) was kept constant in all the multilayer films irrespective of number of bi-layers. The top surface of all the films was always covered with pure TiO₂ of ~100 nm to protect the metal ions from leaching out in the electrolyte.

The structural characterization of the multilayered V-doped TiO₂ films was carried out by X-ray diffraction (XRD) technique (Cu K α radiation, $\lambda = 1.5414 \text{ \AA}$) in Bragg-Brentano (θ - 2θ) configuration. Surface electronic states of the photocatalyst were established by using X-ray photoelectron spectroscopy (XPS). X-ray photoelectrons spectra were acquired using a SCIENTA ESCA200 instrument equipped with a monochromatic Al K α (1486.6eV) X-Ray source and a hemispherical analyzer. No electrical charge compensation was required to perform XPS analysis. Optical measurements in the Ultraviolet (UV) and visible range were performed using a Bruker IFS66 spectrometer equipped with reflection and transmission units with near normal incidence of the incoming beam. The wavelength range between 250 nm and 750 nm was used to obtain the absorbance spectra of samples deposited on glass slides. The surface morphology of the TiO₂ samples was characterized by means of a scanning electron microscope (SEM-

FEG,JSM-7001F, JEOL) and atomic composition was analysed by Energy Dispersive Spectroscopy (EDS,INCA PentaFET-x3) attached to SEM.

Photocatalytic activity of multilayer-V-doped TiO₂ films was tested by measuring both photo-current and hydrogen production rates by water-splitting. Photo-electrochemical cell constructed with TiO₂ as photo-anode, Pt mesh as cathode, and aqueous electrolytes was employed to measure photocatalytic activity. In order to establish a chemical bias we used two chambers containing electrolytes with different pH values. The TiO₂ photo-anode was kept in contact with a NaOH (1 M) solution, while the cathode was immersed in a H₂SO₄ (1 M) solution. A salt bridge containing NaCl (1 M) was used to provide a path for ion conduction between the two solutions. The photo-anode was exposed to visible light, generated by a 250 W tungsten halogen lamp, to measure both open-circuit photo-voltage and closed-circuit photocurrent. Reactor is made up of borosilicate glass, thus no UV filter was used and reactant water solution acts as filter for IR radiation. Oxygen from the reaction chamber was completely removed by purging the chamber with pure Ar gas (99.9%) for 1 h before performing measurements. The separate evolution of H₂ originated by the water-splitting process at the cathode was measured on-line, as a function of time, by using a gas chromatographer (GC, Agilent MIRCOGC-3000A). Finally, the hydrogen evolution was measured in both ON- and OFF- light regimes.

2.5.2 Results and discussion

A. Scanning Electron morphology (SEM):

A surface morphology, as observed by SEM, of V-doped TiO₂ films appears quite flat, smooth, and without major defects, while the cross-section of the V-doped films showed a typical dense columnar structure [1]. The uniform distribution of V-metal in the TiO₂ film was confirmed, in the sampled volume, by compositional line scan using EDS. The dopant concentration uniformity is clearly connected to the adopted co-deposition procedure. The V concentration of about 2 ± 0.2 , 4 ± 0.3 , 5 ± 0.4 and 6 ± 0.4 at.% was obtained in four different TiO₂ films as confirmed by EDS.

B. X-Ray Diffraction:

Fig 1 shows the XRD spectra of V-doped TiO₂ film of different concentration synthesized on amorphous glass by sputter deposition.

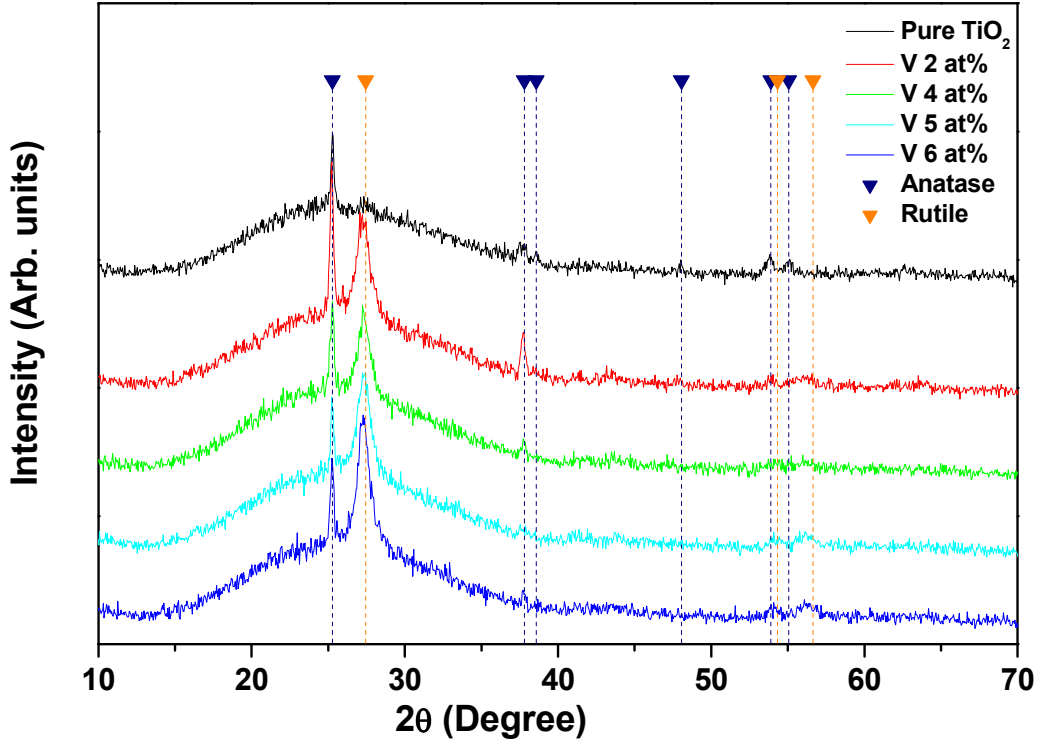


Figure 1: XRD spectra of un-doped and V-doped TiO₂ films deposited by RF-magnetron sputtering with different dopants concentration.

The crystal grain sizes of the anatase and rutile phase for all the samples are calculated by the Debye-Scherrer equation from peak A(101) at 25.2° and R(110) at 27.5° respectively, and summarized in Table 1. The intensity ratio of anatase (101) to rutile (110) peak is also reported in Table 1. The peaks observed in the spectra of undoped TiO₂ thin film are mainly due to the anatase phase while some additional reflexes of rutile phase could be identified in the form of broad peak. Crystal size (table 1) suggests that rutile

phase for pure TiO₂ is almost amorphous with very finely dispersed grain, while anatase phase is in nano crystallized form. By increasing the doping concentration of vanadium, the amount of anatase diffraction peak is gradually decreasing and peak corresponding to rutile increasing. The TiO₂ doped with high concentration of vanadium (~5 and ~6 at.%) is exhibits peak of rutile phase prevailing over the anatase phase. The reflexes of the rutile phase are now shifted to lower 2θ values, as compared to those of pure TiO₂ film. This indicates a slight increase in the spacing value between the lattice planes which might be caused by the insertion of V in the lattice. No characteristic peaks due to vanadium oxides (V₂O₅ or VO₂) were detected in XRD pattern. These results indicate that V ions are incorporated in the TiO₂ lattice which at high metal-acceptor dopant concentration causes the formation of oxygen vacancies whose mobility may account for the rearrangement of Ti⁴⁺ and O²⁻ ions in the lattice and finally favoring the anatase to rutile phase transformation [2].

C. X-ray Photo-electron Spectroscopy:

XPS spectrum is carried out to confirm the concentrations and to determine chemical states of V in the samples. Figs. 2a and 2b shows the XPS spectra of Ti2p and V2p electronic levels, respectively, for pure TiO₂ and V-doped TiO₂ (~6 at.%). For pure TiO₂, two peaks Ti 2p_{3/2} and Ti 2p_{1/2} appear at 459.35 and 465.09 eV that corresponds to chemical states of Ti in the samples having +4 valence. For V-doped TiO₂, the Ti2p peaks position shows slight shifts of about 0.35 eV towards higher energy side. This indicates that V ions are incorporated into TiO₂ lattice thus influencing the local chemical state of Ti⁴⁺ ions. To achieve local charge balance in the TiO₂ lattice, some of the Ti ions may acquire higher oxidation state by releasing electrons, a process that explains the XPS peak shift for V-doped TiO₂. XPS spectrum of V2p_{3/2} level was deconvoluted into two peaks having binding energy values of 517.3 and 516.2 eV attributed to V⁵⁺ and V⁴⁺ states of vanadium respectively [3,4]. This indicates that V species exist in the lattice of TiO₂ in the form of V⁵⁺ and V⁴⁺ with higher content of V⁵⁺ ions as indicated by the area under the peak in XPS spectrum (Fig. 2b).

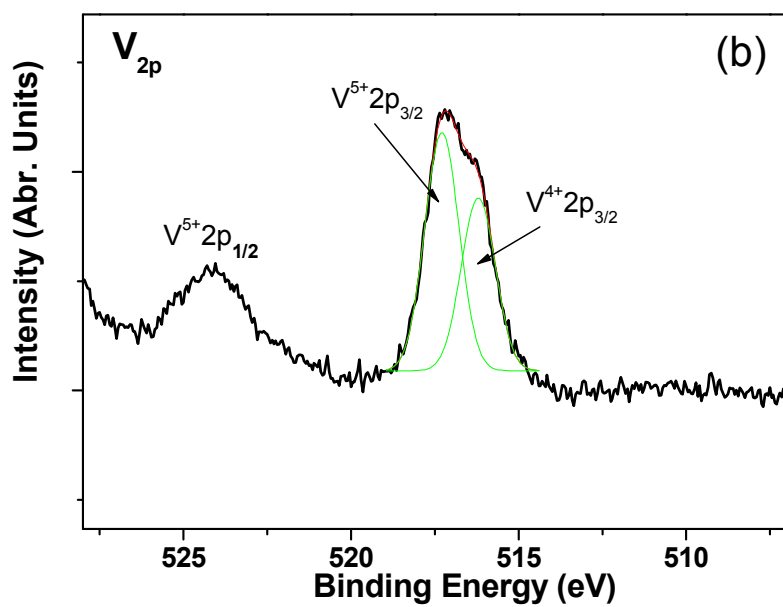
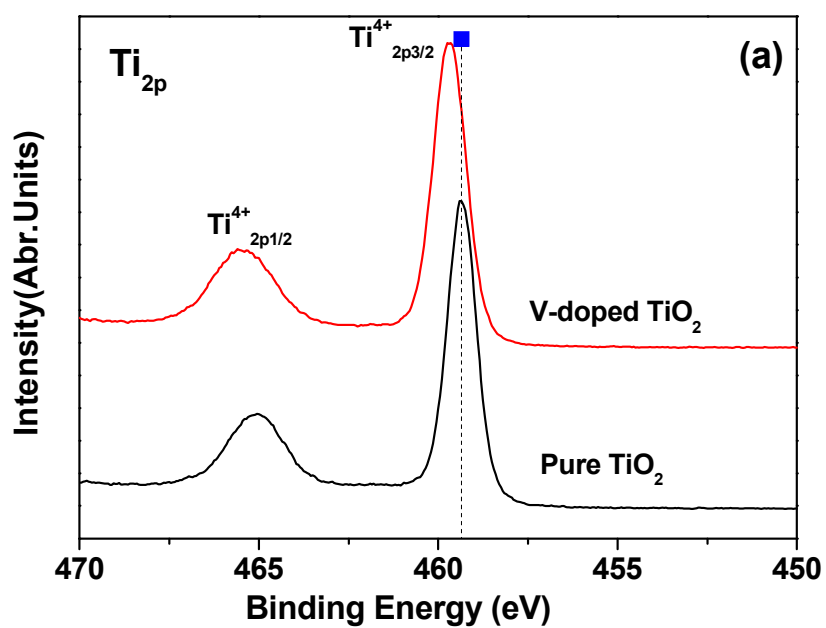


Figure 2: X-ray photoelectrons spectra of (a) Ti_{2p} and (b) V_{2p} levels for pure TiO_2 and V-doped TiO_2 (6 at.%)

D. UV-Visible Spectroscopy:

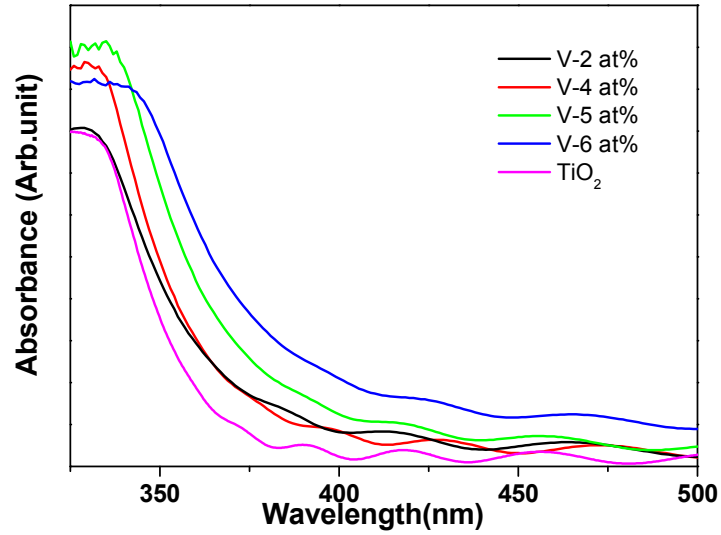


Figure 3: UV-VIS absorption spectra of un-doped and V doped TiO₂ films deposited by RF-magnetron sputtering with different dopants concentration.

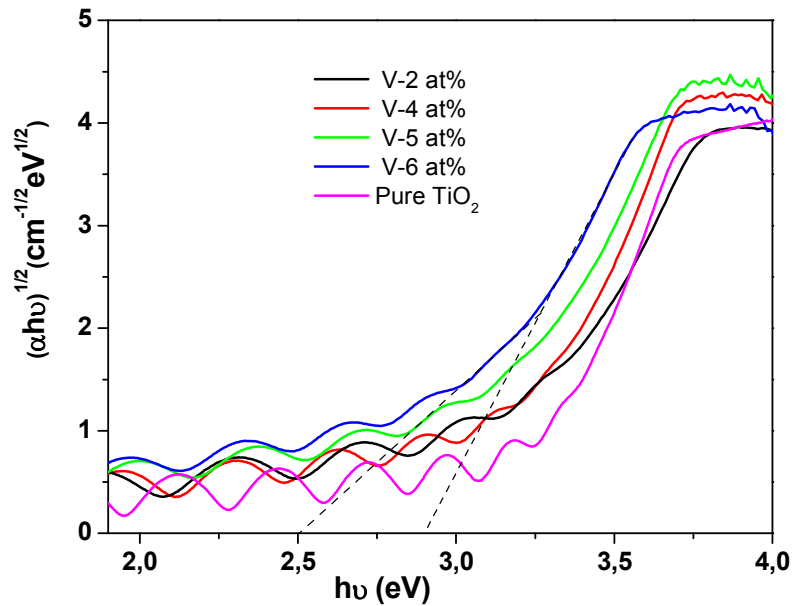


Figure 4: Tauc plot of undoped and V-doped TiO₂ films deposited by RF-magnetron sputtering with different dopants concentration.

The optical properties of the pure and V-doped TiO₂ were studied by measuring the absorption spectra ranging from UV (250 nm) to visible (750 nm) wavelengths and presented in Fig. 3. Using Tauc plot (Fig. 4), i.e. $(\alpha h\nu)^{1/2}$ versus $(h\nu)$, the band gap energies were deduced by extrapolating the linear region of the plot to intersect the photon energy axis: the obtained values are reported in Table 1.

V concentration in TiO ₂ film (at. %)	Crystal size (nm)		Intensity ratio of Anatase/Rutile	TiO ₂ optical band-gap values (eV)	Doping energy level values (eV)
	Anatase (101)	Rutile (110)			
Pure TiO ₂	45	6	1.14	3.25 ± 0.1	-----
2 at. %	39	12	1.12	3.17 ± 0.1	2.96 ± 0.1
4 at. %	35	11	1.01	3.10 ± 0.1	2.83 ± 0.1
5 at. %	37	12	0.91	3.05 ± 0.1	2.75 ± 0.1
6 at. %	39	10	0.81	2.85 ± 0.1	2.50 ± 0.1

Table 1: Crystal size and intensity ratio of anatase and rutile phase obtained from A(101) and R(110) peak, TiO₂ optical band-gap and doping energy level values for undoped and V-doped TiO₂ films deposited by RF-magnetron sputtering with several V concentration.

The figures clearly show a slight shift in the absorption band edge towards longer wavelengths when increasing the V concentration in the TiO₂ film. Most importantly a tailing of the absorption band is observed that indicates the existence of additional energy levels in the band gap. This can be assigned to the charge-transfer transition from the d orbital of V⁵⁺ and V⁴⁺ to the conduction band of TiO₂. For V-TiO₂, V⁵⁺ and V⁴⁺ ions are incorporated in the TiO₂ lattice which forms three isolated impurity energy levels located just below the bottom of the TiO₂ conduction band (CB). Because of these impurity energy levels in the band gap, the electrons in the valence band can be excited to the impurity energy levels and then subsequently excited to the CB by absorption of visible light. So these impurity energy levels are beneficial for extending the absorption spectrum wavelength towards the visible-light region [5].

As seen from the above results, V-doped TiO₂ with 6 at.%, shows the maximum lowering of the photon-absorbed energy with impurity energy level in visible range. Thus we preferred to perform the photocatalytic activity measurements only with this V-doped-film by making comparison with undoped TiO₂. Henceforth, 6 at.% V-doped TiO₂ film will be assigned as V6-doped TiO₂ film.

E. Open circuit Voltage-Current Measurement:

V6-doped TiO₂ film (about 750 nm thick) was deposited on an ITO layer (80 nm), previously deposited on glass substrate, and the obtained bilayer was covered with thin layer of pure TiO₂ (100nm) to protect the film from possible corrosion induced by contact with the electrolyte. This single bilayer film was used as photocatalyst for water-splitting experiments. To make comparison, the undoped TiO₂ film with total thickness of 850 nm was similarly deposited on an ITO layer (80 nm). Reason behind the use of ITO layer is that it provides the necessary electrical path for the photo-generated electron from TiO₂ to Pt electrode. In addition, most importantly the ITO/TiO₂ stack film is able to partially limit the recombination of photo-generated holes and electrons (h⁺ and e⁻) because the conduction band edge of ITO (~ -4.5 eV) is at an energy value lower than that of TiO₂ (~ -4.0 eV) thus making favorable for electrons injection from the later into the former.

The photo-induced voltage and current are measured for undoped and V6-doped TiO₂ in light ON-regime in photoelectrochemical cell with open- and closed-circuit

configuration, respectively. The open-circuit photo-voltage value was more than ~ 1.4 V for both these TiO_2 samples which is greater than the required voltage (1.23 V) to break the water molecule. However, the photo-current measured using V6-doped TiO_2 ($\sim 53 \mu\text{A}$) is negligible as compared to pure TiO_2 films ($\sim 290 \mu\text{A}$) measured in the light-ON regime. This is mainly due to recombination of the photo-generated charges on defects associated to the dopant $\text{V}^{5+}/\text{V}^{4+}$ ions.

A simple and efficient route to suppress the recombination of charge carriers is by immediately removing the photo-electron from the generation site before it recombines with the holes through radiative or non-radiative processes. This fast separation can be achieved through the use of coupled semiconductors with appropriate conduction energy levels. For instance, as mentioned previously, in the ITO/ TiO_2 coupled system, the conduction band edge of ITO (~ -4.5 eV) is at an energy value lower than that of TiO_2 (~ -4.0 eV) thus making favorable electrons injection from the later into the former. Once the photoelectron from TiO_2 is injected in ITO, it has a very low probability of back transfer and, as a result, electrons and holes are definitely separated. However, to be efficient, ITO should be located near the electron generation site to provide the driving force for the photoelectron transfer.

Having this in mind, we have deposited multilayer films with different numbers (2-, 3-, 4-, 5-, 6- and 7-bilayers) of ITO/V6-doped TiO_2 bilayers and finally covering with thin layer of pure TiO_2 (100 nm) the surface layer that will be in contact with the electrolyte. The bottom portion of the overall multilayer is also in contact with the electrolyte through the pure TiO_2 (100 nm) layer (while the corresponding top portion is electrically connected to cathode of the photo-electrochemical cell). The total thickness of V6-doped TiO_2 was kept constant (750 nm) in all the multilayer films by decreasing the thickness of each V6-doped TiO_2 layer when increasing the number of the bilayers. The thickness of ITO (~ 80 nm) was kept constant in all the multilayer films irrespective of number of bilayers.

In Figure 5 we present the cross-section SEM image, in back scattering mode, of single multilayer film with 6-bilayers of ITO/V6-doped TiO_2 .

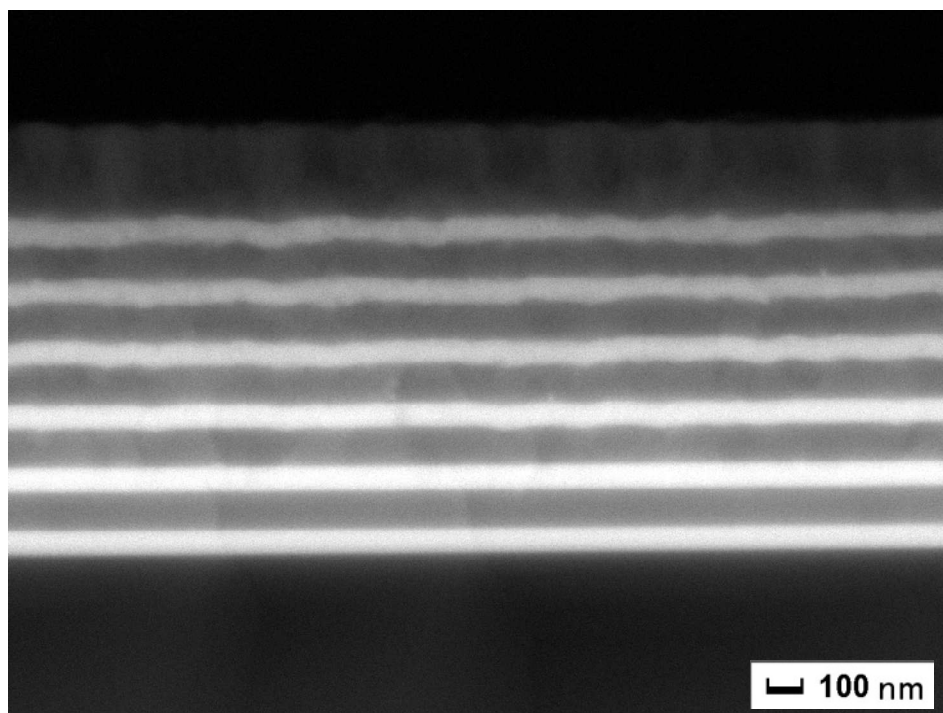


Figure 5: SEM Images, in back scattering mode, of multilayer film with 6-bilayers of ITO/V6-doped TiO_2

The white layer of ITO can be easily distinguished from the dark layer of V6-doped TiO_2 and for this reason both the periodicity and continuity of the layers are clearly visible. The figure 6 shows the thickness of single V6- TiO_2 layer, measured through cross-section SEM images, as a function of number of bilayers. The figure confirms that as the number of bilayers increases, the thickness of single V6-doped TiO_2 layer decreases.

Here we want to note that ITO deposited on the top of TiO_2 layer does not affect the amount of photons reaching the TiO_2 layer because ITO is a transparent conducting oxide with a direct band gap in the range of 3.9 to 4.2 eV which is significantly higher than the absorption edge of V6-doped TiO_2 layer. This feature was experimentally confirmed by measuring the absorbance of the V6-doped TiO_2 -ITO bilayers, with ITO on top, in the UV-Visible range: the spectra showed similar red shift in the band edge as that observed with single layer.

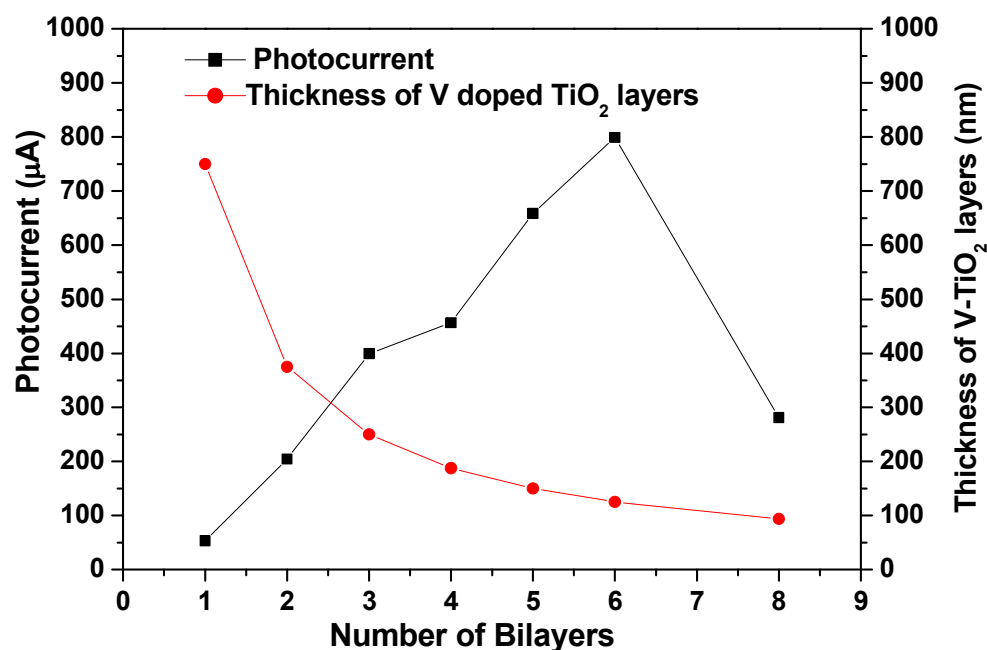


Figure 6: Photocurrent and thickness of each V6-doped TiO₂ layer as a function of number of bilayers.

To check the photo-catalytic activity of the multilayer films we measured photo-voltage and photo-current for light-ON regime in photo-electrochemical cell by using ITO/V6-doped TiO₂ multilayer films as photo-anode. Each ITO layer in the multilayer films is directly connected to the platinum cathode and so as soon as the electrons are injected from the V6-doped TiO₂ layers into the ITO layers, they are immediately transferred to the cathode. The photo-voltage measured on all the multilayer films (about 1.4 to 1.5 V) is greater than that required to split the water molecule. The measured photocurrent as a function of number of bilayers is reported in Figure 6. As the number of ITO/V6-doped TiO₂ bilayers increases the photo-current increases and reaches the maximum value with 6-bilayers (~800 μA). However, with 7-bilayers the photocurrent decreases to the value of ~280 μA. The photo-current value measured with 6-bilayers V6-doped TiO₂ film (~800 μA) is about 2.75 times higher than that obtained with pure TiO₂ (~290 μA) with same total thickness of TiO₂. These results are consistent with that reported in our previous work for ITO/Cr-doped TiO₂ multilayer films where similarly photo-current increases with number of bilayers and reaches maximum for 6-bilayers film.

This can be explained on the basis that when semiconductors having different energy bands are brought in contact with each other, on both sides a band bending occurs near the interface to make Fermi level equal. This band bending generates an interface space charge layer, having thickness of several tens of nanometer, where a large electric field is developed. When photo-electrons are generated in this interface region (or very near) they are instantaneously pushed out to the adjacent semiconductor due to the driving force provided by the electric field and the electron-hole separation is definitely obtained, a process well known in p-n semiconductor junctions. In the present ITO/TiO₂ system, the interface region presents electrical features that provide an efficient route for the *e-h* separation. Hence, by adopting a multilayer structure, we are able to produce many interfaces of ITO/TiO₂ which establish fast transport channels along with efficient *e-h* separation.

Now let's understand in detail the mechanism of the electron flow in the multilayer films and how the number of bilayers affects the generation of the photo-current. Schematic of the mechanism is demonstrated in figure 7.

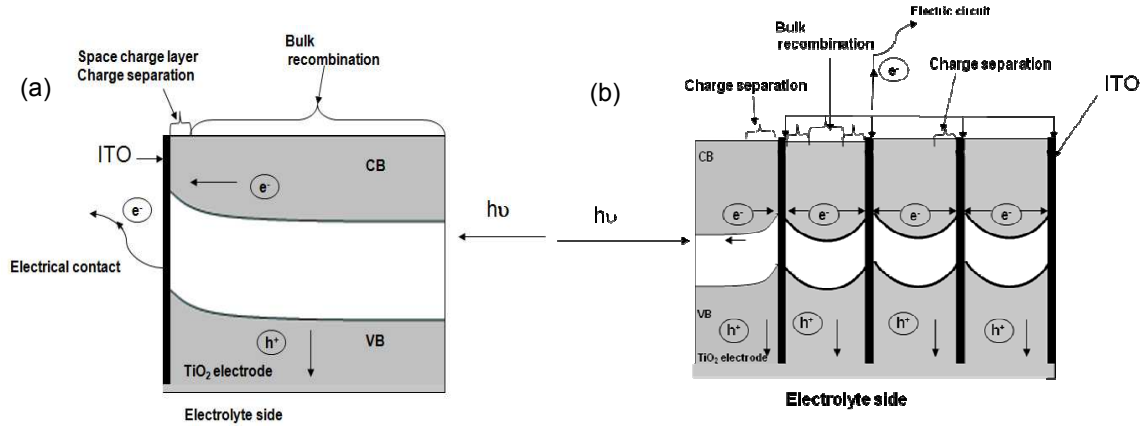


Figure 7: Schematic representation of the mechanism involving the electrons flow in the (a) single-Bilayer film and (b) multilayer film with 4-bilayers of ITO/V-doped TiO₂.

Our results show that the photo-current obtained with single bilayer of ITO/V6-doped TiO₂ is very low. In this single bilayer film there is only one interface of ITO/ V6-doped TiO₂ at the bottom with the thick layer of V6-doped TiO₂ (750 nm) over it (Fig. 7a). Most of the photo-electrons are generated in the bulk of the doped-TiO₂ where they have to travel some distance within the TiO₂ itself before entering the space-charge region of the

interface to feel the driving field for final injection into ITO. In V6-doped TiO₂ the probability of *e-h* recombination is much higher because of the presence of recombination sites associated to the V⁵⁺/V⁴⁺ ions. By depositing 4-bilayers film the photocurrent increases significantly from ~53 μA (for single bilayer film) to ~456 μA. In this film, the previous V6-doped TiO₂ layer having thickness of 750 nm was divided into four layers of ~185 nm by introducing three more ITO layers. The resulting film now contains seven ITO/TiO₂ interfaces where space charge layer is formed and the decreased thickness of the V6-doped TiO₂ layers assures that the photo-generated electrons have to travel a short distance into TiO₂ (the unshielded region) before being injected into the ITO layer where recombination is definitely hindered (Fig. 7b). Another relevant point to be considered is that in single bilayer film the photo-electrons, generated in the V6-doped TiO₂ layer, have to move only along one direction towards the ITO layer placed at the bottom of the layered structure. On the contrary, in multilayer film each V6-doped TiO₂ layer is sandwiched between the two ITO layers and so the photo-electrons can move along either of two directions to avoid recombination (Fig. 7b). All these reasons favor the increment of the photo-current in the 3-bilayers film.

In addition we observe that by increasing the bilayers number there is an almost linear increment in the photo-current, mainly attributed to the better conditions for charge separation and transport with reduced number of recombination processes: here we have to further underline the key role of number of ITO/TiO₂ interfaces. The measured photo-current reaches the maximum value (~800 μA) with 6-bilayers film; the measured photocurrent is one order of magnitude higher than that measured with single bilayer film (~53 μA). For 6-bilayers film, the thickness of V6-doped TiO₂ layer (125 nm) in each bilayer may be lower than the total thickness of the space charge layer of the pertinent interface. Thus photoelectrons generated in the V6-doped TiO₂ are already in space charge region where the electric field provides them the driving force to instantaneously inject into the ITO layers: this means that the 6-bilayers film creates the best conditions for charge separation. In addition, this film is able to absorb more visible light than pure TiO₂ due to the impurity energy levels by V⁵⁺/V⁴⁺, hence generating higher amount of photoelectrons. With 7-bilayers film the photo-current decreases (Fig. 6); we suggest this might be due to the poor crystallinity of very thin films of TiO₂ (92 nm). Takahashi et al. [6] and Nasr et al.

[7] showed the increase in photo-current by decreasing the TiO_2 layer thickness and reaches maximum value at particular thickness. Below this thickness the photo-current decreases drastically and, as indicated by the authors, this is attributed to the low crystallinity achieved with thinner films. For the moment with our XRD setup it is difficult to acquire the spectra of such a thin layer of TiO_2 . However, we will address this open problem with dedicated experiments in the future.

The reduced probability in charge recombination processes observed with multilayer films can be further analyzed by studying the photo-current kinetics curve. Fig. 8A shows the schematic diagram of photo-current transient curve.

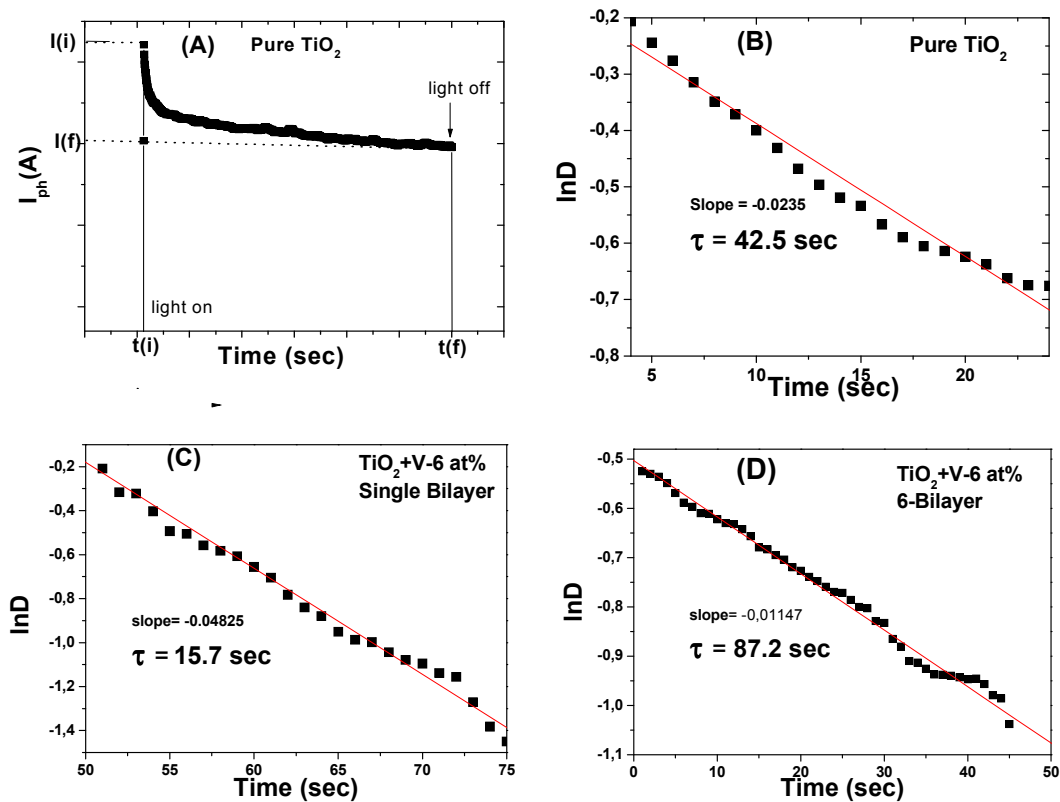


Figure 8: (A) Schematic representation of the photocurrent transient curve. Normalized plot of current-time dependence for: (B) pure TiO_2 , (C) single bilayer, and (D) 6-bilayers of ITO/V6-doped TiO_2 multilayer film.

The initial anodic photocurrent spike is denoted by $I(i)$. This current signals the separation of the electron-hole pairs by movement of holes towards the semiconductor surface where they are trapped or reduced by the species in the electrolyte, while the electrons are transported to the back contact. After $I(i)$ has been attained, then a continuous

decrease of the photocurrent with time is observed until a steady-state photocurrent, $I(st)$, is reached. The photocurrent decay indicates that charge recombination processes are occurring. The holes reaching the semiconductor surface may, instead of capturing electrons from the electrolyte, accumulate at the surface and recombine with electrons from the conduction band, i.e. the decay is determined by the rate at which minority carriers trapped at surface states capture majority carriers [8]. The photocurrent transient can be defined by the following kinetic equation [9]:

$$D = \exp\left(-\frac{t}{\tau}\right) \quad (2.19)$$

Where D is defined as

$$D = \frac{I(t) - I(st)}{I(in) - I(st)} \quad (2.20)$$

Here, τ is the transient time constant, $I(t)$ is the current at time t , $I(in)$ is the current at $t = 0$, and $I(st)$ the stationary current. Figs. 8B, C, and D illustrate the $\ln D$ vs. time plot for pure TiO_2 film, single bilayer, and 6-bilayers of ITO/V6-doped TiO_2 films respectively. The slope of this plot provides τ which is related to the time for charge recombination processes in the films. The measured τ for V6-doped TiO_2 with single bilayer film is about three times lower than that for the undoped TiO_2 . Specifically, the photocurrent decays within a few seconds in V-doped TiO_2 is due to recombination of the photo-generated charges on defects associated to the $\text{V}^{5+}/\text{V}^{4+}$ ions. On the contrary, with 6-bilayers the transient time constant is about two times greater than that for undoped TiO_2 film where there are no defect sites. This again proves that by introducing space charge regions in form of ITO/ TiO_2 interfaces and by decreasing the thickness of TiO_2 layer favors charge separation and recombination processes are suppressed even if recombination sites such as $\text{V}^{5+}/\text{V}^{4+}$ are still present.

After optimizing the thickness of the V-doped TiO_2 in the multilayer films, it is necessary to study the effect of the number of bilayers on the photocurrent. Thus we deposited different number of ITO/ TiO_2 bilayers by keeping constant the thickness of V6-doped TiO_2 and ITO layers (125 and 80 nm respectively). The photo-voltage and photocurrent measured in light ON regime with these multilayer films are reported in table 2.

Number of ITO/TiO ₂ Bilayers	Photo-voltage (V)	Photo-current (μ A)
1	1.446	230
2	1.458	390
4	1.403	467
6	1.460	586
7	1.394	548

Table 2: Photo-voltage and photo-current measured for different numbers of ITO/TiO₂ bilayers by keeping constant the thickness of each single bilayer.

All the multilayer films were able to produce photo-voltage greater than 1.4 V irrespectively on the number of bilayers. On the contrary, the photo-current increases with the number of bilayers and reaches a nearly constant value for the highest number of bilayers (6 and 7). A saturation effect is clearly expected on physical basis but what is important here is that the photo-current value depends not only on thickness but also on the number of bilayers, *i.e.* on the ability of the multilayer structure to efficiently avoid charges recombination. Here, another important point is that with 7 bilayers there is not a dramatic decrease of the photocurrent as observed in Fig. 6. This supports the point that the low crystallinity achieved with very thin films is deleterious to photocurrent generation.

F. Hydrogen Measurement:

The photo-catalytic activity of the V-doped TiO₂ multilayer films was finally tested by measuring the amount of H₂ generated by water-splitting in photo-electrochemical cell. Fig. 9 shows the H₂ evolution, as function of time, from water-splitting by irradiating multilayer films with single, 4- and 6- bilayer of ITO/V6-doped TiO₂ with light (250 W tungsten halogen lamp) which contains mostly visible light and includes a very small portion of UV light (1 %).

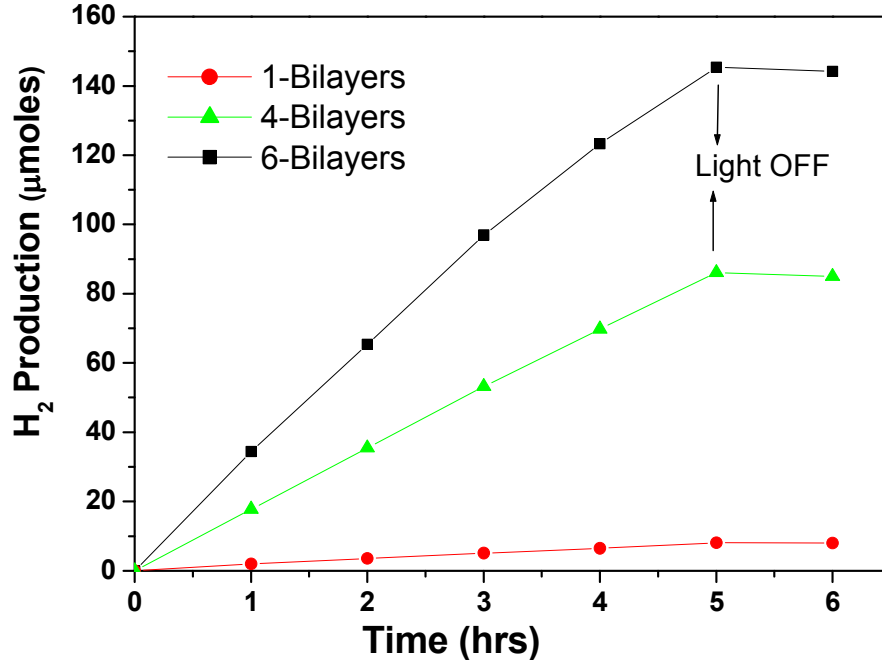


Figure 9: Hydrogen evolution, as a function of time, from water-splitting in photo-electrochemical cell containing two electrolytes of different pH by using photo-anode as sputter-deposited multilayer films with single, 4- and 6-bilayers of ITO/V6-doped TiO₂ (see procedure in ref. [10]).

The amount of the photo-catalytically produced H₂ increases linearly with the exposure time. The H₂ production completely stops after termination of light irradiation: this proves that H₂ is only produced photocatalytically. The constant production rate observed in the present case is simply due to the employ of TiO₂ photo-catalyst in form of thin film in an apparatus [10] where H₂ and O₂ evolve separately. During the measurement, the same amount of surface area (13.75 cm²) is exposed to the light for both the films. As the number of bilayers increase the H₂ generation rate increases for multilayer films showing the same trend as that obtained for the photocurrent values, and maximum rate is obtained with 6-bilayers. The obtained high generation rate is again due to better photo-generated charge separation by introducing space charge layers in form of ITO/TiO₂ interfaces. The H₂ generation rate was measured to be 31.2 ± 0.1 μmole/h for 6-bilayers

based V6-doped TiO₂ multilayer film and is about 2.5 times higher than that measured with pure TiO₂ film (12.5 ± 0.1 $\mu\text{mole/h}$) (as reported in ref [10]). The greater H₂ generation rate with V6-doped TiO₂ multilayer film is definitely attributed to the visible light absorption which is higher than pure TiO₂ and to reduced charge recombination processes. However, a comment must be included now to explain the hydrogen production results. Indeed, while the photo-generated electrons are easily collected by the established electrical contact to produce the measured photo-current, the positive holes that are produced inside the V-doped TiO₂ layers sandwiched by the ITO films, may arrive at the TiO₂ irradiated surface that is in contact with water. We suggest that holes migrate through the bottom deposited TiO₂ layer towards the irradiated surface where the H₂O molecules are get oxidized.

2.5.3 Conclusions:

TiO₂ doped with V ions (~6 at.%) shows an increase in the optical absorption efficiency due to the formation of impurity energy levels in the band gap. However, in photo-electrochemical cell, negligible photocurrent is measured with ITO/V-doped-TiO₂ (6 at.%) single bilayer, a problem that we attribute to the increased recombination rate of the photo-generated charges. To reduce the charge recombination rate we prepared multilayer films with different numbers of ITO/V6-doped-TiO₂ bilayers (namely, 2-, 3-, 4-, 5-, 6- and 7-bilayers) by keeping the total thickness of TiO₂ constant. The reduced thickness of the V-doped TiO₂ film, deposited on ITO, significantly contributes to reduce the charge recombination rates. This is because the generated photoelectrons, traveling into TiO₂ film of limited thickness, rapidly enter the space charge interface of the ITO-TiO₂ films from where they are instantaneously injected into the ITO layer and then removed towards the cathode of the photo-electrochemical cell: here, H⁺ reduction occurs. When the multilayer film is exposed to visible light, we observe that the photocurrent increases as function of the number of bilayers. The maximum value of the photocurrent is obtained with 6-bilayers of ITO/V6-doped-TiO₂. The enhanced photocurrent is attributed to both higher absorption of visible light by V-doped-TiO₂ and to the number of space-charge ITO/TiO₂ interfaces in multilayer films. With six bilayers, the H₂ production rate obtained through water splitting is about 31.2 $\mu\text{mole/h}$.

2.5.4 References

- [1] Dholam R, Patel N, Adami M, Miotello A. Hydrogen production by photocatalytic water-splitting using Cr- or Fe-doped TiO₂ composite thin films photocatalyst. *Int J Hydrogen Energy* 2009;34:5337-46.
- [2] Gennari FC, Pasquevich DM. Enhancing effect of iron chlorides on the anatase-rutile transition in titanium dioxide. *J Am Ceram Soc* 1999;82:1915-21.
- [3] Iketani K, Sun RD, Toki M, Hirota K, Yamaguchi O. Sol-gel-derived V_xTi_{1-x}O₂ films and their photocatalytic activities under visible light irradiation. *Mat Sci Eng B-solid* 2004;108:187
- [4] Ares MAB, Alemany LJ, Jimenez MC, Larrubia MA, Delgado F, Granados ML, Marti'nez-Arias A, Blasco JM, Fierro JLG. The Role of Vanadium Oxide on the Titania Transformation under Thermal Treatments and Surface Vanadium States *J Solid State Chem* 1996; 124:69
- [5] Zhou W, Liu Q, Zhu Z, Zhang J. Preparation and properties of vanadium-doped TiO₂ photocatalysts. *J. Phys. D: Appl. Phys.* 2010;43:035301
- [6] Takahashi M, Tsukigi K, Uchino T, Yoko T. Enhanced photocurrent in thin film TiO₂ electrodes prepared by sol-gel method. *Thin Solid Films* 2001;388:231-6
- [7] Nasr C, Kamat PV, Hotchandani S. Photoelectrochemistry of composite semiconductor thin films. Photosensitization of the SnO₂/TiO₂ coupled system with a ruthenium polypyridyl complex. *J Phys Chem B* 1998;102:10047-56.
- [8] Hagfeldt A, Lindstrom H, Sodergren S, Lindquist SE. Photoelectrochemical studies of colloidal TiO₂ films: the effect of oxygen studied by photocurrent transients. *J. Electroanal. Chem.* 1995;381:39-46.
- [9] Redeka M, Wierzbicka M, Komornicki S, Rekas M. Influence of Cr on photoelectrochemical properties of TiO₂ thin films. *Physica B* 2004;348:160-8
- [10] Dholam R, Patel N, Adami M, Miotello A. Physically and chemically synthesized TiO₂ composite thin films for hydrogen production by photocatalytic water splitting. *Int. J Hydrogen Energy* 2008;33:6896-903.

2.6 Low energy ion-beam modification of TiO₂ photocatalyst thin film for visible light absorption

This study attempt to verify effects of incorporation of anions in TiO₂ and chemical composition, structure, and optical properties of anions doped TiO₂ film. A variety of elements such as N, S, P, F and B have been adopted in past literature to dope in TiO₂ [1-5]. Nakamura et.al [6] proved that, N-implantation causes the activation of TiO₂ to 550 nm wavelength by the formation of TiO_{2-x}N_x and mixing the electron orbital's of N and O. Previous research showed that oxygen vacancies (TiO_{2-x}) created by ion implantation can be more sensitive beyond 400 nm wavelength than TiO₂ [6]. Thus, doping using ion implantation is a crucial technique to change microstructure as well as the chemical structure of TiO₂ to enhance the visible light absorbance. In the present study, anatase TiO₂ thin films have been synthesized using sol-gel method. Ion implantation was used to introduce Ar⁺ or N⁺ ions into the TiO₂ thin film in order to improve the sensitivity in the visible light region. Ar⁺ ions implanted TiO₂ clearly showed the increase of visible light absorption, with the implantation dose, in the full visible absorption range, while N⁺ implantation caused the absorption edge to shift to the low energy value. The obtained results are discussed in terms of variation in the band gap of TiO₂ thin film caused by defect formation during implantation.

2.6.1 Experiment

Material and chemicals:

Titanium butoxide [Ti(OC₄H₉)₄], Ethanol (C₂H₅OH) and Nitric Acid (HNO₃) were used as received. These chemicals were of analytical grade and purchased from Sigma Aldrich. All solutions were prepared using high purity deionized water.

Synthesis of Ar⁺ and N⁺ ions doped TiO₂ films

TiO₂ thin films were synthesized by sol-gel method using titanium butoxide [Ti(OC₄H₉)₄] as the starting material. Ti(OC₄H₉)₄ was mixed with ethanol under constant

stirring for 1 h at room temperature. Further a mixture of water, ethanol and HNO₃ was added drop-wise under a vigorous stirring to the above solution. The resultant solution was stirred for 1 h at room temperature to increase homogeneity before spin coating. The molar ratio of Ti(OC₄H₉)₄:ethanol:H₂O:HNO₃ for sol was 1:20:0.5:0.1. TiO₂ sol was spun for 40 s at 3000 rpm on glass and Si (100) substrate to obtain TiO₂ thin film which was further baked at 125 °C for 1 h. Obtained samples were thermally treated in static air at 500 °C for 2 h with a slow heating rate of 1 °C min⁻¹ (referred as untreated henceforth).

Ion implantation was carried out by using an ion-beam apparatus described in Ref. [7]. Ar⁺ and N⁺ ions with energy of 30 keV were used for irradiating the TiO₂ sample in vacuum (10⁻⁴ Pa) with different doses ranging from 1×10¹⁶ to 2×10¹⁷ ions/cm², at room temperature. The ion beam was swept in order to cover an area of 5×5 cm² to establish uniform implanted surface area in the film. The ion current density was kept constant in the range of 1–3 μA cm⁻².

Fourier Transform Infrared spectroscopy (FT-IR) measurements were carried out in transmission mode at normal incidence in the spectral range between 4000 and 400 cm⁻¹ using a Bruker (Equinox 55) spectrometer at room temperature. Optical measurement in the Ultraviolet (UV) and visible range was performed using a Bruker IFS66 spectrometer equipped with a reflection and transmission unit with near normal incidence of the incoming beam. The wavelength range of 250 nm to 750 nm was used to obtain the absorbance spectra. The sample deposited on glass slide was used for this measurement. The surface morphology of the TiO₂ samples was observed using scanning electron microscope (FEG-SEM JSM 7001F, JEOL)

2.6.2 Results and discussion

A. Fourier Transform Infra-red Spectroscopy:

TiO₂ films synthesized by sol–gel method were structurally characterized by FT-IR due to the low thickness (150 nm) achieved. Fig.1 presents the IR spectra of the TiO₂ films

prepared by sol-gel after heat treatment and implantation with Ar^+ or N^+ ions at different doses. Essentially, we see no distinct peaks in the as deposited sample, but after heat treatment at $500\text{ }^\circ\text{C}$ a peak at 433 cm^{-1} is observed, which corresponds to the vibration of the TiO_2 units in anatase phase [8-10]. This anatase phase still remains even after bombardment with Ar^+ or N^+ ions with some broadening of the peak. The broadening may be due to the formation of nano crystalline structure caused by the damage produced by the ion implantation [9]. No indication of rutile phase formation was observed and thus it shows that the implanted TiO_2 films possess only anatase phase with low crystalline degree.

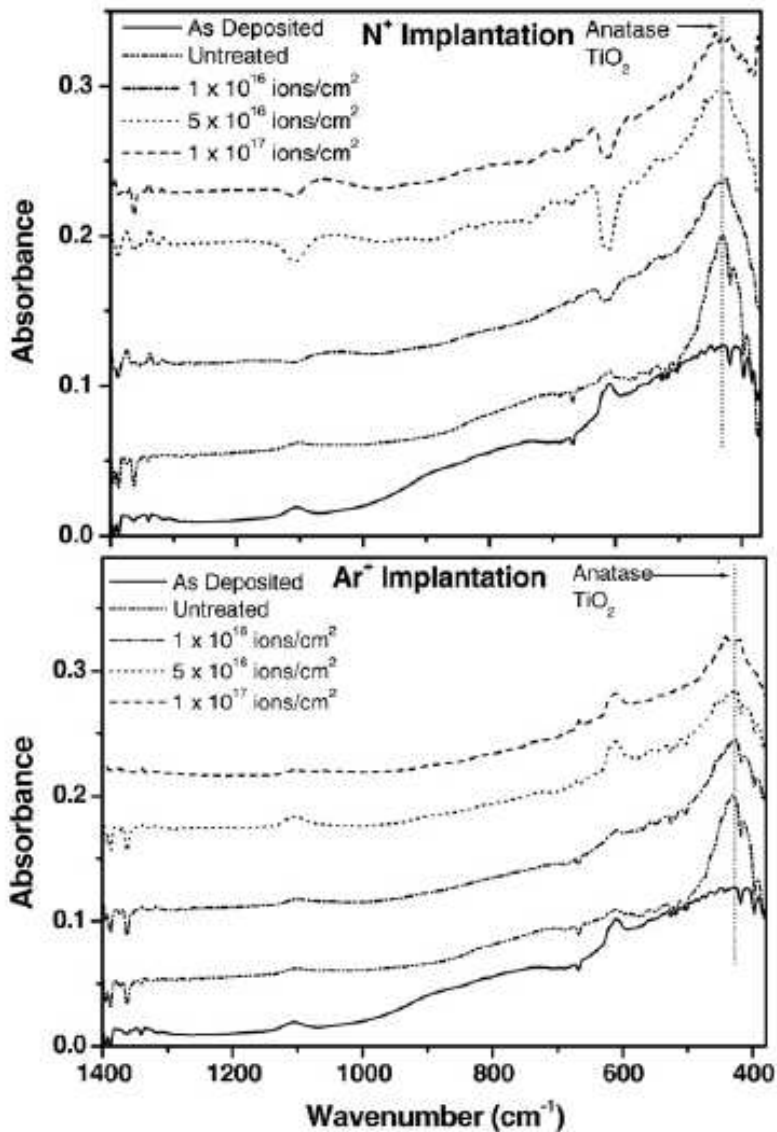


Figure 1: FT-IR spectra of untreated TiO_2 film and implanted films with Ar^+ and N^+ ions at various doses.

B. Scanning Electron Microscopy (SEM)

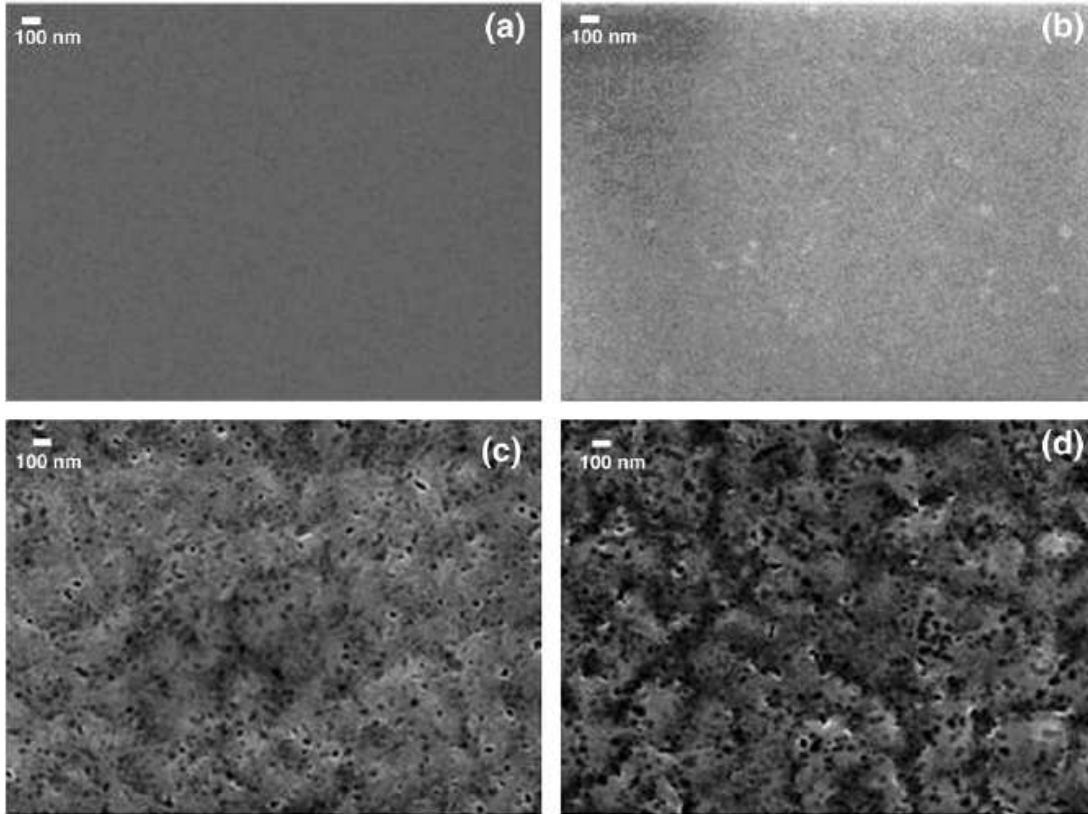


Figure 2: SEM images of: (a) untreated TiO_2 film and Ar^+ ion implanted at different doses (b) 1×10^{16} (c) 5×10^{16} and (d) 1×10^{17} ions/ cm^2 .

The SEM images of untreated, Ar^+ and N^+ ion implanted TiO_2 at different doses are reported in Figs. 2 and 3 respectively. The surface morphology (Fig. 2a) of untreated TiO_2 film appears to be very smooth and flat. Ar^+ implantation at low ion dose of 10^{16} ions/ cm^2 , does not cause any significant variation on the surface (Fig. 2b) of the film. However, TiO_2 film implanted at higher Ar^+ doses showed the formation of voids of about 50 nm with quite irregular surface caused by radiation damage (Fig. 2c and d). This evolution of surface texture can be advantageous in terms of an increased effective surface area for surface reactions such as photo-catalysis.

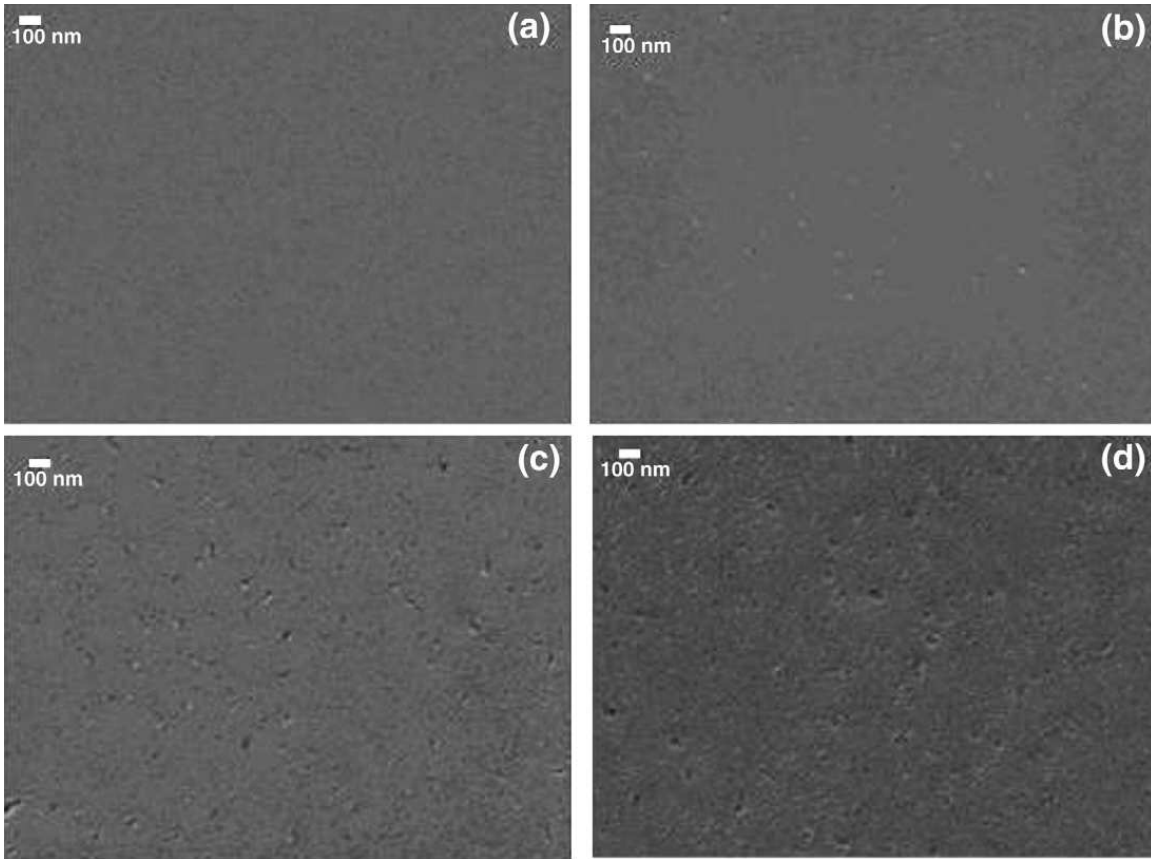


Figure 3: SEM images of: (a) untreated TiO_2 film and N^+ ion implanted at different doses (b) 1×10^{16} (c) 5×10^{16} and (d) 1×10^{17} ions/ cm^2

N^+ ions implanted TiO_2 film showed similar evolution of morphology (Fig. 3) but at higher doses the surface was more flat with less density of voids than that for Ar^+ ion implantation.

C. UV-Visible Spectroscopy:

Fig. 4 shows the UV–Visible spectra over the wavelength range of 300–750 nm for TiO_2 films implanted with 30 keV Ar^+ or N^+ ions with different doses. The spectra clearly show the increase in absorption of visible light with implantation dose for both kinds of ions. However, N^+ -implanted TiO_2 also showed a shift of absorbance edge. The band gaps were obtained by fitting the absorption edge of UV–Visible spectra by using the following equation [11]:

$$\ln T = \ln T_0 - C \frac{(\hbar\omega - E_g)^\nu}{\hbar\omega} \quad (2.19)$$

where E_g is the band gap, C is a constant, and T_0 is the transmission of the substrate. Depending on the type of transition, ν assumes different values: for direct, allowed (forbidden) transitions $\nu=1/2$ ($\nu=3/2$) and for indirect, allowed (forbidden) transitions $\nu=2$ ($\nu=3$). For our nano crystalline or amorphous films $\nu=2$ is used, according to Ref. [12]. Near the absorption edge, T_0 and C are approximately constant and fitting the absorption edge with Eq. (2.19) gives E_g for the TiO_2 samples.

To better understand the UV–Visible spectra, the value of absorbance at 650 nm (visible light range) and of band gap as function of dose is, plotted in Fig. 5 for both Ar^+ and N^+ implantations. The figure shows very low absorption of visible light for the untreated samples with a band gap around 3.2 eV indicating the formation of anatase phase. Ar^+ implantation causes activation of TiO_2 to absorb visible light and the absorption increases with implantation dose till the highest dose where there is a small decrease in absorption. It was also found that the band gap remains at around 3.2 eV for all the Ar^+ implantation doses: this means that there are no structural changes caused by implantation, as confirmed by the previous FT-IR results.

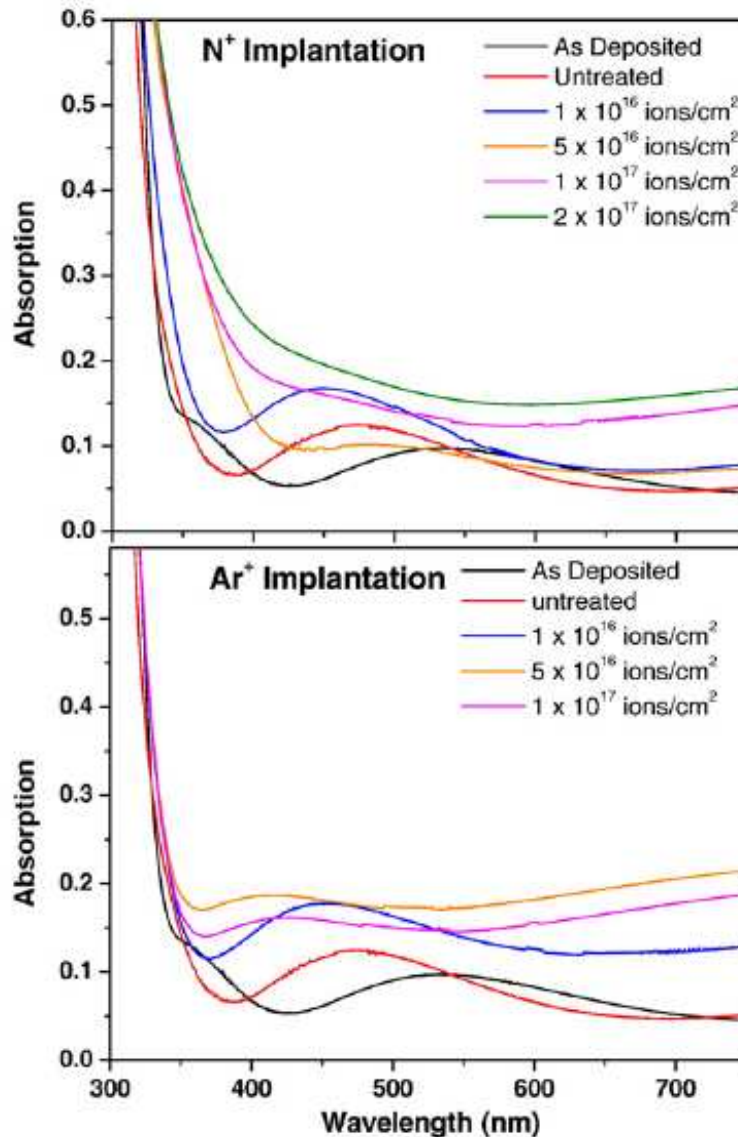


Figure 4: UV–Vis spectra of untreated TiO_2 film and implanted films with Ar^+ and N^+ ions at various doses

N^+ -implanted samples show minor increase in the absorbance in visible range at lower dose, but it increases at higher dose (Fig. 5a). However, the most significant change observed in N^+ -implanted samples is related to the decrease in the band gap as a function of ion dose. The minimum value of the band gap corresponds to 2.78 eV (visible range of wavelength of 445 nm) and is obtained with the highest implantation dose of 2×10^{17} ions/cm². Since rutile phase has lower band-gap value (3.0 eV) than anatase phase, the possible narrowing of the band gap could be due to the rutile phase formation by

implantation. But this speculation is not consistent with the absence of a peak at 495 cm^{-1} [8] attributed to rutile phase in FT-IR spectra (Fig. 1).

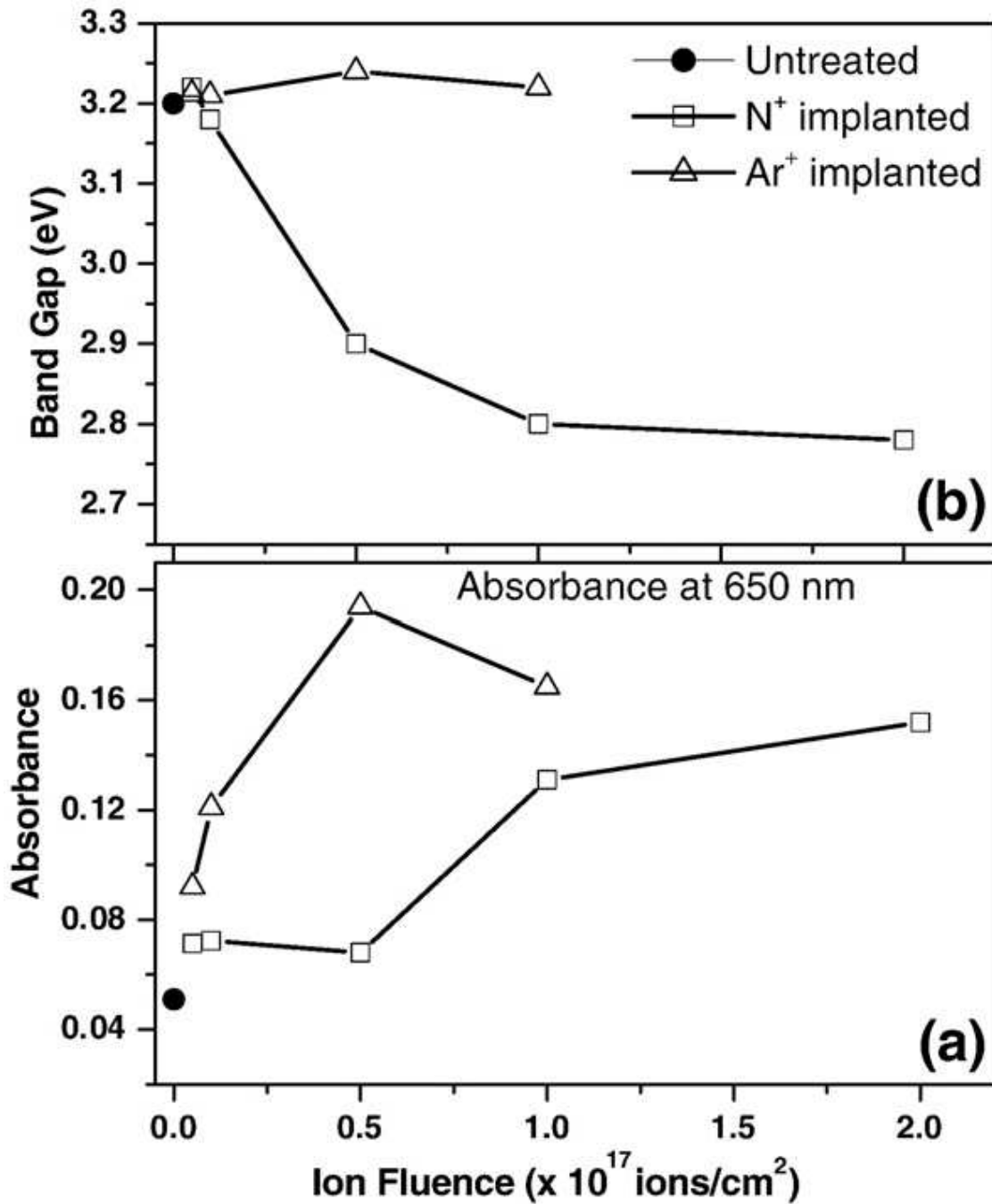


Figure 5: (a) Absorption of implanted TiO_2 films at wavelength of 650 nm (visible range) as function of ion dose. (b) Variation of energy band gap of implanted TiO film as function of ion dose.

D: Depth distribution of vacancies:

The optical trend obtained in the TiO₂ films after implantation was further understood by simulating the experimental condition using SRIM-2008 program. Fig. 6 shows the depth distribution of vacancies caused by Ar⁺ and N⁺ ions in the TiO₂ film.

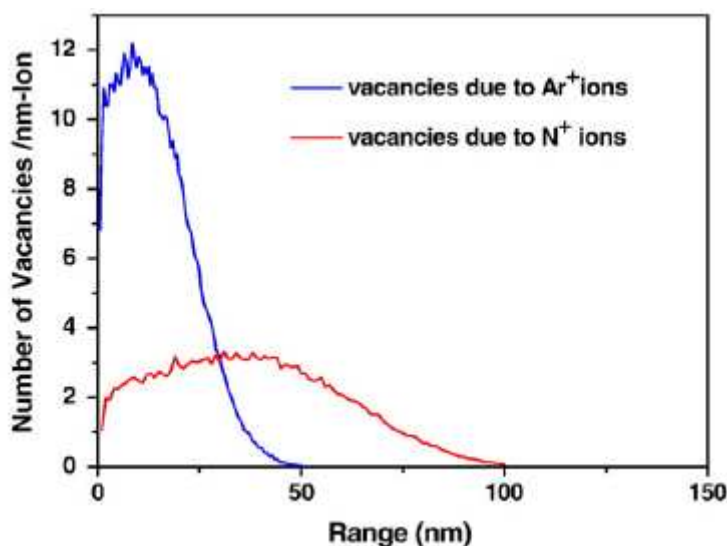


Figure 6: Depth distribution of vacancies formed in TiO₂ films after Ar⁺ and N⁺ implantations.

The average number of vacancies formed by heavier Ar⁺ ions is around 4 times higher than that of N⁺ ions as calculated by area under the curves. Thus it shows that a single Ar⁺ ion can create 4 times higher oxygen vacancies as compared to N⁺. However Ar is chemically inert element so that it could only cause displacement damage leading to the oxygen vacancies in TiO₂ lattice and thus the formation of TiO_{2-x}. Experiments reported previously show that oxygen vacancies in un-doped TiO₂ introduce defect states in the band gap at energy of about 0.8 to 1.18 eV below the conduction band; these are assigned to Ti³⁺ 3d [13] states on the basis of EPR experiments [14]. This means that the Ar⁺ implantation caused the formation of defect energy levels, corresponding to the oxygen vacancy, in the band gap which participates in the visible light absorption. The amount of oxygen vacancies created by N⁺ implantation at low dose was not enough to form the

defect energy level in band gap for the visible light absorption. However visible light absorption increases at higher dose of 2×10^{17} ions/cm² by the formation of defect level. In Ref. [1,15] it was numerically proved that if N⁺-ions substitute for the oxygen in the TiO₂ lattice, the corresponding N 2p states are located above the valence band edge. By increasing the concentration of nitrogen causes the mixing of N 2p states with O 2p states which reduces the band gap. This assures the photocatalytic activation in the visible light region. The interstitial accumulation of N does not activate the TiO₂ in the visible region. The formation of N-bonding in TiO₂ depends on implantation energy; with low energy (few 100 eV) nitrogen is located interstitially because the energy is not enough to break the Ti–O bonds [16]. N⁺ ions with moderate energy (a few keV) are able to break the bonds and substitute the oxygen atoms in the TiO₂ lattice in order to decrease the band gap [17]. Thus red shift in the band gap and visible light absorption in our TiO₂ samples by N⁺ implantation is due to the substitution filling of nitrogen in place of oxygen. Further studies are underway to investigate the above effect in terms of elemental electronic interaction.

2.6.3 Conclusion

TiO₂ thin films were synthesized by the sol–gel method with subsequent annealing at 500 °C, yielding the anatase phase. Ar⁺ or N⁺ ion implantation of energy 30 keV was adopted to vary the energy band gap of TiO₂ film in order to absorb visible light. The original anatase phase was not changed by implantation. Increase in full visible absorption range was observed for both kinds of ion implanted-TiO₂ films which further increased with the ion dose while N⁺ ion implantation also caused the shift of the absorption edge from UV to visible light range. N⁺ implanted TiO₂ showed narrowing of band gap from 3.2 eV for untreated anatase TiO₂ to 2.78 eV for dose of 1×10^{17} ions/cm⁻². Ar⁺ and N⁺ implantations create oxygen vacancies related defect energy levels in the band gap. In case of N⁺ implantation, nitrogen also substitutionally replaces the oxygen atoms thus forming an energy level just above the valence band which further interacts with O 2p states resulting in the narrowing of band gap.

2.6.4 References

- [1] Asahi R, Morikawa T, Ohwaki T, Aoki K, Taga Y. Visible-Light Photocatalysis in Nitrogen-Doped Titanium Oxides. *Science* 2001;293: 269.
- [2] Morikawa T, Asahi R, Ohwaki T, Aoki A, Taga Y. Band-Gap Narrowing of Titanium Dioxide by Nitrogen Doping. *Jpn. J. Appl. Phys.* 2001; 40:561.
- [3] Umebayashi T, Yamaki T, Itoh H, Asai K. Band-Gap Narrowing of Titanium Dioxide by Sulphur Doping *Appl. Phys. Lett.* 2002;81: 454.
- [4] Moon S, Mametsuka H, Tabata S, Suzuki E. Photocatalytic production of hydrogen from water using TiO₂ and B/TiO₂ Catal. *Today* 2000;58: 125.
- [5] Sakthivel S, M. Janczarek, H. Kisch. Visible Light Activity and Photoelectrochemical Properties of Nitrogen-Doped TiO₂. *J. Phys. Chem. B* 2004;108: 19384.
- [6] Nakamura I, Negishi N, Kutsuna S, Ihara T, Sugihara S, Takeuchi K. Role of oxygen vacancy in the plasma-treated TiO₂ photocatalyst with visible light activity for NO removal. *J. Mol. Catal. A* 2000; 161: 205.
- [7] Bonelli M, Calliari L, Elena M, Ghabashy MA, Guzman LA, Miotello A, Ossi PM. Titanium nitride coatings obtained using new apparatus for ion beam assisted deposition. *Surf. Coat. Technol.* 1991;49:150.
- [8] Djaoued Y, Badilescu S, Ashrit PV, Bersani D, Lottici PP, Robichaud J. Study of anatase to rutile phase transition in nanocrystalline titania films. *J. Sol-Gel Sci. Technol.* 2002;24: 255.
- [9] Alam MJ, Cameron DC. Preparation and characterization of TiO₂ thin films. *J. Sol-Gel Sci. Technol.* 25 (2002) 137.
- [10] Duenas S, Castan H, Barbolla J, San Andrés E, Del Prado A, Màrtel I, González Diaz G. A comparative study of anodic tantalum pentoxide and high-pressure sputtered titanium oxide. *J. Mater. Sci.: Mater. Electro.* 2003;14: 375.
- [11] Lohstroh W, Westerwaal RJ, Van Mechelen JLM, Chacon C, Johansson E, Dam B, Griessen R. Structural and optical properties of Mg₂NiH_x switchable mirrors upon hydrogen loading. *Phys. Rev. B* 2004; 70: 165411.
- [12] Davis EA, Mott NF, *Philos. Mag.* 1970;22 : 903.

- [13] Hashimoto K, Irie H, Fujishima A. TiO₂ Photocatalysis: A Historical Overview and Future Prospects. *Jpn. J. Appl. Phys.* 2005; 44 :8269.
- [14] Hurum DC, Agrios AG, Gray KA, Rajh T, Thurnauer MC. Explaining the Enhanced Photocatalytic Activity of Degussa P25 Mixed-Phase TiO₂ Using EPR. *J. Phys. Chem. B* 2003;107:4545.
- [15] Di Valentin C, Pacchioni G, Selloni A, Livraghi S, Giamello E. Characterization of Paramagnetic Species in N-Doped TiO₂ Powders by EPR Spectroscopy and DFT Calculations. *J. Phys. Chem. B* 2005;109: 11414.
- [16] Shen H, Mi L., Xu P., Shen W, Wang PN. Visible-light photocatalysis of nitrogen-doped TiO₂ nano -particulate films prepared by low-energy ion implantation. *Appl. Surf. Sci.* 2007 ;253: 7024.
- [17] Yang TS, Yang MC, Shiu CB, Chang WK, Wong MS. Effect of N₂ ion flux on the photocatalysis of nitrogen-doped titanium oxide films by electron-beam evaporation. *Appl. Surf. Sci.* 2006; 252: 3729.

Chapter 3

Development of a Solar Concentrator based water heating system

This Chapter reports results on development of solar absorber for water heating system using concentrated solar power. We divided chapter into seven sections. The first section gives introduction of different water heating techniques. The second section describes the design of water heating system used in present work. The third section is devoted to the experimental details and method to form efficient solar absorber. In this work we also developed Anti-Reflecting coatings which increases efficiency of water heating system. The details of this are included in section four. The efficiency of water heating system and its comparison with commercial systems are elucidated in fifth and sixth section, respectively. The last section summarizes the results of the presented work.

3.1 Introduction:

Using the sun's energy to heat water is not a new idea. More than one hundred years ago, black painted water tanks were used as simple solar water heaters in a number of countries. Solar water heating (SWH) technology has greatly improved during the past century. Today there are more than 30 million m² of solar collectors installed around the globe. Hundreds of thousands of modern solar water heaters, such as the one shown in *Fig. 1*, are in use in countries such as China, India, Germany, Japan, Australia and Greece [1].



Figure 1: Evacuated Tube Solar Collector in Tibet, China.

In addition to the energy cost savings on water heating, there are several other benefits derived from using the sun's energy to heat water. Most solar water heaters come with an additional water tank, which feeds the conventional hot water tank. Users benefit from the larger hot water storage capacity and from the reduced likelihood of running out of hot water. Some solar water heaters do not require electricity to operate. For these systems, hot water supply is secure from power outages, as long as there is sufficient sunlight to operate the system. Solar water heating systems can also be used to directly heat swimming pool water, with the added benefit of extending the swimming season for outdoor pool applications.

In past three decades, solar water heaters with flat plate collectors (FPC) have been widely installed in residential and office buildings for water heating [2]. Flat plate collectors work on the basis of copper pipes running through a glass covered collector, often connected to a water storage tank on the roof. These panels are easy to install with low cost hence they are most preferred water-heating systems for residential purpose: bathing, cooking, cleaning, swimming pool heating etc. However, large collector area is necessary to reach useful temperature of the water but at the same time it causes higher heat losses through this large surface area to decrease the overall system efficiency. This is the reason why flat plate collector is not adopted for the room or floor heating purpose in winter where water with high temperature (70-80 degree) is required. The problem related to FPC can be solved by using evacuated tube solar collectors, which consist of glass tubes with a layer of heat absorbent coating inside them. The tubes encasing the water pipes are kept in vacuum to greatly reduce heat loss. However, the cost of such a system is generally unacceptable. The system seems to be delicate because glass tubes could break easily in a hail storm or from falling branches and in winter by formation of ice in the tubes.

Here we suggest a better solution by using concentrated solar radiation in the small absorber area to achieve high efficiency. Exposed area smaller than that of FPC would decrease the heat loss and hot water for room heating can be achieved by either increasing the concentrated power or changing the water flow. In the current project we developed the water-heating system to be used under concentrated solar radiation and measured the overall efficiency of the system to compare with the flat plate collector or evacuated tube collector.

3.2 Design of water heating system:

Fig. 2 shows the schematic diagram of the heat exchanger system. The system is composed of two chambers with stainless steel body. To reduce the heat loss by conduction, vacuum was maintained between the inner chamber and outer chamber. The water flows through the inner chamber where solar radiation is concentrated through quartz window. Solar light absorber in form of circular copper plate is placed inside the water to reduce the convective heat loss by the wind which cannot be avoided in FPC. At the same

time the temperature of the copper absorber is maintained by the water flow so that the heat loss due to radiation is also minimized. Radiative heat loss is usually caused by IR light emission from the surface of the object. But in present design since copper absorber is placed in the water, copper emits IR light that is readily absorbed by the water. The water flows through the helix behind the copper target before reaching the outlet to ensure the heat transfer from copper to water.

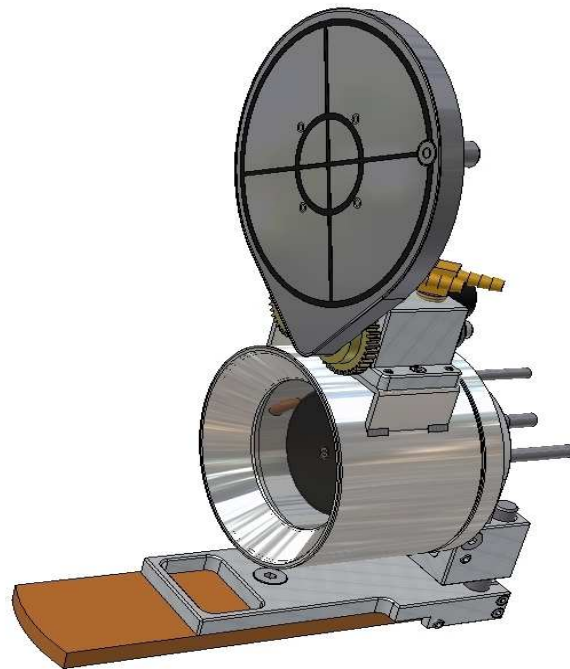


Figure 2: Schematic diagram of heat exchanger system for water heating by concentrated solar radiation.

3.3 Synthesis of Solar Absorber material: copper oxide:

In our present design for water heating system a copper target is used to collect all the concentrated solar radiation and then transfer heat to the surrounding water. Since

copper surface is shiny and reflects incident light thus it is necessary to have an absorber layer on surface of copper target which absorbs almost completely the radiation incident on it. This layer must be of black color for the total absorption.

One of the options to obtain black color layer [3] is by coating the surface of the copper with black high temperature paints which has absorbance of 98 %. However, this kind of coating is highly unstable and does not possess corrosion resistance properties in the aqueous medium. Another alternative is to deposit the black colored thin film of materials (few microns) like graphite, DLC, AlN, SiC etc. on copper substrate with physical vapour deposition (PVD). In this case certain issues like adhesion and incomplete coverage of the surface has to be solved. In addition it requires sophisticated techniques to deposit the film which in turn increases the cost of the product. The film deposited by PVD is usually flat and shiny which does not provide the texture effects for enhance absorption. To obtain irregular surface it is necessary to optimize the deposition condition which is time consuming and this may also lead to deteriorate the adhesion properties.

Another simplest way is to convert the copper target surface itself to black color oxide. Since this copper oxide layer is part of the target surface then the problem of adhesion and incomplete coverage of coating are automatically solved. The copper oxide can be produced by simple chemical conversion method in which by just immersing the copper substrate in the chemical, with proper composition, for certain period of time will lead to the chemical oxidation. Important advantage with this technique is that by just changing the precursor composition and exposure time will lead to the formation of range of textures on the surface. These include geometrically roughened surfaces and coatings with microcrystalline metal particle gradients or artificially produced optical constant gradients formed through changes in the composition of the oxide coatings.

In the present work copper oxide layer is formed on copper substrate by chemical oxidation treatment using alkaline solution of $K_2S_2O_8$ [4]. Optical and morphological properties are measured and presented in this chapter.

3.3.1 Experimental:

Synthesis of textured copper oxide:

Before chemical treatment of copper substrate to form oxide, it is necessary to polish and clean the surface of the copper. Firstly, a copper substrate was well polished with different grade silicon carbide papers and then with diamond paste to achieve mirror like surface. The polished copper was further cleaned and degreased with a systematic procedure: (1) dipping in Rodaclean supra (5 %) for 2-3 mins at 60 °C, (2) subsequently immersing in NGL solution (special solution used to degrease the copper substrate) for 5-10 mins at 70 °C and (3) finally inserting in 1% HCL solution for 10 mins at 40 °C to remove thin surface oxide. Cleaned copper samples were washed with distilled water followed by drying in air.

Black copper surface was prepared by chemical oxidation of a copper substrate in an alkaline bath. The cleaned copper substrate was immersed into a sealed glass container containing alkaline solution (0.1 M NaOH) of $K_2S_2O_8$ and left still at 70 °C for 16 hrs. The pH of solution was kept at 13. Such oxidation of copper normally proceeds through the precipitation of copper oxide salt on the surface, which then decomposes to produce copper oxide film. After reaction sample was washed with distilled water and dried in air. A black film was obtained, which covered uniformly on the copper substrate.

Characterization of copper oxide:

The capability of copper oxide to absorb the solar light was tested by measuring percentage reflectance in the range of solar wavelength due to opaque nature of the samples. Optical measurements in the Ultraviolet (UV), visible and near infrared range were performed in a Bruker IFS66 spectrometer in a reflection mode with different incident angle of the incoming beam. Measurements have been performed in the wavelength range between 300 nm to 1200 nm to obtain the reflectance spectra. Highly reflecting Gold mirror was used as the reference sample. The surface morphology of the copper oxide samples was observed by using scanning electron microscope (SEM, JEOL) equipped with Energy Dispersive Spectroscopy (EDS) which permitted compositional studies of the samples.

3.3.2 Results and Discussion:

In Fig. 3 the measured percentage reflectance (R), at incidence angle of 15° , is presented for polished pure copper and copper oxide synthesized by chemical conversion process. Polished copper showed a high reflectance between 50 to 60 % for complete wavelength range while after formation of black copper oxide decrease of the reflectance is observed up to almost zero percent for the same wavelengths. Since the copper oxide samples are opaque thus all the light which falls on black copper oxide is completely absorbed.

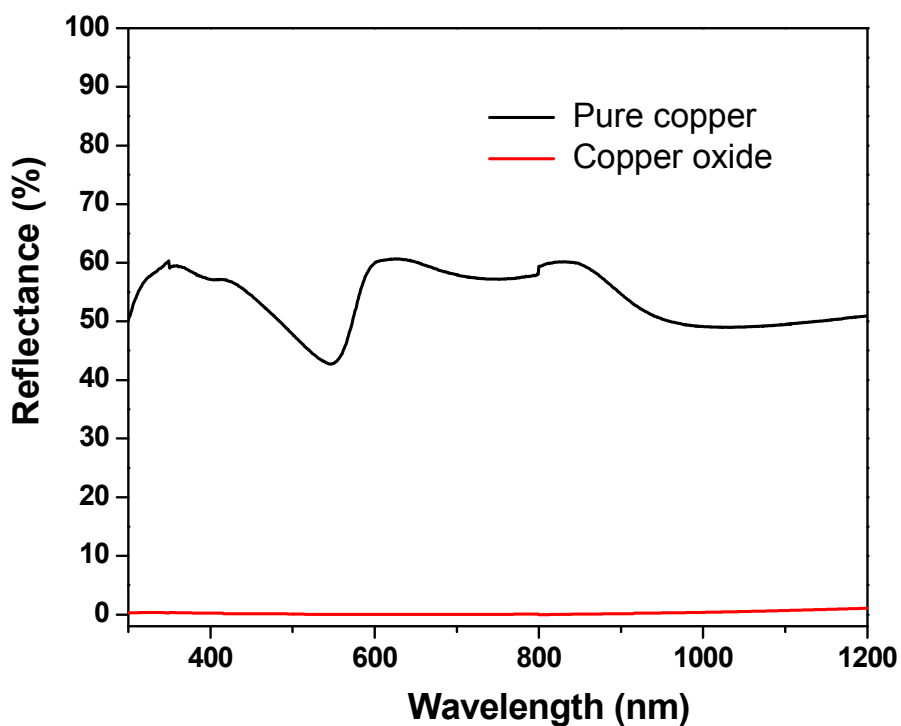


Figure 3: Percentage reflectance spectra, at incidence angle of 15° , of pure polished copper and copper oxide.

The plots of percentage reflectance and absorbance (obtained at incidence angle of 15°) are reported in Fig. 4 which helps to better understand the absorption nature of the

copper oxide. The figure clearly shows that black copper oxide can absorb about 99.8 % of visible light (400 to 800 nm) while in near IR region the absorbance varies from 99 to 99.6 %. Thus we were able to form the layer of black copper oxide which can almost completely absorb solar radiation.

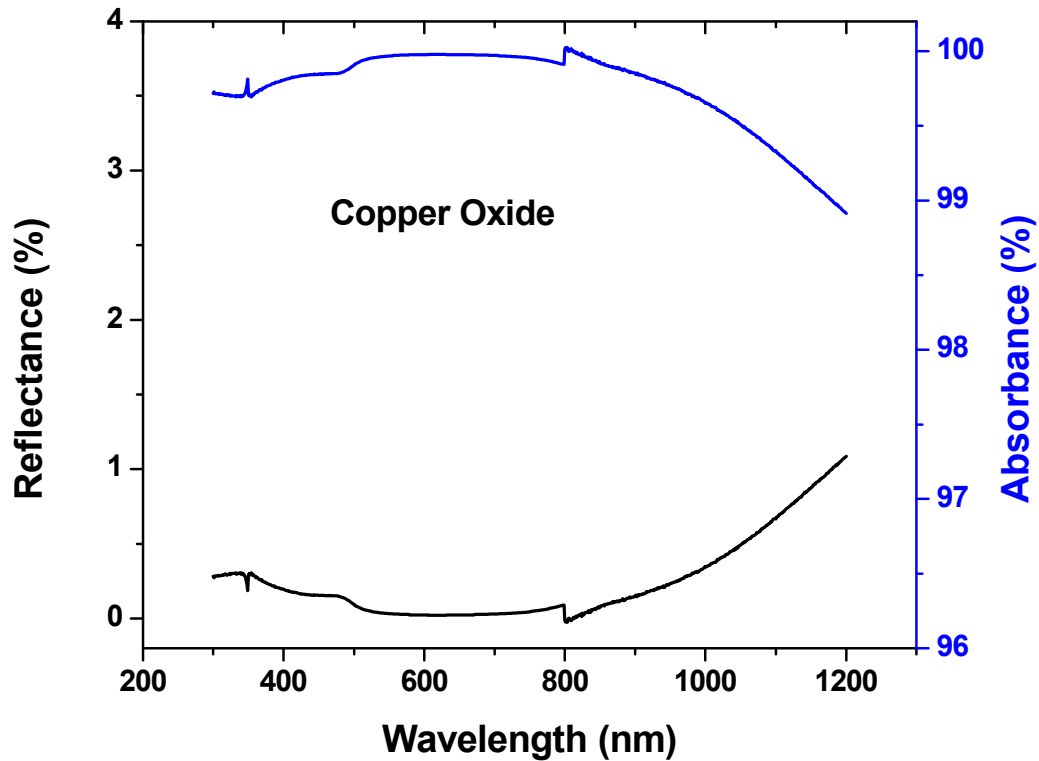


Figure 4: Percentage reflectance and absorbance spectra, at incidence angle of 15° , of black copper oxide.

With our solar concentrator the incident angle of the radiation falling on the copper target will vary from normal to 45 degree. Thus the percentage absorption at different angle of incidence of incoming beam in the visible range (300 nm to 800 nm) was measured and reported in Fig. 5. The absorbance decreases by very marginal amount as the angle of incidence increases. However, the solar spectrum (Fig.6) contains maximum amount of photons in the visible range from 350 to 700 nm. In this range the copper oxide samples demonstrated the decrement in percent absorbance from 99.8 % to 99 % with highest angle

of incidence. Thus it proves that black copper oxide is able to totally absorb the incident radiation even at different angle of incidence.

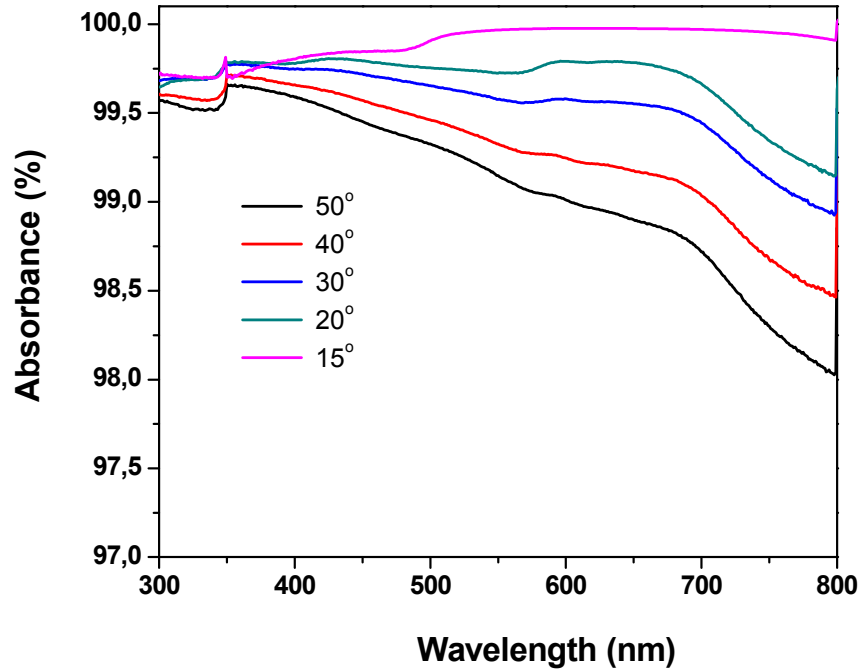


Figure 5: Percentage absorbance spectra at different angle of incidence of black copper oxide

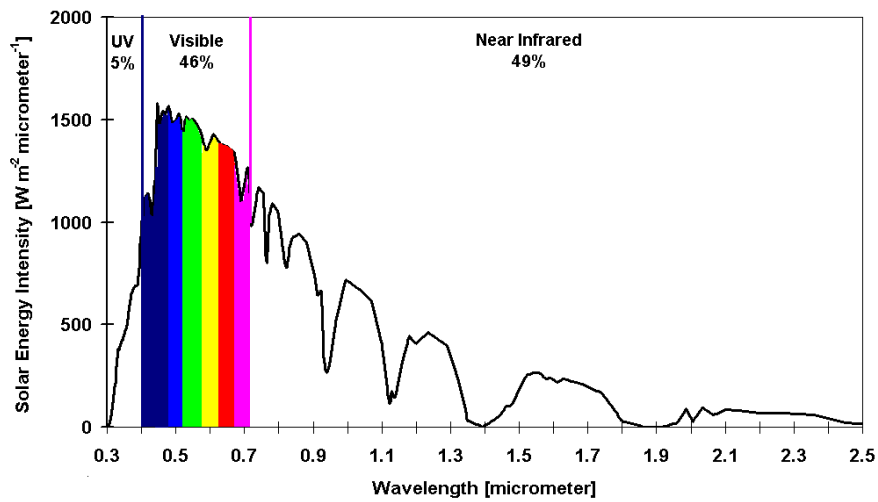


Figure 6: Full wavelength range of solar spectrum

Fig. 7(A) and Fig. 7(B) presents the digital photos of copper substrate before and after formation of copper oxide by chemical conversion method, respectively. The reflection of the digital camera is clearly observed, while taking the photo, on the surface of the polish copper substrate (Fig. 7A) indicating the mirror like surface with high reflectance (Fig. 3). However the chemical oxidation treatment of the copper substrate causes the formation of total black color copper oxide (Fig. 7B). SEM images of the copper substrate before and after formation of copper oxide are reported in Fig. 7(C) and Fig. 7(D) respectively. Polished copper substrate seems to be quite flat and smooth with some small pit marks (Fig. 7C). Fig 7D reveals the formation of porous black copper oxide film with high surface to volume ratio. The copper oxide surface is formed of nano-petals like structures with a thickness of around 5-10 nm. These petals grow with their surface perpendicular to Cu substrate and intermesh with each other to form continuous porous film. Thus immersing a piece of copper substrate into hot NaOH solutions leads to the formation of 3D structure on its surface.

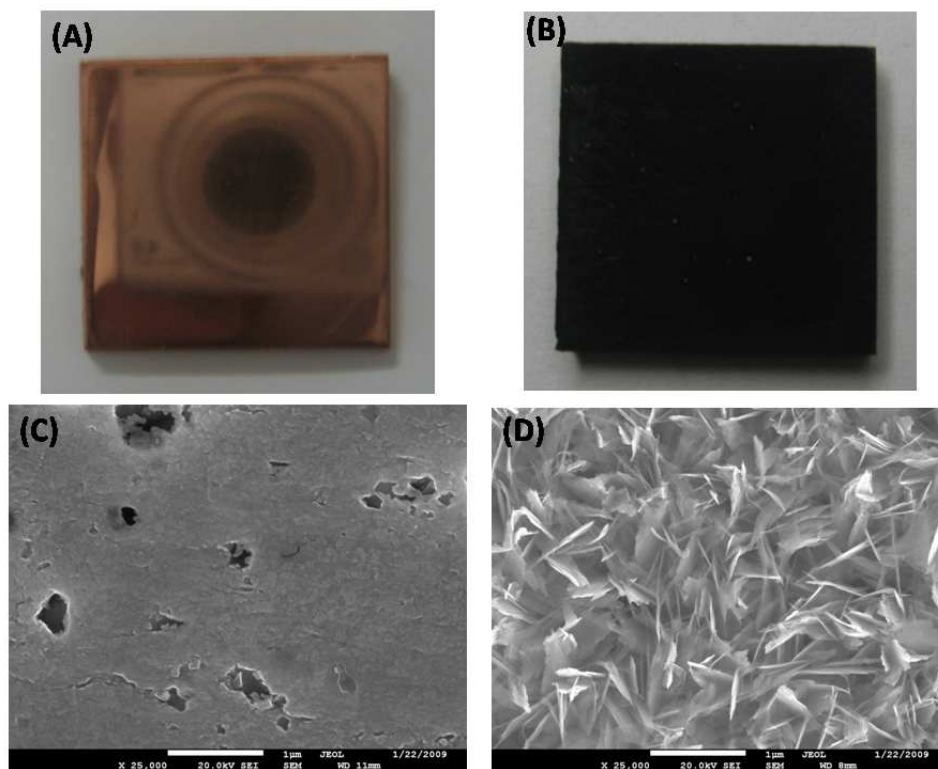


Figure 7: Digital photographs of copper substrate (A) before and (B) after formation of copper oxide. SEM images of copper substrate (C) before and (D) after formation of copper oxide.

The SEM images at different magnification of copper oxide surface texture are reported in Fig. 8. At low magnification 2D nanosheets with quite uniform distribution is observed. However at high magnification one can clearly see the nano-petal like structure where at some places these 2D nano-petals self-assemble into 3D flowerlike architectures. Significant importance of such kind of surface is given by the gaps between nano-petals which vary from 1-2 microns to 50-100 nm. This particular feature is able to cause the surface texture effect for higher absorption where surface irregularities, such as grooves and pores with dimensions comparable or larger than the wavelength of the incident radiation, simply increase the solar absorptance by multiple reflections [5]. In the present case, for the visible wavelengths, which are smaller compared to the actual gaps between the nano-petals, the surface looks rough and radiation may be trapped through multiple forward reflections and partial absorptions in the micro-cavities.

The above results shows that the complete absorption of the incident radiation is due to the combined effect of black colored nature of copper oxide and the texturing effect on the surface which arises by the formation 3D structure with the cavities in the range of incident wavelengths.

EDS spectra (Fig. 9) obtained from the surface of the copper oxide shows presence of some impurities (Si, C, and Ca) in addition with copper and oxygen. The atomic percentage of each element is summarized in Table 1. The atomic percentage of copper and oxygen showed nearly similar values indicating the formation of CuO phase which is confirmed by structural characterization. Silicon and carbon are present in the copper substrate while the presence of calcium was really surprising because none of the chemical used during the cleaning or oxidation treatment contains calcium. However the amount of calcium is quite low to affect the absorption properties of the copper oxide. This calcium is present in form of loose particles on the surface (Fig.10) which can be removed by proper rinsing or cleaning in distilled water. An XRD spectrum presented in Fig. 11 clearly shows the intense peak of Cu substrate in addition with low intensity peaks of CuO phase. Single peak of CaCO_3 is also observed in the spectra indicating the presence of CaCO_3 particles on the surface of the copper oxide

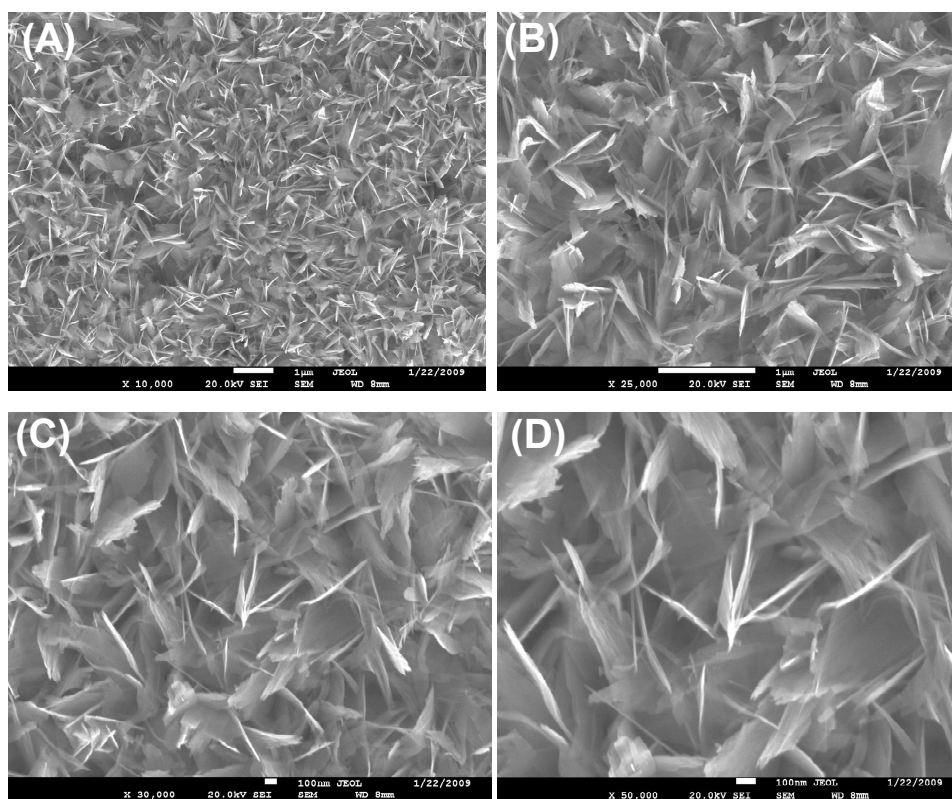


Figure 8: SEM micrographs of copper oxide surface at different magnification (A)10,000 X, (B) 25,000 X (C) 30,000 X and (D) 50,000 X.

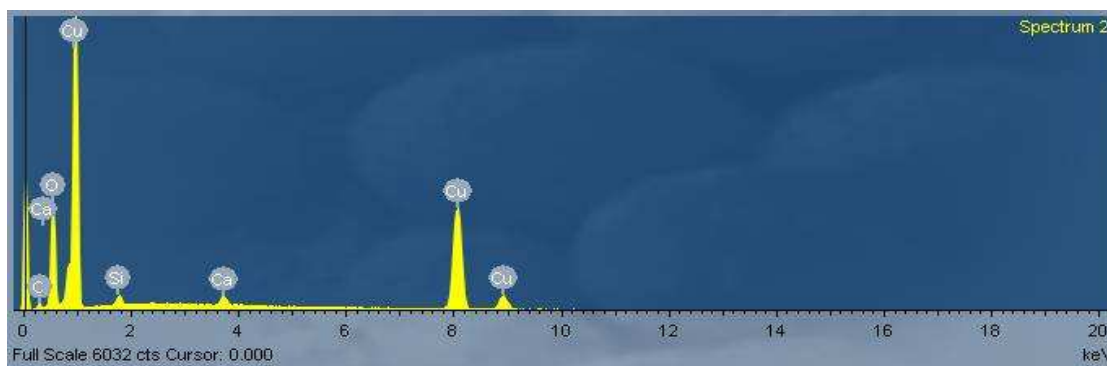


Figure 9: Elemental composition plot of the copper oxide surface obtained by EDS measurement.

Elements	At %
Cu	43.09
O	44.87
Ca	1.01
Si	1.34
C	9.69

Table 1: Elemental atomic composition of copper oxide surface, obtained by EDS measurement.

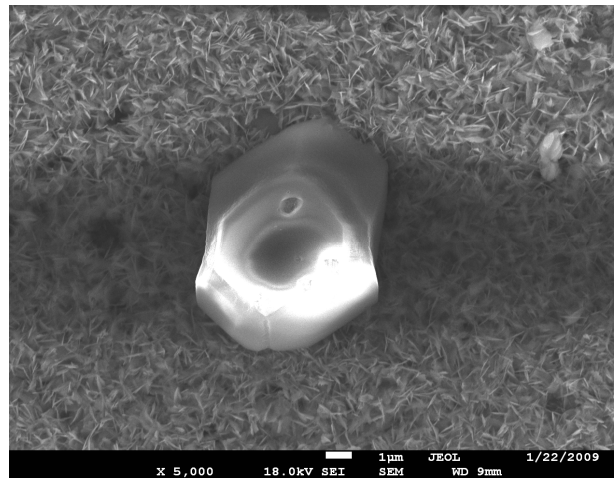


Figure 10: SEM micrographs of copper oxide surface with calcium particle.

Since the copper target with copper oxide on the surface will be fixed in the hot water surrounding for our water heating system, thus it is necessary to check the long duration thermal stability and corrosion resistance in hot water. To check these properties copper oxide samples are kept still in the water at 85 °C for about 140 hours (Fig.12). Indeed, no significant visual changes were observed as compared to as-treated samples and the film was well attached to the surface.

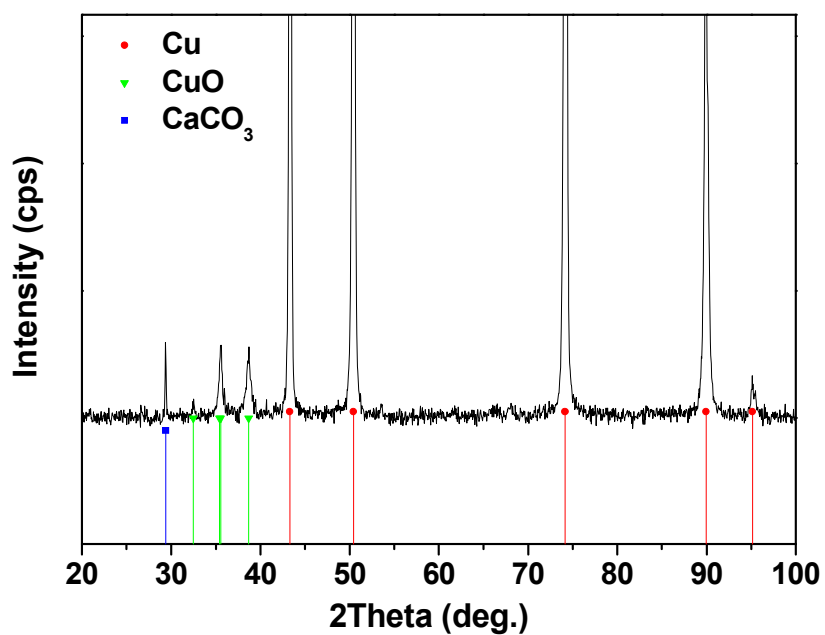


Figure 11: XRD spectra of the copper oxide samples synthesized by chemical conversion Method

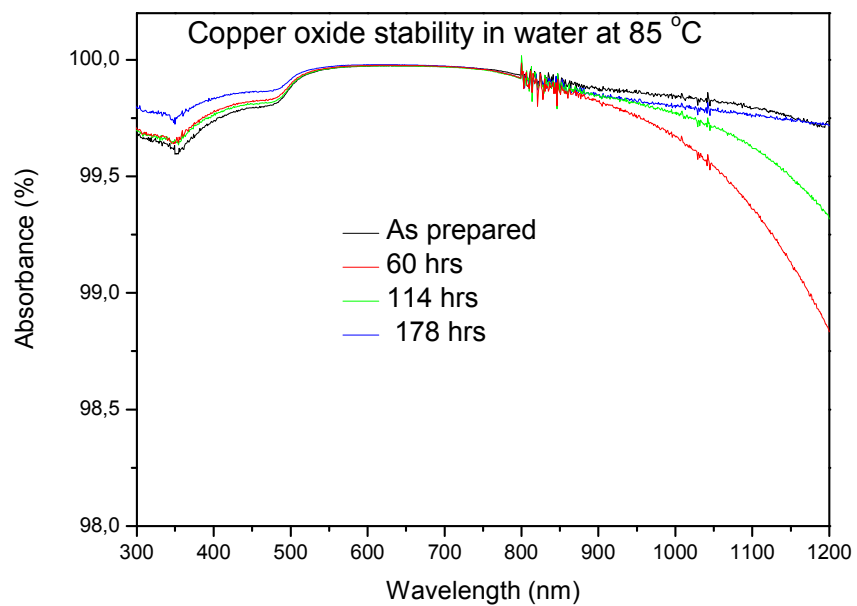


Figure 12: Thermal stability of CuO at 85°C

3.4 Synthesis of multilayer antireflection coatings

In our present design for water heating system a quartz window is used through which the solar radiation enters the systems. Thus in order to acquire high power conversion efficiency it is necessary for quartz window to transmit the entire solar radiation incident on it without much loss due to the reflection on the surface. In general quartz window is able to transmit 90-91 % of the solar radiation while 1-2 % is absorbed and 7-8 % is reflected from the surface. Thus to have nearly complete transmittance of the solar radiation it is obligatory to decrease both absorbance and reflectance of the quartz substrate. Since absorption of light is the intrinsic characteristic of the material, it is difficult to reduce it. Reflectance of the material can be decreased by depositing anti-reflecting coating on the surface of the quartz window. Anti-reflective or antireflection (AR) coatings are a type of optical coating applied to the surface of lenses and other optical devices to reduce reflection. This will improve the efficiency of the system since less light will be lost. Many AR coatings are made of transparent thin film multilayer structures[6] with alternating layers of contrasting refractive index. Layer thicknesses are chosen to produce destructive interference in the beams reflected from the interfaces, and constructive interference in the corresponding transmitted beams. Single-layer and multi-layer AR coating is used to reduce the reflectance in single specific wavelength and broad-band wavelength range respectively.

In present work we have developed the single-layer and multi-layer AR coating in order to reduce the percentage reflectance of the quartz window in the visible range. Low reflective index material like MgF_2 is deposited by e-beam technique to obtain single-layer AR coating. While Al_2O_3 and ZrO_2 , deposited by RF-magnetron sputtering, with MgF_2 are used to develop multi-layer AR coating.

3.4.1 Experimental:

Electron-beam deposition (EBD) and RF-magnetron sputter deposition were used to synthesize single and multilayer AR-coating respectively. Single layer in form of MgF_2 was deposited by e-beam evaporation on polished and cleaned quartz substrate. Prior to

deposition the chamber was pumped to a base pressure of 10^{-6} mbar. MgF_2 film was deposited with the rate of 2-3 nm/min and the final thickness was kept around 100 nm. Materials like ZrO_2 and Al_2O_3 were used for the multilayer AR-coating. Thin films of both these materials were deposited by RF-magnetron sputtering using pure ZrO_2 (99.9%) and Al_2O_3 (99.9%) as the target. High vacuum (HV) with base pressure $< 3 \times 10^{-5}$ Pa was achieved before deposition while the working Ar pressure of 1 Pa was used for the deposition. Before sample deposition, both oxide targets were pre-sputtered for 20 mins in order to remove any surface contamination. ZrO_2 and Al_2O_3 targets were sputtered on both quartz and Si (100) substrates at room temperature using RF power of 150 W and 200 W respectively. The sample and target distance was kept constant at 6 cm for all the samples. Two-layer AR-coating was obtained by first depositing Al_2O_3 thin film by sputtering and then transferring to the EBD chamber for MgF_2 thin film deposition on top of Al_2O_3 layer. Three-layer AR-coating was synthesized by depositing Al_2O_3 thin film with ZrO_2 thin film on top by sputtering and then depositing MgF_2 thin film by EBD. Additional layer of MgF_2 was first deposited on the substrate, by EBD, before depositing above mentioned three layers stacks ($\text{Al}_2\text{O}_3/\text{ZrO}_2/\text{MgF}_2$) to achieve four-layer AR-coating. The thickness of each layer of the multilayer coating was selected after a proper calculation to achieve broad band antireflection.

The efficiency of different AR-coatings was tested by measuring percentage reflectance in the range of solar light wavelength. Optical measurements in the Ultraviolet (UV) and visible range were performed in a Bruker IFS66 spectrometer in a reflection mode with incidence angle of 15 degree for incoming beam. Measurements have been performed in the wavelength range between 300 nm to 800 nm to obtain the reflectance spectra. The surface morphology of the samples was analyzed by using scanning electron microscope (SEM, JEOL) equipped with Energy Dispersive Spectroscopy (EDS) which permitted compositional studies of the samples.

3.4.2 Results and discussion:

When light travels from one media to another it get reflected from the surface depending upon the reflective index (n) of both the medium. In the more complicated scenario of multiple reflections, say with light travelling through a glass window, light is reflected both when going from air to glass and at the other side of the window when going from glass back to air. The size of the loss is the same in both cases. Light also may bounce from one surface to another multiple times, being partially reflected and partially transmitted each time it does so. In all, the combined reflection coefficient is given by $2R/(1+R)$. For glass in air, this is about 7.7%. This reflection can be reduced by depositing thin film on the glass or quartz substrate having a reflective index given by [2].

$$n_1 = \sqrt{n_o n_s} \quad (3.1)$$

Where n_o is the reflective index of air and n_s is the reflective index of the substrate. By substituting n_o as 1 for air and in our case n_s is 1.47 as for quartz substrate. The value of n_1 is calculated as 1.21. However, there is no naturally occurring transparent material having the reflective index of 1.21 so MgF_2 which have the closest n value of about 1.38 is used as the anti-reflecting coating for quartz substrate.

The thickness of the single layer AR coating must be $\lambda/4$, where λ is the wavelength to be transmitted and this coating is called quarter-wave coating which produces anti-reflection by interference effect. For this type of coating the incident beam when reflected from the second interface of the thin AR-film, will travel exactly half its own wavelength further than the beam reflected from the first surface. If the intensities of the two beams are exactly equal, they will destructively interfere and cancel each other since they are exactly out of phase. Therefore, there is no reflection from the surface, and almost all the energy of the beam must be in the transmitted ray. Practically the light is refracted in the medium thus the wavelength of the light is reduced inside the film and so the thickness of the AR coating practically is calculated as $\lambda/n_1/4$. In solar spectrum maximum amount of photons lies in visible range with the peak position at around 550 nm hence the AR coating is

developed for the visible range. The thickness of single layer MgF_2 based AR coating is calculated about 100 nm for the wavelength of 550 nm.

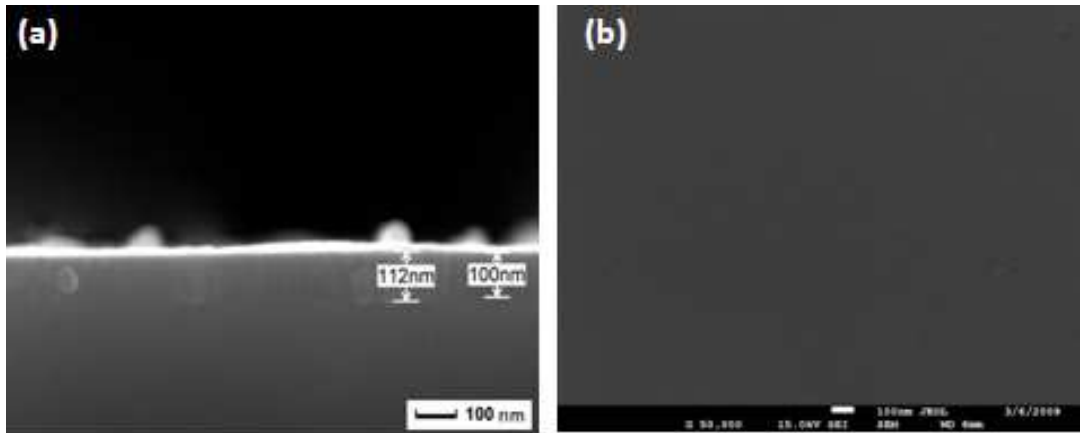


Figure 13: (a) Cross-section and (b) surface SEM micrographs of single-layer (MgF_2) AR coating.

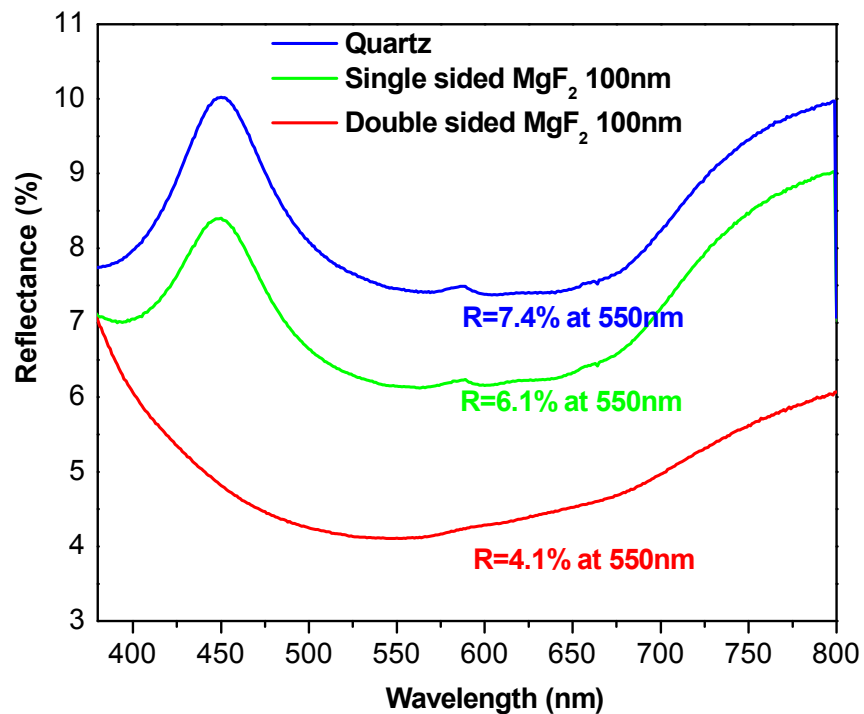


Figure 14: Reflectance spectra of single-layer (MgF_2) AR coating on quartz substrate.

MgF₂ thin film was deposited by e-beam deposition technique on quartz substrate with thickness of around 100 nm as confirmed by cross-section SEM image (Fig.13a). The cross-section image (Fig.13a) of the MgF₂ film shows that it is quite compact and dense while the top view (Fig.13b) of the film shows that surface is smooth and flat without any major defects. Figure 14 reports the reflectance spectra in the visible light range of the bare quartz substrate and with MgF₂ AR coating. The percentage reflectance of about 7.5 % is observed at wavelength of 550 nm for quartz substrate and this value is consistent with the theoretical value obtained after reflection from both the side of the quartz substrate. Percentage reflectance decreases to value of about 6.1 % at 550 nm by depositing MgF₂ AR layer on the single side which further decreases to the lower value of 4.1 % for the double sided AR coating. This shows that it is necessary to coat the quartz substrate on both the sides to decrease the reflection. However the reduction in reflectance value with single layer MgF₂ coating is not sufficient for our purpose.

The two-layer quarter/quarter AR coating is used as an alternative to the single-layer coating. It is developed because of the lack of available materials with the indexes of refraction needed to improve the performance of single-layer coatings. The basic problem associated with single-layer antireflection coatings is that the refractive index (RI) of the coating material is generally higher than required, resulting in too strong a reflection from the first surface which cannot be completely canceled through destructive interference with the weaker reflection from the substrate's top or second surface. In a two-layer coating, the first reflection is canceled through destructive interference with two weaker out-of-phase reflections from underlying surfaces. A quarter/quarter coating consists of two layers, both of which have an optical thickness of a quarter wave at the wavelength of interest. The outer layer is made of a low-refractive-index material, and the inner layer is made of a high-refractive-index material (compared to the substrate). Thus the beam reflected from the high RI material below will have the intensity to form destructive interference with the reflected beam from top surface.

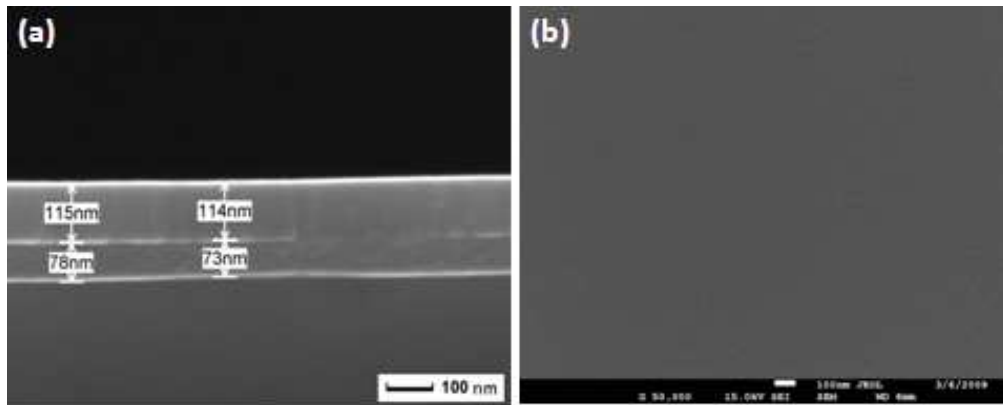


Figure 15: (a) Cross-section and (b) surface SEM micrographs of two-layer Al_2O_3/MgF_2 AR coating.

Alumina (Al_2O_3) with the refractive index of 1.62 is selected to deposit below MgF_2 layer for quarter/quarter double layer AR coating. The alumina layer thickness of around 85 nm is calculated by equation $\lambda/4n$ for wavelength of 550 nm. Sputter deposited alumina seems to be compact and dense as observed by the cross-section SEM image (Fig. 15a) of the two-layer. The surface of MgF_2 , synthesized by e-beam deposition, is flat and smooth similar to that of single-layer AR coating (Fig. 15b). Figure 16 reports the reflectance spectra in the visible light range of the bare quartz substrate and with two-layer (Al_2O_3/MgF_2) AR coating. Percentage reflectance decreases to a value of about 4.2 % at 550 nm after depositing Al_2O_3/MgF_2 AR stack layers on the single side of the quartz which further decreases to the lower value of about 1.3 % for the double sided AR coating. At 500 nm the percentage reflectance of two-layer AR coating is about 0.3 %. This shows that double-layer AR coating is able to reduce the reflectance of quartz substrate much efficiently as compared to single-layer. However two-layer AR coating is useful for the near monochromatic applications because it shows minimum reflectance at the designed wavelength such as 500-550 nm. But for our purpose we need the AR coatings which have the low reflectance in broad-band range of visible light.

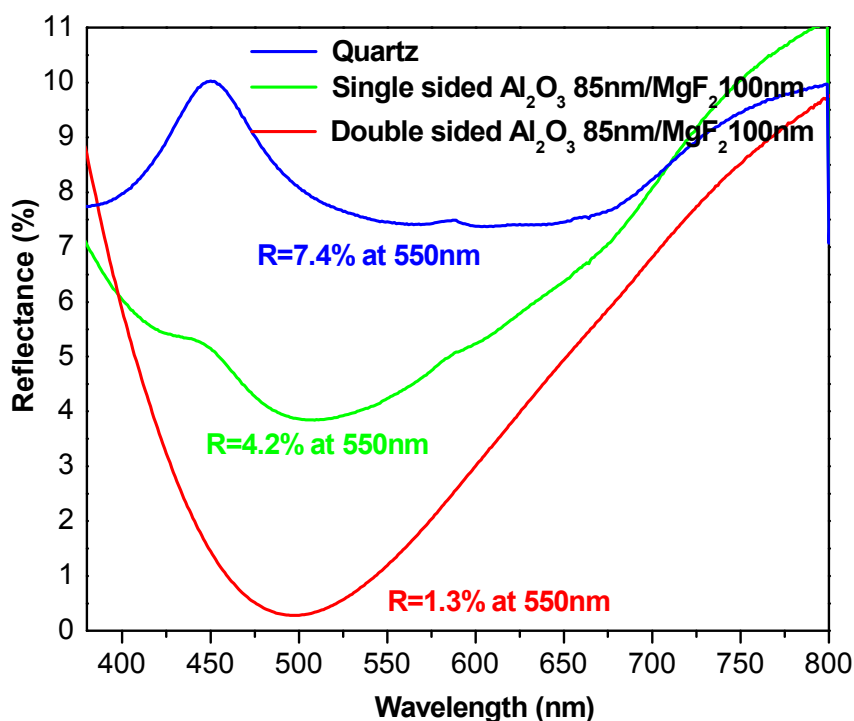


Figure 16: Reflectance spectra of two-layer ($\text{Al}_2\text{O}_3/\text{MgF}_2$) AR coating on quartz substrate.

Broad-band AR coating is synthesized in form of three or four-layer thin film on a quartz substrate. For three layer coating we have sandwiched high RI material like ZrO_2 (2.14) in between two low RI materials like Al_2O_3 (1.63) in the bottom near to substrate and MgF_2 (1.38) as the top layer. Thickness of the ZrO_2 layer is kept one-half of the wavelength ($\lambda/2n$) of interest (550 nm) while the thickness of Al_2O_3 and MgF_2 is kept about one-quarter of the wavelength ($\lambda/4n$). Al_2O_3 and ZrO_2 is deposited in-situ by sputtering while e-beam evaporator is used to deposit MgF_2 . Since it was difficult to obtain a cross-section image of three-layer AR coating thus EDS is used to view three layers by compositional line scan along the cross-section as reported in Figure 17. The figure clearly shows the existence of ZrO_2 layer in between Al_2O_3 and MgF_2 . Figure 18 reports the reflectance spectra in the visible light range of the bare quartz substrate and with three-layer ($\text{Al}_2\text{O}_3/\text{ZrO}_2/\text{MgF}_2$) AR coating. By coating three-layers on single side of quartz

causes the percentage reflectance to decrease in broad-band range of visible light spectrum with a value of about 3.1 % at 550 nm. Surprisingly, on both side coating of these layers does not cause the further decrease in the reflectance value as observed in single and two-layer AR coating. In addition there is disappearance of broad-band antireflection effect by double-side coating. However, even single side three-layer coating is not able to provide the antireflection effect in complete visible light spectrum that is 400-750 nm. The three-layer coating show a cutoff wavelength near 500 nm below which the reflection increases drastically to a very high value (Fig. 18). Thus light in range of 350-500 nm is largely reflected and does not transmit. Thus four-layer AR coating is further developed for broad-band antireflection.

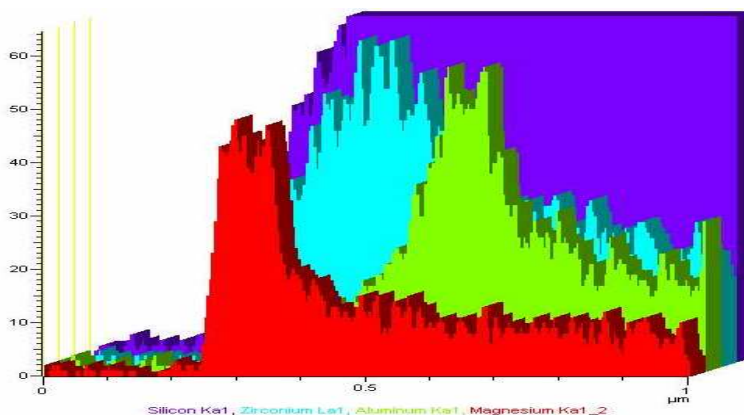


Figure 17: Composition analysis along the cross-section of the three-layer ($Al_2O_3/ZrO_2/MgF_2$) AR coating.

For four-layer coating an additional layer of MgF_2 , with thickness of one-quarter wavelength ($\lambda/4n$), is first deposited on the quartz substrate before depositing the above mentioned three-layer stack film of $Al_2O_3/ZrO_2/MgF_2$. The thickness of each layer is kept same as that for three layer coating. Four-layer coating is clearly visualized in cross-section SEM image as shown in Fig. 19. All the layers are compact and dense similar to single and two-layer AR coating. Figure 20 reports the reflectance spectra in the visible light range of the bare quartz substrate and with four-layer ($MgF_2/Al_2O_3/ZrO_2/MgF_2$) AR coating. By coating four-layers on single side of quartz causes the percentage reflectance to decrease in complete broad-band range of visible light spectrum (400-750 nm) with a value of about 3.9 % at 550 nm. Percentage reflectance decreases further by double sided four-layer AR

coating to a value of 0.8 % in complete broad-band range of visible light spectrum.

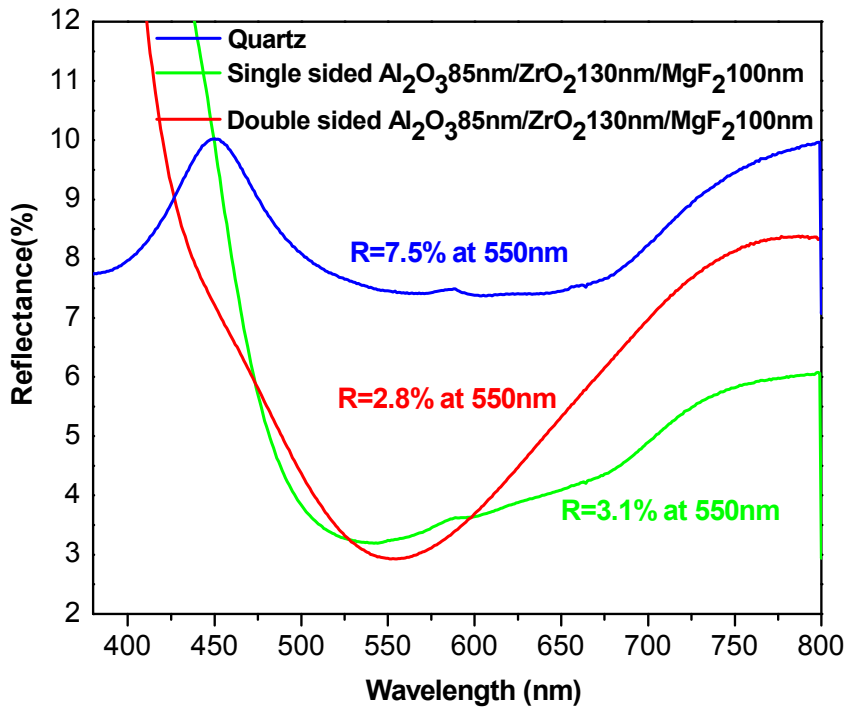


Figure 18: Reflectance spectra of three-layer ($\text{Al}_2\text{O}_3/\text{ZrO}_2/\text{MgF}_2$) AR coating on quartz substrate.

The reflectance spectra are normally obtained with respect to some standard mirror with high reflectance, but in the present case due to unavailability of standard mirror we have used some normal mirror which was not as good as the standard mirror. Thus the peak observed in the reflectance spectra (Fig. 20) at 450 nm is due to the effect caused by local mirror used for the baseline. But for the moment we have observed that four-layer coating of $\text{MgF}_2/\text{Al}_2\text{O}_3/\text{ZrO}_2/\text{MgF}_2$ is efficient to provide antireflection effect in the broad-band visible light range with the reflectance value below 1 %. Comparison of all the different AR coating developed in the present work is reported in figure 21. Thus the quartz window which will be used for the water heating system is coated with four-layer AR coating.

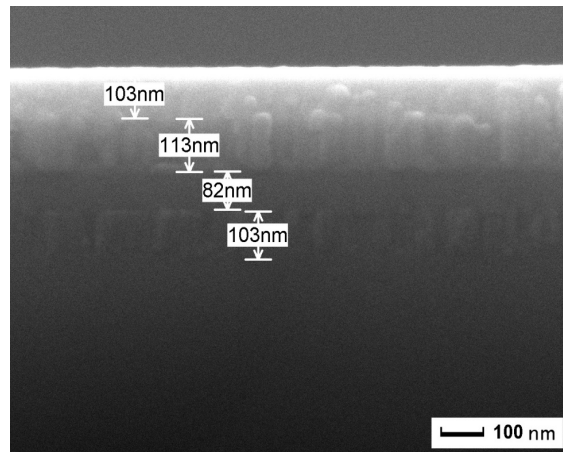


Figure 19: Cross-section SEM micrographs of four-layer ($\text{MgF}_2/\text{Al}_2\text{O}_3/\text{ZrO}_2/\text{MgF}_2$) AR coating.

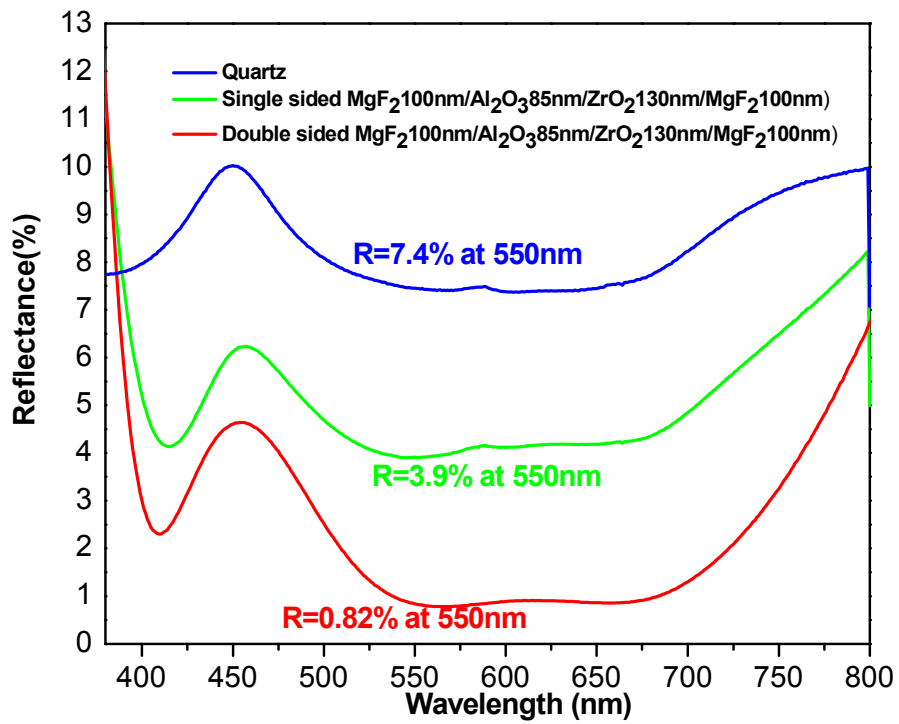


Figure 20: Reflectance spectra of four-layer ($\text{MgF}_2/\text{Al}_2\text{O}_3/\text{ZrO}_2/\text{MgF}_2$) AR coating on quartz substrate.

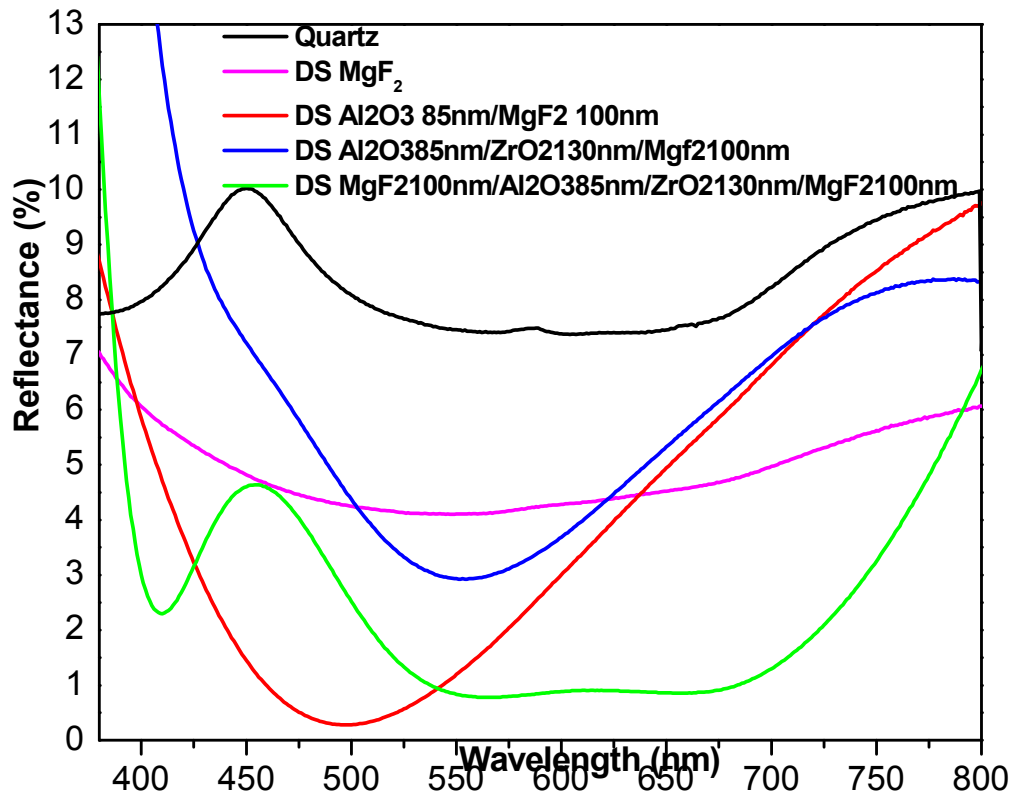


Figure 21: Reflectance spectra of all the different AR coating deposited on double-sided quartz substrate.

3.5 Efficiency of water-heating system:

Fig. 22a and 22b represent heat exchanger system with arrangement for thermocouple connected to black code and real time measurement setup with three mirrors concentrating solar radiation into the heat exchanger for water heating, respectively.



(a)



(b)

Figure 22: (a) Heat exchanger system with arrangement for thermocouple connected to black code. (b) Photograph of real time measurement setup with three mirrors concentrating solar radiation into the heat exchanger for water heating.

ASHRAE 93 standard efficiency testing methodology was used to calculate efficiency for this system which is given by:

$$\eta = \frac{\text{Output power}}{\text{Input power}}$$

Where Output power is given by:

$$O/P = \dot{a} \times C_p \times \Delta T$$

Where \dot{a} = water flow rate (g/sec)

C_p = specific heat of water = 4.18 J/g °C

ΔT = Temperature difference (°C)

Temperature difference (ΔT) of water between inlet and outlet was accurately measured online through computer by using K type thermocouple with swazlock connection as shown in Figure 4a. Water flow rate (\dot{a}) was measured manually as well as by flow meter. Both the parameters (ΔT and \dot{a}) were used to calculate output power which is summarized in Table 1. The calibrated Pyranometer instrument was used to measure global radiation of the sun which was further multiplied with the area of the mirror to obtain input power. Overall system efficiency with i/p and o/p power at different water flow rate is summarized in table 1. The data in the table shows that system is more efficient in converting the solar power at low water flow rates as compared to that at high flow rate (1.87 L/min). This is well understood by the fact that at high flow rate the heat loss due to the conduction is much higher as compared to that at low rates. The overall system efficiency ranges from 65-67 %. However the efficiency value of the system is also calculated by considering only direct radiation from the sun. This value was obtained by subtracting the measured diffuse radiation from the total global radiation. The overall system efficiency is calculated around 75 % by considering only direct radiation. To calculate the heat exchanger efficiency we have considered only 92 % of the input power because the total reflectivity of the mirror is about this value. It shows the heat exchanger efficiency is quite high at around 83 %. The maximum temperature of the water reached by our system is around 72 °C with the flow rate of about 30 L/hour: sufficient for the room or floor heating for residential house as well as for office buildings.

Flow rate (L/min)	Temp Difference (°C)	o/p power (watts)	Radio meter (mV)	Power density (W/m ²)	i/p power (watts)	Overall system efficiency (%)	Overall system efficiency direct (%)	Heat exchanger efficiency (%)
1.875	11.7	1524.95	10	990.09	2524.7	60.39	68.63	74.60
1.2	19.9	1659.97	9.8	970.29	2474.2	67.09	76.45	83.09
0.888	26.7	1648.13	9.7	960.39	2449.0	67.29	76.79	83.47
0.695	32.4	1565.30	9.6	950.49	2423.7	64.58	74.69	81.19
0.455	49.5	1565.61	9.5	940.59	2398.5	65.27	75.62	82.19

Table 1: Performance data of solar concentrator based water heating system

3.6 Comparison with flat plate and vacuum tube collectors:

Now let's make a comparison of our solar concentrator based water heating system with the flat plate or vacuum tube collector available in the market. To do this we have acquired a published data on efficiency of flat plate and vacuum tube collector from the Switzerland based institute Solartechnik Prufung Forschung (SPF) [2] (this institute is involved in measuring the efficiency of the solar water heating system and on providing the performance certificate to the manufacturing companies). They have measured collector efficiency based on the absorber area (A_A) as well as on the collector gross area (A_G). Absorber area is the maximum projected area of an absorber and Gross area is the maximum projected area of a complete solar collector module, exclusive of integral means of mounting and connecting fluid conduits. The efficiency values of the different collectors are shown in table 2 which is directly copied from the published article [7] by the SPF institute. This article also quotes that “*To get information about the quality of the components used in the collector (such as absorber, cover etc.) the efficiency η_A , based on the absorber area is more powerful. However, for the design of a solar energy system it might be more convenient if η is based on the collectors gross area (i.e. η_G)*”. Thus to make comparison with our data on efficiency we have to consider their efficiency value calculated from the gross area (i.e. η_G). The η_G value for the temperature difference of 50

K does not exceed above 50 % for all the collectors while our system overall efficiency for the same ΔT is 65 %, far better than the collectors available in the market. Also make a note that the values indicated in the table 2 are for the best collectors they have measured. In conclusion we have developed heat exchanger for water heating through solar concentrator with the best solar energy conversion efficiency.

values based on area:	<i>vacuum tube</i>		<i>vacuum tube (CPC)</i>		<i>flat plate (TIM)</i>	
	A_A	A_G	$A_A^{(1)}$	A_G	A_A	A_G
$\eta(50K)$ [-]	0.759	0.440	0.566	0.499	0.604	0.483
$U_L(50K)$ [W/(m ² K)]	1.69	0.980	1.04	0.915	2.42	1.94
$\eta(100K)$ [-]	0.625	0.362	0.492	0.433	0.419	0.335
$U_L(100K)$ [W/(m ² K)]	2.59	1.50	1.34	1.18	3.52	2.82
$\eta(150K)$ [-]	0.435	0.252	0.399	0.351	0.164	0.131
$U_L(150K)$ [W/(m ² K)]	3.49	2.02	1.64	1.44	4.62	3.70

Table 2: Summary of the collector test results published by SPF institute.

3.8 Conclusion:

Heat exchanger for water heating using solar concentrated radiation was designed, built, and tested in the present work. Black textured copper oxide as an absorber layer was successfully synthesized on copper substrate by chemical conversion method. This copper oxide absorber layer showed total absorbance (99.8 % to 99 %) of solar radiation at different angle of incidence. The high absorbance property acquired by oxide layer is mainly attributed to its black color and surface textured effect obtained by adopted chemical treatment. This layer also showed long term thermal stability in the hot water surrounding with no significance change in solar absorption. The multilayer AR coating was developed for quartz window to have complete transmittance of incident concentrated solar radiation. By depositing 4 layers AR coating in form of $MgF_2/Al_2O_3/ZrO_2/MgF_2$ on both side of quartz window showed significant reduction in reflectance from 7.4 % (for bare quartz) to 0.82 % (for multilayer coating) for the broad-band visible light range. The combination of good solar absorber (CuO) and AR coating (multilayer film) leads to excellent efficiency of designed water heating system which is far better than commercially available flat plate or vacuum tube collector.

3.7 References

- [1] Solar Water Heating Project Analysis. Minister of Natural Resources Canada 2001 – 2004.
- [2] Kalogirou S. Solar thermal collectors and applications. Progress in Energy and Combustion Science 2004; 30: 231–295
- [3] Orel ZC, Gunde MK, AL ek and Benz N. The preparation and testing of spectral selective paints on different substrates for solar absorbers. Solar Energy 2001;69 : 131-135
- [4] Richharia P, Chopra KL, Bhatnagar MC. Surface analysis of black copper selective coating. Solar energy Materials 1991;23:93-109
- [5] Liu J, Huang X, Li Y, Sulieman KM, He X and Sun F. Hierarchical nanostructures of cupric oxide on a copper substrate: controllable morphology and wettability . J of Materials Chemistry 2006; 16: 4427-4434
- [6] Shanbhogue HG, Nagendra CL, Annapurna MN, Kumar SA, GKM Thutupalli. Multilayer antireflection coatings for the visible and near-infrared regions. Applied optics 1991;36(25): 6341.
- [7] Brunold S, Frey R, Frei U. A comparison of three different collectors for process heat applications. <http://www.spf.ch/publ/kollektoren/procheat.pdf>

Chapter 4

Solar absorber for high temperature application

This chapter presents development of spectral selective solar absorber for high temperature application (700-800°C). Here we select the cermet combination in the form of Ni/Al_xN_(1-x)/AlN metal-dielectric composite multilayer coating as a solar absorber. The chapter is divided into four sections. The first section introduces the various solar absorbers which can be used for high temperature applications. The second section gives details on experimental method and deposition conditions used for the synthesis of cermet multilayer. The third section describes characterization of the cermet coating. The last section concludes that developed cermet film shows a high solar absorbance and low IR thermal emittance even after heat treatment of composite coating at 700°C.

4.1 Introduction

Among the present renewable energy resources, solar energy is considered to be an infinite and easy to handle energy which is available anywhere on the earth. Furthermore, energy obtained from sun is CO₂ free. Concentrating solar power (CSP) systems can utilize the full solar system to convert sunlight to thermal electric power by using solar absorber. One such example is the parabolic dish/Stirling engine systems which converts the thermal energy of solar radiation to mechanical energy and then to electrical energy. Dish/Stirling systems use a mirror array to reflect and concentrate incoming direct normal insolation to a receiver, which transfer sheat to the working medium to achieve the temperatures required to efficiently convert heat to work [1]. Of all solar technologies, dish/engine systems have demonstrated the highest solar-to-electric conversion efficiency (29.4%) [2], and therefore have the potential to become one of the less expensive sources of renewable energy. Dish/Stirling receiver design involves dealing with non-uniform and highly concentrated solar flux at high temperatures (700-800°C) and, therefore, presents a variety of technical challenges.

The solar energy is commonly absorbed by a close-to-black surface with a strong absorption spectrum covering the whole range from the UV to the infrared (IR) with similar efficiency, as in the case of copper oxide mentioned in the previous chapter. However, for the CSP system the heat loss, caused by the reemission of thermal IR rays, reduces the heat transfer from the absorbing surface to a suitable transport medium, such as water or working gas. A solar selective absorber must capture the largest possible amount of solar energy, at the same time minimizing losses by thermal radiation emission. Ideally, these materials should be perfect absorbers over the solar spectrum and perfect reflectors in the thermal infrared (IR). The latter is in order to avoid heat losses due to the emission of radiation from the surface according to Kirchhoff's law. A low reflectance ($\rho \approx 0$) at wavelengths (λ) $\leq 3\mu\text{m}$ and a high reflectance ($\rho \approx 1$) at $\lambda \geq 3\mu\text{m}$ characterize spectrally selective surfaces [3], as shown in Figure 1. For practical reasons, a selective absorber can be considered good if its total emissivity $\varepsilon \leq 0.20$ and absorbance $\alpha \geq 0.90$. This goal is extremely difficult to achieve with a homogeneous material [4]. While composite media,

materials with a rough or porous surface, and multilayered films are the practical candidate for selective material [5–7].

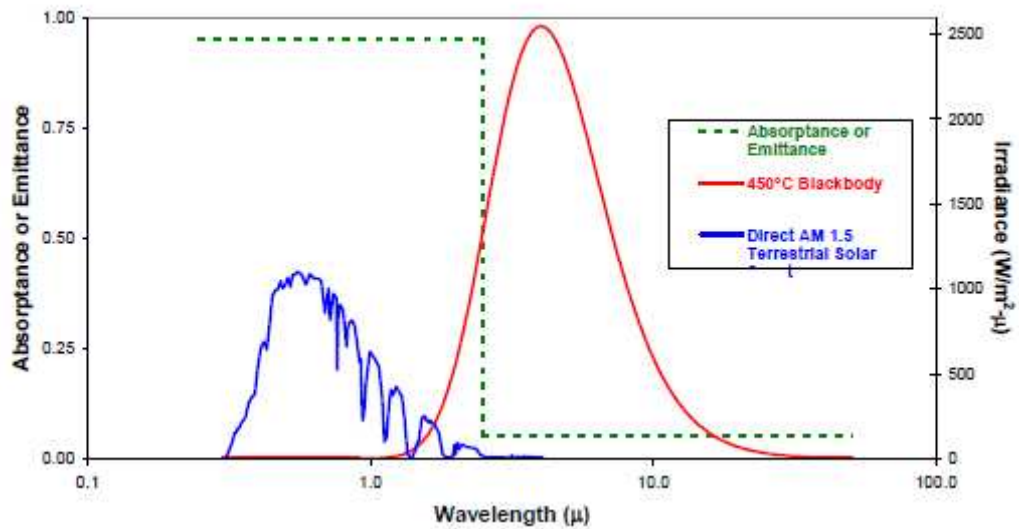


Figure 1: Spectral performance of an ideal selective solar absorber.

The search for selective solar absorbers has to consider a number of aspects. Firstly, the ‘spectral’ properties have to be optimized, i.e., the materials should possess a high absorbance, but should be essentially IR-inactive at high operating temperature. Secondly, the material has to be stable against heat, water, exposure to heat-transfer solvents, and corrosive environments. Thirdly, the components of these materials have to be nontoxic, must be sufficiently cheap, and easy to produce. Among the selective composite materials, cermets are the best to fulfill all these mentioned criteria’s with high thermal stability, which makes them particularly suitable for high-temperature applications in photo-thermal solar energy conversion. Cermets for solar applications usually consist of nanometre-sized metal particles (1–20 nm) embedded in a ceramic binder. This material is deposited over a metallic substrate and may be covered with anti-reflection coatings to enhance their solar absorbance. Also, it has been found that grading the concentration of the metal particles from more dilute near to the front end of the cermet to more dense near to the substrate improves the response. In particular, a system with two cermet layers of different constant concentrations provides the best results [4]. The selectivity of cermets is a tandem effect: the cermet itself absorbs radiation strongly in the region before the cutoff and is almost

transparent in the IR. Meanwhile, the metallic substrate provides high IR reflectance and contributes a small portion of the absorption in the ultraviolet (UV) and visible regions.

Various transition metals—particularly those formed from the refractory metals of groups IVA, VA, and VIA and their binary and ternary compounds—have been suggested for high-temperature applications because of their high melting point and chemical inertness [5]. These materials also have a high degree of spectral selectivity, high hardness, and improved wear, corrosion, and oxidation resistance [6,7]. Large number of cermet solar selective coatings, such as black chrome, Ni-Al₂O₃, SS-C, Al-AlN, Mo-Al₂O₃ etc. [8-10], have been studied which were expected to absorb almost all short wavelength solar radiation and restrain the IR radiation in the wavelength above 2.5 μ m [11]. Al-AlN seems to be the best choice as the solar selective cermet layer not only due to its high melting point and chemical inertness but also the ease to produce this material with low cost. Al-AlN cermet films is deposited by DC reactive sputtering in a gas mixture of argon and nitrogen, and by just varying the N₂ gas pressure during deposition the amount of Al can be conveniently altered in the AlN matrix. This provides big advantage to deposit multilayer film with gradation from surface to substrate in a single step. As reported in literature, the graded cermet multilayer film of Al-AlN deposited by sputtering showed solar absorptance of 0.92 and thermal emittance of 0.06-0.1. These values vary by only small amount when using Al-AlN cermets film at elevated temperatures (700-800 °C) in vacuum and air, thus showing the thermal stability.

In the present work, we developed Al-AlN based multilayer cermet films by RF magnetron sputtering. The 3 or 4 layers film with grading of metal content was synthesized by varying N₂ flow during deposition. The optical properties before and after heat treatment at 700 °C has also been studied.

Characteristics of Selective Surfaces

The performance of a candidate solar absorber can be characterized by its solar absorptance and thermal emittance. They as defined as follows:[12]

$$\alpha = \frac{\int_{\lambda_1=0.3}^{\lambda_2=2.5} [[1 - R(\lambda)]G(\lambda)]d\lambda}{\int_{\lambda_1=0.3}^{\lambda_2=2.5} G(\lambda)d\lambda} \quad (4.1)$$

Where $R(\lambda)$ is reflectance at wavelength λ . $G(\lambda)$ is intensity of solar radiation with air mass 1.5. For instance solar radiance $G(\lambda)$ can be restricted to range between 0.3-2.5 μm .

$$\varepsilon = \frac{\int_{\lambda_1=3}^{\lambda_2=3} [[1 - R(\lambda)]\beta(T, \lambda)]d\lambda}{\int_{\lambda_1=3}^{\lambda_2=50} \beta(T, \lambda)d\lambda} \quad (4.2)$$

Where $\beta(T, \lambda)$ is intensity of black body radiation at operating temperature T of the material which is also restricted to a finite region with limits depending on the value of T .

$$\beta(T, \lambda) = \frac{2\pi hc^2}{\lambda^5} \frac{1}{\exp^{hc/kT\lambda} - 1} \quad (4.3)$$

$f = \frac{\alpha}{\varepsilon}$ is called figure of merit which indicate good spectral selectivity; however the figure of merit is not always well suited to estimate solar thermal power conversion efficiency of optical absorber.

4.2 Experimental Method:

The selective solar absorber multilayer films were synthesized by RF magnetron sputtering. Cermet material in form of $\text{Ni}/\text{Al}_x\text{N}_{(1-x)}/\text{AlN}$ metal-dielectric composite coating was adopted as solar absorber for concentrated radiation. We used stainless steel (SS) as a substrate due to its high stability at elevated temperature and strong corrosion resistance properties. The role of Ni in this combination is to reflect IR radiation above 2500 nm range to provide low emittance value. In addition, Ni is quite stable at elevated temperatures with high melting point and diffusion rate of Ni in SS substrate at high temperature is also very low. $\text{Al}_x\text{N}_{(1-x)}$ act as a absorber layer for UV and visible range of

solar spectrum whereas transparent AlN as the top layer works as anti-reflecting coating to enhance their solar absorptance.

Synthesis of Ni film:

For the Ni film deposition, pure Ni (99%) disc and Ar (99.99%) gas were used as sputtering target and working gas respectively. Before film deposition, the Ni target was pre-sputtered for 10 min in order to remove any surface contamination. Ni film was deposited on glass, Si (100) and SS substrates at room temperature using RF power of 150 W and Ar pressure of 0.8 Pa. Set of Ni samples were deposited by varying time (Table 1 shows variation in thickness at different time) to achieve thickness between 100 to 125 nm. The sample and target distance was kept constant at 7.5 cm for all the samples.

The thickness was measured through cross-section SEM images of the films. Ni thickness of 117 nm (Fig. 2) was selected as the bottom layer because thicker Ni layer might lead to rapid increase in thermal emittance.

Sputtering Time	Thickness of Ni film (nm)
1 hr	2830
20 mins	980
10 mins	469
2.5 mins	140
2 mins	117

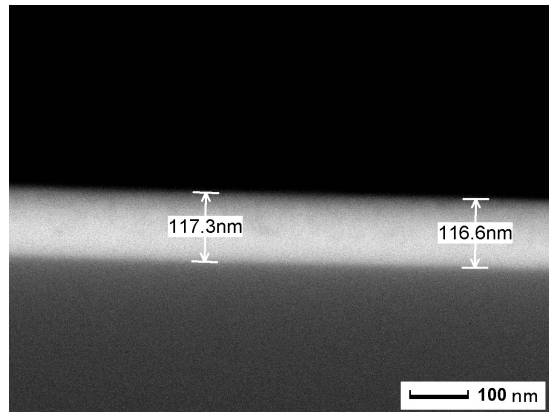


Table 1: Ni thickness, obtained by cross-section SEM as a function of sputtering time

Figure 2: Cross-section SEM image of Ni sputtered for 2 mins

Synthesis of $Al_xN_{(1-x)}$ black film:

For black $Al_xN_{(1-x)}$ film, we used Al (99%) disc as the sputtering target and pure Ar and N_2 (99.99%) as working gases. Before sample deposition the Al target was pre-

sputtered for 30 min in order to remove any surface contamination. During pre-sputtering the gas mixture of Ar and N₂ with pressure of 1Pa was used, in which Ar flow of 28 sccm and N₂ flow of 9 sccm was maintained. Nitrogen gas was introduced during pre-sputtering in order to convert target surface from metallic shiny to black. Al_xN_(1-x) film was deposited on glass, Si (100) and SS substrates at room temperature using RF power of 150 W. The sample and target distance was kept constant at 7.5 cm for all the samples. Al_xN_(1-x) films were deposited with different values of x by varying the N₂ gas flow rate during the deposition. By EDS we analyzed the amount of Al and N as a function of N₂ flow rate in the AlN film and summarized in Table 2. From this measured data, nitrogen flow rate of 3, 5 and 7 sccm was selected to deposit multilayer film with graded layer having Al atomic content of 75% , 60% and 55% in Al_xN_(1-x) film.

N ₂ flow rate (sccm)	N concentration (at%)	Al concentration (at%)
1	1.4	98.6
1.5	11	89
2	13.7	86.3
3	24.3	75.7
4	34.7	65.3
5	41	59
6	41.3	58.7
7	45	55
14	55	45

Table 2: Atomic concentration of Al and N in AlN film deposited under various N₂ gas flow rate during sputtering

To optimize the required thickness of each layer in multilayer film, the single layer of Al_xN_(1-x) film with Al concentration of 75, 60 or 55 at% was deposited separately with constant deposition time of 5 mins. The thickness of the each film was analyzed by using cross-sectional SEM images (Fig. 3).

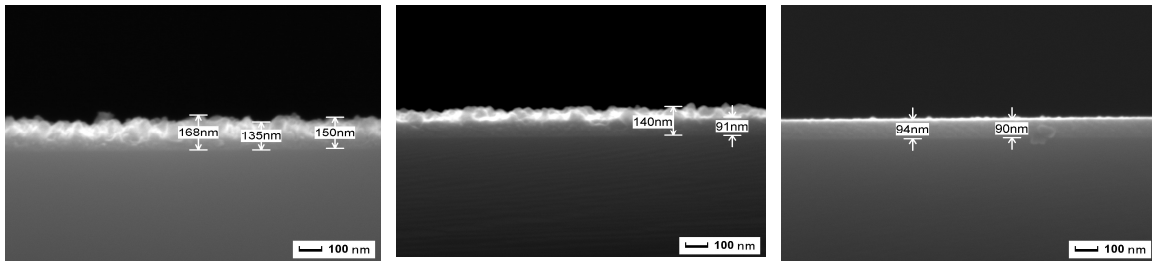


Figure 3: Single layer thickness of $Al_xN_{(1-x)}$ film deposited for 5 mins with different Al concentration a) 75 at.% b) 60 at.% or c) 55 at.%.

Synthesis of anti-reflecting transparent AlN film:

For anti-reflecting coating, AlN disc (99%) and pure Ar and N_2 (99.99%) was used as sputtering target and working gas respectively. Before sample deposition, the AlN target was pre-sputtered for 10 min in order to remove any surface contamination. AlN film was deposited on glass, Si (100) and SS substrates at room temperature using RF power of 150 W and working gas pressure of 0.8 Pa. To obtain favorable thickness of 100 nm, various AlN films were deposited by varying the deposition time. The optimized deposition time was about 11.5 mins to deposit the anti-reflecting AlN film of around 100 nm (as confirmed by cross-section SEM image in Fig. 4).

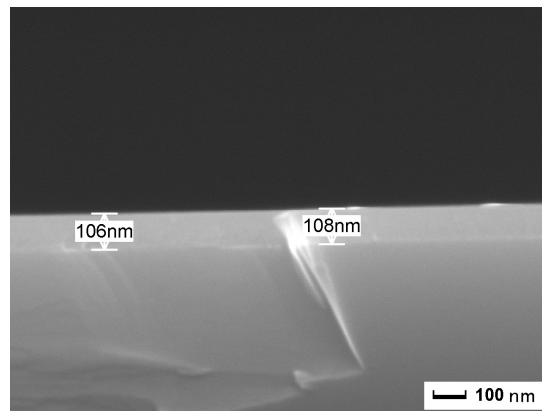


Figure 4: Cross-section SEM image of anti-reflecting transparent AlN film deposited with a time of 11.5 mins.

After optimizing the condition to obtain required thickness and concentration of each layer, the multilayer film was deposited in situ by RF sputtering. Before deposition, SS substrate was polished to obtain mirror like surface and then later cleaned with different

cleaning solutions to remove surface contamination. However, the multilayer films were deposited on SS, glass and Si substrate. Ni film of about 100 nm was first deposited with the condition mentioned above. Then 3 or 4 layers of $Al_xN_{(1-x)}$ with different metal concentration were deposited with varying thickness. Detailed description about these multilayer films in terms of thickness and metal concentration is summarized in table 3. Grading of layers is such that the metal concentration decreases from bottom to top of the film. Thickness of each layer is selected such that there is destructive interference which results in low reflectance and high absorption in the visible range, but metal gradation is more important than layers thickness of the composite film. All the films were covered with transparent AlN film of around 100 nm as an anti-reflecting coating.

Characterization of multilayer films:

The surface morphology and cross-section thickness of all films were studied by scanning electron microscope (SEM-FEG, JSM 7001F, JEOL) equipped with energy-dispersive spectroscopy analysis (EDS, INCA PentaFET-x3) to determine the composition of the samples. Optical measurements in the Ultraviolet (UV), visible and near Infrared (NIR) range were performed in a Bruker IFS66 spectrometer in a reflection mode with incidence angle of 15 degree for incoming beam. Measurements have been performed in the wavelength range between 250 to 2500 nm to obtain the reflectance spectra.

Multilayer films	Layers	Thickness (nm)	Al concentration (at%)
3-layer film (A3)	Ni layer	100	---
	1 st $Al_xN_{(1-x)}$	110	75
	2 nd $Al_xN_{(1-x)}$	60	60
	3 rd $Al_xN_{(1-x)}$	25	55
	AlN (AR film)	100	50
4-layer film (A4)	Ni layer	100	---
	1 st $Al_xN_{(1-x)}$	110	75
	2 nd $Al_xN_{(1-x)}$	60	60
	3 rd $Al_xN_{(1-x)}$	25	55
	4 th $Al_xN_{(1-x)}$	16	52.5
	AlN (AR film)	100	50

Table 3: Detailed description about multilayer films in terms of thickness and metal concentration.

4.3 Results and Discussion:

Multilayer films with 3 and 4 $\text{Al}_x\text{N}_{(1-x)}$ layers are designated as A3 and A4 respectively. Fig. 5a and 5b presents the plot of percentage reflection (%R) as a function of wavelength for A3 and A4 samples respectively. The absorptance value is calculated from the %R in the range of 250 to 2500 nm using equation (1). The absorptance for A3 and A4 on glass is **0.93** and **0.92** and that on SS is **0.86** and **0.875**, respectively (table 4). This indicates that extra fourth layer is insignificant to put any effect on the absorption properties of the absorber film. The difference between the absorptance value for glass and SS substrate is not well understood.

Presently we do not have any facilities in our department to measure %R in far IR range (2.5 to 25 μm) which would assist to calculate thermal emittance of the films. But accordingly to Fig. 1 the selective absorber layer must reflect all the IR light ($\lambda > 2500$ nm) and absorb UV-Vis light ($\lambda < 2500$ nm). So the %R measured for the selective layer should make a rapid transition from 0 to 100 % in the range of 2000 to 5000 nm. Thus to have a rough estimation about the ability of our multilayer films to reflect the IR light we measured the %R value at 2500 nm. Higher reflectance at 2500 nm for the film indicates the rapid transition of %R in IR range and low emittance. So the %R for the 3 and 4 layers film on glass is 44 % and 42 % and that on SS is 46 % and 22 % (table 4) respectively. These results demonstrate that 3 layers has better tendency to reflect IR light than 4 layers films.

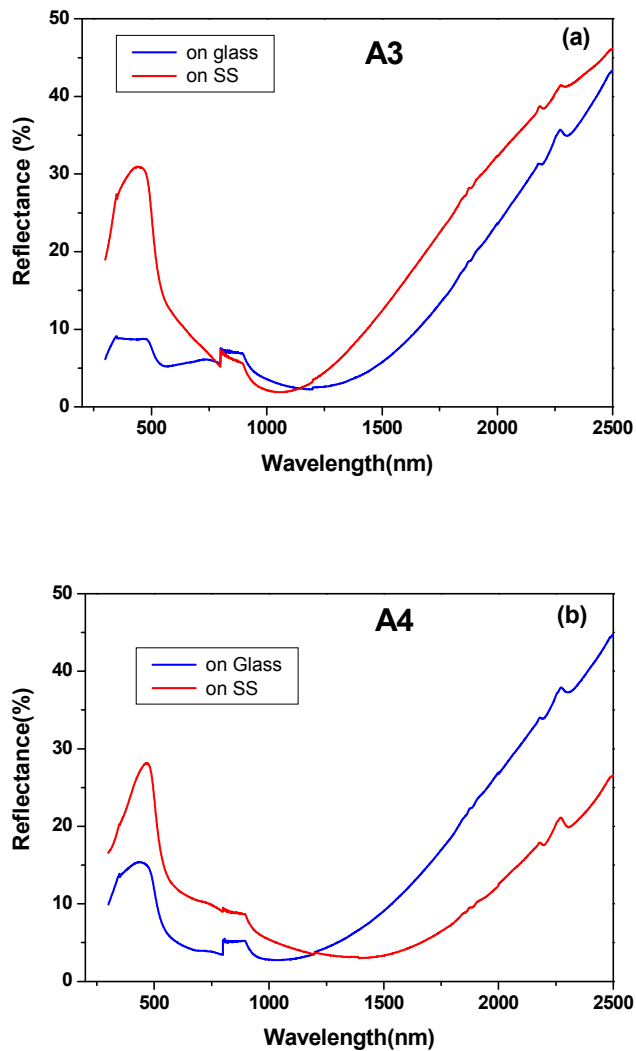


Figure 5: Reflectance spectra of (a) A3 and (b) A4 multilayer films.

To improve the % R at 2500 nm for 4 layers we increased the thickness of each layer by 10 nm. But we found that %R at 2500 nm decreases further (table 4). Therefore, in this study we conclude that between 3 and 4 layers film, there is no much difference in the absorption, but the %R is better for 3 layers film than 4 layer film at wavelength 2500 nm. Thus further studies were conducted by using only 3 layer films.

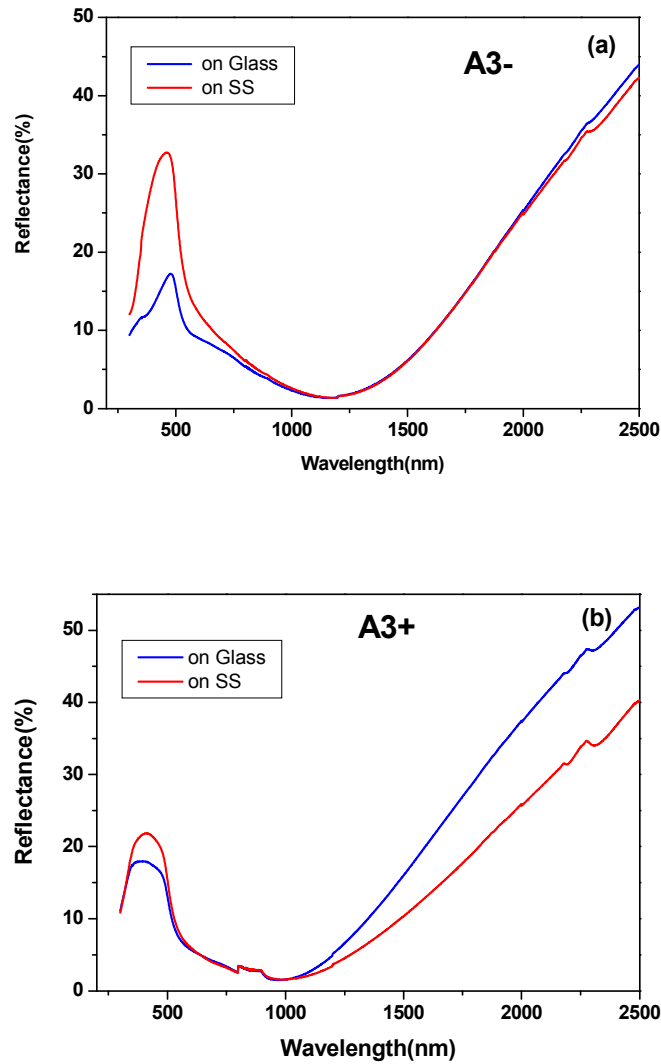


Figure 6: Reflectance spectra of (a) A3- and (b) A3+ multilayer films.

To advance further with 3 layer films, we varied the thickness of each layer of $Al_xN_{(1-x)}$ and measured the %R. We decreased and increased the thickness of each $Al_xN_{(1-x)}$ absorber layer of A3 samples by 10 nm which is designated as A3- and A3+ respectively. Figs. 6a and 6b represents the plot of %R as a function of wavelength for these samples. The absorbance value for A3- and A3+ is 0.91 and 0.935 on glass and 0.86 and 0.90 on SS, while %R at 2500 nm is 41 % and 55 % for glass and 43 % and 42 % for SS respectively (table 4). Comparing these values with that obtained for A3 sample shows that decreasing thickness does not cause any change in optical properties. But by increasing the

thickness there is slight increase in absorptance as well as %R (specially on glass). So we decide to further increase the thickness of each absorber layer of A3 sample by 20 nm which is designated as A3++. The absorptance value increases further to 0.96 and 0.93 on glass and SS respectively. However, the %R at 2500 nm decreases drastically to 28 % and 26 % for glass and SS respectively (table 4).

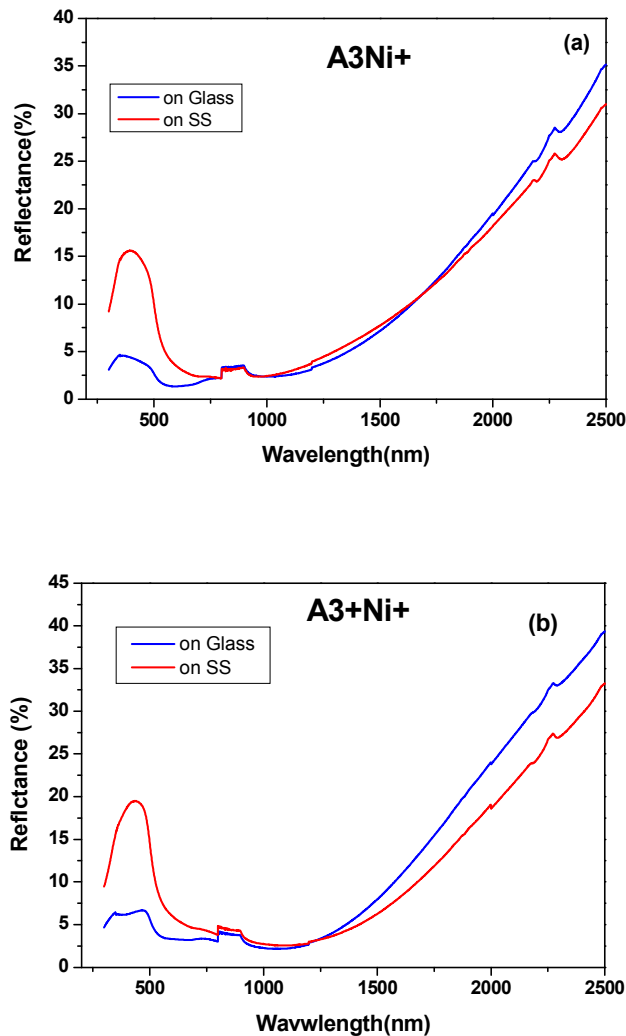


Figure 7: Reflectance spectra of (a) A3Ni+ and (b) A3+Ni+ multilayer films.

These results show that A3+ is the best sample with absorptance more than 0.90 and high %R at 2500 nm. To study the effect of Ni, we increased the thickness of Ni from 100 nm to 200 nm and then deposit A3 and A3+ samples with AlN AR-coating on top. These samples are designated as A3Ni+ and A3+Ni+, and %R reflection graph as function of

wavelength is shown in Fig. 7a and 7b respectively. The absorptance value increases for both A3Ni+ and A3+Ni+ samples to 0.96 and 0.97 for glass and 0.935 and 0.93 for SS respectively (table 4). While % R at 2500 nm was decreased to value of 34 and 28 % for glass and 31 and 26 % for SS, respectively. This shows that increase in Ni thickness causes increment in absorptance value but imposes negative effect on % R at 2500 nm and that on emittance. Between all samples with different configuration we found that A3+ showed very good optical properties with optimized thickness.

AlN Samples	Absorptance		% Reflection at 2500 nm	
	Glass	SS	Glass	SS
A3	0.93	0.86	46 %	43 %
A4	0.92	0.875	44 %	22 %
A4+	0.92	0.90	33 %	16 %
A3-	0.91	0.86	41 %	43 %
A3+	0.935	0.90	55 %	43 %
A3++	0.96	0.93	28 %	26 %
A3Ni+	0.96	0.935	34 %	31 %
A3+Ni+	0.97	0.93	28 %	26 %

Table 4: Absorptance and % R value at 2500 nm for all the multilayer films

This absorber layer will be coated on receiver used in stirling engine where operating temperature is around 700 °C. So we heat treated A3+ and A3+Ni+ samples at 700 °C with holding time of 2 hrs in air or vacuum condition. Only films deposited on SS were used for annealing purpose. % R was measured for these heat treated samples and summarized in table 5 with calculated value of absorptance. The results shows that absorptance and %R (at 2500 nm) does not varies much after heat treatment thus showing the thermal stability of the films.

AlN Samples	Annealing condition	Absorptance	% Reflection at 2500 nm
A3Ni+	In air	0.89	43 %
	Low vacuum (0.1 mbar)	0.885	39 %
	High vacuum (1×10^{-5} mbar)	0.90	42 %
A3+Ni+	In air	0.94	42 %
	Low vacuum (0.1 mbar)	0.91	34 %
	High vacuum (1×10^{-5} mbar)	0.93	41 %

Table 5: Absorptance and % R value heat treated A3Ni+ and A3+Ni+ multilayer films at 700°C for 2 hrs in different conditions.

4.4 Conclusion:

Multilayer cermet films as a solar absorber for high temperature applications were developed by RF-magnetron sputtering. The Cermet material in the form of Ni/Al_xN_(1-x)/AlN metal dielectric composite was deposited on SS and glass substrates with optimized thickness to acquire better optical properties as a solar absorber. The 3 and 4 layers of Al_xN_(1-x) with metal gradation were synthesized with varying thickness and found that 3 layer exhibit highest solar absorptance (more than 0.90) and lowest thermal emittance (%R at 2500 nm). Increasing reflecting Ni layer thickness causes the increment in solar absorptance value but thermal emittance decreases drastically. Heat treatment of multilayer samples at 700 °C for 2 hrs in air and vacuum did not cause major variation in solar absorbance thus showing the thermal stability of the cermet films.

4.5 References:

- [1] <http://theenergylibrary.com/node/451>
- [2] EPRI Report, Performance of the Vanguard Solar Dish-Stirling Engine Module, Electric Power Research Institute, AP 4608, Project 2003-5, July 1986.
- [3] Kennedy CE. Review of Mid- to High-Temperature Solar Selective Absorber Materials NREL July 2002.
- [4] Zhang QC. and Mills DR. New cermet film structures with much improved selectivity for solar thermal applications. *Appl.Phys.Lett.*1992; 60: 545
- [5] JJ Cuomo, JF Ziegler, JM Woodall. A new concept of solar energy thermal conversion. *Appl. Phys. Letters* 1975;26 (10): 557–559.
- [6] Blickensderfer R, Deardorff DK, and Lincoln RL. Spectral reflectance of TiN_x and ZrN_x films as solar selective absorbers.*Solar energy* 1977;19: 429-432; Blickensderfer R, July4,1978; Us patent No.4,098,956.
- [7] Schüler A, Thommen V, Reimann P et al. Structural and optical properties of titanium aluminium nitride films ($Ti_{1-x}Al_xN$).*J. Vac. Sci. Technol* 2001;19: 922–929.
- [8] Ananadan C, William GVK, Rajam KS. Investigation of surface composition of electrodeposited black chrome coatings by X-ray photoelectron spectroscopy. *Appl. Surf. Sci.* 2002; 191 : 254
- [9] Karmhag R, Tesfamichael T, Wackelgard E. Oxidation Kinetics of Nickel Particles: Comparison Between Free Particles and Particles in an Oxide Matrix. *Sol. Energy.* 2000; 68 : 329
- [10] Zhang QC. Metal-AlN cermet solar selective coatings deposited by direct current magnetron sputtering technology. *J. Phys.* 1998; 31: 355
- [11] Zhang QC, Shen YG. High performance W–AlN cermet solar coatings designed by modelling calculations and deposited by DC magnetron sputtering. *Sol. Energy Mater. Sol. Cells.* 2004; 81: 25
- [12] Schon JH, Bucher E. Computer modeling of the performance of some metal/dielectric multilayers for high-temperature solar selective absorbers *Solar energy materials and solar cells* 1996;43: 59-65.

Summary:

Energy is at the heart of most critical economic, environmental and developmental issues facing the world today. Clean, efficient, affordable and reliable energy services are indispensable for global prosperity. This thesis illustrates the key role of renewable energy in a long-term transition towards a clean and sustainable energy future. In presented work we study the essential problems encountered during the hydrogen production from water splitting using TiO₂ Photocatalyst such as low visible light absorption and recombination of photo-generated charges (electron and holes).

1) Hydrogen will likely become the primary energy carrier in the future. However, production of hydrogen for fuel-cells will require catalyst. Thus catalyst in the form of thin film is developed to obtain a pure H₂ from water splitting using solar energy. Using physical method such as RF sputtering and chemical method like sol gel (spin coating) we have successfully synthesized TiO₂ thin film, which is most preferred material to be used as photoanode in H₂ production by photoelectrochemical water splitting. It also has advantage over bulk powder. The depositions of TiO₂ thin film were performed on electrical conducting ITO whose electrical properties play vital role to reduce the photon energy loss. The photo-anodes have been characterized by several techniques to infer on their optical, structural and compositional properties. The H₂ generation rate was measured to be 12.5 ± 0.1 and 4.3 ± 0.1 $\mu\text{mole/h}$ for the sputter and sol-gel deposited TiO₂ films, respectively. The observed differences in hydrogen production have been attributed to the peculiarities in absorption properties of the two TiO₂ films that in the case of sputter-deposited films are more prone to absorb radiation also because of the produced defects during the deposition process.

1A) The hydrogen production obtained by TiO₂ based photoelectrochemical cell is low due to the relatively large band gap E_g of TiO₂ and consequently its poor absorption of visible light. It was found that doping with metal ions may extend the photo-response of TiO₂ into the visible spectrum by introducing additional energy levels in the band gap of TiO₂. This large band gap of TiO₂ has been reduced by doping TiO₂ by transition metals such as Cr and Fe by RF sputtering and sol gel. UV-Visible spectra show that the sputter-metal-doped-TiO₂ films are much more efficient than the chemically

prepared samples to induce red shift of the absorption edge for absorbing visible light. In addition, we proved that dopant atoms must be located, at low concentration, near the ITO–TiO₂ interface to avoid the formation of recombination centres for photo-generated electron–hole pairs. H₂ production rate is higher with Fe-doped TiO₂ (15.5 μmol/h) than with Cr-doped TiO₂ (5.3 μmol/h) because Fe ions trap both electrons and holes thus avoiding recombination. On the other hand, Cr can only trap one type of charge carrier.

1B) TiO₂ doped with Cr ions (9 at.%) shows an increase in the optical absorption efficiency and photons with energy as low as 2.1 eV are absorbed as compared to the lower limit of 3.2 eV for undoped TiO₂. However, in photo-electrochemical cell, negligible photocurrent is measured with ITO/Cr-doped-TiO₂ (9 at.%) single bilayer, a problem that we attribute to the increased recombination rate of the photo-generated charges. It becomes essential to solve the recombination problem of photo-generated charges for metal doped TiO₂. This was achieved by depositing ITO/ doped TiO₂ multilayer films with different numbers of ITO/Cr-doped-TiO₂ (9 at. %) bilayers (namely, 3-, 4-, 5-, 6- and 7-bilayers) by keeping the total thickness of TiO₂ constant. The reduced thickness of the Cr-doped TiO₂ film, deposited on ITO, significantly contributes to reduce the charge recombination rates. This is because the generated photoelectrons, travelling into TiO₂ film of limited thickness, rapidly enter the space charge interface of the ITO/TiO₂ films from where they are instantaneously injected into the ITO layer and then removed towards the cathode of the photo-electrochemical cell: here H⁺ reduction occurs. When the multilayer film is exposed to visible light, we observe that the photocurrent increases as function of the number of bilayers. The maximum value of the photocurrent is obtained with 6-bilayers of ITO/Cr-doped-TiO₂. The enhanced photocurrent is attributed to both higher absorption of visible light by Cr-doped-TiO₂ and to the number of space charge ITO/TiO₂ interfaces in multilayer films. With six bilayers, the H₂ production rate obtained through water-splitting is about 24.4 μmol/h, a value about two times higher than that of pure TiO₂ (12.5 μmol/h).

To further check the multilayer concept we doped TiO₂ with efficient vanadium ions in order to absorb visible light by forming impurity level within the band gap. The results of Vanadium doped TiO₂ has been repeated similarly as Cr-doped TiO₂ multilayer stacks. The hydrogen production rate of 31.2 μmol/h was measured for 6-

bilayers based V6-doped TiO₂ multilayer film and is about 2.5 times higher than that measured with pure TiO₂ film.

Thus in the present work we showed that multilayer structure for metal doped TiO₂ is not only capable of absorbing visible light but also with reduced recombination processes.

- 2) Solar water heating (SWH) systems are mature renewable energy technology which has been accepted in most countries for many years. Heat exchanger for water heating using solar concentrated radiation was designed, built and tested. Black textured copper oxide as an absorber layer was successfully synthesized on copper substrate by chemical conversion method. This copper oxide absorber layer showed total absorbance (99.8 % to 99 %) of solar radiation at different angle of incidence. The high absorbance property acquired by oxide layer is mainly attributed to its black color and surface textured effect obtained by adopted chemical treatment. This layer also showed long term thermal stability in the hot water surrounding with no significance change in solar absorption. The multilayer AR coating was developed for quartz window to have complete transmittance of incident concentrated solar radiation. By depositing 4 layers AR coating in form of MgF₂/Al₂O₃/ZrO₂/MgF₂ on both side of quartz window showed significant reduction in reflectance from 7.4 % (for bare quartz) to 0.82 % (for multilayer coating) for the broad-band visible light range. The combination of good solar absorber (CuO) and AR coating (multilayer film) leads to excellent efficiency of designed water heating system which is far better than commercially available flat plate or vacuum tube collector.
- 3) The spectral selective solar absorber in the form of multilayer cermet film was developed for high temperature application (700-800°C) using RF sputtering. The Cermet material in the form of Ni/Al_xN_(1-x)/AlN metal dielectric composite was deposited on SS and glass substrates with optimized thickness to acquire better optical properties as a solar absorber. The 3 and 4 layers of Al_xN_(1-x) with metal gradation were synthesized with varying thickness and found that 3 layer exhibit highest solar absorbance (more than 0.90) and lowest thermal emittance (%R at 2500 nm). Increasing reflecting Ni layer thickness causes the increment in solar absorbance value but thermal emittance decreases drastically. Heat treatment of multilayer samples at

700 °C for 2 hrs in air and vacuum did not cause major variation in solar absorbance thus showing the thermal stability of the cermet films.

Acknowledgements:

I would like to express my thanks to people who have been very helpful to me during time of my PhD.

First and foremost, I like to convey my deepest gratitude to my Supervisor **Prof. Antonio Miotello** for giving me opportunity to work in his lab. I appreciate in particular his support and assistance throughout my study. I am very grateful for his patience, motivation, enthusiasm, and immense knowledge, taken together, make him a great guide.

Secondly I am absolutely indebted to my co-advisor who is also my beloved husband **Dr. Nainesh Patel** for his brilliant academic guidance, constant encouragement and valuable input regarding my work. Without his understanding, patience and emotional support, I could not have finished this dissertation successfully. His help started from the first day of this thesis and never stopped until the end of the thesis. I dedicate my every achievement to him. He is my solely origin of success and happiness.

I am greatly thankful to my **dear parents** and my **dear mother in law** for giving me constant support. From thousands of kilometres, they provided me love, hope and happiness.

Let me also say 'thanks' to all my group members. Start with **Cludio Cestari** who is great technician I ever met. He is the one who built my experimental set up. Without this set up my PhD degree would have incomplete. Secondly **Nicola Bazzanella** for SEM analysis and also giving co-operation in lab work. I like to thank **Marco Adami** and **Alessandra Santini** for giving assistance in my research activity. I wish to thank **Damiano Avi** for providing Gas Chromatographer and FTIR measurement. Thanks to **Cristina Armellini** for XRD measurement. I am extending my thanks to **Marco Betonte** for solar water heating measurement.

I also thank to **Prof. D.C. Kothari** and **Prof Arun narsale** for their motivation. I would like to thank to my Indian colleague **Rohan Fernandes** and **Dr. Ashwin kale** for their helpful hands and company in the working atmosphere.

My time at Trento was made enjoyable in large part due to the many friends I have made along the way and that became a part of my life. I like to thank all my friends with whom I had a nice time with having parties, talking. My special thanks to **Archana**

Bajpai who is my close mate, I surely will miss you in India. Thanks to **Ahmed & Qadir** for their delicious recipes which I learned from them during my stay in Italy. Thanks to **Seema Ahmad, Deepa Fernandes, Kiran Baktha, Devendra Saroj, G.R.Gangadharan and indian volleyball team and rest** (who's name I missed) for your company and lots of enjoyment.

Finally I would like to mention the name of the most beautiful city **Trento** where I feel like my second hometown. I will miss its beauty of mountain, trekking, snow and time spent in this stunning valley.

List of Publications:

- [1] **R. Dholam**, N. Patel, M. Adami, A. Miotello, *Physically and chemically synthesized TiO₂ composite thin films for hydrogen production by photocatalytic water splitting.* **International Journal of Hydrogen energy** 33 (2008) 6896.
- [2] **R. Dholam**, N. Patel, M. Adami, A. Miotello, *Hydrogen production by photocatalytic water-splitting using Cr- or Fe-doped TiO₂ composite thin films photocatalyst.* **International Journal of Hydrogen energy** 34 (2009) 5337.
- [3] **R. Dholam**, N. Patel, A. Santini, A. Miotello, *Efficient indium tin oxide/Cr-doped-TiO₂ multilayer thin films for H₂ production by photocatalytic water-splitting.* **International Journal of Hydrogen energy** 35 (2010) 9581.
- [4] **R. Dholam**, N. Patel, A. Miotello, *Efficient Hydrogen production using vanadium doped TiO₂ thin film and comparison with other transition doped TiO₂ thin films.* **Under preparation.**
- [5] R. Fernandes, N. Patel, **R. Dholam**, M. Adami, A. Miotello, *Low energy ion beam modification of TiO₂ photocatalyst thin film for visible light absorption.* **Surface & Coatings Technology** 203 (2009) 2579.

APPENDIX:

Synthesis methods for TiO₂ thin film

TiO₂ can be prepared in the form of powder, crystals, or thin films. Both powders and films can be built up from crystallites ranging from a few nanometres to several micrometers. Thin films have advantage over powder in terms of the surface area which is the most important property required by catalyst. The surface morphology of the thin film can be varied with an ease by using different deposition conditions and by decreasing the thickness of thin film, the high surface to volume ratio can be obtained which in turn enhances the properties of the material. One more advantage of thin film prevail over powder is reusability of the films. Following paragraph explains the experimental techniques used in our lab for synthesis of TiO₂ films.

1) RF Sputtering:



RF sputtering

Sputter deposition is a physical vapor deposition process for depositing thin films, sputtering means ejecting material from a target and depositing it on a substrate such as a silicon wafer. The target is the source material. Substrates are placed in a vacuum chamber and are pumped down to a prescribed process pressure. Sputtering starts when a negative charge is applied to the target material causing a plasma or glow discharge. Positive charged gas ions generated in the plasma region are attracted to the negatively biased target plate at a very high speed. This collision creates a momentum transfer and ejects atomic size particles from the target. These particles are deposited as a thin film into the surface of the substrates.

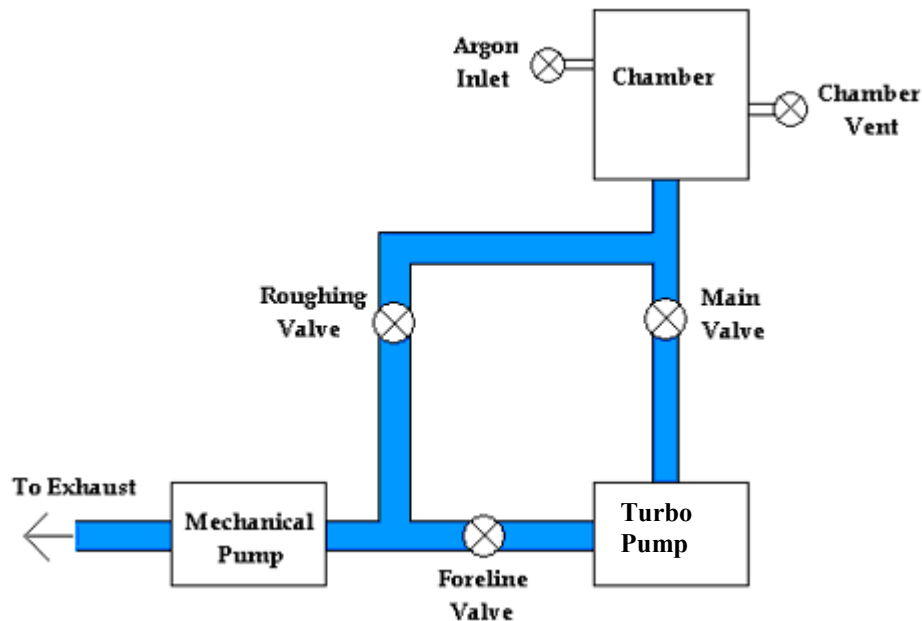
Sputtering is extensively used in the semiconductor industry to deposit thin films of various materials in integrated circuits processing. Thin anti reflection coatings on glass, which are useful for optical applications are also deposited by sputtering. Because of the low substrate temperatures used, sputtering is an ideal method to deposit contact metals for

thin- film transistors. This technique is also used to fabricate thin film sensors, photovoltaic thin films (solar cells), metal cantilevers and interconnects etc.

Sputtering can be done either in DC or RF modes. DC sputtering is done with conducting materials. If the target is a non conducting material the positive charge will build up on the material and it will stop sputtering. RF sputtering can be done for both conducting and non conducting materials. Here, magnets are used to increase the percentage of electrons that take part in ionization of events and thereby increase the probability of electrons striking the Argon atoms, increase the length of the electron path, and hence increase the ionization efficiency significantly.

Operation procedure for RF sputtering system

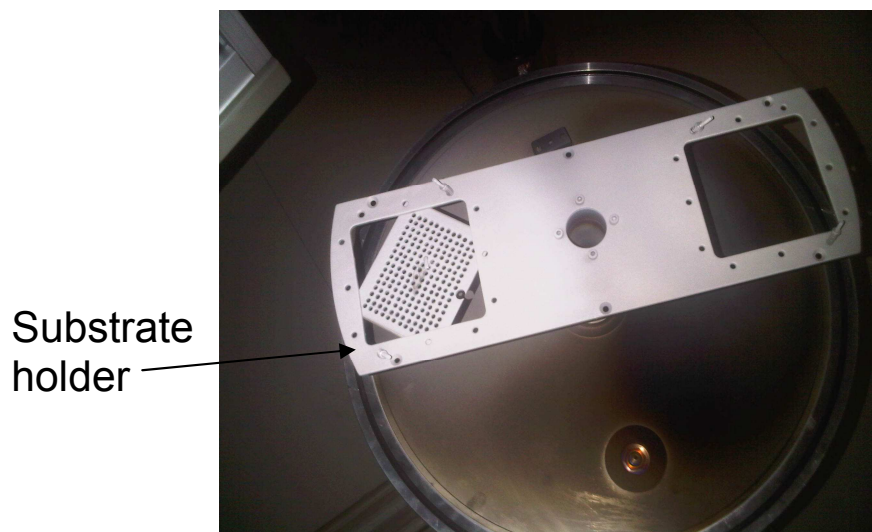
Block Diagram for evacuation system



A. Sample loading procedure:

1. Fix the target material on cathode and the thickness of target material should not exceed over 5mm.
2. Mount the substrate on the substrate holding plate; which can be found on the sputtering system itself.

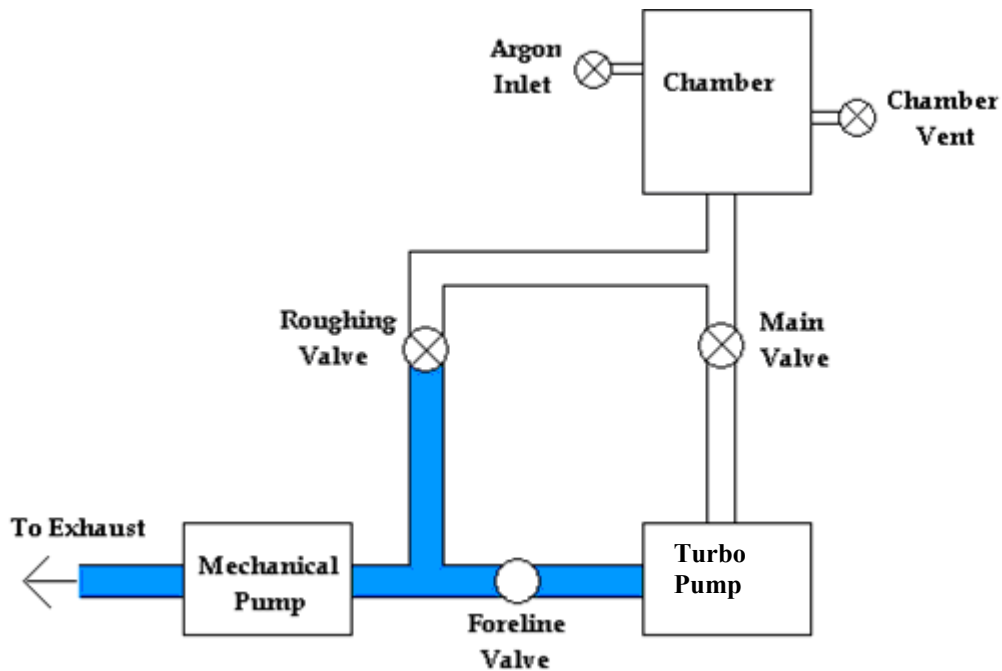
(The area of uniform deposition, to a great extent depends on the distance of target and the holder; though it depends on the gas pressure, sputtering power and the target material also).



3. Fix the substrate holding plate onto the substrate holder inside the chamber.
4. CLOSE the vacuum chamber.

i. Starting up of system/ Turbomolecular Pump (TP):

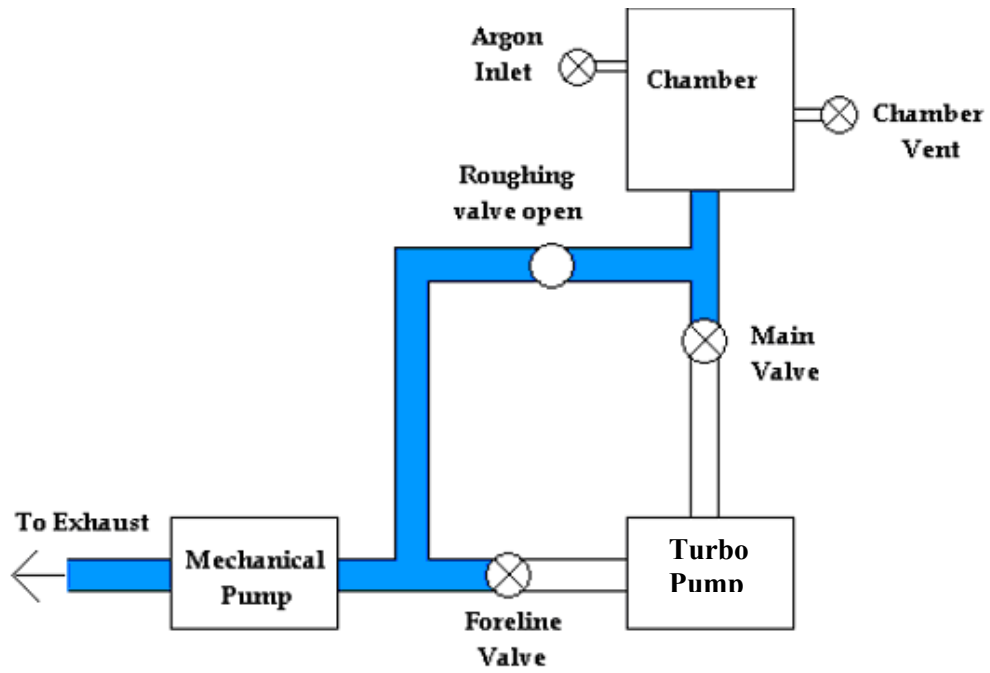
1. Switch On the chiller, open water inlet valve and check for water circulation.
2. Before starting up of TP, the status of each valves have to be confirmed as follows;
Main valve.....CLOSE
Roughing valveCLOSE
Foreline (backing) valve.....CLOSE
Chamber vent valve.....CLOSE
3. Turn ON the main power switch and rotary pump (RP) switch.
4. After RP working noise becomes small, OPEN backing valve and turn ON TP switch.



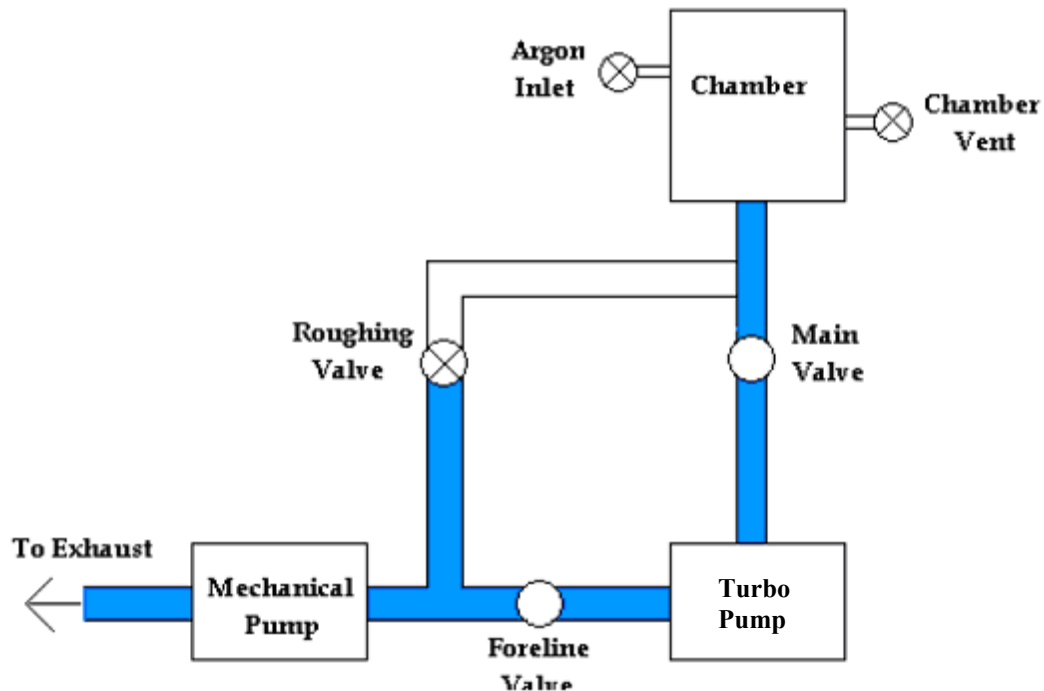
5. After approx.20 min DP will start by itself.

C. Creation of vacuum:

1. OPEN roughing valve and wait till the pressure on Pirani gauge shows 0.05mbar (approx 15min).



2. CLOSE roughing valve and OPEN backing valve.
3. Pour liquid nitrogen through LN2 trap.
4. Open main valve.



5. Switch ON the Pirani gauge and wait till chamber pressure reaches 2×10^{-5} mbar

D. Setting of deposition pressure:

1. Once the vacuum reaches to 2×10^{-5} milli bar; introduce Argon gas (Ar) to the chamber by opening the argon inlet valve gradually. Please be careful not to exceed the pressure over 2×10^{-2} mbar to protect TP performance.
2. Close the main valve gradually so as to approach the deposition pressure.
3. Confirm if the pressure is stable.

Note: The deposition rate for any given material depends on the deposition pressure. Hence for reproducible results use same values.

4. Flush argon for 5 min; ie leave it in the set deposition pressure condition (this is done to flush out the air molecules if any are left after evacuation)

E. Sputtering:

1. Before starting to sputter make sure that the right cathode is selected (as the system has 3 targets), using the cathode selection switch. Same applies to the cathode shutter.

2. After glow discharge occurs, set matching again as RF controller incident power meter to maximum and reflected power to minimum.
3. Carry out the Pre sputtering on the condition slide shutter is CLOSED to clean the substrate surface, remove oxide layer and discharge conditioning. The Pre sputtering time depends on the sort of material to be deposited and aimed film property.
4. OPEN the slide shutter to perform main sputtering after Pre sputtering.
5. Once finished close the slide shutter.
6. If there are more than 1 sample to be sputtered then move the samples using substrate motion control panel.
7. Repeat the same process for other samples.
8. For multi-material sputtering; after finishing one material decrease the voltage; change the cathode selector and cathode shutter. Repeat the same process again.

Sputtering can be done in either DC or RF modes

DC sputtering:

- DC sputtering is done with conducting materials.
- If target is non-conducting material, the positive charge will built up on target material and stops sputtering

RF sputtering:

- Both conducting and non-conducting materials can be sputtered.
- Higher sputter rate at lower pressure.

Advantages of vacuum deposition:

- Reducing the particle density so that the mean free path for collision is long.
- Reducing the contaminants
- Low pressure plasma environment

ADVANTAGES OF MAGNETRON SPUTTERING

□ Here magnets are used to increase the percentage of electrons that take part in ionization events, increase probability of electrons striking Argon, increase electron path length, so the ionization efficiency is increased significantly.

□ **Other reasons to use magnets:**

- Lower voltage needed to strike plasma.
- Controls uniformity.
- Reduce wafer heating from electron bombardment.
- Increased deposition rate

Operating parameters:

- Argon pressure
- Sputter voltage
- Substrate temperature
- Substrate to target distance
- Deposition time

Comparison of Thermal Evaporation and Sputtering:

Evaporation	Sputtering
Low energy atoms	High energy atoms
High vacuum path	Low vacuum path
Few collision	Many collision
Larger grain size	Smaller grain size
Poorer adhesion	Better adhesion

II) Sol gel method:

In sol gel method, TiO₂ thin film deposited by spin coating technique. Spin coating is a procedure used to apply uniform thin films to flat substrates. This technique utilizes centrifugal forces created by a spinning substrate to spread a coating solution evenly over a surface. This coating technique is quick and efficient. It can be used on a laboratory scale as well as in a production setting. Some technologies that depend heavily on high quality spin coated layers are:

- Photo-resist for defining patterns in microcircuit fabrication.
- Dielectric/insulating layers for microcircuit fabrication – polymers, SOG, etc.
- Magnetic disk coatings - magnetic particle suspensions, head lubricants, etc.
- Flat screen display coatings. - Antireflection coatings, conductive oxide, etc.
- Compact Disks – DVD, CD ROM, etc.
- Television tube phosphor and antireflection coatings.

Basic Process: There are four distinct stages involved in the spin coating process

1. Dispense Stage: The deposition process involves dispense of an excessive amount of fluid onto a stationary or slowly spinning substrate. The fluid is deposited through a nozzle at the centre of the substrate or over some programmed path. An excessive amount of fluid is used to prevent coating discontinuities caused by the fluid front drying prior to it reaching the wafer edge. For many solutions it is often beneficial to dispense through a sub micron sized filter to eliminate particles that could lead to flaws.

2. Spin up Stage: In the spin up stage, the substrate is accelerated to the final spin speed. As rotational forces are transferred upward through the fluid which forms a wave front and flows to the substrate edge by centrifugal force, leaving a fairly uniform layer behind.

3. Spin off Stage: The spin off stage is the spin coating stage where the excess solvent is flung off the substrate surface as it rotates at speeds between 2000 and 8000 RPMs. The

fluid is being thinned primarily by centrifugal forces until enough solvent has been removed to increase viscosity to a level where flow ceases. The spin off stage takes place for approximately 10 seconds after spin up.

4. *Evaporation Stage:* Evaporation is the complex process by which a portion of the excess solvent is absorbed into the atmosphere. If significant evaporation occurs prematurely, a solid skin forms on the fluid surface which impedes the evaporation of solvent trapped under this skin and, when subjected to the centrifugal forces of the spinning substrate causes coating defects.

Stage 3 (flow controlled) and Stage 4 (evaporation controlled) are the two stages that have the most impact on final coating thickness. *Figure 8* represents different stages in spin coating.

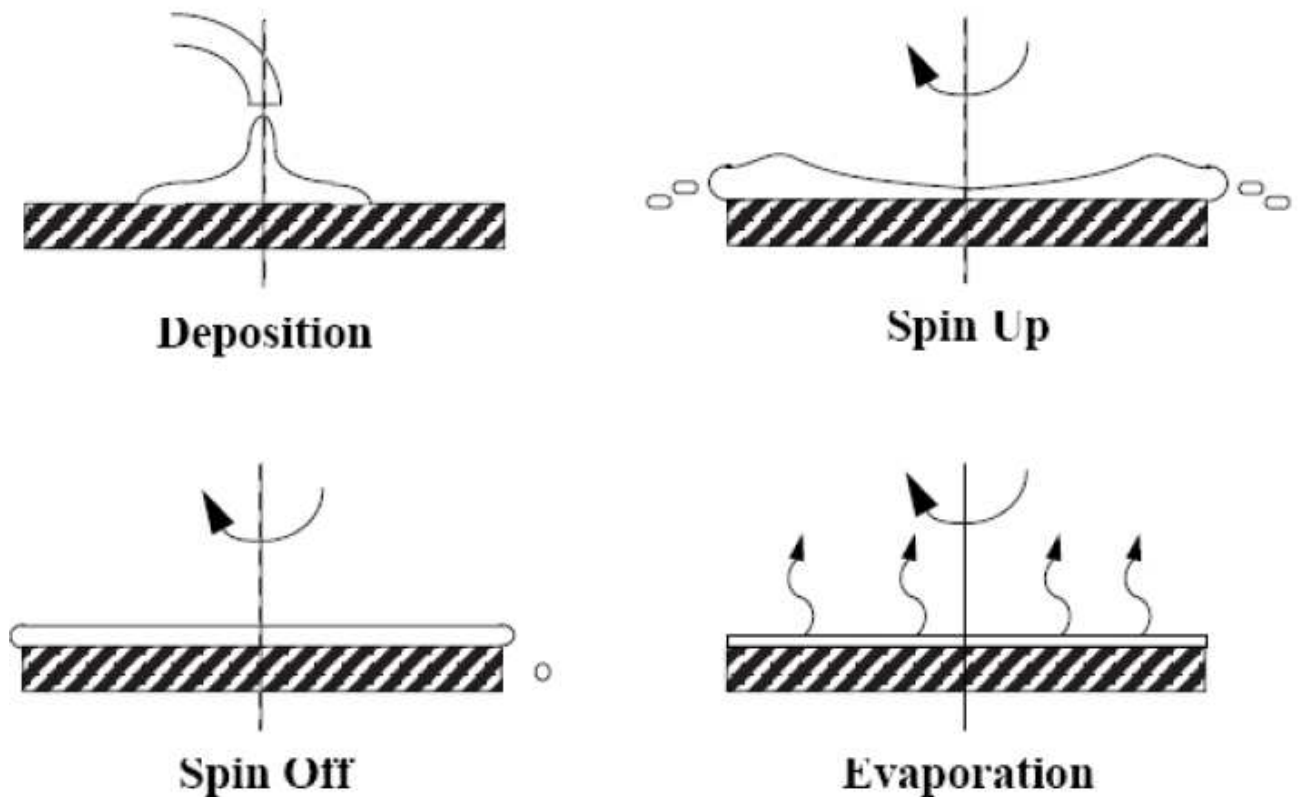


Figure 8: Four different stages involved during spin coating.

Deposition parameters: The process parameters that control this coating procedure are dispensing amount and location, spin speed, spin time and acceleration/deceleration rate. A minimum amount of coating solution must be applied to fully cover the substrate. To do this, an excess of coating solution is required. As the sample spins at higher spin speed, rotational acceleration and the force on the liquid increases. Correspondingly, the amount of liquid forced from the sample is also increased, leaving a lower coating coverage or thickness. Similarly, if the sample is spun for longer time more coating solution is removed over the substrate. So this means that by controlling the spin speed and time the final thickness of the film is varied. The effect of spin time on coating coverage is large for short time periods, but as the time increases a point of diminishing returns will occur, and the influence is minimal. In addition to centrifugal forces that are used to spread the liquid over the surface, there is also force due to acceleration from low to high spin speed. This acceleration will influence the final coating coverage.

In addition to spin coating parameter the solution properties must also be considered when designing a spin-coating profile. The viscosity of the solution must be low enough to cover the substrate surface during spinning. As in any coating application, the surface tension of the coating must be appropriately matched with the substrate that is being coated upon. If a surface tension mismatch, the coating will not completely wet out and thus leaving behind defects in the coating.

Experimental set-up: Spin coating system is basically consists of vacuum chuck attached to the vacuum pump to hold the substrate during rotation. Schematic diagram of basic spin coater is shown in figure 9 (a). Motor is used to rotate the vacuum chuck at different speed controlled by a digital control unit. The body of our spin coater (SPS spin150) is made of Natural Polypropilene (NPP) (figure 9 (b)). Maximum speed of 6000 rpm with maximum acceleration of about 3000 rpm per second is attainable by our system with accuracy of 1 rpm/second. This spin coater can be programmed upto 20 programs with 99 steps per program.

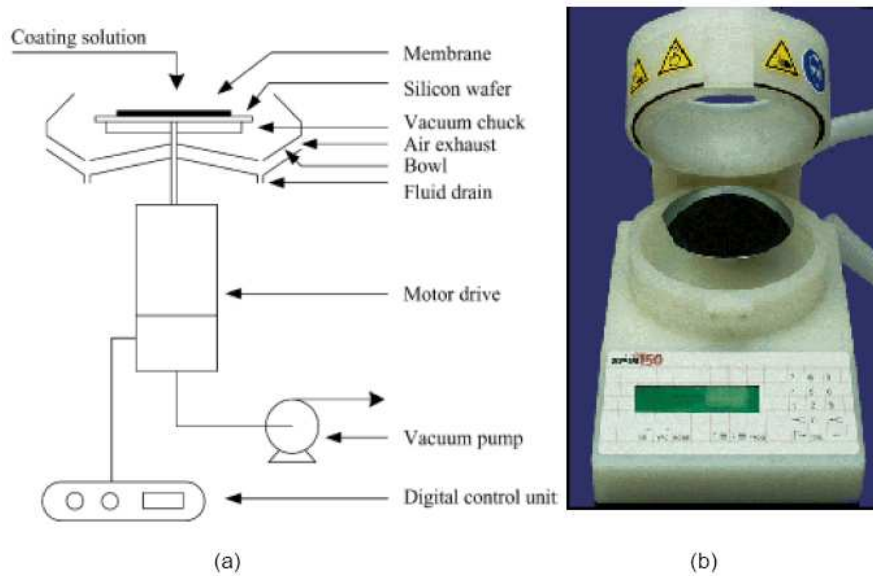


Figure 9: (a) Principle schematic diagram of spin coater. (b) Our SPS spin 150 spin coater.

Advantages:

1. Film thicknesses are easily changed by changing the spin speed, or switching to a different viscosity solution.
2. Another advantage of spin coating is the ability of the film to get progressively more uniform as it thins, and if the film ever becomes completely uniform during the coating process, it will remain so for the duration of the process.
3. Easy to handle, compact and low cost.

Disadvantages:

1. As substrate sizes get larger, the throughput of the spin coating process decreases. Large substrates cannot be spun at a sufficiently high rate in order to allow the film to thin and dry in a timely manner resulting in decreased throughput.
2. The biggest disadvantage of spin coating is its lack of material efficiency. Typical spin coating processes utilize only 2-5 % of the material dispensed onto the substrate, while the remaining 95-98 % is flung off into the coating bowl and disposed. This increases the prices of the raw materials as well as increases disposal costs.

